



THE UNIVERSITY OF
WAIKATO
Te Whare Wānanga o Waikato

Research Commons

<http://researchcommons.waikato.ac.nz/>

Research Commons at the University of Waikato

Copyright Statement:

The digital copy of this thesis is protected by the Copyright Act 1994 (New Zealand).

The thesis may be consulted by you, provided you comply with the provisions of the Act and the following conditions of use:

- Any use you make of these documents or images must be for research or private study purposes only, and you may not make them available to any other person.
- Authors control the copyright of their thesis. You will recognise the author's right to be identified as the author of the thesis, and due acknowledgement will be made to the author where appropriate.
- You will obtain the author's permission before publishing any material from the thesis.

**Determining estuarine seagrass density measures
from low altitude multispectral imagery flown by
remotely piloted aircraft.**

A thesis
submitted in fulfilment
of the requirements for the degree
of

Doctor of Philosophy in Biological Sciences

at
The University of Waikato
by

Ross D. Martin



THE UNIVERSITY OF
WAIKATO
Tē Whare Wānanga o Waikato

2020

Abstract

Seagrass is the subject of significant conservation research. Seagrass is ecologically important and of significant value to human interests. Many seagrass species are thought to be in decline. Degradation of seagrass populations are linked to anthropogenic environmental issues. Effective management requires robust monitoring that is affordable at large scale. Remote sensing methods using satellite and aircraft imagery enable mapping of seagrass populations at landscape scale.

Aerial monitoring of a seagrass population can require imagery of high spatial and/or spectral resolution for successful feature extraction across all levels of seagrass density. Remotely piloted aircraft (RPA) can operate close to the ground under precise flight control enabling repeated surveys in high detail with accurate revisit-positioning.

This study evaluates a method for assessing intertidal estuarine seagrass (*Zostera muelleri*) presence/absence and coverage density using multispectral imagery collected by a remotely piloted aircraft (RPA) flying at 30 m above the estuary surface (2.7 cm ground sampling distance). The research was conducted at Wharekawa Harbour on the eastern coast of the Coromandel Peninsula, North Island, New Zealand.

Differential drainage of residual ebb waters from the surface of an estuary at low tide creates a mosaic of drying sediment, draining surface and static shallow pooling that has potential to interfere with spectral observations. The field surveys demonstrated that despite minor shifts in the spectral coordinates of seagrass and other surface material, there was no apparent difference in image classification outcome from the time of bulk tidal water clearance to the time of returning tidal flood.

For the survey specification tested, classification accuracy increased with decreasing segmentation scale. Pixel-based image analysis (PBIA) achieved higher classification accuracy than object-based image analysis (OBIA) assessed at a range of segmentation scales. Contaminating objects such as shells and detritus can become aggregated within polygon objects when OBIA is applied but remain as isolated objects under PBIA at this image resolution. There was clear separability of spectra for seagrass and sediment, but shell and detritus confounded the classification of seagrass density in some situations. High density seagrass was distinct from sediment, but classification error arose for sparse seagrass.

Three classifiers (linear discriminant analysis, support vector machine and random forest) and three feature selection options (no selection, collinearity reduction and recursive feature elimination) were assessed for effect on classification performance. The random forest classifier yielded the highest classification accuracy, with no accuracy benefit gained from collinearity reduction or recursive feature elimination. Spectral

vegetation indices and texture layers substantially improved classification accuracy. Object geometry made a negligible contribution to classification accuracy using mean-shift segmentation at this image-scale.

The method achieved classification of seagrass density with up to 84% accuracy on a three-tier end-member class scale (low, medium, and high density) when using training data formed using visual interpretation of ground reference photography, and up to 93% accuracy using precisely measured seagrass leaf-area. Visual interpretation agreed with precisely measured seagrass leaf area 88% of the time with some misattribution at mid-density. Visual interpretation was substantially faster to apply than measuring the leaf area. A decile class scale for seagrass density correlated with actual leaf area measures more than the three-tier scale, however, was less accurate for absolute class attribution.

The research demonstrates that seagrass feature extraction from RPA-flown imagery is a feasible and repeatable option for seagrass population monitoring and environmental reporting. Further calibration is required for whole- and multi-estuary application.

Acknowledgements

I am very grateful for the direction and guidance of my supervisors Dr. Joanne Ellis, Prof. Marnie Campbell, and to Prof. Chris Battershill, Dr. Lars Brabyn and Prof. James Brasington who provided supervision at various periods of the research. Sincere thanks to the project funders Waikato Regional Council, Bay of Plenty Regional Council, New Zealand Coastal Society, and to the University of Waikato for three years of Doctoral Scholarship. Thanks to SAFE for their FME Desktop software grant. Thanks to Lyn Hunt and Steven Miller for statistical advice, and Dr. Fleur Matheson, Dr. Hannah Jones and Dr. Lars Brabyn for project design considerations. Thanks to Dean Sandwell, Cheryl Ward, Dr. Matthew Allan, Dr. Moritz Lehman, Dr. Lee Streeter and Assoc. Prof. Michael Mucalo for advice and expert knowledge. Thanks also to Gill Lawrence for making rectified historical imagery available. Thanks to Robert Schoonderwoerd for estuary site access through the forestry block, and to Alan Bridson for access across the paddocks. Thanks to Dr Charlie Lee for making available the large processing computer. Thanks also to Dean Sandwell, Prof. Marnie Campbell, Ella van Gool, and Paola Rodríguez Salinas for assistance in the field. Endless thanks to my partner Pippa Wallace for support and inspiration during the PhD years.

Table of Contents

Abstract.....	ii
Acknowledgements.....	iv
Table of Contents.....	v
List of Figures.....	x
List of Tables.....	xv
List of Abbreviations.....	xviii

Chapter 1. Introduction, objectives and approach

1.1 Research context and justification.....	1
1.2 Thesis Objectives.....	4
1.2.1 Overarching purpose.....	4
1.2.2 Research questions.....	5
1.3 Thesis structure.....	5

Chapter 2. Background literature review - seagrass and remote sensing

2.1 Introduction.....	10
2.2 Chapter objectives.....	12
2.3 Seagrass ecology.....	12
2.3.1 Seagrass in New Zealand.....	12
2.3.2 Ecological role and ecosystem services.....	14
2.3.3 Seagrass degradation and decline.....	15
2.3.4 Seagrass seasonality and patch dynamics.....	18
2.3.5 Measurement of seagrass extent and condition.....	19
2.4 Overview of remote sensing for seagrass mapping.....	21
2.4.1 Remote sensing of seagrass and coastal environments.....	21
2.4.2 Sensor trade-offs.....	23
2.5 Remote sensing platform design considerations.....	26
2.5.1 Sources of spectral contamination.....	26
2.5.2 Spectral mixing and motion blur.....	29
2.5.3 Microtopography, lens distortion and sun glint.....	33
2.5.4 Radiometric correction, reflectance and normalisation.....	37
2.5.5 Photogrammetry.....	41
2.6 Remotely piloted aircraft (RPA).....	42
2.6.1 RPA applications.....	45

2.6.2 Autonomous flight control.....	47
2.6.3 Interaction with aviation regulatory environment	51
2.7 Discussion and Conclusion.....	53
2.8 Chapter appendices:.....	55
2.8.1 Appendix 2.8.1. Seagrass remote sensing literature cross-section (2010 to 2019) using the Scopus data base search string given below*.....	56
2.8.2 Appendix 2.8.2. Sources of imaging error and approach taken to mitigate problems.	61
2.8.3 Appendix 2.8.3. Hardware and software configuration for the remotely piloted aircraft setup used for this study.....	63

Chapter 3. Study Area - Wharekawa Harbour status and trend

3.1 Introduction.....	64
3.1.1 Chapter objectives	64
3.1.2 Study site selection	65
3.2 Geology, landform, soil and land use	65
3.3 Estuary values	71
3.4 Pressures	74
3.4.1 Stock damage.....	74
3.4.2 Mangroves	74
3.4.3 Sediment	75
3.4.4 Saltwater paspalum.....	84
3.4.5 Other threats.....	86
3.5 Seagrass extent on Wharekawa Harbour - analysis	87
3.5.1 Survey Methods	87
3.5.1.1 Current day seagrass extent	87
3.5.1.2 1997 and 2008 seagrass extent	89
3.5.1.3 Recent and historical imagery	89
3.5.2 Error estimation	90
3.5.3 Uncertainties on area calculations	93
3.5.4 Persistence of seagrass.....	94
3.6 Results.....	95
3.6.1 GNSS/GPS error calculation	95
3.6.2 Polygon placement error, and feedback into mapping methods	101
3.6.3 Long term seagrass trend	101
3.7 Discussion.....	107
3.8 Conclusion	110
3.9 Chapter appendices	112

3.9.1 Appendix 3.9.2. Aerial photography (2017) converted to greyscale for textural reference during photointerpretation of 1945 and 1971 imagery.....	118
--	-----

Chapter 4. The influence of residual low-tide water on the ability to differentiate seagrass from associated scene content

4.1 Introduction.....	119
4.1.1 Seagrass monitoring.....	119
4.1.2 Survey over a drained estuary.....	120
4.1.3 Chapter objectives	122
4.2 Method.....	122
4.2.1 Study Area	122
4.2.2 Research approach and overview	124
4.2.3 Aerial imagery capture	130
4.2.4 Ground reference data collection.....	132
4.2.5 Photogrammetry and data compilation	136
4.2.6 Spectral shift across the tidal sequence.....	137
4.2.7 Change in classification outcome with tidal drainage	138
4.2.8 Comparison of multispectral and scouting cameras	138
4.3 Results.....	139
4.3.1 General observations	139
4.3.2 Spectral shift across the tidal sequence.....	142
4.3.3 Change in classification outcome with tidal drainage	146
4.3.4 Comparison of multispectral and scouting cameras	147
4.4 Discussion.....	154
4.4.1 Spectral change across the tidal sequence	155
4.4.2 Change in classification outcome with tidal drainage	155
4.4.3 Comparison of multispectral and scouting cameras	156
4.4.4 Applicability and limitations	157
4.5 Conclusion	158
4.6 Chapter appendices	159
4.6.1 Appendix 4.6.1. Parrot Sequoia camera and downwelling sunshine light sensor / GPS module.....	159

Chapter 5. Assessment of object-based image analysis for seagrass feature extraction

5.1 Introduction.....	160
5.2 Chapter objectives.....	161
5.3 Method.....	162
5.3.1 Study area	162
5.3.2 Aerial imagery capture	162

5.3.3	Ground reference data collection	162
5.3.4	Photogrammetry and data compilation	166
5.3.5	Image segmentation	168
5.3.6	Optimal segmentation scale	171
5.3.7	Model training and test data	172
5.3.8	Classifier comparison and predictor importance	173
5.3.9	Variable importance and feature selection.....	174
5.3.10	Seagrass mapping and replication.....	175
5.4	Results.....	178
5.4.1	Image preparation and segmentation	178
5.4.2	Segmentation and assessment.....	178
5.4.3	Classification and assessment.....	181
5.4.4	Seagrass mapping and replication.....	192
5.5	Discussion.....	198
5.6	Conclusion	201
5.7	Chapter appendices	203
5.7.1	Appendix 5.7.1. Background literature review relevant to object-based image analysis for seagrass feature extraction.	203
5.7.1.1	Object-based image analysis components	203
5.7.1.2	Input and derived bands.....	206
5.7.1.3	Segmentation	209
5.7.1.4	Segmentation assessment	219
5.7.1.5	Classification	220
5.7.1.6	Classification assessment	223
5.7.1.7	Collinearity and feature selection	225
5.7.2	Appendix 5.7.2. Summary of seagrass, debris, cloud cover and sun angle for survey periods used in this replicated classification assessment.	227
5.7.3	Appendix 5.7.3. Attributes resulting from iterations upon increasing <i>minimum segments size</i> , the parameter within the segmentation process that controls the smallest allowable segment size.	228
5.7.4	Appendix 5.7.4. Per-class user and producer accuracy levels for the three classifiers tested.....	229
5.7.5	Appendix 5.7.5. Predictor sets obtained from collinearity reduction/ recursive feature elimination (random forest classifier), for each respective segmentation scale.	231
5.7.6	Appendix 8.7.6. Contribution of camera-bands, derived indices and texture layers in overall classification accuracy for the three classifiers tested.....	232
5.7.7	Appendix 5.7.7. Classification outcomes for predictor subsets comprising the camera-bands, derived indices and texture layers for the three classifiers tested.	233
5.7.8	Appendix 5.7.8 Per-class producer and user accuracy statistics for map classification at the survey times of April 2017, Feb. 2018 and March 2018.	236

Chapter 6. Mapping of seagrass leaf area and change

6.1 Introduction.....	237
6.2 Chapter objectives.....	239
6.3 Methods	239
6.3.1 Study area, ground observations and aerial survey.....	239
6.3.2 Image-processing and data preparation	240
6.3.3 Horizontally projected seagrass leaf-area index classification	243
6.3.4 Analysis	244
6.3.4.1 Classification assessment for leaf area estimates	244
6.3.4.2 Measurement of change in leaf area	246
6.3.4.3 Visual interpretation-based classification.....	246
6.3.4.4 Classification of mid-altitude imagery using a low altitude reference	246
6.4 Results.....	247
6.4.1 Classification assessment for leaf area estimates.....	247
6.4.2 Measurement of change in seagrass density (leaf area).....	251
6.4.3 Visual interpretation-based classification	251
6.4.4 Classification of mid-altitude imagery using a low altitude reference	255
6.5 Discussion.....	260
6.6 Conclusion	263

Chapter 7 Determining estuarine seagrass density measures from low altitude multispectral imagery flown by remotely piloted aircraft

7.1 Justification and purpose	265
7.2 Main findings by chapter	266
7.3 Operationalising the method.....	270
7.4 Linkage to management.....	275
7.5 Method limitations	276
7.6 Research recommendations	282
7.7 Conclusion	282
7.8 Chapter appendices	284

8 References.....	285
-------------------	-----

List of Figures

Figure 1.1. Summary of chapter arrangement with key stages in the assessment of low altitude RPA for seagrass feature extractyion.....	7
Figure 2.1. Seagrass growing in Whangapoua Estuary, February 2016.	13
Figure 2.2. Example of pixel mixing as a result of motion blur.....	30
Figure 2.3. Example of pixel colour mixing.	32
Figure 2.4. An example of vignetting (radial attenuation) in a raw sensor image (Nokia Lumia 1020 camera).	33
Figure 2.5. Repeat-photographs of the same seagrass scene, Tuapiro, Tauranga Estuary: a) large-format airborne aerial photography taken at a time of overhead sun with substantial sun glint on the wet surface, and b) RPA-sourced aerial photography (Gopro Hero5 photogrammetry-derived image mosaic).	36
Figure 2.6. Two images above of the same scene (two week time separation) where lighting conditions are a) overcast skies with no direct sunlight or shadow and b) direct sunlight with cloud-free skies showing significant sun glint patterns that obscure some of the dark-hued seagrass coverage.....	36
Figure 2.7. Schematic depiction of a simple solar radiative transfer relationship..	38
Figure 2.8. Uncorrected image mosaic patches showing radiometric difference at capture, across a ~2 km wide airborne aerial photography scene.....	40
Figure 2.9. Key steps in the photogrammetric processing chain with examples from a low altitude aircraft survey over an area of mangrove and coastal forest at Wharekawa Harbour.	43
Figure 2.10. Example of a (sample) RPA flight plan, constructed using Mission Planner software.....	50
Figure 2.11. Controlled airspace for RPA Operations, Coromandel Peninsula.....	53
Figure 3.1. Wharekawa Harbour position with respect to major estuaries.	67
Figure 3.2. Wharekawa Harbour and surrounding drainage catchment.....	68
Figure 3.3. Soil composition and land use within the Wharekawa Harbour catchment..	70
Figure 3.4. Wharekawa Harbour at low tide, with herons, oystercatchers, godwits, seagulls and dotterels feeding together on the same meadow.....	73
Figure 3.5. Early (1889) photography of the ‘Lucky at Last’ Whangamata Gold Corporation stamper battery, illustrating the denuded landscape within the Wharekawa Catchment following native forest clearance.....	77

Figure 3.6. Study area two-year rainfall profile to end of 2017 field work period.	79
Figure 3.7. Major slips and sediment/debris entering Wharekawa Harbour at the time of the Tasman Tempest and Tropical Cyclone Cook rainfall events.	80
Figure 3.8. Sediment accreting in large piles upon the estuary inflow from a tributary stream which drains an area of significant slope failure and landslip resulting from the ‘Tasman Tempest’ rain event, 7-12 March 2017.	81
Figure 3.9. Examples of sediment incursion upon seagrass.	82
Figure 3.10. Forestry-derived landslide avalanche and sedimentation event spilling from steep slopes onto Wharekawa Harbour marginal salt-marsh, arising from the Tasman Tempest heavy rainfall event 7-12 March 2017.	83
Figure 3.11. Various presentations of saltwater paspalum infestation of marsh, rush and mangrove communities, Wharekawa Harbour.	85
Figure 3.12. Seagrass on Wharekawa Harbour can be subjected to intensive grazing from swans and Canada goose.	86
Figure 3.13. Schematic example of capture of a polygon boundary representing the seagrass edge (black dashed line) using a concave-hull approach.	89
Figure 3.14. Layout of GNSS/GPS accuracy assessment.	92
Figure 3.15. Spatial layout of the reference shapes (grey) with deviation lines from reference points for the Etrex20, GPS64, and Trimble receivers.	96
Figure 3.16. Plot of percent difference between the measured area of simulated seagrass shapes mapped using a) the Garmin consumer GPS units (data from two GPS receivers pooled) and b) Trimble GNSS survey instrument, as compared to reference shapes mapped at high precision.	99
Figure 3.17. Plot of numerical difference between area of simulated seagrass shape mapped using the Garmin consumer GPS units (data from two receivers pooled) and a Trimble GNSS survey instrument (a and b respectively) as compared to reference shapes mapped at high precision.	100
Figure 3.18. Seagrass extents (green polygons) as visible in imagery from 1945 to the present day (grey scale frames) with reference colour image (Spot 6 satellite imagery at March 2018).	103
Figure 3.19. Change in calculated area of seagrass on the estuary determined from imagery or survey data.	104
Figure 3.20. Occurrence of seagrass tallied across the thirteen datasets from 1945 to 2018.	105
Figure 3.21. Distribution of seagrass that is found in the present day and persistent back through the time-series, colour-coded to indicate how long it has been continuously present back in time from 2018 to the respective historical dataset.	106

Figure 3.22. An example of a diffuse gradient between seagrass and sediment where true edge is difficult to establish and scale dependent.	110
Figure 4.1. Layout of study area with respect to: a) North Island New Zealand location; b) catchment source area; c) main body of estuary; and d) the focal seagrass meadow.	123
Figure 4.2. Processing flow for development of classification models and performance assessment relating to key research questions.	129
Figure 4.3. Camera drone inflight over seagrass meadow; multispectral camera with downwelling sunlight sensor mounted at front.	131
Figure 4.4. Seagrass on the study area (overcast sky conditions), 8 April 2017, showing transect and marker layout.	133
Figure 4.5. Example of nadir ground photography showing 1 m wide reference tube and transect line.	134
Figure 4.6. Apparent radial growth pattern of seagrass expansion as seen by drone at 60 m meters above ground level (exaggerated contrast applied).	140
Figure 4.7. Spectral coordinate plot of raw image digital numbers in pairwise combinations of image bands for: a) seagrass and sediment; and b) seagrass, sediment, detritus and shell content.	141
Figure 4.8 Spectral shift in normalised image value within each band (units of reflectance in range 0-1), after advancing from the earliest to latest (driest) low-tide drainage state, and grouped by whether the points are inside or outside of the GNSS-surveyed seagrass extent.	143
Figure 4.9. Spectral shift in normalised image value within each band (units of reflectance in range 0-1), when advancing from the earliest to latest (driest) low-tide drainage state and grouped by ground cover class.	144
Figure 4.10. Spectral shift with changing low-tide drainage state (in pseudo colour of multispectral image bands)..	145
Figure 4.11. Change in mean classification (iterated with 1000 repeats) for a) overall accuracy and b) true positive rate (TPR) and true negative rate (TNR) classification accuracy statistics per seagrass density class.	148
Figure 4.12. Classified seagrass maps (right frames) for early, mid and late low-tide drainage/drying states, with seagrass meadow boundaries (solid red line).	149
Figure 4.13. The calculated difference maps for agreement on predicted seagrass density class for mid-late comparison (b) and early-late comparison (c).	150
Figure 4.14. Relative importance of predictors contributing to the classification model for each of the three surveys, early, mid and late.	151

Figure 4.15. Comparison of multispectral image classification (left set) with equivalent classification using the red-green-blue scouting camera (right set) for early, mid and late stages in low-tide residual water drainage (top to bottom).....	154
Figure 5.1. Analysis workflow for data preparation, segmentation assessment and comparison of classifier and variable selection variants.....	164
Figure 5.2. A seagrass scene (~30 m wide) within the main study area showing the respective Haralick’s texture depictions with a grey-scale colour-ramp running from low (black) to high (white).. ..	169
Figure 5.3. Survey site showing the transects.....	177
Figure 5.4. Example of the segmentation size-range resulting from an increase in the segment size threshold parameter.	179
Figure 5.5. Measures used in the unsupervised assessment of segmentation fit.....	180
Figure 5.6. Sensitivity analysis on the <i>n_{tree}</i> parameter, comparing out of bag error rates across a range of <i>n_{tree}</i> values for different image segmentation scales.. ..	181
Figure 5.7. User and producer accuracy for target ground classes, in each of the five segmentation scales assessed, and comparing classifiers.	184
Figure 5.8. Accuracy statistics across all ground cover and density classes.....	185
Figure 5.9. Relative predictor importance for spectral, texture and segment geometry predictors across the range of segmentation scales and the three classifiers tested.....	186
Figure 5.10. Predictor importance in decreasing order of relative influence (least influential on the right) for the five segment scales test under the random forest classifiers tested.	187
Figure 5.11. Mean overall accuracy of random forest classification models under three variable-selection regimes: no reduction; collinear reduction; and recursive feature elimination.	189
Figure 5.12. Mean accuracy of classification models under three variable-selection regimes in terms of producer and user accuracy, and by seagrass density class, iterated across the separate segmentation scales.....	190
Figure 5.13. Comparison of the performance of near infra-red and red-edge directly as predictors, and indirectly as alternative components of the respective vegetation index calculation.....	191
Figure 5.14. Comparison of accuracy outcome across three sample periods. Distribution plots depict median accuracy levels and the frequency distribution around the median, for each of the three aerial surveys.....	192

Figure 5.15. Ground cover and seagrass density estimate as generated from the random forest classification model for each of the three surveys: a) 9 th April 2017; b) 2 nd Feb 2018; and c) 28 th Mar 2018.....	195
Figure 5.16. Enlargement of an area of seagrass under pressure from sediment.....	196
Figure 5.17. Examples of non-seagrass surface content that can be mis-classified as seagrass.....	197
Figure 5.18. Generalised OBIA process as applied to the current study.....	205
Figure 5.19. Seagrass meadow depicting various scales of interest that might be the subject of an image classification.....	213
Figure 5.20. Point cloud model from a fixed-wing RPA photogrammetry flight near Waiponga Reserve, Wharekawa Harbour on 25 May 2017.....	214
Figure 6.1. Overlapping (LAI > 1) and disparate (LAI = 0.6) seagrass.....	239
Figure 6.2. Seagrass upon the study area at time of 28 March 2018 survey, with transects and location of ground photography quadrats.....	241
Figure 6.3. Example of digitised seagrass inside of 200 mm x 200 mm test-squares....	245
Figure 6.4. Classified seagrass-density maps for February and March 2018 surveys, and for 10- and 3-tier class sets, with aerial photography overview.....	249
Figure 6.5. Relationship between predicted map class and actual mean seagrass leaf area of the square test-areas for the two surveys: a) February 2018; and b) March 2018.....	250
Figure 6.6. Change in seagrass density-class between February and March 2018 survey times, and for the two class-sets tested (10- and 3-tier class system).....	256
Figure 6.7. Predicted and actual change in seagrass density within 48 test-areas. Axis units are shift in density class, where a positive value indicates gain in seagrass density, and negative indicates decline.....	257
Figure 6.8. Classification outcome after using the 30 m altitude multispectral classification map to train multispectral imagery collected at 250 m - 300 m altitude...	259
Figure 7.1. An RPA flying under GPS guidance.....	273
Figure 7.2. Hypothetical example of an operational work-breakdown for an exhaustive estuary-wide survey of Wharekawa Harbour using an RPA flying at 30 m altitude.....	273
Figure 7.3. Hypothetical example of how the method described here might be escalated to estuary scale by sampling, to provide measures of seagrass condition for long term monitoring.....	274

Figure 7.4. Change in seagrass across the year of the research study as estimated by NDVI levels (frames on the right), with equivalent multispectral false colour imagers for reference.....	280
Figure 7.5. Illustration of the amount of non-seagrass photosynthetic material upon the northern half of Wharekawa Harbour as indicated by the NDVI channel.....	281

List of Tables

Table 2.1. Source of potential variation or error in incident light or sensor response to surface composition.....	27
Table 2.2. Summary from Rule Consolidation Part 101 for remotely piloted aircraft (RPA) (Civil Aviation Authority 2018) at time of writing.....	52
Table 3.1. Major estuarine systems of Waikato Region. Estuaries are organised by major coastal area as per the Waikato Regional Coastal Plan (Waikato Regional Council 2011), with attributes presented after the national inventory by Hume et al. (2016).....	66
Table 3.2. Significance of differences between the mean deviation from reference shape for GPS/GNSS units used for rapid seagrass mapping.....	95
Table 3.3. Significance of pairwise comparison of differences in the performance of GPS/GNSS units for rapid seagrass mapping in terms of deviation from reference shape..	96
Table 3.4. Mean deviation of rapid survey lines derived from two consumer multi-constellation GPS units (Garmin Etrex 20 and Garmin GPS64) and rapid survey capture using a Trimble survey instrument as compared to a high-precision reference capture of a simulated seagrass meadow drawn into the sand.....	97
Table 3.5. Mean deviation of measured total shape area compared to actual area of high-precision reference shapes (simulated seagrass reference areas), based on the rapid survey lines derived from walking the shape boundaries using two consumer multi-constellation GPS units (Garmin Etrex 20 and Garmin GPS64) and rapid survey capture using a Trimble R8+TSC3 survey instrument.....	98
Table 4.1. Timing of the three low-tide drainage states sampled in this survey at northern arm, Wharekawa Harbour.....	126
Table 4.2. Classification variables and their definition based on content of each pixel selected by random sampling.....	127
Table 4.3. Summary of camera specifications for the Parrot Sequoia imagery	130

Table 4.4. Orthomosaic production steps using the Agisoft Photoscan normal workflow.	136
Table 4.5. Correlation by image band between the image numbers going from early to late low-tide drainage states for each ground cover group (n=804).....	145
Table 4.6. Correlation between predicted map seagrass class attribution for two summary grid scales (0.5x0.5m and 1x1 m). Seagrass density figures are correlation coefficients.	151
Table 4.7. Comparison of classification accuracy between co-mounted multispectral and colour scouting cameras.....	152
Table 4.8. Comparison between camera types of classification accuracy values per seagrass density class under random forest classification, for early, mid and late stages in low-tide residual water drainage.....	153
Table 5.1. Ground cover classes applied to seagrass meadow image classification.	165
Table 5.2. Spectral and derived bands calculated and compiled into the analysis layer package, used for segmentation and classification.	167
Table 5.3. List of predictors available in the analysis image prior to feature selection (see Table 5.2).	170
Table 5.4. Mean variable importance for each segmentation scale, aggregated by the type of predictor as one of the class-set ‘band’ (green, red, red-edge, NIR), ‘index’ (e.g., NDVI), ‘texture’ (e.g., entropy) or segment ‘geometry’ (e.g., perimeter/area ratio).....	183
Table 5.5. Estimated detritus and shell content for each of the three surveys, to illustrate the difference in detritus contamination between surveys.....	194
Table 5.6. Proportion of predicted seagrass within and outside of the actual ground-surveyed seagrass meadow zone as depicted in Figures 5.15 and 5.16..	194
Table 5.7. Derived layers and indices used in studies of relevance to the multispectral high-resolution seagrass segmentation context.....	208
Table 5.8. Segmentation families according to Garcia-Lamont et al. (2018).	210
Table 5.9. Comparison of main software considered for segmentation and classification using object-based image analysis framework.....	218
Table 6.1. Summary of seagrass, debris, cloud cover and sun angle for survey periods used in this replicated classification assessment.....	241
Table 6.2. Summary of data preparation stages and analysis.....	242
Table 6.3. Within-classifier accuracy metrics (n=5633 points) for the ten-tier decile scale..	252

Table 6.4. Within-classifier accuracy metrics (n=5633 points) for the 3-tier scale of high, medium and low seagrass density (proportions $> \frac{2}{3}$, $\frac{1}{3} - \frac{2}{3}$, $< \frac{1}{3}$ respectively). 253

Table 6.5. Within-classifier accuracy metrics in terms of agreement in classification outcome between the predicted map and actual measured seagrass density class of independently measured square test-areas, for 10-tier (decile) and 3-tier (high, med. low) class sets, and human-interpreted classes. 254

Table 6.6. Classification outcome after using the 30 m altitude multispectral classification map (Parrot Sequoia camera, 2.7cm pixel GSD) to train multispectral imagery collected at 250-300 m altitude (Micasense Red-Edge camera, 250 mm pixel GSD). 258

List of Abbreviations

Abbreviation	Full
ANOVA	Analysis of variance
AUC	Area under ROC curve
CAA	Civil Aviation Authority
DEM	Digital elevation model
DVI	Difference vegetation index
EVI	Enhanced vegetation index
FPV	First person view
GIS	Geographical information system
GNSS	Global navigation satellite system
GPS	Global positioning system
GSD	Ground sampling distance
LAI	Leaf area index
LCDB4	Landcover database version 4
LDA	Linear discriminant analysis
LINZ	Land Information New Zealand
MPB	Microphytobenthos
NDVI	Normalised difference vegetation index
NIR	Near infra-red
OA	Overall accuracy
OBIA	Object-based image analysis
PBIA	Pixel-based image analysis
REC2	River environments classification v.2
RF	Random forest
RFE	Recursive feature elimination
RGB	Red-green-blue cartographic bands
RMSE	Root mean square error
ROC	Receiver operating curve
RPA	Remotely piloted aircraft
RTK	Real-time kinetic
RVI	Ratio vegetation index
SAVI	Soil-adjusted vegetation index
SVM	Support vector machine
UAS	Unmanned aerial system
UAV	Unmanned aerial system
UV	Ultra-violet
VFR	Visual flying rules
VIS	Visible bands of the spectrum
VRS	Virtual reference system
WRC	Waikato Regional Council

CHAPTER 1

Chapter 1. Introduction, objectives and approach

1.1 Research context and justification

This research aims to fill a methodological gap that exists in the published range of remote sensing approaches available for intertidal seagrass mapping. The study sets out to assess options for providing seagrass presence/absence and coverage density metrics using imagery collected using a remotely piloted aircraft (RPA) flying close to the ground. Method-development under this goal pursues photogrammetric survey, classification and feature extraction algorithms suitable for referencing and training larger-scale feature extraction from sources such as satellite or aircraft.

Methods are based around the photogrammetric process whereby extended aerial capture sessions comprising hundreds of images in each flight, are integrated into single or multiple geo-registered mosaic scenes (Ai et al., 2015; Candiago et al., 2015). Spatial or temporal comparison of quantitative spectrometric imagery for the purpose of change detection or time-series analysis requires standardisation of image values so that information is independent of sun angle, cloud cover, time of day/year, air clarity and lens geometry. Recent developments in multispectral camera technology and photogrammetry software provide for retrieval of reflectance values, which improves comparison between datasets (Bouvet 2014; Oliver 2017; Zheng et al., 2018). Although there are many published assessments of the components of survey and classification workflows, currently there are no accepted integrated approaches that are immediately applicable to mapping of seagrass from RPA-flown imagery. This research tests a selection of the published range of procedure components applicable to the problem of quantifying seagrass extent and density, then recommends an integrated workflow from that selection. It is anticipated that the workflow will be applicable to other seagrass species, although it will be developed using *Zostera muelleri* as a test case species.

Seagrass is the subject of significant conservation research (Katwijk et al., 2015). Large areas of seagrass are in decline globally (Waycott et al, 2009), with some indication that New Zealand seagrasses are following this global trend (Matheson et al., 2011). Monitoring of the condition of a seagrass population requires survey and sampling methods able to detect decline that is significant relative to the normal seasonal/annual variability in extent and condition. Seagrass meadow patches oscillate in size and connectivity, driven by a range of cycles of environmental condition and disturbance

(Roelfsema et al., 2014; Kilminster et al., 2015; Soissons et al., 2016). Rates of change may vary between estuaries at varying temporal and spatial scales. For some New Zealand sites, the variability is becoming understood (e.g., Park 2016), however many sites receive little or no attention and hence there is a dearth of local information. In New Zealand research has focussed on only a few regions and times, with the true extent of seagrass fluctuation largely unknown or unmapped (Turner and Schwarz 2006a; Matheson et al., 2009; Anderson 2019).

Effective management and resource policy require monitoring methodology to track change and detect the levels of decline required to invoke a management intervention. There is currently no policy in New Zealand for when protection and/or restoration is triggered. The most sensitive methods in current use involve lengthy ground-level inspection and assessment of plants and substrate by ecologically trained personnel (e.g., McKenna et al., 2015, Carter et al., 2018). These methods applied at large scale have potential to damage delicate estuarine plant communities through foot-traffic (Travaille et al., 2015) and are effort-intensive.

Seagrass can be difficult to detect at low density or where young plants or rhizome extensions are minor parts of the substrate scene which could include sediment of varying size and hue, wrack, detritus, and patches or clumps of algae and diatom (Ismail 2001; Lathrop et al., 2006; Pu et al., 2012, Kohlus et al., 2020). This has presented issues for airborne mapping (Baumstark et al., 2013; Hossain et al., 2015a; Baumstark et al., 2016; Nahirmick et al., 2019b). Similarly, the surrounding co-habitant flora and fauna and non-living material (e.g., sedimentation and floating debris) can oscillate by day, season, and exposure to stressors. Floating material can deposit and relocate in substantial volume of material with each tide cycle. Interpretation of seagrass habitat can be dependent on the spatial scale of observation, seagrass metapopulation structure, patch-transience and community complexity (Kilminster et al., 2015; Kovacs et al., 2018, Grech et al., 2018). Scenes comprising mixed seagrass species of differing morphological size and patch characteristics be difficult classify (Chayhard et al., 2018). These components add to the spectral complexity and variance of a seagrass meadow (Soissons et al., 2016).

Remote sensing of seagrass decline using conventional satellite and aircraft imagery can be challenging due to the fine scale structure of many estuarine seagrass species being order(s) of magnitude smaller than the typical image pixel size of satellite/airborne imagery. For example, in New Zealand the leaves of *Zostera muelleri* are typically only a few mm wide and shoots comprise only a few leaves per shoot (Turner and Schwartz 2006b). At the high altitudes of observation of satellites and aircraft, heterogeneity blends together hue and detail within the image pixel, potentially reducing classification specificity. Close range observation provides detail and specificity

yielding increased seagrass definition, reduced noise, and therefore improved seagrass feature extraction (e.g., Duffy et al., 2018).

Ground-level survey by field personnel allows observation of leaf damage and signs of microhabitat stress. However, ground survey is expensive to deploy repeatedly over large areas, is subject to observer interpretation, and has potential to damage the interest-areas of seagrass through trampling (Travaille et al., 2015).

Remotely piloted aircraft operate close enough to the ground to collect high-detail information about the structure and condition of seagrass and its environment (Duffy et al., 2018). RPA survey also benefits from autonomous positional control, and have moderately long flight time (e.g., 15-40 minutes per battery-set depending on configuration and frame-size), so enable efficient data collection over large areas (e.g., 1 km² per flight is plausible larger for a large airframe flying at 120m). These capabilities allow for repeat-surveys over time at precise locations with accurate revisit positioning, and scales of survey that are significantly greater than can be covered on foot by a survey team. However, application of image analysis methods for characterising the condition of a target vegetation requires model calibration and tuning. Image classification methods require development of an analysis process-chain that can include photogrammetric mosaicking and normalisation of data across an image-set, spatial ortho-correction to rectify geographic position, radiometric correction for ambient light levels, and feature extraction algorithms that reliably generate condition attributes. No method currently exists that bring these facets together in a way that is suitable to measure intertidal seagrass.

Intertidal estuarine seagrass grows upon a variable substrate comprised of a range of sediment types, shells and detritus of varying live or dead content, and grows amid other photosynthesising biota that can seasonally vary in abundance (e.g., algae, diatoms). In terms of the visual content of an image pixel, estuarine seagrass can vary in plant and/or leaf density (affecting the proportion of the pixel covered by the seagrass), and in the condition of the plant/leaves within that subset. Seagrass can be found at densities ranging from sparse, to saturated and highly overlapping. In New Zealand, *Zostera muelleri* can be found with leaf width <1 mm and up to 4 mm wide, and leaves of varying length, lying flat on the ground or curled when the tidal water has drained. When submerged in tidal water or residual pooling, the seagrass floats standing upright and sways with water movement. So, there is the potential for highly varied scene content. Overarching this variability in material content is the cyclical change in surface water during the tidal drainage process. Macro- and micro ground topography on an estuarine seagrass meadow brings about variability in drainage speed, with wetness ranging from near-dry to saturation and varying levels of short-term or permanent pooling. Upper

reaches of the estuarine intertidal height-field can dry completely, and lower areas can remain saturated. Drying is accelerated by sun, wind and air temperature, so water content and drying can potentially vary with time of day, weather, and season.

Sunlight is known to absorb strongly in the red to near infra-red (NIR) region of the electromagnetic spectrum. Many indices of vegetation condition use the relative intensity of red wavelengths (used by photosynthesising plants) compared to an infra-red reference, to establish the amount of photosynthetic material present. Some plant health assessment methods further use the “red-edge” region of the spectrum to identify photosynthetic condition (e.g., Eitel et al., 2011; Bandyopadhyay et al. 2017). Variable water content on the estuary might impose a requirement for correction-factors when calculating standardised vegetation indices.

The research conducted in this thesis is therefore an explorative image classification problem that also addresses the problem of variable water content, and in the context of developing aerial survey methodology. There is currently no integrated method available in the literature for application of RPA to seagrass feature extraction in New Zealand estuaries. There is also little previous New Zealand or international research on mapping seagrass character while the tide is out (e.g., Barrell et al., 2015).

1.2 Thesis Objectives

1.2.1 Overarching purpose

The research aims to fill the current aerial survey methodology knowledge gap and explore what can be achieved for mapping seagrass beds by flying low to the ground over an estuary with the tide out. Research outcomes from the thesis are intended to provide information to guide development of indices of seagrass condition related to detecting changes in density and the spatial extent of seagrass beds for long term condition-monitoring.

The operational goal is to enable rapid collection of quantitative ground observation data for the purpose of training landscape-scale image classification using airborne or satellite derived imagery. An automated RPA survey method could be deployed so as to perform a role similar to a field-ecologist inspecting the site directly but achieving a greatly expanded survey area due to flight and capture speeds, with minimal damage to seagrass through trampling.

This research also aims to generate information contributing towards the development of functional remote sensing methods for seagrass mapping that can be applied by semi-technical GIS and spatial analysis operators (e.g., in Local or Central

Government agencies) such that the seagrass monitoring can be executed within ‘business as usual’ environmental monitoring operations.

The scope of this research is remote sensing of estuarine seagrass from low altitude RPA, with the tide out, on an estuary location where variability in seagrass density and abundance of surface materials can be observed in a short time span.

1.2.2 Research questions

The following specific research questions were investigated:

- i) Can seagrass character be accurately extracted from aerial imagery flown by remotely piloted aircraft over an estuary with the tide drained?
- ii) Does the spectral character of seagrass and non-seagrass materials change with varying residual water drainage during low tide?
- iii) Is there a specific optimal image processing and analysis method, within a small selection of candidate methods, for achieving high classification accuracy with respect to seagrass detection and density measurement?
- iv) Does the optimal method also yield good classification results at other survey times?
- v) Does the efficacy of the tested seagrass feature extraction methods vary with segmentation scale? and
- vi) Can the optimal method detect change?

The following thesis structure and chapter objectives were set out to address these questions.

1.3 Thesis structure

The thesis chapter layout provides a systematic approach to delivering the research objectives (Figure 1.1). The method development employs autonomous RPA aerial survey, quantitative multispectral photogrammetry and precision global navigation satellite system (GNSS) survey to test suitability of low flying RPA for seagrass detection and monitoring.

In short, Chapter 1 sets the research context. Chapter 2 reviews seagrass ecology, values, pressures and population trends, largely in the context of *Zostera muelleri* in New Zealand and provides an overview of relevant remote sensing methods. Chapter 3 describes the study area. Chapters 4-6 are a logical work-breakdown by which a seagrass

feature extraction method is developed, assessed and replicated. Chapter 7 provides summary and synthesis of findings.

Chapter 1 Introduction

Introduces the research, outlining motivations, justification, purpose, and the overarching approach taken to address the research questions.

Chapter 2 Background literature review – seagrass and remote sensing

Chapter 2 provides a general review of literature relevant to the research. An effective remote sensing strategy for measuring seagrass on an estuary requires an understanding of the morphological structure, growth, meadow structure and physical presentation of *Zostera muelleri* upon the substrate. This includes the material that deposits upon seagrass to obscure the aerial view. The use of RPA for remote sensing of seagrass requires an assessment of feasibility for operation in the coastal marine area, and to establish appropriate hardware and control systems to address the specified research questions. These factors are reviewed from the existing publication base. The following chapter objectives are addressed:

1. Summarise the ecology, values, pressures and population trends of *Zostera muelleri* in New Zealand;
2. Provide a high-level overview of remote sensing methodology relating to seagrass application;
3. Discuss RPA hardware and trade-offs in RPA survey design;
4. Identify aerial survey factors that need to be accounted for in the survey design for subsequent chapters; and
5. Establish feasibility and limitations of RPA for use as a survey tool for seagrass on New Zealand estuaries.

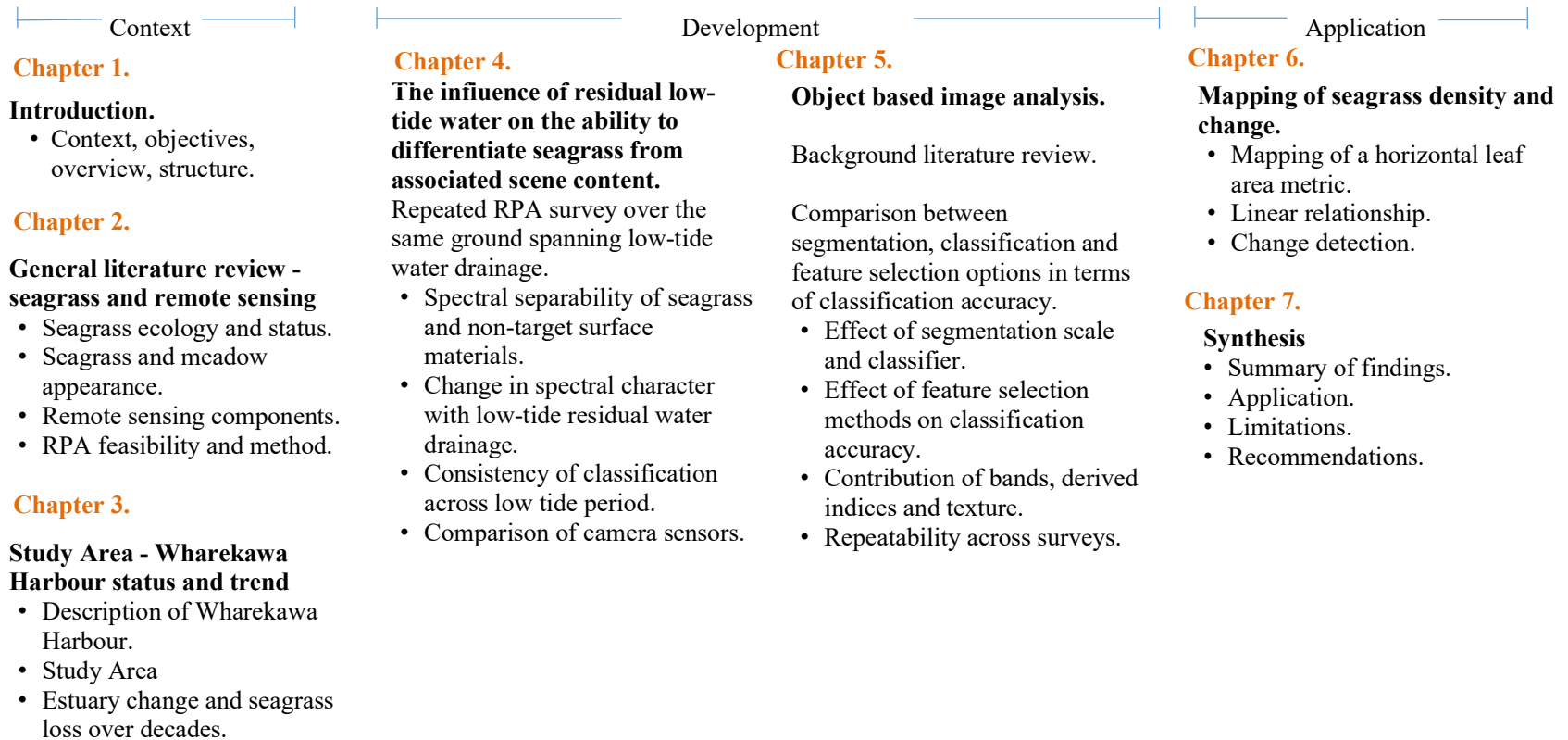


Figure 1.1. Summary of chapter arrangement with key stages in the assessment of low altitude RPA for seagrass feature extractyion.

Chapter 3 Study Area - Wharekawa Harbour status and trend

This chapter explains the basis for selecting Wharekawa Harbour as a study area. The research objectives require a seagrass population with a range of seagrass density, surface material and substrate type present within a scene of a size suitable for the available RPA and camera. The research requires there to be change in the seagrass population within the filming area. This requires an assessment of short- and long-term fluctuation in seagrass on the estuary. The following chapter objectives are addressed:

1. Determine the characteristics of Wharekawa Harbour in terms of its ecosystem and catchment environment;
2. Determine the current seagrass population of the estuary and short term (one year) stability of seagrass distribution in response to a significant rain and sedimentation event; and
3. Measure the long-term pattern of change in seagrass and estimate future trend.

Chapter 4. The influence of residual low-tide water on the ability to differentiate seagrass from associated scene content

This chapter examines the consistency of spectral character and classification outcome at different stages of residual tidal water draining, i.e., after the bulk tidal water has cleared at low tide. The effect of seagrass, detritus and shell density on classification outcome is also assessed, as well as the effect of pooling. To achieve this, two specific objectives are addressed:

1. Quantify the effect of advancing residual water drainage on seagrass classification accuracy; and
2. Quantify consistency in predicted map outcome with residual water drainage.

Chapter 5. Assessment of object-based image analysis for seagrass feature extraction

In this chapter, a small subset of available image classification components are contrasted in terms of classification outcome so as to determine an optimal procedure.

The six specific objectives of this chapter are:

1. Selection of a small subset of object-based image analysis workflow components that are indicated to yield moderate to high classification accuracy in a range of vegetation mapping cases;
2. Assemble a semi-automated process-chain that ingests RPA imagery, ground observations and spatial referencing data to yield spatially explicit classification results;

3. Compare segmentation scale, classification algorithms and variable selection in terms of seagrass detection and classification accuracy;
4. Assess a range of spectral bands, indices and texture layers for contribution to classification outcome;
5. Select a classifier, segmentation scale and variable-selection method for subsequent testing on repeat surveys; and
6. Verify the method for mapping of seagrass in repeat surveys undertaken in the following year.

Chapter 6 Mapping of seagrass leaf area and change

In this chapter, the classification model is trained and assessed in terms of accurately digitised horizontal leaf area of seagrass. This explores the upper limit of classification performance that is possible using this survey framework. Condition maps are generated for two repeat surveys and the change in seagrass density quantified, with change-outcome compared to a precisely measured control dataset. The following chapter objectives are addressed:

1. Map seagrass density distribution based on measured horizontal leaf area for two replicated surveys;
2. Examine the relationship between seagrass density estimation and measured horizontal 2-dimensional leaf area;
3. Quantify change in seagrass presence and density class;
4. Contrast the cost and benefit of visual photo interpretation vs. measured seagrass density attribution; and
5. Demonstrate the use of low-altitude RPA imagery for training a subsequent classification using fixed wing aircraft imagery.

Chapter 7 Synthesis and conclusion

In this chapter, the results are reported in terms of the thesis and chapter objectives. The research findings are summarised within the context of developing of a monitoring method. Recommendations are made with respect to advancing this work to address multiple estuaries and time-series analysis.

CHAPTER 2

Chapter 2. Background literature review - seagrass and remote sensing

2.1 Introduction

Seagrass is an important component of estuarine and coastal ecosystems, providing a host of ecological functions required for ecosystem resilience, and a range of benefits in terms of human wellbeing and economic prosperity (Needham et al., 2013; Morrison et al., 2014; Anderson et al., 2019). Seagrass is in decline globally (Coles and Fortes 2001; Orth et al., 2006b; Waycott et al., 2009), and New Zealand seagrass (*Zostera muelleri*) may be following this trend with decline evident at a number of locations (Turner and Schwarz 2006a; Matheson et al., 2009; Matheson et al., 2011; Park 2016; Anderson 2019). Management of seagrass requires timely and accurate information about its condition.

Trends in seagrass condition can be masked by high natural oscillation in seagrass extent due to both seasonality, stochastic events (e.g., storms) and/or reactions to long term stressors. However, understanding how stressors influence seagrass condition, and differentiating stressor-induced changes from natural patterns, can be difficult. To date this has been attempted via monitoring seagrass extent, which acts to examine changes, but fails to link to causality. Rarely has seagrass extent and condition been monitored.

Remote sensing is the collection, analysis and interpretation of information about a subject from a remote vantage point (Klema 2015). Much of the remote sensing field concerns the acquisition and preparation of raster or point cloud datasets from passive sensors (imagery in the visual context) or active sensors (e.g., laser terrestrial scanning and synthetic aperture radar), and the statistical quantification of content compared to a reference or benchmark. A long-term overarching motivation of remote sensing is to enable efficient repeatable mapping of surface characteristics at landscape, regional or greater scale, with a repeat-capture timeframe useful for change-detection and time-series analysis (Johnson and Patil 2006; Klema 2001).

To effectively monitor changes in seagrass condition requires statistically robust measures of condition for the target site. Field sampling of seagrass provides options for quantifying change but are labour intensive and can be prohibitively expensive at the landscape scale. Remote sensing techniques provide efficient options for quantifying seagrass at large scale. Satellite and airborne imagery have yielded successful characterisation of seagrass from the shore to the deep-water limit of seagrass and provide

useful information: but largely in terms of coarse meadow extent and community structure.

Remote sensing analysis requires moderate volumes of ground-surveyed reference information in order to train and validate the computer image classification, and model variability in surface spectra. Collecting ground reference data for remote sensing application, that is representative of estuary-scale variability in condition and appearance, can also be labour intensive. Valid model training also requires ground surveys at the time of image capture, before the scene changes significantly. Hence, consideration of the temporal application of ground survey is needed, ideally with ground-truthing occurring within days of image capture. A rapid ground survey method would aid in application of satellite or airborne remote sensing. Remotely piloted aircraft (RPA) are a novel technology for remote sensing that may offer a solution to rapid collection of ground reference data.

Quantitative survey using RPA has been applied to a range of vegetation monitoring problems including seagrass at a range of complexity levels with varying success (Chayhard et al., 2018b; Duffy et al., 2018; Ruwaimana et al., 2018; Nahirnack et al., 2019a). Survey design requires a number of decisions to be made regarding drone mount, flying height and speed, camera choice and a range of capture parameters relating to aerial photography and/or photogrammetric model construction. There is no validated RPA based survey 'recipe' that can generally be applied with confidence to the problem of mapping seagrass extent and/or condition, and published research on the field may not be immediately transferrable to the case of *Zostera muelleri* on New Zealand estuary types due to morphology differences (Kuo and den Hartog 2006; Turner and Schwartz 2006b). Therefore, a key driver in developing this research is to develop a framework using RPA to support large scale survey of *Zostera muelleri*.

RPA technology in the current day has limited flight time, and flying restrictions that limit range-from-observation (Civil Aviation Authority 2018). These factors limit total area that can be surveyed in a single sortie (flight) by RPA, and thereby logistically prohibitive on large and/or inaccessible estuaries. Therefore, RPA are not immediately suitable for regional scale contiguous mapping of large estuarine systems without extension to fuel longevity and changes to line-of-sight control regulations. However due to potential proximity to the ground and programmability for small scale quantitative capture, there is immediate value for RPA in operating as a support tool for training larger scale airborne or satellite imagery. This research explores a survey capture method using RPA that can be applied rapidly in discrete sorties to accumulate volumes of ground reference (model training/test) information to support remote sensing using larger scale imagery.

2.2 Chapter objectives

The purpose of this chapter is to set the scene and context for this research by reviewing the ecology, morphology, growth, and distribution of seagrass in the context of trend analysis and population condition monitoring and the visual presentation of seagrass on an estuary. Remote sensing methods are introduced here (but expanded in chapter 5) and important aerial survey design factors discussed. The review then examines the opportunity presented by RPA, and limitations in their use for survey on New Zealand estuaries under the following specific objectives:

1. Summarise the ecology, values, pressures and population trends of *Zostera muelleri* in New Zealand;
2. Provide a high-level overview of remote sensing methodology relating to seagrass application;
3. Discuss RPA hardware and trade-offs in RPA survey design;
4. Identify aerial survey factors that need to be accounted for in the survey design for subsequent chapters; and
5. Establish feasibility and limitations of RPA for use as a survey tool for seagrass on New Zealand estuaries.

2.3 Seagrass ecology

2.3.1 Seagrass in New Zealand

Seagrasses are a group of ~72 marine-adapted angiosperm species found world-wide in many shallow coastal waters and estuarine habitats (Short et al., 2007; Short et al., 2011). This group is comprised of marine flora that have similar basic anatomy and function and have common structural modifications to enable growth and reproduction in saline environments (Kuo and den Hartog 2006; Touchette 2007). Morphological differences between seagrass taxa can be attributed to biogeographical differences in each species' evolutionary environment (den Hartog and Kuo 2006; Short et al., 2007).

Seagrass in New Zealand occurs as a single species *Zostera muelleri*, which was previously known as *Zostera novazelandica*. *Zostera muelleri* is the accepted scientific name and has been synonymised with *Z. capricornia*, *Z. mucronata* and *Z. novazelandica* (Les et al., 2002; Jacobs et al., 2006). *Ruppia megacarpa* is also present in New Zealand and is considered by some to be a seagrass (e.g., Short et al., 2007), however *R. megacarpa* is often associated with freshwater systems (Robertson and Funnell 2012).

Zostera muelleri is monoecious, monopodial and has a perennial life history (Turner and Schwartz 2006a; den Hartog and Kuo 2006; Moore and Short 2007). The genetic variability of *Z. muelleri* across New Zealand suggests slow genetic exchange between populations (Jones et al., 2008).

Seagrasses typically maintain their ecosystem presence via clonal growth although in some species presence is also maintained by sexual reproduction (Turner 2007). Seagrass plants consist of one or many shoots emerging by a single stem and sheath from underground root and rhizome networks. Leaves can be covered in deposited particles or epiphyte growth and are often surrounded by detritus and decaying seagrass material (Figure 2.1).



Figure 2.1. Seagrass growing in Wharekawa Harbour, February 2016.

Leaf width and length vary regionally in New Zealand (Ismail 2001; Turner and Schwartz 2006b). For example, mean leaf width ranged from 1.4-2.4 mm for sites across Tauranga Harbour (Kohlmeier et al., 2014), while a narrower leaved *Z. muelleri* (1.1-1.2 mm at Whangamata estuary and 1.3-1.8 mm at Whangapoua and Wharekawa estuaries) is present at sites on Coromandel Peninsula (Turner and Schwarz 2006b), with average leaf length measuring in the range 5.5 to 9 cm. However, leaf length can reach up to 48cm at sub-tidal sites in this region (Schwarz et al., 2006). Mean summer shoot density ranged from 2700–3800 m⁻² across three Coromandel estuaries (Turner and Schwarz 2006b). However, it is noted that density can reach more than 5000 m⁻² (Turner and Schwarz 2006a). Growth rate and biomass of seagrasses are modulated by a number of factors including water temperature, photosynthetically available light, nutrient availability, epibiota smothering, and intertidal exposure to air and solar radiation (Lee et al., 2007; González-Correa et al., 2009; Collier and Waycott 2009; Kim et al., 2016; Nelson 2017; Wilkes et al., 2017). Consequently, a seagrass monitoring program would need to consider sub-regions with different rates of change in seagrass density depending on

proximity to sources of nutrient, sedimentation, detritus, contaminants and marginal (overshadowing) vegetation, or position within the tidal hydrology. These are sources of variability that may need to be modelled within an image classification and seagrass feature extraction.

2.3.2 Ecological role and ecosystem services

Seagrass plays an important function in maintaining structure and resilience of estuarine systems (Duarte 2002; Duarte et al., 2006; Carr et al., 2012; Morrison et al., 2014). Seagrass contributes to the estuarine ecosystem at a multitude of structural, biophysical and trophic levels: they are primary producers that are consumed by macro and meiofauna (Horinouchi et al., 2012; Ha et al., 2014); they provide habitat resulting in high infaunal meadow biomass (Leduc and Probert 2011); and indirectly facilitate nutrient recycling through herbivory and resulting promotion of seagrass growth (Christianen et al., 2012). Faunal biomass has been quantified as correlating with below-ground seagrass biomass (Lee et al., 2001). Seagrass also promotes sediment stabilisation (Basterretxea et al., 2004; Bos et al., 2007; Reidenbach and Timmerman 2019), reduces current velocities within the bed (Eckman 1990; Koch and Gust 1999; Heiss et al., 2000; Bryan et al., 2007; Widdows et al., 2008; Wang et al., 2009; Hendriks et al., 2011; John et al., 2015) and acts as refugia for fish and crustaceans (Cooper 2015; Espino et al., 2015a; Espino et al., 2015b). Arponen and Boström (2012) demonstrate that edge effects are more pronounced upon species diversity than patch size effects, and that smaller isolated patches can have value for overall diversity. *Zostera marina* was found to reduce currents by 40% in the winter and 60% in the summer (Hansen and Reidenbach 2013), with an effect that extended up to 0.5 m above the benthic surface. Bryan et al. (2007) demonstrated that seagrass meadows extend the current-boundary layer upwards, thereby reducing velocity interacting with the meadow ('baffling').

Seagrass provides a range of recognised human ecosystem services that are becoming increasingly quantified (Duarte 2002; Fourqurean et al., 2012; Duarte et al., 2013; Cullen-Unsworth and Unsworth 2013; Needham et al., 2013; Anderson 2019). Seagrass ecosystem services can include providing raw materials and food, coastal protection, erosion control, water purification, maintenance of fisheries, carbon sequestration, as well as tourism, recreation, education and research opportunity through various direct or indirect mechanisms (Barbier et al., 2011). The value of seagrass has also been quantified for the fishery industry and food supply (Unsworth et al., 2010; Tuya et al., 2014; Unsworth et al., 2019). For example, Tuya et al. 2014 established a monetary

value for commercially relevant fish species using seagrass (*Cymodocea nodosa*) meadows amounting to 95.8 euros ha⁻¹ y⁻¹.

Seagrass value has been expanded recently to include carbon sequestration (Fourqurean et al., 2012; Greiner et al., 2013; Lavery et al., 2013; Macreadie et al., 2014; Marbà et al., 2015), which has climate change implications especially where blue carbon is being considered as an offset to international obligations or as a mechanism for carbon offsetting. However, seagrass carbon sequestration statistics may be overestimated where meadow structure and heterogeneity in seagrass carbon storage is not factored into calculations (Ricart et al., 2015). Authors Campagne et al. (2015) concluded that the economic value of seagrass is largely undervalued by policy makers. The full potential value of seagrass internationally may not be fully exposed (Barbier et al., 2011).

2.3.3 Seagrass degradation and decline

Loss of seagrass in coastal or estuarine systems has ecological consequences in terms of reduced biodiversity, water quality, and sediment stability (Waycott et al., 2009). Economic effects of seagrass loss are expected to include: potential loss of fisheries; impacts on waterway access; coastal infrastructure maintenance; reduced ability of the estuarine system to remove nutrient excess derived from upstream agricultural runoff; carbon sequestration; as well as numerous aspects of ecological human wellbeing and economic integrity as described above (McArthur and Boland 2006; Unsworth et al., 2010; Bertelli and Unsworth 2014; Cullen-Unsworth et al., 2014; Campagne et al., 2015).

Direct and indirect signs of decline are not always obvious and can be masked by ecological and coastal process (Fonseca et al., 2002; Cullen-Unsworth and Unsworth 2016). Contraction or fragmentation of a seagrass population may be short-term within a longer-term metapopulation extent, such that decadal monitoring may be required to reveal significant stressor impacts at landscape scales and trigger a management intervention.

Causes of decline can include a range of environmental stressors, including i) changes in light; ii) climate change impacts; iii) disease; iv) eutrophication; and v) physical disturbance. Each of the mechanisms is considered in turn below.

The first significant mechanism identified is light reduction resulting from sediment or silt deposition (e.g., Matheson and Schwarz 2007; González-Correa et al., 2009), or algal or other epiphytic smothering accretion (e.g., Nelson 2017; Wilkes et al., 2017). Coating of seagrass leaves by silt or epibiota can arise from anthropogenic sources including excess nutrients (resulting in excessive epiphyte growth), sediment inflow, mechanical re-suspension of substrate, and altered flow dynamics from coastal structures

that can lead to scouring (e.g., Udy and Dennison 1997; Duarte et al., 2004; Turner and Schwartz 2006a; Erfteimeijer and Robin Lewis 2006; Cabaço et al., 2008; Erfteimeijer et al., 2006; Román et al., 2019). Anthropogenic generation of sediment may be minor compared to the scale of impact of stochastic weather events during which low sediment inflow or resuspension (chronic stressor) may be exacerbated to significant smothering (acute stressor) over a short period of time (Basterretxea et al., 2004; Fonseca et al., 2008). Storms have potential for catastrophic loss of seagrass given sufficient storm intensity and consequential high river and tidal water flow intensity (Yang and Yang 2009; Pollard and Greenway 2013; Kim et al., 2015).

Reduction of light at depth or with particulate covering, shifts the balance from photosynthesis to respiration, thereby reducing organic production, such as carbohydrate investment in rhizomes and seeds (Ralph et al., 2007). Natural processes, such as surface/ground water inflow associated with rainfall events and marine storms or wave activity can cause suspension of estuarine particulate or organic material and contribute directly to the natural variations of seagrass condition (Cabaço et al., 2008; Gera et al., 2014). Similarly, different seagrass species have varied thresholds for burial in terms of stress and recovery (Cabaço et al., 2008).

Temperature increase and rising sea levels induced by climate change are another major threat with potential for significant seagrass loss (Campbell et al., 2018; Chefaoui et al., 2018). Seagrass growth can be driven by the amount and fluctuation in solar irradiance for photosynthesis (Lee et al., 2007; Collier and Waycott 2009), emersion time (Apichanangkool and Prathep 2014), nitrogen and potassium limitation, and the impact on light availability from turbidity where smothering may lead to photosynthetic stress, disease or biomass loss (de Boer 2007; Carr et al., 2012; Carr et al., 2016). There are minimum levels of light that allow for increased growth in seagrasses, with these thresholds differing between species.

Intensive light and temperature can stress seagrass (e.g., Carr et al., 2012). York et al. (2013) found for a seagrass (*Zostera muelleri*) population in the barrier estuary Lake Macquarie (temperature range 23-33°C with optimal seagrass growth at 27°C), that adverse temperature effects were determined at 32°C resulting in reduced above-ground biomass and leaf size. A shading experiment in this study found reduced leaf density, above-ground biomass and shoot biomass in artificially reduced light levels (York et al. 2013).

Temperature increase from climate change presents a threat to seagrass species that may lack tolerance to increased water temperature (Campbell et al., 2006; Jordà et al., 2012; Koch et al., 2013; Chefaoui et al., 2018). However, it should be noted that one study found increase in temperature associated with seagrass health gains due to relief

from pathogen infection (Olsen et al., 2015). The effect of climate-change related temperature increase on seagrass may be contingent upon a number of factors such as nutrient and light availability, and photosynthetic stress, as increased temperature should accelerate consumption of nutrients and raise photosynthetic impact of smothered light levels (Lee et al., 2007).

The protist endophyte *Labyrinthula zosterae* is a potential large-scale threat to seagrass through ‘wasting disease’ (Short et al., 1986; Muehlstein et al., 1988; Ralph and Short 2002). Background association between seagrass and *L. zosterae* has been documented globally (Vergeer and den Hartog 1994). This disease is also known to be naturally co-existing with *Zostera sp.* without measurable impact (Brakel et al., 2014), with pathogenic incidences in New Zealand being rare (Armiger 1964) and Australia (Trevathan-Tackett et al., 2018). Thus, the threat of *L. zosterae* may be patchy, but when triggered it has been known to cause severe wasting of *Zostera* and remains a potential threat (Muehlstein 1989; Ralph and Short 2002; Sullivan et al., 2013).

Seagrass damage from eutrophication can happen through a number of pathways, including direct ammonia toxicity, oxygen stress from algae (epiphyte leaf load and periphyton bloom) related reduction of solar radiation, surface-smothering from algal blooms (Schmidt et al., 2012; Bishop and Kelaher 2013; Qiuying and Dongyan 2014), as well as exacerbating feedback mechanisms such as sediment re-suspension (and resulting light attenuation) after seagrass density reduction (Burkholder et al., 2007; Lee et al., 2007; Serrano et al., 2016).

Significant coarse disturbance to seagrass can also arise from human mechanical damage. Direct damage can arise from boat propeller and hull contact, and anchor-drag (Okudan et al., 2011; La Manna et al., 2015). Research by Li (2018) observed seagrass damage from boat scars, with faster recovery in higher density areas than sparse areas. Di Carlo and Kenworthy (2008) measured both above and below-ground damage resulting from vessel-groundings and manatee feeding damage, with higher recovery rate for above-ground biomass. Human trampling damage has also been documented (Eckrich and Holmquist 2000; Travaille et al., 2015).

Therefore, seagrass density and extent are driven by seasonality and other variability in environmental and land-use factors that integrate to vary seagrass growth, damage and survival throughout the year. Seagrass condition can be subject to the interaction of multiple growth factors and stressors (e.g., Eldridge et al., 2004; York et al., 2013). Exposure to certain stress can exacerbate the impact of other stressors reducing resilience (Moreno-Marín et al., 2018). The overall pattern of change in condition may be particular to the latitude, morphology of the site, surrounding soil composition and land-use fluctuation in the catchment.

2.3.4 Seagrass seasonality and patch dynamics

Perennial seagrass meadows show seasonal patterns of growth that can be generalised as having peaks in spring and summer, with reduced growth and shedding of leaves in autumn, and little to no growth in winter (Turner and Schwartz 2006b; Andrade and Ferreria 2011; Kim et al., 2014; Soissons et al., 2016). These patterns may be attributed to seasonal change in growth associated with annual change in solar radiance, modulated by average water temperature, light conditions, nutrients and the annual photoperiod cycle (Orth et al., 2000; Duarte et al., 2006; Orth et al., 2006a; Ralph et al., 2007; Roelfsema et al., 2013; Kim et al., 2014; Kohlmeier et al., 2014; Moore et al., 2014).

Seagrass from several Coromandel estuaries have higher shoot densities within seagrass patches during January (austral summer), but the reverse has been detected during austral winter (July) where in some cases high shoot density occurred at the patch-edge (Turner and Schwartz 2006b). Seagrass condition is also known to vary on different temporal and spatial scales (Collier and Waycott 2009; Kim et al., 2014) and is difficult to detect at low density or where young plants or rhizome extension are minor parts of the substrate scene. The winter reductions in seagrass growth and biomass can be recovered quickly once spring and summer growth intensifies (Kirkman et al., 1982; Ismail 2001; Turner 2007; Fonseca et al., 2008; Carr et al., 2012). This scenario was observed on Wharekawa Harbour (see census data Chapter 3).

Seagrass has biomass above (leaf and stem) and below (stem, rhizome and root) the benthic surface (Kirkman 1985; Ismail 2001; Turner and Schwartz 2006b). The surface appearance of seagrass can change predictably upon damage (e.g., change in leaf shape) or degradation (e.g., change in photo-pigments and therefore colour). However, such signals of impact upon seagrass resulting from human environmental pressure could easily be confounded by natural seasonal processes (Soissons et al., 2016). For example, Arumugam et al. (2013) noted that patch layout on the landscape were related to substrate physiochemical properties which varied with season and storm activity, and possibly shaped seagrass layout within this variation.

The pattern and variability in the structure of a seagrass population in an estuary is a complex interaction of hydrodynamics, macroclimatic conditions, sediment movement and the history of previous seagrass growth that determines where propagates (vegetative or sexual) are deposited. This determines sites of future meadow maintenance and expansion. Long term stability in the extent of seagrass can be rapidly disrupted by stochastic hydrological events (Basterretxea et al., 2004). Temporal dynamics were

explored by Bos et al. (2007) who transplanted seagrass into an unvegetated tidal flat, then demonstrated sediment accretion and a shift towards finer sediments as a consequence of seagrasses presence. Tidal water movement patterns across estuarine seagrass patches can differ during incoming tidal inundation compared to outgoing drainage of the estuary (Bryan et al., 2007), which may also have implications for sediment entrainment and flocculation. Barnes (2013) described for a South African estuary, a largely uniform seagrass population (*Zostera capensis*) despite a large salinity range.

Patch fragmentation can be a normal part of the dynamic of estuarine seagrass meadows at the annual-multiannual timescale and is linked to current strength and bathymetric depth (Fonseca 1983; Fonseca 1987; Fonseca et al., 2002; Bell et al., 2008). Seagrass has been defined by one author as constituting a 'meadow' form where contiguous seagrass area exceeds 10,000 m², below which growth is considered a patch (Anderson 2019). Sediment movement and wave damage can partition intact meadows into discrete patches. Both large and small patches have important value for recolonising an area after disturbance (Greve et al., 2005; Almela et al., 2008; Arponen and Boström 2012).

Authors Bell et al. (2001) concluded from their research that there is little effect of fragmentation on infauna content of a seagrass meadow, and that patch size alone didn't account for variation in observed fauna. Epifaunal density can be positively related to fragmentation (Arponen and Boström 2012). In another study, variability in epifauna species was greater at within-meadow scale of measurement (10 m and 1 km context) compared to greater scales reflecting a need to include attributes at these scales when undertaking predictive modelling of seagrass ecology (Gullström et al., 2012). In a global review, Boström et al. (2006) found a mix of evidence across published studies (positive, negative or inconclusive) for the effect of seagrass patch size and edge on faunal abundance or diversity.

2.3.5 Measurement of seagrass extent and condition

Conservation management of seagrass requires methods for detecting change in condition of seagrass at spatial scales of capture meaningful to local and regional population maintenance. Changes in extent and density need to be understood in terms of long-term persistence of source seagrass populations at landscape scales. Perception of seagrass condition can be subjective. For example, in a study of populations of seagrass *Posidonia angustifolia*, Wood and Lavery (2000) determined that perceived seagrass health varied between respondents, and for many factors there were no actually

significant differences in characteristic between sites when measured. Furthermore, for the set of factors confirmed as different between perceived healthy and unhealthy sites (e.g., seagrass canopy coverage and shoot density), there was seasonal difference in the usefulness of factors as a perceptive indicator of condition. Duarte (2002) urged that effective seagrass conservation requires development of quantitative models in how seagrass responds to disturbance and pressure.

Over several decades of seagrass research there have been a multitude of methods that have been applied to quantitatively measure various components of seagrass population condition and develop prospective indicators. Significant reviews have collated various approaches employed at a range of investigative scales (e.g., Kirkman 1996; Short and Coles 2001; Duarte et al., 2006; Marbà et al., 2013).

Understanding seagrass condition integrates plant abundance (distribution, composition), performance (survival, growth, spread) and reproductive success (flowering, fruiting, seedbank development, seedling success, genetic diversity) (Kilminster et al., 2015)

Indicators of seagrass condition could include seagrass distribution and contributing factors such as abundance, cover, above/below ground biomass, shoot, leaf and rhizome characteristics, chemical/nutrient/mineral content and connected community composition as well as indirect detection using observations of seagrass herbivores (Irving et al., 2013; Marbà et al., 2013; Roca et al., 2016; Hayes et al., 2018; Anderson et al., 2019).

Indicator methods can involve manual inspection and/or collection of material at seagrass field sites to generate detailed data for point locations, as cores, quadrats and/or positions on transects (e.g., Burdick and Kendrick 2001; Fonseca et al., 2002; Turner and Schwartz 2006b; Dos Santos 2011; Neckles et al., 2012; Irving et al., 2013). In some instances, researchers have alluded to seagrass population condition by capturing meadow extent and tracking changes in extent (Mount 2007; Needham et al., 2013; Park 2016). In-field habitat mapping is labour intensive, and data accumulates slowly (Felsing and Giles 2011). Likewise, collection of seagrass/conspecific or substrate samples and/or spatially located surface references can amount to significant accrued time and effort at the estuary scale of sampling (e.g.; Short and Coles 2001; Robertson et al., 2002; Short et al., 2006). Field preparations and operational planning requirements can escalate response and execution timeframe for in-situ seagrass mapping, especially at remote locations.

The response time of a condition indicator, in terms of change detection time relative to the timeframe of pressure-induced change under environmental stressors, is an important success factor for seagrass condition monitoring (Roca et al., 2016). The use of a condition indicator (e.g., leaf area index) can be sensitive to timing with respect to

environmental stressors (Soissons et al., 2016). Observable condition measures, such as shoot density and biomass, can be sensitive to general meadow changes, however Roca et al. (2016) have noted that physiological/chemical measures can be more sensitive to early stages of environmental stress.

Successful detection of change in any one estuary may therefore rely on effective sampling design, correction and control of covariate factors, and a statistically robust modelling procedure (Schultz et al., 2015). As such, understanding spatial complexity of a seagrass population is important for ascribing the spatial and temporal accuracy of any seagrass monitoring standard (Barrell et al., 2015; Hossain et al., 2015a). Contiguous monitoring was found in one study to be more appropriate than a disparate grid-sampling approach (Fonseca et al., 2002). The authors also found that additional attributes (hydrodynamic setting, wave exposure, temperature salinity and water depth) improved modelling performance.

Roca et al. (2016) highlight that no single indicator can satisfy every management objective, but propose a general framework for selecting seagrass indicators depending on knowledge of the seagrass system, based on synthesis of the literature. Although there are several suggested metrics that can indicate seagrass condition, no agreement has been published on a “best-practice” or consistently effective method. Once such methods are established, remote sensing and associated computer mapping automations could potentially enable large scale quantification of condition with favourable efficiencies.

Remote sensing methods are a mechanism to greatly enhance seagrass monitoring extent and cost-return in terms of data volume and coverage. But these methods rely upon being able to see condition metrics upon the ground surface, through the water column, or where underground conditions correlate with surface measurements.

A remote-sensing solution to this problem would first require that high likelihood seagrass objects are determined within the imagery, and isolated from non-target and potentially confounded information (i.e., *seagrass feature extraction*). Therefore, this project aims to investigate if remote sensing-based seagrass feature extraction can be achieved.

2.4 Overview of remote sensing for seagrass mapping

2.4.1 Remote sensing of seagrass and coastal environments

A number of studies have set out to map vegetation within coastal or specifically estuarine systems using a variety of manual field survey and/or cartographic methods (Table 2.1) (Stevens and Asher 2005; Holmes et al., 2007; Rebelo et al., 2009; Hillock and Rohan 2011; Knudby and Nordlund 2011; Graeme 2012; Timm and McGarigal 2012;

Tiner 2015). Earlier remote sensing using satellite imagery and methods were generally insufficient for discriminating wetland species in fine detail due to limitations in spatial and spectral resolution of the imagery compared to the scale of structure in wetland communities (Adam et al., 2010). In more recent years, imagery has become available with greater spatial resolution for yielding structural detail of coastal and freshwater wetland communities (Ashraf et al., 2010; Klemas 2011; Allan 2016).

Remote sensing has been applied to estuarine mapping at a number of scales of observation (Ismail 2001; Pasqualini et al., 2005; Alexander 2008; Lee and Yeh 2009; Borfecchia et al., 2013a; Roelfsema et al., 2015; Traganos et al., 2018a; and Appendix 2.8.1). Lyons et al. (2013) demonstrated use of satellite derived time-series mapping of seagrass for understanding long term spatial and temporal trends but emphasises the importance of complementary ground monitoring. Airborne/aircraft mounted sensors have been used to quantify seagrass (Mount 2006; Casal et al., 2012; Borfecchia 2013b; Hill et al., 2014) as well as other target coastal vegetation types (Alexander 2008; Zhang and Baas 2012). Seagrass has been mapped using visual and multispectral wavelength imaging, acoustic (sonar) (e.g., Sánchez-Carnero et al., 2012; Barrell et al., 2015) and laser scanning (Pan et al., 2016) in different studies. Scale of application has generally been limited to coarse scale meadow/population-level assessments due to limitations of spectral and spatial sensor resolution in earlier imagery (Peneva et al., 2008; Torres-Pulliza et al., 2013; Lapray et al., 2014; Roelfsema et al., 2014; Barrell et al., 2015; Hossain et al., 2015b; Lang et al., 2015). Acoustic methods have been useful for identifying and characterising seagrass or calibrating other image analysis (Gagnon et al., 2008; Lyons et al., 2011), although local complexities in habitat structure can affect integration with other datasets such as satellite imagery (Barrell et al., 2015).

Discrete large-scale remote sensing solutions for estuarine seagrass systems, demonstrating high level of accuracy and of a scale suitable for regional seagrass monitoring are uncommon in the literature (e.g., Roelfsema et al., 2015). Authors Torres-Pulliza et al. (2014) mapped seagrass extent across a part of the Coral triangle using Landsat satellite imagery and gained up to 78% seagrass mapping accuracy, but recognised that areas of seagrass were being excluded from the map due to coarse topography-based image segmentation criteria, and identified a source of error where their method failed to detect seagrass growing at low density. An approach such as this may have potential for seagrass mapping in New Zealand, however in order to fully quantify trends in seagrass condition, a much finer resolution of imagery with higher levels of spectral differentiation would be required. Multispectral imagery that is of high spatial resolution or use of existing multispectral sensors at much lower altitude, may provide options for mapping of seagrass condition in sparse patches.

2.4.2 Sensor trade-offs

To map seagrasses there are trade-offs that need to be made in sensor configuration, selection and deployment. At the sensor level, a trade-off between the spectral granularity, image size, scan speed (e.g., rolling shutter vs. global shutter) and image capture frequency needs to occur. These features are collectively limited by the microelectronic bus design, bandwidth and speed of transfer to storage within the camera. When using a particular sensor, there is a survey design trade-off. Decreasing sensor height improves detail levels, but at the cost of the survey area achievable per unit of effort. This is due to the time to accumulate coverage. It also relates to the airframe needing to fly slower in order to avoid motion blur and maintain image clarity.

Cost-effective seagrass monitoring at landscape scale requires spatially explicit maps of seagrass distribution and structure (Neckles et al., 2012). Remote sensing of surface biota has the advantage of high-altitude vantage point, long term deployment, spectral consistency across a time-series, and persistence of sensor availability allowing time-series analysis (Lyons et al., 2013; Tiner et al., 2015; Guo et al., 2017). Satellite imagery has provided useful information for large scale seagrass mapping, but generally the spatial pixel resolution and spectral specificity in current sensors is still lacking for widespread seagrass resource monitoring (Hossain et al., 2015a).

Lower altitude sensors (airborne, balloon, or RPA derived) have been applied when the spatial resolution of satellite data is insufficient (Klema 2015). Choice of approach is dependent on the extent of seagrass, funding and the survey frequency required (Kovacs et al., 2018).

Consumer colour cameras have been used for mapping seagrass. Mount (2006, 2007) used aircraft-mounted camera photography to quantify seagrass down to the maximum visible water depth, with change measured through a proposed geostatistical “mega-quadrat”. Barrell and Grant (2015) successfully mapped seagrass *Z. marina* in Nova Scotia using a consumer digital camera and global positioning system (GPS) receiver attached to a helium balloon, which for that scale of site (sub-estuary) and target resolution (pixel width ~4cm) allowed seagrass classification accurate to detect change in patch-edge movement across a 26 month period of 0.29-0.46 m y⁻¹. Oblique airborne imagery was used to successfully map benthic seagrass habitat revealing seasonal change in coverage (Andrade and Ferreira 2011). There are limitations for the use of consumer cameras as quantitative sensors for image analysis due to the broad and overlapping spectral sensitivity range of the conventional camera sensor type.

Low altitude, very high-resolution imagery may allow individual seagrass shoots or leaves to be resolved (whole or in part), and thereby enable specific feature extraction and analysis of optic character within the target feature. Seagrass leaves are small in dimension compared to many vegetation types that are the subject of remote sensing analysis. Seagrass measured in one study in the range of 55-90 mm for mean leaf length on Wharekawa Harbour (Turner 2007), although up to 480 mm in one recorded instance in sub-tidal waters of New Zealand (Schwarz et al., 2006). Leaves are thought to plateau in width at ~2 mm width (Turner and Schwartz 2006b). Seagrass leaves are slightly buoyant such that when the tide is flooded, leaves raise up to some state of partial or fully upright orientation, at which point there are three key changes in how the leaves present to a nadir-oriented camera from above: i) the leaf area visible from above reduces due to the aspect change; ii) view of the substrate increases; and iii) there is a substantial increase in shadow, which for long-leaved sparse seagrass can result in considerable change in tone.

Authors Pasqualini et al. (2005) reported seagrass mapping accuracy in the range 73-96% using an earlier satellite multispectral product (SPOT 5) and highlighted the benefit of increased pixel resolution on the usefulness of the maps and their match with field observations. Phinn et al. (2008) compared a range of satellite sensors for measuring seagrass extent, biomass, disturbance patterns and other biophysical characteristics, and found the hyperspectral sensor provided the best accuracy levels. The authors attributed the low overall accuracy across sensor-types to difficulties in matching the raster georeferencing to the actual ground location of field observation. Additionally, authors Pinkerton et al. (2014) highlight the errors that can enter a remote sensing model when image pixels and in-situ training data don't match in their measured location on the ground. Roelfsema et al. (2013) undertook mapping of multiple seagrass species in a large estuary highlighting the importance of image alignment and use of comparable methods. These cases accentuate the importance of precision ground survey for collection of training data in the current study. This is vital, in order to compare field observations with imagery given the separate location accuracy constraints of the respective data acquisition.

Remote sensing using multispectral or hyperspectral imaging has proven useful for wetland mapping due to strong correlation between differential reflectance and transmission of specific spectral bands (frequency ranges) across species and different biophysical characteristics (Ozesmi and Bauer 2002; Adam et al., 2010; Kuenzer et al., 2011). In some studies, for some vegetation sites, there has been clear spectral distinction between the various plant and/or macro-algal species in an estuarine assemblage (Pasqualini et al., 2005; Zomer et al., 2009; Timm and McGarigal 2012). Hyperspectral

imagery (contiguous discrete bands spanning the useful electromagnetic spectrum) has improved vegetation classification (e.g., Hladik et al., 2013; McDowell and Kruse 2016), with potential indicated for seagrass (Fyfe 2003). In one study comparing satellite with airborne hyperspectral imagery, the hyperspectral data provided the highest classification accuracy rates for measurement of seagrass cover and biomass (Phinn et al., 2008). In a western Atlantic study, seagrass was found to be largely distinct from algae species in full spectrum signatures (Thorhaug et al., 2007).

The spectral definition and statistical contrast possible under hyperspectral analysis provides opportunity for seagrass feature extraction and attribute characterisation (Phinn et al., 2008; Lu and Cho 2011; Li et al., 2012; Cho et al., 2014), including three-dimensional structure of the seagrass (Hedley et al., 2016). However hyperspectral data has the constraint for many users that it is generally expensive to capture and compile into a georeferenced image resource, requires complex statistical workup and dimensionality-reduction in order to extract information, and has relatively small sensor size compared to visible and multispectral cameras. This is due to the electronic trade-off between the number of spectral bands that can be processed in a capture frame, the pixel size of the sensor, and speed of successive image capture during a flight.

Classification performance has been increased by including point cloud data derived from lidar laser scanning in the classification model (Chust et al., 2008; Hladik et al., 2013; Hannam and Moskal 2015; Rapinel et al., 2015). However, application of this innovation to seagrass on New Zealand estuaries would require very high resolution lidar scanning as much of the seagrass would sit flat and wet when the tide is out. As such lidar scanning at this density of capture and spatial precision may be prohibitively expensive for many end-users at landscape scale especially where repeated surveys were required over time.

Multispectral and hyperspectral methods for seagrass remote sensing, utilising the IR band in contrast ratios and vegetation indices, share the general issue that seasonal change in scene chlorophyll could confound spectral contrast in the imagery. For example, Bargain et al. (2013) measured higher concentration of chlorophyll during summer than winter with impact on derived vegetation indices.

Dekker et al. (2005) identified epiphytic growth as a possible issue for resolving seagrass in a satellite image scene. In New South Wales Australia, mixed seagrass species (including *Zostera muelleri*) were spectrally distinct at ground level despite varied epibiotic cover and factoring spatial and temporal variability within species (Fyfe 2003). Each biogeographical environment may differ in how epiphyte content might confound an image classification, and therefore require site-specific survey design to account for the variation.

In summary, high altitude (satellite, aircraft) versus low altitude sensors (RPA) have advantages and disadvantages. High altitude sensors offer large scale tracking however lack spatial pixel resolution and specificity for monitoring changes. Whereas low altitude sensors can acquire detail levels that are unattainable by aircraft or satellite and have flexibility and specificity in time and location of deployment. Multispectral and hyperspectral sensors have greater potential for feature extraction compared to conventional colour cameras. However, these are expensive and lower in resolution than conventional sensors due to the higher data volumes involved.

2.5 Remote sensing platform design considerations

2.5.1 Sources of spectral contamination

Image classification design that is accurate and repeatable requires i) sufficient volume of representative ground-validated training data for developing model signatures; and ii) spatial and temporal consistency in pixel scale and spectral response at the sensor and between images. Sensor photo-sites (the pixels) record values in proportion to the radiance of ground-objects with consistent sensor response across all the images in an image-set (Dunford et al., 2009; Kennedy et al., 2009; Sankaran et al., 2015; Gómez et al., 2016). Inconsistency in response contaminates the classification model, by increasing variance around a separation threshold or function, or other classification error. There are a number of sources of spectral inconsistency that require consideration in aerial survey design for estuary remote sensing when the tide is out or draining (Table 2.1).

External sources of radiometric variation include sun angle to zenith (which varies with time of day and season), cloud cover, atmospheric composition (e.g., aerosol, dust), and shadow (Honkavaara et al., 2012). Internal sources of variation can arise from sensor noise or instability (Markelin et al., 2010), and background (random) electronic interference at the sensor photo-site (Del Pozo et al., 2014). There is potential for these factors to introduce random or systematic spectral error into sensor intensity values for each band.

Table 2.1. Source of potential variation or error in incident light or sensor response to surface composition.

Source of variation	Mechanism	Explanation / example
Variation at sensor.	<ul style="list-style-type: none"> - Sensor photo-site response. - Vignetting across image. - Lens distortion. 	<ul style="list-style-type: none"> - Dead/weak photo-sites (e.g., dim pixels). - On the raw image, outer pixels are dimmer than inner pixels due to oblique vs. normal light incidence. - Scale (GSD) difference at different positions within the raw image.
Variation at radiative transfer.	<ul style="list-style-type: none"> - Sun angle to atmosphere. - Atmosph./aerosol absorbance / scatter. 	<ul style="list-style-type: none"> - Solar radiation passes through more or less thickness of atmosphere. - Differential spectral intensity loss from light passing through different airspace composition.
Variation at the ground.	<ul style="list-style-type: none"> - Sun angle to surface. - Macro/micro topography (roughness, morphology, angle of incidence interaction). 	<ul style="list-style-type: none"> - Dimmer pixel with oblique angle of incidence. - Greater shadow with increasing angle of incidence, as macro- (large areas without direct solar illumination) or micro-shadow (different textural definition).
Variation from sensor motion.	<ul style="list-style-type: none"> - Motion blur. - Variable image position. 	<ul style="list-style-type: none"> - Aircraft/drone motion. - Variable external camera orientation (e.g., drone with no gimbal, windy day) causing positioning error.

(Table 2.1 ctd.)

Source of imagery variation	Mechanism	Explanation / example
Variation across a landscape.	<ul style="list-style-type: none">- Anisotropic variation in appearance across scene.- Change in tide drainage / residual water state (across a site).	<ul style="list-style-type: none">- Different appearance at different positions on the image.- Spatial variation in degree of residual water / pooling after bulk water has drained at low tide, resulting in variable water absorption, reflection, glint effects on spectral appearance/texture.
Variation across survey timeframe.	<ul style="list-style-type: none">- Change in cloud cover.- Change in sun angle.- Change in tide drainage / residual water state (with time).- Variation in flying altitude.	<ul style="list-style-type: none">- Solar intensity / spectral composition may vary across image set.- Incident radiation changes with time, especially early/late in day → variation across image set.- Slow residual water drainage and drying, spatial variation in residual water changes with time up to stage of estuary tidal flood → water absorption, reflection and glint effects on spectral appearance and texture.- Pixels sample different ground scale.

2.5.2 Spectral mixing and motion blur

Classification non-specificity can arise when there is overlap in spectral character between target and non-target subjects on the ground. Aside from this issue of spectral separability, confounding of the classification model can also arise due to sub-pixel blending of object colour (e.g., Hedley et al., 2012). Sub-pixel mixing may be dependent on the scale of the vegetation structure relative to the size of the image pixels. At the small extreme, 'hyperspatial imagery', where the pixel size is much smaller than the dimensions of the target object, would have direct pixel colour representations over most of the object (Rango et al., 2009; Peña et al., 2013; Anker et al., 2014). Seagrass typically presents upon a sandy or muddy substrate, whereby substrate spectra contaminates the seagrass spectra depending on seagrass density and substrate type (Bargain et al., 2012).

Another potentially significant source of radiometric error is spectral mixing from motion blur, where photo-sites sample more than one location while the camera shutter is open (Figure 2.2). Classification methods can identify and adjust for blur (Peng and Jun 2011; Tiwari et al., 2014; Yang and Qin 2016) but require prior knowledge of detectable blur-characteristics in the image. For airborne photography, fast camera shutter speeds are required to surmount normal motion-blur associated with moderate to fast flying speeds. There are in-flight events, such as bumps from turbulence, spurious winds, and course / attitude corrections made by the RPA airframe that could bring about rapid rotation or translation shift of the camera sensor creating blur. For example, Lisein et al. (2015) experienced a batch of blurred imagery (deciduous forest scene) on a particularly windy day of flying, and Puliti et al. (2015) experienced blur impacting images at wind speed of 7 ms^{-1} over a mixed forest scene. Rosnell and Honkavaara (2012) determined for their large multi-rotor RPA that a shutter speed of $1/2000 \text{ s}$ was required to eliminate motion blur over an agricultural setting. Watts et al. (2010) used $1/2000 \text{ s}$ shutter speed to manage motion blur for multiple settings. Turner et al. (2015) set shutter speeds $1/1250 - 1/1600 \text{ s}$ under shutter priority (variable aperture with light intensity) to minimise blur. None of these studies examined classification accuracy, coverage or operational performance impacts resulting from blurring effects experienced.

A number of studies reported on blur issues relating to height. Breckenridge et al. (2011) found images too blurry for identification at heights 153m and 305m above ground, but at 76m images became "useful". Some studies also removed blurred images in a large photoset by manual inspection (e.g., Lehman et al. 2010; Bryson et al. 2013). Shutter speeds were automatically set high to minimise potential blur in Dulava et al. (2015) and Lucieer et al. (2014), although the latter still experienced blurred imagery despite fast shutter speeds that required removal after later inspection. Göktoğan et al.

(2010) used vibration dampeners to minimise blur from vibration as far as possible. Hung et al. (2014) identified escalating blur from the sensor displacement associated with attitude change compounded by increasing altitude. Barrell and Grant (2015) also report blurring as a source of error during RPA photography.

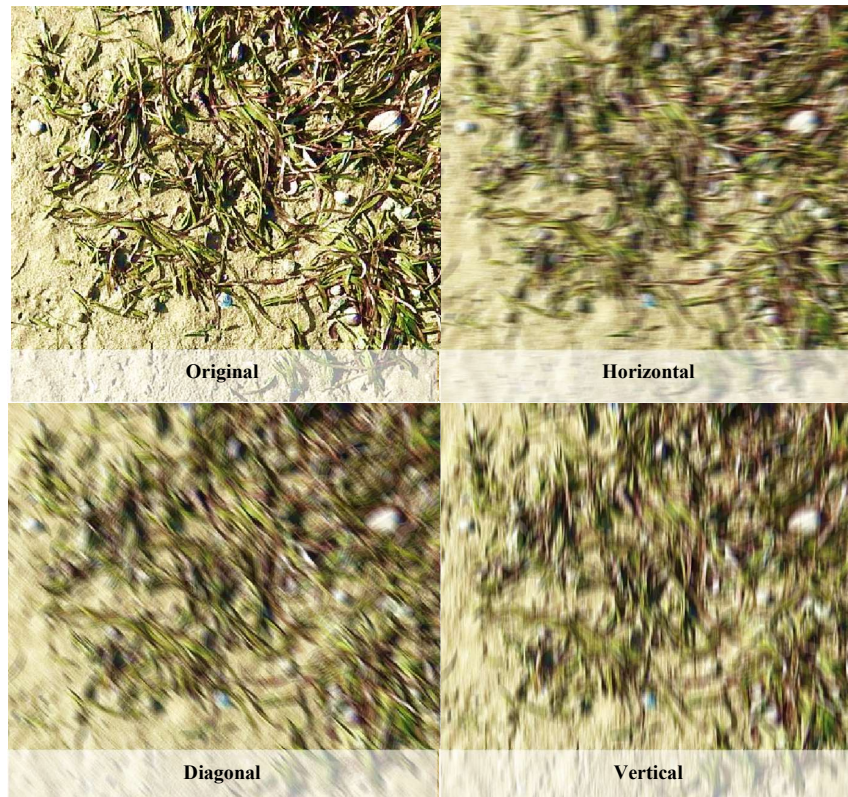


Figure 2.2. Example of pixel mixing as a result of motion blur, by simulated blur effect (four-pixel blur distance in the direction noted on the image).

Carbonneau et al. (2012) calculated the number of pixels of blur across a sensor from vehicle motion as follows (Equation 2.1):

$$\text{Blur} = V.T.H.f \times 10^{-3}. P \times 10^{-6} \quad (\text{Equation 2.1})$$

Where:

V	=	velocity (m/s)
T	=	shutter time (s)
H	=	height above the ground (m)
f	=	focal length of the lens (mm)
p	=	pixel size on the sensor (μm).

Therefore, motion blur increases with the velocity and height of the aircraft and attenuates with shutter time. Reduction of shutter time can reduce blur (e.g., Turner et al., 2015), but there is also a trade-off made in terms of the amount light allowed past the camera shutter onto the sensor. Over-reliance on shutter speed to control motion blur may be at a cost to spectral information, so configuration of flight speed and sensor orientation control is an important consideration. A literature search of World of Science and Scopus databases did not detect any published studies that set out to attribute different remote sensing classification outcomes to flight-planning parameters or in-flight events associated with blur. Carbonneau et al. (2012) remark that motion blur is often overlooked when setting flying conditions for image capture. If blur is unavoidable then an image correction or exclusion criterion may need to be applied during image dataset preparations, to detect, remove or eliminate blur. There are methods published for achieving blur-detection and correction in satellite imagery that could be applied to RPAs (e.g., Sieberth et al., 2014; Yang and Qin 2016). Intuitively, increasing flying height would be expected to result in pixel colour blending (e.g., Figure 2.3), which would have similar impact on image classification as motion blur. While the motion blur and pixel blending are correctable using software algorithms (e.g., Clemens 2012), the impact of these sources of error upon classification outcomes and elimination through optimised flight control has not been explored in the literature for very low altitude high resolution imagery.

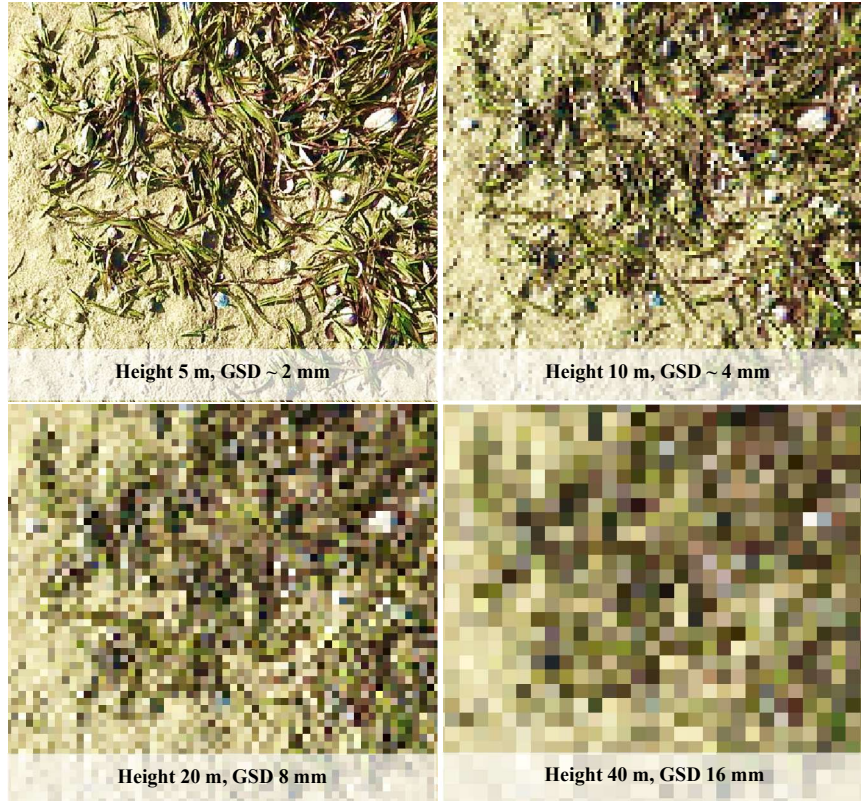


Figure 2.3. Example of pixel colour mixing with simulated doubling of flying height in each subsequent photo (as doubling of pixel width for the same scene, by resampling with bicubic averaging). Seagrass leaves are ~ 2 mm wide, so this width is the minimum that will resolve the colour of the seagrass leaf, which equates to ~ 5 m flying height for this camera and lens.

2.5.3 Microtopography, lens distortion and sun glint

Surface roughness can decrease reflectance levels on an otherwise uniform material (Herodowics 2017), with small scale shadow likely contributing to the reduction. Kipp et al., 2014 reported limited variability in reflectance with varying incident light conditions, but higher variability in radiometer-measured reflectance when the sensor placed close to the target object depending on the sensor.

Geometric distortion of imagery can arise from radial curvature or misalignment of lens elements, or from fine scale irregularity in the sensor pixel layout. Correction of distortion can be achieved by photographing a reference grid or other graphic and calculating residual vectors between observed and expected locations in the image (e.g., Honkavaara et al., 2012; Hruska et al., 2012).

Vignetting is the radial attenuation of light intensity that results from dilution as light passes through the elements of the camera lens system (Figure 2.4), and dispersion of intensity with angle from normal. It also arises to a lesser degree from alignment difference between the plane of the sensor and the plane of the ground. The specific degree of vignetting may vary by camera lens: measurement and correction for each lens type may be required (Lelong et al., 2008; Del Pozo et al., 2014). Generally vignetting is most visible in wide angle imagery. Camera systems with an individual lens for each band could potentially have different overall vignetting and geometric patterns on each lens.



Figure 2.4. An example of vignetting (radial attenuation) in a raw sensor image (Nokia Lumia 1020 camera) elevated at 5m height over a patch of seagrass.

Sun glint is contamination of all, or parts of an image whereby direct sunlight is reflected onto the sensor. Glint can be a source of error for remote sensing of surface attributes (e.g., Doxaran et al., 2004). Glint is prominent in an image if the material at the

surface has high reflectivity and has an angle of reflection so as to pass solar light rays into the sensor. Varying roughness and wetness of ground material can result in different degrees of glint. Many issues of glint in a photographed landscape arise from waterbody or general wetness. Waterbodies or wet surfaces can have microtopography resulting from wind action, varying degree of drying or from meniscus-surface around underlying hard material (Figure 2.5). For oceans (and presumably also lakes) the wind speed and direction form a numerical relationship with water slope distribution and resulting surface glint (Cox and Monk 1954, Bréon and Henriot 2006).

Authors Kay et al. (2009) summarised a range of glint removal methods used in remote sensing. At that time most methods related to satellite imagery with respect to open water, and these methods rely on some knowledge about the wave slope and direction characteristics.

Sun glint in an estuarine situation would vary widely with tidal state. When full, glint would depend on water depth, benthic topography, wind fetch, variable wind currents around adjacent terrain, and water flow within the estuary and entering from tributary streams. At low tide, moisture content ranges from dry and wet matt surfaces (e.g., sand) to waterlogged sand, mud and pools with high specular reflectance. In direct sunlight, wet vegetation with a glossy surface such as seagrass and macrophytic algae, as well as detritus, can create a heterogeneous scene upon the substrate background, of intensely varying meniscus surface-angle at the sub-leaf scale such that true colour may be masked.

Some glint removal procedures have been explored. Hedley et al. (2005) used a linear adjustment equation to offset visible frequency bands based on distance between NIR band over a glinted area, and that of the part of the image where substrate NIR reflectance would likely be at its lowest (e.g., deep water). Authors Eugenio et al., (2014) determined that histogram matching between some images was required to compensate for the impact of large glint areas on large waves. Other more statistically intensive methods have been applied (Kay et al., 2009). Overstreet and Legleiter (2017) modified regression relationships between glinted and unglinted regions using difference between the NIR band (as a reference) and each respective band the image stack, and then correcting the observed values in each band according to the function of linear relationship. Kutser et al., 2013 used UV and NIR bands (350 nm and 900 nm) to form a 'power function', derived from a best fit line through reference points of zero glint, which was applied to subtract values along that curve for other bands in the hyperspectral stack. Shah et al. (2017) used index features common across a video frame sequence to attribute un-glinted image values upon a glinted region. While this study was applied to video manipulation, the same principal could be applied to a sequence of overlapping

photogrammetry images. Sun glint effects on nadir-oriented aerial photography can vary with time of day and its respective sun angle in the sky. Doxaran et al. 2004 demonstrated higher surface reflection with oblique viewing angle than overhead for both clear and overcast skies. Bréon and Henriot 2006 demonstrated higher glint effect as the camera moved away from zenith.

Kay et al. (2009) advocated that “*the most straightforward way to deal with the sun glint problem is to avoid it*”. Avoidance of sun glint during airborne or RPA aerial survey may require conducting flight at a time of day with low sun angle to minimise the component of reflection able to enter the camera, although a trade-off in image quality at low sun angle comes about due to increased contamination from the longer shadows upon the scene. The diffuse illumination of cloudy survey conditions may avoid or reduce effect of glint (Figure 2.6). Authors Jaud et al. (2016) minimised sun glint by limiting operations to cloudy conditions. This approach however introduces an additional source of radiometric error that may require standardisation, because differing cloud composition may filter spectral wavelength components differently.

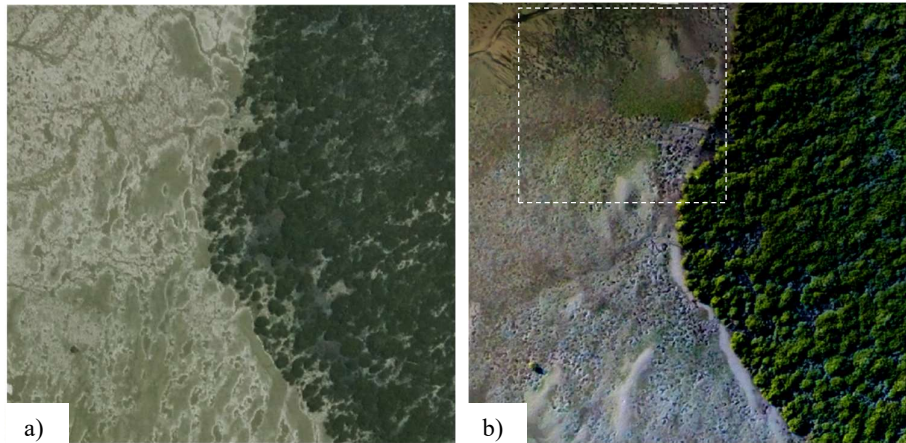


Figure 2.5. Repeat-photographs of the same seagrass scene, Tuapiro, Tauranga Estuary: a) large-format airborne aerial photography taken at a time of overhead sun with substantial sun glint on the wet surface, and b) RPA-sourced aerial photography (Gopro Hero5 photogrammetry-derived image mosaic) taken at near to sunset to eliminate sun glint (right). Despite similar pixel size, the imagery taken near sunset reveals low-density seagrass meadow patches (white boxes), as well as stingray feeding pits and hydrology structure not easily visible in the imagery with overhead sunlight (a).

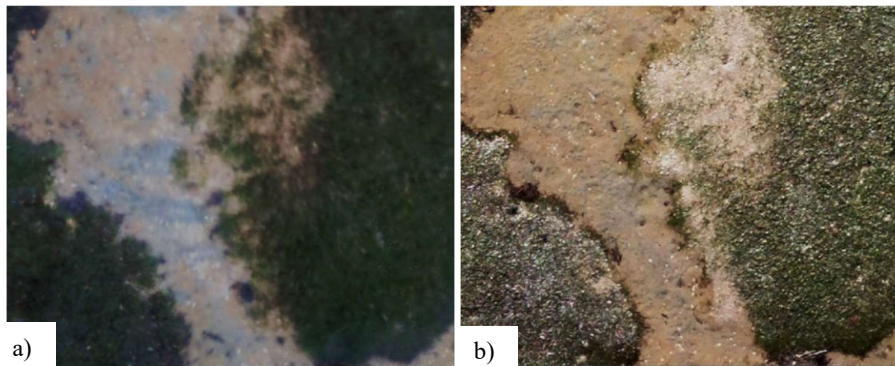


Figure 2.6. Two images above of the same scene (two week time separation) where lighting conditions are a) overcast skies with no direct sunlight or shadow and b) direct sunlight with cloud-free skies showing significant sun glint patterns that obscure some of the dark-hued seagrass coverage, and introduce texture and spectral content that is not representative of the scene. Sun angle to horizon and tidal water drainage is matched as near-identical.

2.5.4 Radiometric correction, reflectance and normalisation

Solar radiation is absorbed, scattered or transformed differentially across the electromagnetic spectrum, as the light passes through the atmosphere to the ground, reflects from the remote sensing target then travels to the sensor (Schowengerdt 2007). Underwater targets receive incident light that is subject to further absorption and scattering within the water column (e.g., Misbari and Hashim 2016). Light hitting the target is therefore a combination of residual direct light from the sun, or residual diffuse light resulting from scattering from other directions (Schowengerdt 2007).

Content of a water body over an estuary can absorb and/or scatter incoming radiation depending on organic, photosynthesising (e.g., algal) or particular material suspended in the water column (e.g., Dekker et al., 2011; Shi and Wang 2014). Water column corrections can be applied when bathymetric depths are available with improvement to resulting classification (e.g., Lu and Cho 2011; Pu et al., 2014). It has been argued that radiometric water correction is essential for retrieving ground reflectance (Pu et al., 2014). Water interference would be reduced or eliminated for a survey undertaken with the tide out, noting that the effects of residual pooling on classification spectra remain unmeasured.

Procedures for radiometric correction have been explored in various mathematical treatments for standardising satellite and airborne remote sensing imagery (Furby and Campbell 2001; Schaepman-Strub et al., 2006; Kobayashi and Sanga-Ngoie 2008; Honkavaara et al., 2009; Gu et al., 2011; Cheng et al., 2012). Radiative transfer theory can be modelled at different levels of complexity, factoring the various atmospheric components that light must pass through before reflecting off an object and onto a sensor (Figure 2.7). For example, Cheng et al. (2012) defined at-sensor radiance for any given zenith and azimuth of sensor relative to the target (Equation 2.2).

$$L_{s\lambda}(\theta_r, \varphi_r) = L_{p\lambda} + r_{d\lambda} \pi^{-1} [E_{0\lambda} \cos \sigma \tau_1(\lambda) + FE_{d\lambda}] \tau_2(\lambda) \quad (\text{Equation 2.2})$$

where:

$L_{s\lambda}(\theta_r, \varphi_r)$	= at sensor radiance for a zenith (θ_r) and azimuth angle (φ_r) from target to sensor	$\tau_1(\lambda)$	= transmittance from sun to target
$L_{p\lambda}$	= path radiance	F	= shape factor (local topographic correction)
$r_{d\lambda}$	= diffuse reflectance	$E_{d\lambda}$	= downwelled irradiance at the target
$E_{0\lambda}$	= exoatmospheric solar irradiance	$\tau_2(\lambda)$	= transmittance from target to sensor
σ	= incident angle of solar irradiance		

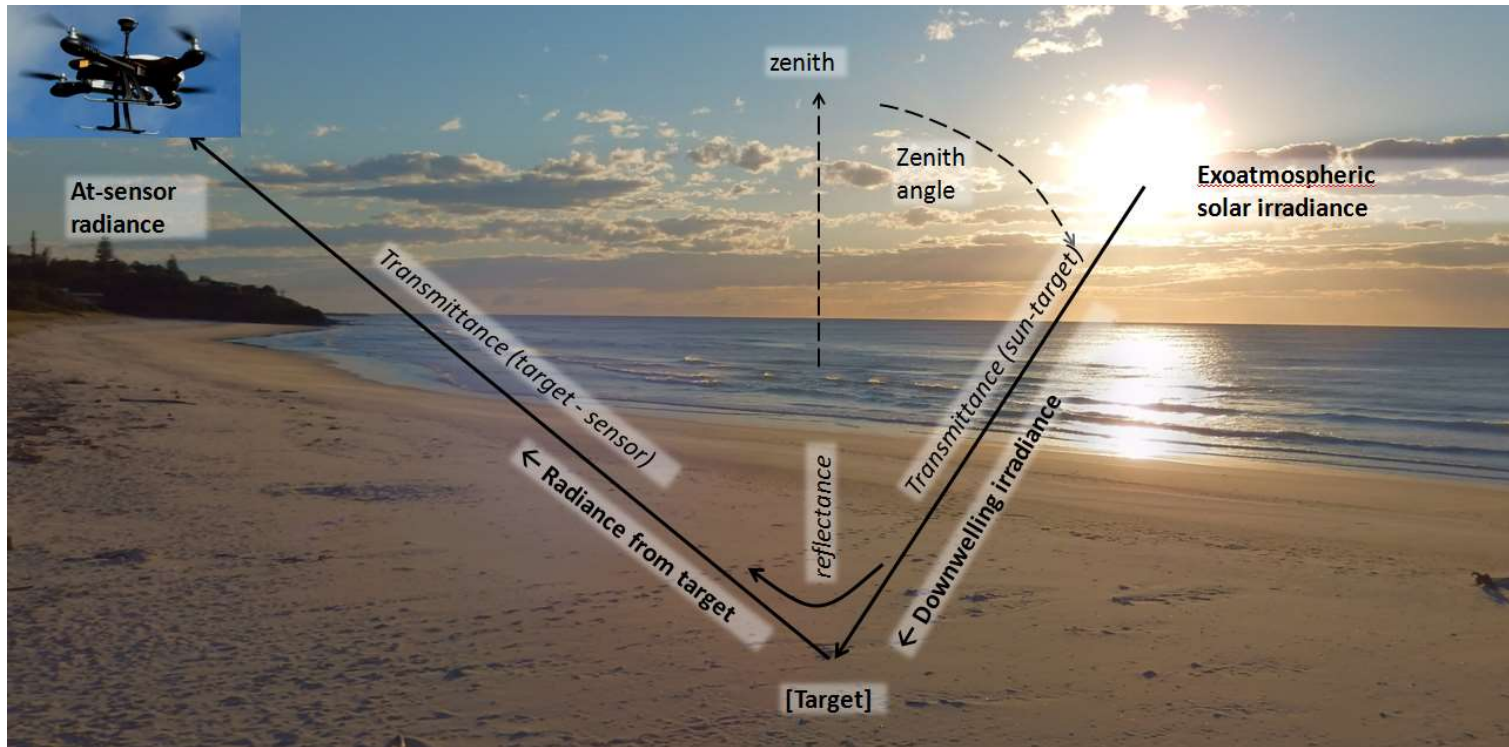


Figure 2.7. Schematic depiction of a simple solar radiative transfer relationship. Radiance at the sensor is dependent on solar power, transmission efficiency through the atmosphere (which varies with wavelength and decreases with increasing zenith angle), the target material reflectance factor, transmission efficiency to the sensor, and then the quantum efficiency of the sensor at different wavelengths.

Radiative transfer models solved for the earth's atmosphere allow satellite imagery to be corrected for sun and surface angle relative to the sensor, and imagery providers maintain a database of correction factors from which a correction equation can be approximated. Corrections however can be erroneous at some spatial and spectral scales due to local variability in conditions (Huang et al., 2016). Exhaustive radiometric calibration requires measuring both incident solar radiation and reflected radiation across the spectrum, to calculate a bidirectional reflectance distribution function (BRDF) as a basic measure of spectral response of the target material (Nicodemus et al., 1977). A range of bidirectional models can be applied depending on the diffusion and scatter of incoming and outgoing light (Schaepman-Strub et al., 2006).

In comparison to satellite and airborne imagery, low-altitude RPA-derived imagery is typically captured with significantly less atmosphere between the ground and the sensor, so in clear air radiometric changes between image captures should be largely influenced by downwelling light conditions, and $\tau_2(\lambda)$ (Equation 2.2) tending to 1 (full transmittance to sensor). However, in the marine environment there may be higher concentrations of aerosol close to the ground derived from sea spray, surf and evaporative transport of material (Zieliński et al., 2012; van Eijk et al., 2014). Airborne or RPA-mounted sensors generally require specific calibration for each camera and potentially each site (e.g., Laliberte et al., 2011; Clemens 2012). Furthermore, Hakala et al. (2013) determined that radiometric correction factor was dependent on RPA flight direction.

Radiometric correction has been applied to imagery taken from RPA in the terrestrial environment (Levin et al., 2005; Laliberte et al., 2011; Clemens 2012). In these studies, large reference boards of known spectral character are placed on the ground to provide an invariant spectral reference, from which the respective radiance factors (functional image transformations for each band) could be calculated for each situation. Barium sulphate has been used as a reflectance referencing material due to its high reflectance, good cosine attenuation with oblique angle of incidence, and consistent response across the UV-VIS-NIR region of the spectrum (Grum and Lucky 1968).

A calibrated correction equation should allow temporal and spatial standardisation of images. No widely accepted approach was evident in the literature that can be confidently applied to an estuarine study without project-specific calibration, and no publication provides specific guidance or photogrammetric parameters for operating in the aerosol-variable marine environment.

Radiometric normalisation is the process of making corrections to images in a photo-set so that digital values are describing a similar spectral response to the illuminated surface. Methods of normalisation are well established for satellite imagery (Du et al., 2002; Hong and Zang 2008). Illumination varies with sun angle which varies

with time of day and year, and incident light can vary rapidly over the duration of a capture mission if clouds are mobile (Dunford et al., 2009). For a photo-set to be integrated for quantitative remote sensing, the radiometric response needs to be consistent across the whole set, and standard reflectance units calculated. Images collected during aerial photography should be similar within a flight track, however error between tracks is possible due to change in the incident light level during the lapse of time between passes (Asmat et al., 2011) (Figure 2.8).

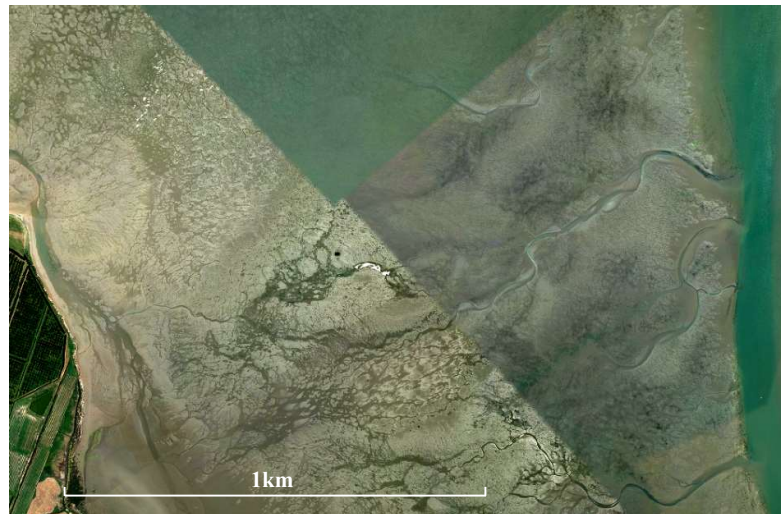


Figure 2.8. Uncorrected image mosaic patches showing radiometric difference at capture, across a ~2 km wide airborne aerial photography scene. Imagery sourced from Bay of Plenty Regional Council 2014 aerial photography dataset.

Hong and Zhang (2008) compared a range of normalisation methods present in the literature, and generalise the methods into two groups: *absolute*, where corrections are made based by sensor parameters, atmospheric constants and scene attributes, and *relative*, where images are corrected in comparison to other images. Biday and Bhosle (2010) classify radiometric normalisation methods into three categories: statistical methods; histogram matching; and linear regression methods. Statistical methods apply a simple offset to each band to match general differences between photos. Histogram methods partition the range of values into histogram bins (e.g., 0-256 in the case of standard camera imagery), and photo matching is achieved by applying offsets per histogram-bin using some intensity transformation function to equalise histogram cumulative profiles. Regression-based normalisation applies band-adjustments based on least-squares distance between the mean band values between two images. Relative normalisation is computer-intensive due to the large data volumes analysed and compared within and between images, especially in large image-sets. Efficient computational

workflows for relative normalisation have been devised (e.g., Chen et al., 2014) but with compromise in accuracy due to simplified calculation of coefficients. Absolute normalisation is computationally simpler, and results can be generated faster than relative methods as calculations are based on pixel statistics across the whole scene.

Carbonneau et al. (2012) described a relative method using one image as a fixed reference, and correcting band values in the photo-set based on the histogram profile of the reference. However, their proposed method requires first partitioning both reference and candidate images into coarse land-cover types (e.g., riparian vegetation vs. river channel in their case). This method is similar to one proposed by Hall et al. (1991), which first forms a radiometric control using one or multiple images, and then apply linear transforms to rectify subsequent images to the control, but the authors urge caution about the use of image partitioning that is based on content, due to the normal alignment differences that arise from spatial registration across an image-time-series. Their approach is not ideal for seagrass feature extraction as estuarine scenes can be complex (seagrass, algae (micro and macro), detritus, shells, other animals) and normalisation is a prerequisite for the image classification that follows (using the authors method would create a circular process dependency).

Asmat et al. (2011) used a k-means spectral clustering algorithm to identify the major spectral groups using an orthogonal cross-flight over the primary flightpaths to create regions of common photogrammetric overlap, and applied regression-based correction algorithm to normalise primary flight images. This method assumes that spectral response is the same for images within each flight-track. Collings and Caccetta (2013) used corrected Landsat-TM imagery as a reference frame for normalisation of set of 30,000 high-resolution airborne photogrammetry images, by using the scene-statistics of the satellite imagery as a benchmark for adjustment of aerial image bands.

RPA based image acquisition would be subject to the same image normalisation issues that apply to airborne aerial photography. Development of remotely sensed survey methods for seagrass condition-monitoring that are suitable for large scale application, based on imagery taken from RPA, would require correction for radiometric variation across and image-set. Modern RPA-focused photogrammetry software (e.g., Agisoft Photoscan Pro 1.4) have incorporated normalisation functionality within the photogrammetry processing chain.

2.5.5 Photogrammetry

Quantitative photogrammetry methods have been in practice for many decades along-side of the evolving field of aerial photography (Graham and Koh 2012). The full

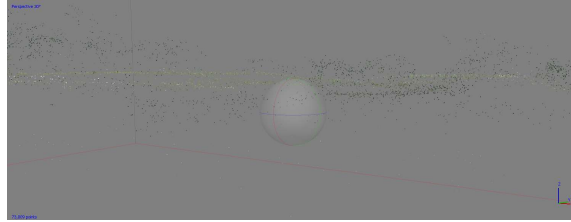
breadth of the subject is too large to review here. If accurate geographic positioning is required, then the technical field of precision-survey is also relevant. For the purpose of this study, methodological focus is directed towards a subset of photogrammetry procedures that relate to quantitative survey using low altitude RPA and piloted aircraft, and associated consumer software, under the objective of forming a geographically accurate orthorectified image mosaic and surface model (Colomina and Molina 2014; Suomalainen et al., 2014; Vasuki et al., 2014; Gonçalves and Henriques 2015).

Formation of a contiguous spatially accurate image mosaic from drone-captured imagery flown on a regular grid, requires that i) contributing images are oriented with respect to the ground; and ii) image pixels are repositioned to their true location accounting for the combined error arising from lens angular distortion and underlying terrain effects. In the context of a grid of RPA-flown overlapping component images, orthorectification using modern photogrammetry software automation typically involves i) identification and matching of common features between overlapping images to determine internal and external camera/frame geometry; ii) repositioning of all pixels across the image-set to the estimated true 3D location based on the calculated camera/image orientation model; iii) combination of images into a seamless mosaic based on a rule (e.g., average, minimum or maximum pixel value from contributing overlapping images) for combining overlapping pixel values (Figure 2.9). Agisoft Photoscan software was identified as one of the better lens correction options by Hastedt et al., 2016. This software was selected for use in the current study due to its ability to resolve lens distortion, normalised colour, apply radiometric correction and form spatially explicit orthorectified image mosaics and digital surface models. The qualities were verified in a benchtop environment using test imagery on a range of cameras.

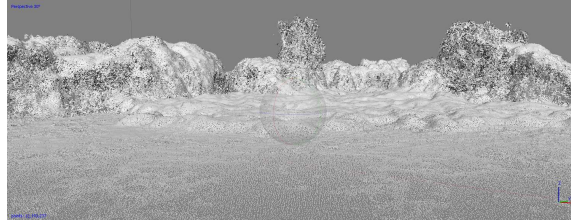
2.6 Remotely piloted aircraft (RPA)

RPA are a broad category of unpowered air vehicle. Commonly they are also termed unmanned aerial vehicles (UAV), unmanned aerial systems (UAS), and remotely operated vehicles (Colomina and Molina 2014; Zolderdo et al., 2015). In New Zealand aviation legislation, they are termed RPA (Civil Aviation Authority 2018). Modern conceptual origins date back to balloon munitions deployment in the late 1800s and early 1900s (Thomas 2014). Simple radio-controlled target or observation drone-planes were in common military use by World War II (Cho 2004; Blom 2009). Advancement of RPA have predominantly been driven by military requirement, developed as miniaturised fuel-propelled light aircraft technology, then adopting electro-mechanical technologies more recently (Blom 2009; Watts et al., 2012).

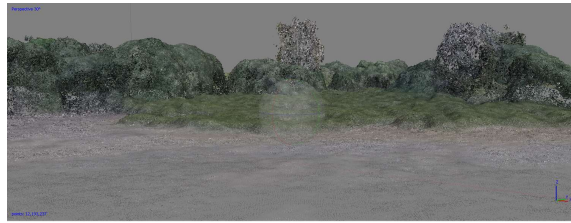
a) Sparse point cloud:
Generation of common tie points
between photos



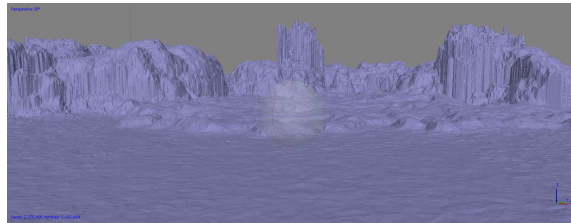
b) Dense point cloud:
Calculation of new pixel
locations.



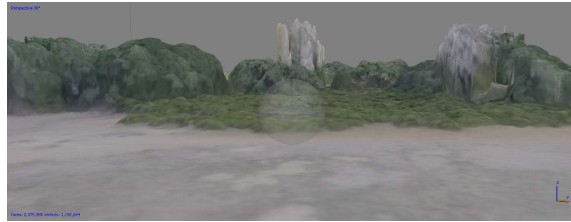
Colouring of dense points.



c) Surface model mesh:
Generation of triangulated face
network between dense points.



d) Surface model mesh:
Texture-calculation for mesh
faces.



e) Orthomosaic generation:
Orientation transformation of
individual images followed by
orthorectification upon surface
model, then generation of flat
normal orthometric raster.



Figure 2.9. Key steps in the photogrammetric processing chain with examples from a low altitude aircraft survey over an area of mangrove and coastal forest at Wharekawa Harbour. The stages illustrate generation of: a) image tie points; b) dense point cloud; c) triangulated surface model; d) surface texture ; and e) orthomosaic. Georeferencing using ground control point is associated with a).

The rapid development of high-speed auto-stabilising microcontrollers and battery technology over the past decade has resulted in an expansion of smaller affordable drone technology accessible to technical and general consumers (e.g., Jones et al., 2006; Linchant et al., 2015). Hardware advancement and affordability has further accelerated over just the past few years due to escalation of the recreational first-person view (FPV) flying, drone racing, and aerial photography/video markets with their significant economies of production scale. Inexpensive open-source autopilot hardware and flight-planning software make GPS-based computer-driven flight operations accessible to most research and educational organisations (Meier et al., 2012; Scherer et al., 2012; Dryanovski et al., 2013).

The broad range of RPA airframe hardware includes a variety of forms and sizes from micro-scale (e.g., Capello et al., 2012) to large civilian drones (e.g., Laliberte et al., 2011; Suomalainen et al., 2014) to the long-range military unmanned drone planes (Springer 2013). The range has included kites, blimps and balloons in some research contexts (Guichard et al., 2000; Klemas 2015). RPA have been classified by different authors according to characteristics of size, weight and function (Limnaios et al., 2012; Watts et al., 2012; Hoffer et al., 2014; Anderson and Gaston 2015). Most current RPA however fit into two basic functional categories: fixed wing planes, that need to sustain velocity in order to stay airborne, and rotor propelled vehicles (rotating wings), which fly or hover with fine control of rotor speed using the position/orientation-aware flight controller. Fixed wing RPA tend to manifest as airplanes (wings on a fuselage, usually with a tail plane and rudder), or flying wings (no fuselage), and each has its functional advantages in the trade-off between weight, speed, control, flight longevity and stability. Single rotor designs (helicopters – e.g., Kaneko et al., 2011) are less common now than multi-rotor RPA (three or more rotors) due to the mechanical complexity of the single-rotor helicopter orientation-control, and the greater manoeuvrability, stability and versatility of multi-rotor design (Austin 2010).

2.6.1 RPA applications

RPA have the benefit over piloted aircraft that they can fly close to the ground (fixed wing aircraft in New Zealand are limited in most cases to 500 or 1000 feet minimum flying height depending on the situation). As a consequence, there is potential for acquisition of high-detail imagery at resolution as fine as several centimetres in pixel ground sampling distance or smaller, and terrain models accurate to <5cm vertical accuracy when used with precision-survey ground referencing (Peña et al., 2013; Gonçalves and Henriques 2015; Räsänen and Virtanen 2019). In one review, RPA based survey achieved the highest of observed classification accuracy statistics, compared to both airborne and satellite image sensors (Ma et al., 2017). Similarly, Anker et al., 2014 demonstrated classification advantage arising from the high spatial detail of imagery possible from an RPA. Flying heights in close proximity to the ground allow structural detail and differentiation from background that would not be feasible at higher altitude (Borra-Serrano et al., 2015).

However, in cases where large scale survey is required outside of the feasible flight-range of the drone power supply, and where high spatial definition is not so critical, low altitude piloted aircraft on a targeted flight plan may yield more cost-effective imaging. For example, in a comparison of satellite, aircraft and RPA based remote sensing of viticulture condition, RPA were found the most cost-efficient for small scale assessment, but efficiency favoured aircraft above 5 hectares survey area (Matese et al., 2015).

There are a number of additional benefits that are particular to RPA, or not easily or safely achieved with piloted aircraft methods. Largely the benefits arise from the close proximity that RPAs can fly to the ground or target objects of interest, and their manoeuvrability and fine spatial positioning control within a vertically varied environment (Madden et al., 2015). Absence of a human pilot, and the light-weight miniaturised form of the RPA, allow flight operations into environments which are otherwise difficult, risky, or inaccessible for personnel, or provide perspectives that are out of reach of other methods of observation. For example, Brouwer et al. (2015) observed coastal process in high resolution from above a surf-zone using two RPA, on alternating duty-cycles that allowed continuous recording from a fixed vantage point in three-dimensional airspace. GPS-guided waypoint-routing allowed two RPA to operate as one instrument. With these flight and survey characteristics, RPA are enabling a wide range of research and modelling opportunities that were prohibitive or difficult prior to current RPA availability (Chabot and Bird 2015; Colomina and Molina 2014).

More recently, multispectral cameras have been engineered that are small enough to mount upon an RPA. Although the sensors on these cameras are still small in pixel-dimension (e.g., 1.2 megapixels) compared to commercial cameras (80-300+ megapixels), the multispectral cameras have enabled a range of vegetation land-cover and health mapping applications at small scale (Kelcey and Lucieer 2012).

Small agile RPA are also adding important capability for ecological monitoring and provide useful data and research efficiencies. For example, Weissensteiner et al. (2015) used small RPA to observe crow nests in a high forest canopy, improving on previous methods (that used manual observation) in terms of cost and animal disturbance. Evans et al. (2015) collected high resolution imagery allowing crocodile nest identification amid tall wetland trees at a remote, sensitive and potentially hazardous location. There are numerous other published examples of RPA being used to generate wildlife data, including counting of nesting terns (Chabot et al., 2015), water-bird census with species discrimination (Dulava et al., 2015), identification of individual killer whales (Durban et al., 2015), abundance and extent of chinstrap penguins (Goebel et al., 2015), counting marine fauna (Hodgson et al., 2013) and elephants (Vermeulen et al., 2013), quantifying sampling spawning behaviour (Whitehead et al., 2014), and photography along lesser kestrel flight paths (Rodríguez et al., 2012).

Similarly, RPA have been applied to problems associated with the monitoring and protection of habitat and species within ecosystems (Koh and Wich 2012; Anderson and Gaston 2013; Chabot and Bird 2015; Linchant et al., 2015). Low altitude flying has enabled detailed assessment of vegetative community structure (Zweig et al., 2015; Lehmann et al., 2016) and detection of weeds (Göktoğan et al., 2010), as well as measuring vegetation condition and aspects of ecosystem health (Husson et al., 2014b; Zahawi et al., 2015; Michez et al., 2016), habitat quality for species (Rodríguez et al., 2012; Chabot et al., 2014), and general support of conservation management operations (Koh and Wich 2012; Mulero-Pázmány et al., 2014). Authors Ramsey et al. (2014) flew a low-cost drone above and within a karst landscape to detect objects and observe exterior and interior karst formation. RPA have been applied to a range of other applications in many scientific and commercial industries (Thompson and Saulnier 2015).

Survey of estuarine surface using low altitude RPA can be dated back nearly two decades to a study using a 6 m blimp carrying an automated 35 mm camera to collect photogrammetrically overlapping imagery yielding sediment surface characteristics (Guichard et al., 2000). Authors Jaud et al. (2016) quantified morphological change in the terrain of an estuarine mud flat across a 12-month change period.

Numerous papers herald the benefits of RPA over piloted aircraft in terms of their lower cost of operation and the survey-detail arising from very small ground sampling

distance. However, this popularity should be balanced by acknowledging the merits of piloted aircraft for collecting moderately high detail imagery (e.g., Hulet et al., 2014). Under New Zealand aviation law, piloted aircraft are required to maintain flight above 500 feet of height above ground (1000 feet over built-up areas) during normal operations (i.e., aside from take-off/ landing and approved low altitude flight and airspace allocation) (Civil Aviation Authority 2018). A small piloted aircraft carrying a medium/large format camera (e.g., Vexcel Ultracam series camera) flying at minimum allowable flying height (with corresponding fine photogrammetric flight-grid spacing) can generate imagery with ground sampling distance approaching that of a small camera mounted on a low altitude drone. Since services are readily accessible in most areas and can provide an equal or greater range of mounted sensor-options due to superior payload weight, many of the benefits of using RPAs can be rationalised in terms of lower cost of capture or greater operational flexibility depending on the operation (e.g., Greenwood 2015). Drone cost-benefits are greatest for smaller study areas where commercial aircraft deployment costs are relatively high, and where terrain makes low controlled grid flight expensive.

Application of RPA in New Zealand for environmental survey is in early stages of uptake compared to the volume of published research from US, Europeans and Asian sources. Authors Nishar et al. (2016) used a small camera drone fitted with an additional thermal infra-red sensor to map land-cover condition and surface temperature in a geothermal field. Alexander and Harvey (2014) have mapped geothermal carbon dioxide levels and a high-detail digital surface model using a small camera drone. Cook et al. (2013) relayed atmospheric temperature and humidity measurements in real time to a recording station. Potential for cost optimisation has been proposed for fire suppression using RPAs mounted with thermal infra-red sensors, to replace the greater helicopter cost, but has yet to be tested in practice (Christensen 2015). Much of the utility of RPA arise from the programmable flight autonomy enabled by modern flight controllers.

2.6.2 Autonomous flight control

There are a wide range of flight-controllers of different expense available for RPA guidance and control. In addition to commercial options, the low-cost public-domain project 'ArduPilot' that has developed over the past decade and provides flight-control hardware, software and telemetry systems that are now made to a commercial manufacturing and performance standard in terms of both functionality and reliability. The product-version adopted for this study was the PX4 controller board, also termed 'Pixhawk' after commercialisation by 3D Robotics (Meier et al., 2012; Dryanovski 2013; Arifianto and Farhood 2015). This is an integrated flight controller with inertial, GPS,

barometer and magnetometer sensors for flight stabilisation and onboard computing for autonomous flight control. The controller board has facility for attaching a laser rangefinder ('lidar lite'), ultrasound acoustic rangefinder, and an optical-flow sensor for enhanced aircraft guidance. The board also has generic data channels that can host analogue sensing devices that can be used to further modulate flight or generate data to be logged to SD card.

Modern RPA flight controllers have active flight path maintenance using a GPS module, including accurate control over route, speed and height above ground. Height is based on the position of the craft relative to starting position of the RPA, unless a specific height adjustment is programmed. Over undulating terrain, where the starting position does not allow an accurate datum, flight plans need to be generated in a Geographical Information System (GIS) that factors ground topography (e.g., using lidar or digital elevation model (DEM)). The elevation change across the topography of a flat estuary is small compared to the accuracy limits of the GPS to effect horizontal and vertical positional control (which is approx. 2-5m horizontal accuracy and 0.5m vertical accuracy). The Pixhawk laser and acoustic ultrasound rangefinder modules enable more accurate height control. The lidar rangefinder was deemed as likely problematic over the water surface of an estuarine tidal flat even with the tide out (there have been crashes reported on user forums due to false height readings, probably from lidar absorption into the water). Acoustic ultrasound combined with lidar could be used if the craft is maintained below ~ 10 m height above the surface, thereby increasing vertical height control during flight above an estuary, as compared to relying on GPS alone.

The Pixhawk flight controller is normally set up with a data telemetry link to either a laptop or tablet (Mission Planner software for Windows systems). Mission Planner provides detailed in-flight monitoring and diagnostic reporting as well as flight plan programming (e.g., Duffy et al., 2018). Mission planner has two key interfaces - a flight data view, which displays real-time orientation, horizon, GPS and status data (flight console), and a flight plan view where waypoint routes and aerial survey grids are constructed and deployed to the drone. The Mission Planner interface displays speed, direction, height, craft orientation, camera orientation and emergency behaviour to be set and executed as an autonomous flight route (Figure 2.10). In Figure 2.10, the top panel shows the flight-grid development process, where parameters can be set for camera type, grid spacing, photo overlap, flight angle, camera-angle, baseline flight altitude and turning characteristics at the end of each flight-run. Once set, the software draws a flight-cost-optimised flight-plan based on an area-of-interest (polygon) drawn by the operator. The flight plan can either run as a cross-grid (as seen in the main panel) or as a single-direction grid (top panel inset), depending the cost-accuracy trade-offs that are required

for the final mosaic or elevation model. Once accepted, the flight plan is computed into a set of geographical waypoints (see the bottom table of lower panel, Figure 2.10) that can be loaded into the flight controller of the RPA using the attached telemetry radio. Once uploaded and engaged, the RPA then flies the flight plan autonomously, taking photos as instructed, then returns home for re-tasking (and battery change). The way-point collection can be edited manually for fine detail control of altitude, speed and position, and the plans saved for replication later. It is in this way that specific flight-plans can be replicated exactly (within the positional accuracy limits of the GPS receiver). This capability allows generation of spectral time-series data and testing capture scenarios over a common focal area and is one of the key benefits that RPA have over piloted survey techniques.

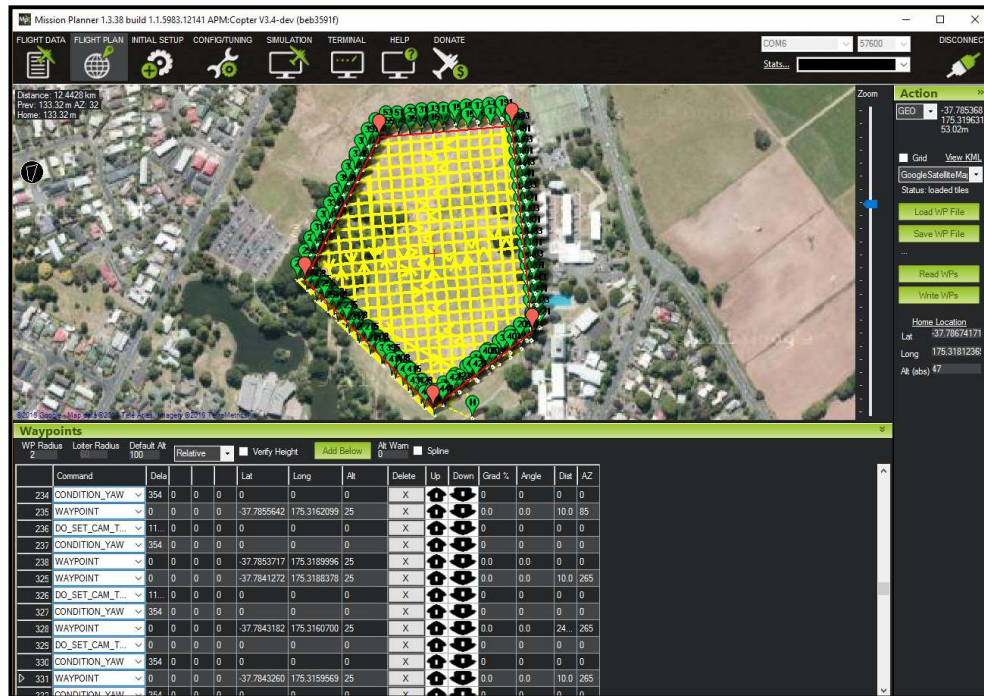
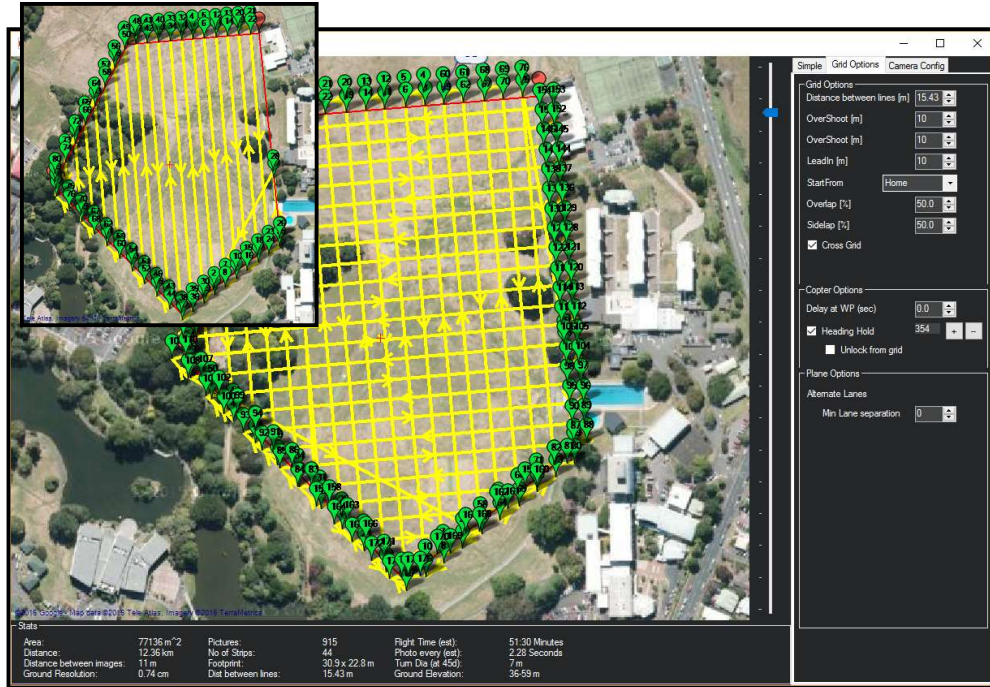


Figure 2.10. Example of a (sample) RPA flight plan, constructed using Mission Planner software. Upper panel shows the flight construction process. Lower panel shows the generated geographical waypoint loaded into the RPA. See main text for further description.

2.6.3 Interaction with aviation regulatory environment

RPA operation has notable flight restriction in New Zealand, which may influence uptake of RPA as a widely used wildlife management tool. Flight rules are documented in a consolidated rule-set (Civil Aviation Authority 2018), and are summarised below (Table 2.2), and the reader is directed to <https://www.caa.govt.nz/rules/part-101-brief/> for full current version, as regulations are updated periodically.

Controlled flight areas for RPA in New Zealand are documented on a live map resource at the web site: <https://www.airshare.co.nz/maps>. The flight map available at this website is authorised by the New Zealand Civil Aviation Authority to depict allowed and restricted flight areas for the purpose of flight planning, and there is a requirement to inspect the map prior to any planning for field survey work.

At the time of writing, the map generated over Coromandel Peninsula was captured (screenshot) in Figure 2.11 and illustrates the restricted airspace over many estuaries due to the presence of service airstrips, and designated aircraft low flying zones. Flying of RPA in restricted airspace requires authorisation that is dependent on the airspace control. Flying in an airfield restriction zone requires RPA control certification and flight-plan permission from the airfield controller (and coordination with an air control tower when one is present). RPA flight in an aircraft low-fly zone is generally not permitted and would generally require temporary (short term) closure of low-fly zone in order to conduct RPA operations.

Wharekawa Harbour has no special restrictions other than normal RPA constraints documented under Civil Aviation Authority (2018).

Table 2.2. Summary from Rule Consolidation Part 101 for remotely piloted aircraft (RPA) (Civil Aviation Authority 2018) at time of writing.

Rule	Lay summary relevant to seagrass survey by RPA	Research project requirement
101.205	No RPA operation within 4 km of aerodrome, with notification/approval depending on whether controlled of uncontrolled type. Flight within this zone is possible with permission <i>and</i> RPA operator certificate, or if operation conforms to criteria for “shielded operation”.	Study area is outside of 4 km proximity to any aerodrome.
101.207	No RPA flight over land without permission of landowner, or over person(s) without permissions from the person(s). No operation above 400 feet above ground (122 m).	At the time of field operations, ground within the Coastal Marine Area (land below mean high water springs) - no specific land ownership (Marine and Coastal Area Taku Moana Act 2011). No requirement for flight above 400 feet.
101.209	RPA operation is restricted to airspace within (unaided) line of sight of operator, or spotter (if communicating operator is flying by live camera (FPV).	All research survey conforms to line of sight operation. All of survey area is within sight of central ground station location without obstacle.
101.211	No outdoors night flying unless conformant with “shielded operation”.	All survey requires sun at moderate to high angle.
101.213	Piloted aircraft have right of way.	Study area is away from main coastal aircraft transit lane.
101.215	Special restrictions exist if RPA above 15kg total flying weight	RPA to be used in this study is <3kg all up weight.

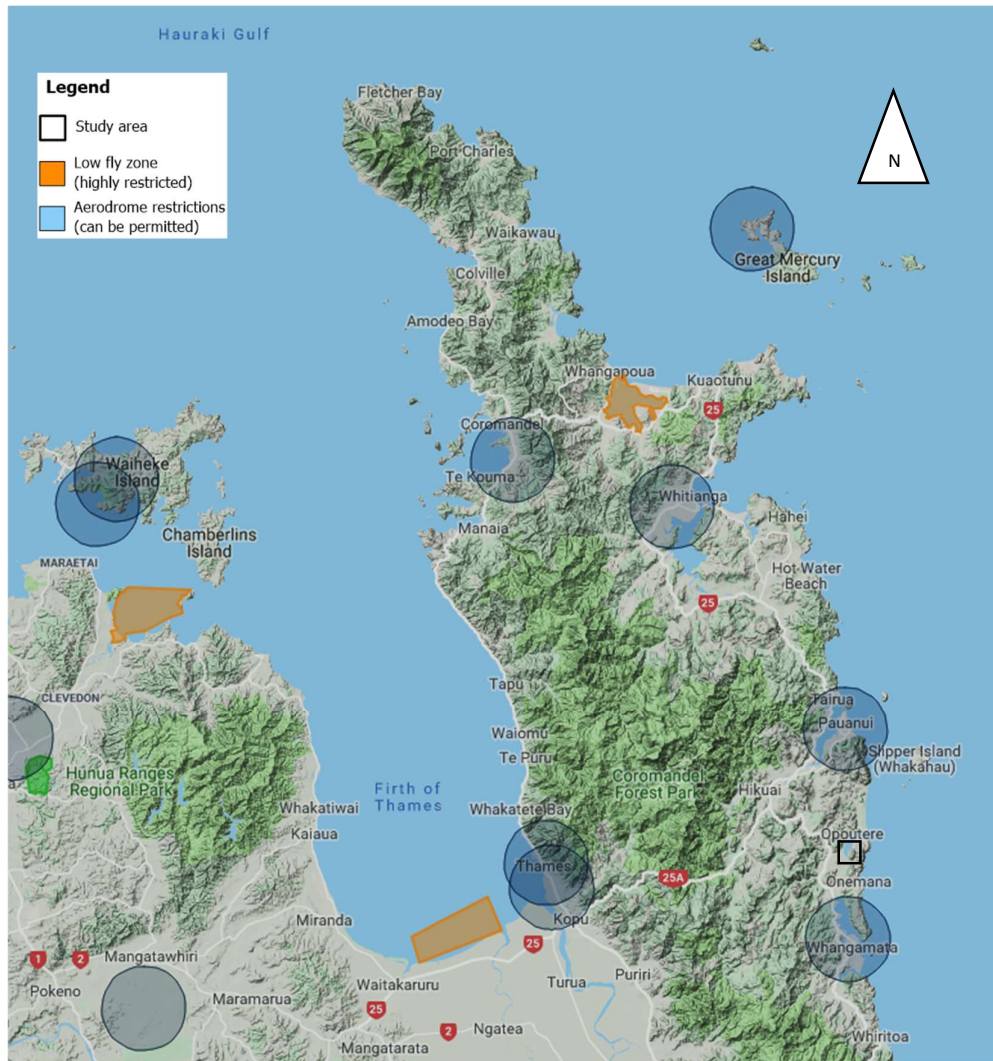


Figure 2.11. Controlled airspace for RPA Operations, Coromandel Peninsula. Image sourced from the Airshare map resource <https://www.airshare.co.nz/maps>.

2.7 Discussion and Conclusion

In this chapter, background literature was reviewed to i) understand seagrass ecology and growth on the ground; ii) summarise relevant feature extraction methodology relating to seagrass; iii) identify trade-offs that need to be considered in research survey design; iv) identify aerial survey factors that need to be accounted for in the survey design for subsequent chapters; and v) establish feasibility and limitations for use of RPA as a survey tool for seagrass on New Zealand estuaries.

Seagrass in New Zealand may be in decline, and data is insufficient to establish its status nationally and for specific estuaries with exception where monitoring has been in

place to measure declining population condition. Based on insights from this review, improved monitoring methodology is warranted. Remote sensing methods of automatic feature extraction are appropriate due to the significant scale of many New Zealand estuaries.

Seagrass plants grow from the sediment in dense or sparse clusters of small leaves when mature and well established but can present on the estuary at sizes down to a scale that is difficult to see at ground level. Seagrass can appear on an estuary as a uniform solid coverage or can grow through or be buried by shell, detritus and a range of substrates of particulate appearance. Seagrass can be covered by epiphyte, coated with silt, or at times with invertebrates upon the leaf surface. Seagrass can also present with damage from storm, flood or herbivory such as swans and geese. A robust reliable seagrass feature extraction method would require that seagrass can be detected from within different proportions of these confounding surface materials. In this research, it is therefore important to factor a range of scene conditions into the testing of feature extraction algorithms, so a study area comprising highly heterogeneous estuarine seagrass, detritus, shell and substrate proportions would be appropriate for the objectives of this study.

The scope of this study is to develop and demonstrate RPA-based procedures suitable for semi-technical users where methods are feasible within normal agency monitoring and geospatial infrastructure. As such the hardware and methods being tested here aim to utilise a multispectral sensor at significantly lower cost than hyperspectral cameras, using much smaller and lower risk RPA airframes than the large airframes required for carrying hyperspectral hardware, and employing where possible open source or low-cost remote sensing software.

The aerial survey design for this study needs to address or accept factors outlined in Section 2.5. Lens geometry, vignetting, image colour normalisation and orthorectification of the resulting image mosaic is addressed within the capabilities of Agisoft Photoscan Pro software (Appendix 2.8.2). Glint was managed by targeting consistently low (but not too low) sun angle and uniformly overcast sky conditions for the timing of RPA operations, which required some calendar and weather coordination to ensure low tide at the same time as the optimal sun angle. Motion blur was addressed by flying the drone at slow speed and equipping the airframe with a motor and propeller set-up prioritising stability in the air at the expense of battery longevity. The considerations above resulted in the remotely piloted aircraft system hardware and software configuration that is summarised in Appendix 2.8.3.

2.8 Chapter appendices:

(see the following A3 pages)

2.8.1 Appendix 2.8.1. Seagrass remote sensing literature cross-section (2010 to 2019) using the Scopus data base search string given below*.

Reference	Target species	Year of capture of remote sensing data	Year of capture of ground survey data	Location	Mapping extent (area or coastal length)	Remote sensing data source (s)	Specified ground sampling distance	Ground truth sampling / attribute	Single or time-series
Amran (2010)	Seagrass, species not specified.	2008	Not specified.	Indonesia.	Not specified	Quickbird satellite.	2.4 m	Sampling not specified; seagrass % cover.	Single estimate.
Barille' et al. (2010)	<i>Zostera noltii</i> .	1991-2005	2005, 2006	France.	340 km ²	SPOT 1,2,5 satellites.	20, 20, 10 m	Field spectrometry, sampling not specified.	Time-series.
Dierssen et al. (2010)	<i>Thalassia testudinum</i> ; <i>Syringodium filiforme</i> ; <i>Halodule wrightii</i> .	2004	2004	Bahamas.	Not specified	SeaWiFS satellite.	1 km	15-20 samples from 25 stations.	Single estimate.
Sridhar et al. (2010)	<i>Halophila</i> spp.; <i>Halodule</i> spp.; <i>Enhalus</i> sp.; <i>Cymodocea</i> sp.; <i>Thalassia</i> sp.	1996, 2000, 2002 and 2004	n/a	India.	Not specified	IRS LISS III satellite.	Not specified	Not clear.	Time-series.
Andrade and Ferreira (2011)	<i>Zostera marina</i> ; <i>Zostera noltii</i> .	Not specified.	Not specified.	Portugal.	Not specified	Oblique aerial photography from building roof, with Nikon D70.	Varied	120 image points; validation method not specified.	Time-series.
Fearns et al. (2011)	<i>Posidonia</i> sp.; <i>Amphibolis</i> sp.	2004	2004	Western Australia.	4 km ²	Hymap airborne hyperspectral.	3.2 m	35 validation sites of underwater video creating 1800 references, seagrass presence/absence.	Single estimate.
Knudby and Nordlund (2011)	<i>Cymodocea rotundata</i> ; <i>Halodule</i> sp.; <i>Thalassia hemprichii</i> ; <i>Thalassodendron ciliatum</i> ; <i>Halophila ovalis</i> ; <i>Syringodium isoetifolium</i> ; <i>Cymodocea serrulate</i> .	2007	2007	Tanzania.	4.1 km ²	IKONOS satellite.	4m	167 point with seagrass biomass by visual estimate.	Single estimate.
Lyons et al (2011)	<i>Halophila ovalis</i> ; <i>Cymodocea rotundata</i> ; <i>Halodule uninervis</i> ; <i>Halophila spinulosa</i> ; <i>Syringodium isoetifolium</i> ; <i>Zostera muelleri</i> .	2004, 2007	2004, 2007	Queensland.	200 km ²	Quickbird satellite.	2.4 m	"Several thousand photos", seagrass presence/absence.	Time-series.

Reference	Target species	Year of capture of remote sensing data	Year of capture of ground survey data	Location	Mapping extent (area or coastal length)	Remote sensing data source (s)	GSD specified	Ground truth sampling / attribute	Single or time-series
Hamylton et al. (2012).	<i>Thalassodendron ciliatum</i> ; <i>Thalassia hemprichii</i> ; <i>Halodule</i> sp.; <i>Halophila ovalis</i> .	Not specified.	2009	Indian Ocean.	226 km ²	Quickbird satellite.	2.4 m	278 video and 209 photograph points.	Single estimate.
Lyons et al. (2012).	Seagrass, species not specified.	1972–2010.	n/a	Queensland.	400 km ²	Landsat (TM) satellite.	30 m	Photo interpretation, no ground validation.	Time-series.
Nobi and Thangaradjou (2012).	Seagrass, species not specified.	2000; 2007/8.	2010	Indian Ocean.	Not specified.	IRS ID and IRS P6 LISS III satellites.	23.5 m	10 points per 6 islands.	Single estimate.
Pu et al. (2012).	<i>Syringodium filiforme</i> ; <i>Thalassia testudinum</i> ; <i>Halodule wrightii</i> .	2009	2009	Florida.	105 km ²	Landsat-5 and Earth Observation 1 (ALI+Hyperion) satellites.	30 m	57 transects, seagrass cover.	Single estimate.
Borfecchia et al. (2013b).	<i>Posidonia oceanica</i> .	2011	2011	Italy.	Not specified.	Daedalus airborne sensor.	2.5 m	Not specified.	Single.
O'Neill and Costa (2013).	<i>Zostera marina</i> .	2008	2008, 2010	Canada (Pacific).	1.78 km ²	AISA hyperspectral aircraft sensor and IKONOS satellite.	2m and 4m	507 points, seagrass cover.	Single estimate.
Paulose et al. (2013).	Not specified.	Not specified.	Not specified	Indian Ocean.	8,249 km ²	IRS P6 LISS III and IV satellite, and historical maps.	Not specified.	Not specified.	Time-series.
Torres-Pulliza et al. (2013).	Seagrass, species not specified.	1999-2003.	2008	Coral Triangle.	170x185 km	Landsat satellite.	Not specified.	356 stations characterised, seagrass cover.	Single estimate.
Ball et al. (2014).	<i>Zostera nigricaulis</i> ; <i>Zostera muelleri</i> ; <i>Halophila australis</i> ; <i>Amphibolis Antarctica</i> .	1939-2011.	2008-2011	Victoria, Australia.	500 ha	Various aerial photography - unsupervised classification.	0.3 m	Underwater video, seagrass density by species.	Time-series.
Cho et al. (2014).	Seagrass, species not specified.	2013	2013	Florida.	Not specified.	Hyperspectral Imager, International Space Station; Aerial photography reference.	Not specified.	Six stations, samples not specified.	Single estimate.
Hogrefe et al. (2014).	<i>Zostera marina</i> .	2002-2009.	2007-2012	Alaska.	Coastline 1200 km.	Landsat 5 and 7 Thematic Mapper (TM) satellite.	30 m	680-point ground inspection, systematic design, % seagrass cover.	Single estimate.

Reference	Target species	Year of capture of remote sensing data	Year of capture of ground survey data	Location	Mapping extent (area or coastal length)	Remote sensing data source (s)	GSD specified	Ground truth sampling / attribute	Single or time-series
Pu et al. (2014).	<i>Syringodium filiforme</i> ; <i>Thalassia testudinum</i> ; <i>Halodule wrightii</i> .	2003, 2005	2005	Florida.	104 km ²	Landsat 5 satellite.	30 m	14 transects. Seagrass cover.	Time-series.
Reshitnyk et al. (2014)	<i>Zostera marina</i> .	2010	2012	Canada (Pacific).	0.18 km ²	Worldview 2 satellite, underwater acoustic.	2 m	Video transect, habitat substrate checks, seagrass presence/absence.	Single estimate.
Roelfsema et al. (2014).	<i>Cymodocea serrulata</i> ; <i>Halophila spinulosa</i> ; <i>Halophila ovalis</i> ; <i>Halodule uninervis</i> ; <i>Syringodium isoetifolium</i> ; <i>Zostera muelleri</i> .	2004-2013	2004-2013	Queensland.	142 km ²	Worldview 2, IKONOS, Quickbird 2 satellite.	Not specified	Photo transect, seagrass cover, biomass.	Single compiled estimate.
Vandermeulen (2014).	<i>Zostera marina</i> .	2008-2009	2008-2009	New Brunswick.	Not specified.	Acoustic.	Not specified	Towed video, seagrass cover.	Single estimate.
Blakey et al. (2015).	<i>Thalassia testudinum</i> .	2007-2011	2007-2011	Florida.	Not specified.	Landsat 5 Thematic Mapper satellite.	Not specified	4-8 samples each for 30 stations, % seagrass cover.	Time-series.
Hossain et al. (2015b).	<i>Thalassia hemprichii</i> ; <i>Halophila minor</i> ; <i>Halophila ovalis</i> ; <i>Cymodocea rotundata</i> ; and <i>Halodule pinifolia</i> .	1982-2013	2013-2014	Malaysia.	Coastline 12 km.	Landsat 5, 7, 8 satellite.	30 m	178-point ground inspection points; presence/absence by seagrass species.	Single estimate.
Saunders et al. (2015).	<i>Halodule uninervis</i> ; <i>Thalassia hemprichii</i> .	2011	2011-2012	Queensland.	Not specified.	Unspecified satellite image, historical maps.	Not specified	Photo transect, seagrass cover, biomass.	Time-series.
Sawayama et al. (2015).	Seagrass, species not specified.	2012	2011	Indonesia.	Not specified.	Worldview 2.	2 m	4781 points from towed underwater video.	Single estimate.
Valle et al. (2015).	<i>Zostera noltii</i> .	2012	2012	Spain.	10.27 km ²	Compact Airborne Spectrographic Imager.	2 m	114 field stations, seagrass cover.	Single estimate.
Baumstark et al. (2016).	Seagrass, species not specified.	Not specified	Not specified	Florida.	Not specified.	Worldview2 satellite.	2 m	Underwater photography, samples not specified, % seagrass cover.	Single.
Hachani et al. (2016).	<i>Posidonia oceanica</i> .	2009	2011	Tunisia.	158 ha	SPOT 5 satellite.	2.5 m	186 spot checks, seagrass presence/absence.	Single estimate.

Reference	Target species	Year of capture of remote sensing data	Year of capture of ground survey data	Location	Mapping extent (area or coastal length)	Remote sensing data source (s)	GSD specified	Ground truth sampling / attribute	Single or time-series
Amran (2017).	<i>Enhalus acoroides</i> ; <i>Cymodocea rotundata</i> ; <i>Cymodocea serrulata</i> ; <i>Halodule pinifolia</i> ; <i>Halodule uninervis</i> ; <i>Halophila ovalis</i> ; <i>Syringodium isoetifolium</i> ; <i>Thalassia hempricii</i> .	Not specified.	Not specified.	Indonesia.	Not specified.	Google Earth imagery	Not specified	Sampling not specified; presence/absence by seagrass species	Single
Asner et al. (2017).	Seagrass, species not specified.	Not specified.	Not specified.	South China Sea.	Not specified.	Planet Dove satellite	4.7 m	Underwater photographic surveys; sampling not specified; seagrass presence/absence	Time-series
Calleja et al. (2017).	<i>Zostera noltei</i> ; <i>Zostera marina</i>	1984-2015.	2001-2015.	Spain.	22.7 km ²	Landsat4-8 satellites	30 m	Not specified	Time-series
Fauzan et al. (2017).	<i>Enhalus acoroides</i> ; <i>Thalassia hemprichii</i> ; <i>Cymodocea rotundata</i> ; <i>Halophila ovalis</i> ; <i>Halodule universis</i> .	2016	2016	Indonesia.	Not specified.	Sentinel-2A satellite	10 m	80 reference points, % seagrass cover	Single estimate
Bajjouk et al. (2018).	Seagrass, species not specified.	2009, 2015.	2011, 2015.	Indian Ocean.	4.5 km ²	Hypex VNIR-1600 sensor; AISA Eagle 1 k system; Lidar	0.4 m	37 stations, seagrass cover rates	Time-series
Chayhard et al. (2018a).	<i>Enhalus accroides</i> ; <i>Halodule pinifolia</i> ; <i>Halodule uninervis</i> .	2011, 2016-2017.	Not specified.	Thailand.	5.59 km ²	WorldView 2, GeoEye 1 satellite; RPA aerial photography	Not specified	Samples not specified, species presence/absence	Single estimate
Duffy et al. (2018).	<i>Zostera noltii</i> .	2016	Not specified.	United Kingdom.	2 km ²	Ricoh GR II compact digital camera or AgroCam RGB sensor on RPA	4 mm and 14 mm	27 quadrats, % seagrass cover	Single estimate
Hamylton et al. (2018).	<i>Thalassodendron ciliatum</i> ; <i>Thalassia hemprichii</i> ; <i>Halodule</i> sp.; <i>Halophila ovalis</i> .	2004-2006.	2009	Indian Ocean.	203 km ²	Quickbird satellite	not specified	486 stations for underwater video sampling, % class coverage	Single estimate
Marcello et al. (2018).	<i>Cymodocea nodosa</i> .	2017	2017, 2015.	Spain.	4 km ²	Airborne Hyperspectral Scanner; Worldview 2 satellite	2.5 m ; 1.8 m	6 underwater video transects, presence/absence	Single estimate

Reference	Target species	Year of capture of remote sensing data	Year of capture of ground survey data	Location	Mapping extent (area or coastal length)	Remote sensing data source (s)	GSD specified	Ground truth sampling / attribute	Single or time-series
Topouzelis et al. (2018).	<i>Posidonia oceanica</i> ; <i>Cymodocea nodosa</i> ; <i>Zostera noltii</i> ; <i>Zostera marina</i> .	2013-2015.	Not specified.	Greece.	13,676 km	Landsat 8 satellite.	30 m	Historical field data.	Single estimate.
Traganos and Reinartz (2018b).	<i>Posidonia oceanica</i> ; <i>Cymodocea nodosa</i> .	2017	n/a	Greece.	12657 ha	Sentinel-2A satellite.	10 m	No seagrass ground measurements.	Single estimate.
Ventura et al. (2018).	<i>Posidonia oceanica</i> .	Not specified.	n/a	Italy.	Not specified.	Gopro Hero4 on RPA.	3 cm	No seagrass ground measurements.	Single estimate.
Innangi et al. (2019).	Seagrass, species not specified.	2015-2016.	2015-2016.	Sicily.	Coastline > 35 km.	Marine acoustic derived raster.	2.5 m	Spot checks, underwater video and hand grab.	Single estimate.
Lidz and Zawada (2013).	<i>Thalassia testudinum</i> ; <i>Syringodium filiforme</i> .	2009	2009	Florida.	14 km ²	Quickbird satellite + continuous underwater imagery.	2.4 m	195000 automatic underwater photo-points, seagrass presence/absence.	Single estimate.
Ratheesh et al. (2019).	<i>Cystoseira indica</i> ; <i>Halophila ovalis</i> ; <i>Halodule unine</i> ; <i>Sargassum tenerrimum</i> ; <i>Sargassum prismaticum</i> .	2016	2015	India.	Not specified.	Airborne AVIRIS hyperspectral.	4-8m	39 points on 13 transects; seagrass presence/absence.	Single estimate.
Sousa et al. (2019).	<i>Zostera noltei</i> .	2003-2005, 2013-2014.	2012-2013.	Portugal.	Not specified.	Aerial photography; Sony NEX-5N camera on RPA.	4 cm	Biomass.	Time-series.
Wilson et al. (2019).	<i>Zostera marina</i> .	2015	2015	Canada (Atlantic).	Not specified.	SPOT 6/7 satellite.	6 m	214 stations, seagrass presence/absence.	Single estimate.
Xu et al. (2019).	<i>Zostera marina</i> .	2017-2018.	2017-2018.	China.	Not specified.	Acoustic.	Not specified	Underwater camera during acoustic capture.	Single estimate.
Nahirnick et al. (2019a).	<i>Zostera marina</i> .	2016	2016	Canada (Pacific).	Not specified.	Gopro Hero3 camera on RPA.	2 cm	792 points from underwater video, seagrass cover.	Single estimate.
Nahirnick et al. (2019b).	<i>Zostera marina</i> .	2017	2017	Canada (Pacific).	Not specified.	DJI Phantom 3 Pro camera.	not specified	Towed video, 2-6 transects per site.	Single estimate.

* Literature query was based on the Scopus database search string: (TITLE-ABS-KEY (seagrass*) OR TITLE-ABS-KEY (eelgrass*)) AND (TITLE-ABS-KEY (survey*) OR TITLE-ABS-KEY (mapping) OR TITLE-ABS-KEY (mapped)) AND (TITLE-ABS-KEY ("remote sensing") OR TITLE-ABS-KEY ("remotely sensed")) AND (LIMIT-TO (PUBYEAR , 2019) OR LIMIT-TO (PUBYEAR , 2018) OR LIMIT-TO (PUBYEAR , 2017) OR LIMIT-TO (PUBYEAR , 2016) OR LIMIT-TO (PUBYEAR , 2015) OR LIMIT-TO (PUBYEAR , 2014) OR LIMIT-TO (PUBYEAR , 2013) OR LIMIT-TO (PUBYEAR , 2012) OR LIMIT-TO (PUBYEAR , 2011) OR LIMIT-TO (PUBYEAR , 2010)) AND (LIMIT-TO (DOCTYPE , "ar")). The resulting reported items were eliminated from the list based on exclusion criteria: If there was mapping purpose; no clear target species; not at least partly aiming to achieve a seagrass map; lab based; algorithm focus; model only; ground only; water quality only; performance/accuracy testing only; not related to seagrass extent, presence, extent or distribution; spectral character only; hardware testing only; literature review; geomorphology only; duplicated from same study published elsewhere. The resulting inclusion items are listed above.

2.8.2 Appendix 2.8.2. Sources of imaging error and approach taken to mitigate problems.

Source of error	Description
Lens vignetting.	The camera has a narrow field of view and quality lens-vignetting is barely detectable within the saved imagery. Flightpath is set such that there is >75% overlap in imagery in the forward and lateral direction, resulting in only small central parts of each image included in the final orthorectified mosaic.
Lens distortion.	Agisoft Photoscan “lens” module computes an accurate parameterised lens model allowing image distortion correction. Lens model is automatically calculated and refined by the software during the camera alignment and optimisation workflows.
Sun angle.	Field work timing was set to achieve aerial survey between 28-35-degree sun angle from horizon, chosen after initial field pilot-testing with the goal of minimising sun glint off residual water surface and minimising shadow cast from relief and small objects on the estuary.
Photo georeferencing and alignment.	The imagery was geotagged with GPS coordinates from the onboard camera GPS module. These GPS coordinates improve initial photogrammetric processing. Final georeferencing was achieved using photogrammetric reference markers placed within the scene, with locations surveyed using precision GNSS survey equipment, and with locations/coordinates linked across all input photogrammetry images to optimise the lens model and photo orientation calculations.
Motion blur.	Flight speed was set to minimise motion blur to below 1-pixel blur-length.

(Appendix 2.8.2 ctd.)

Source of error	Description
Radiometric control.	The radiometric reference panel included within the Sequoia camera was imaged at the start of each survey-sortie to capture the mean image value relative to it's known reflectance value. Agisoft Photoscan software includes functionality to automatically apply a coarse radiometric response correction based on this panel reference.
Sun glint.	Flight times were set to minimise potential for sun glint from water pooling (see 'Sun angle' above). It was not possible to eliminate small-scale sun glint completely from wet seagrass and other wet objects on the estuary, although glint was nearly in-detectable from imagery taken with overcast cloud cover conditions.
Image normalisation.	Agisoft Photoscan Pro v1.4 software applies a proprietary image normalisation correction with good colour equalisation result. Specific algorithm detail not available.

2.8.3 Appendix 2.8.3. Hardware and software configuration for the remotely piloted aircraft setup used for this study.

Component	Configuration
Airframe.	<p>Sky-hero Spyder 600 mm quadcopter frame with 2815 470KV motors.</p> <p>6s 40A power system, 6S 6000 mAh lithium polymer battery 25C rating.</p> <p>13x55 propellers (small for this motor-size, for flight stability).</p> <p>Taranis X9D radio transmitter with X8R receiver.</p> <p>Pixhawk flight controller with M8N multi-constellation GPS receiver.</p> <p>Sik radio telemetry link on 433 MHz.</p>
Ground control station.	<p>Arducopter Mission planner flight control software.</p> <p>Dell ATG 6420 ruggedised laptop.</p> <p>Half-wavelength high gain antenna for radio link (ground end).</p>
Camera.	<p>Micasense Sequoia multispectral camera (green, red, red-edge and NIR) with downwelling light sensor and radiometric reference.</p> <p>Independent power supply for camera 5V 1S 5,000 mAh.</p>
Georeferencing.	<p>White 1 m reference pipes, centre marked, or white 100 mm x 30 mm plastic markers.</p> <p>Trimble R8 receiver with TSC3 controller, under VRS correction service and link to local geodetic reference mark.</p>
Photogrammetry processing.	<p>Agisoft Photoscan v1.4 then 1.5.</p> <p>Lens model calibration using Agisoft Lens within the Photoscan package.</p>

CHAPTER 3

Chapter 3. Study Area - Wharekawa Harbour status and trend

3.1 Introduction

The application of remote sensing to the task of seagrass survey may depend on the nature and rate of change in seagrass. Change that is relevant to seagrass condition monitoring includes patch extent, density change, seagrass plant health/vigor. The significance of change may be timescale-dependant at locations with high colonisation/recolonization rates. The thesis objectives require a site with a wide range of seagrass density and substrate types, and a site likely to change at different scales across the timeframe of the year of study, including parts that remain unchanged.

Wharekawa is an important estuary in the east coast of the North Island of NZ. It provides a range of significant natural values, and provides habitat, stabilisation and food resources above- and below-ground. These attributes support the provisioning of ecosystem services and estuarine resilience (Chapter 2). Wharekawa Harbour has similar composition and pressures as many other estuaries in the region, and hence is a good case subject. In recent years there has been detectable loss of seagrass extent (e.g., as can be observed in the Google Earth imagery time-series). As yet, the nature, rate and significance of change in Wharekawa seagrass has not been quantified against a long-term baseline. Therefore, in response to this uncertainty, the final part of this chapter examines long term change in seagrass, including the change across one 12-month period measured by precision GPS survey conducted alongside of the primary field work that is examined in Chapters 4 to 6.

3.1.1 Chapter objectives

This chapter aims to gain an understanding of the key characteristics of Wharekawa Harbour, and to understand the current and previous long- and short- term trend in seagrass extent on the estuary within the limits of available historical data and the current fieldwork resource. The aim is also to implement seagrass mapping on Wharekawa Harbour using manual photo interpretation to observe types of visual ambiguity in the images, sources of spatial error and to consider detection limits of the different methods. This provides a contrast to the low altitude high resolution method developed in later chapters. The specific objectives are:

1. Determine the characteristics of Wharekawa Harbour in terms of its ecosystem and catchment environment;

2. Determine the current seagrass population of the estuary and short term (one year) stability of seagrass distribution in response to a significant rain and sedimentation event; and
3. Measure the long-term pattern of change in seagrass extent and estimate future trend.

3.1.2 Study site selection

Wharekawa Harbour was selected as study area for thesis research because the estuary provides a range of vegetation and substrate conditions within a relatively small and accessible area, has large persistent meadows of seagrass with a range of density and morphology, and is of a similar geomorphic type to other estuaries in the Coromandel Peninsula and Waikato Region (Hume et al., 2016; Table 3.1, Figure 3.1). At the time of this research, Wharekawa Harbour was also under pressure from sediment derived from forestry clear-felling in the hills immediately adjacent to the estuary margins, and consequently was subject to pulses of sediment accretion and debris deposition during high rainfall events, including damming and subsequent flash-flood release.

Wharekawa Harbour was also selected because i) the airspace over the coastal marine area is amenable to a drone survey without airspace restrictions; ii) operations could be conducted within the standard RPA rule set (Civil Aviation Authority 2018); iii) RPA operations in aviation airspace are safer due to good visibility across and outward from the estuary for observing approaching piloted aircraft; and iv) there are few RPA flight hazards (tall trees are located well away from likely flight paths) and low public presence during weekday working hours.

3.2 Geology, landform, soil and land use

Wharekawa Harbour is classified under the geomorphic ontology of Hume et al. (2016) as class 7A (“permanently open, enclosed with barrier beach/spit”). The surface area of the estuary at spring tide is 1.9 km² and ~86% of the estuary is intertidal. The Wharekawa Harbour tide cycle is asymmetric, with longer drainage time than fill-time (Needham et al., 2013). The hydrological catchment land-area was reported as 83 km² by Hume et al. (2016), 102 km² by O'Donnell (2009), but was calculated as 91 km² using a catchment trace from mean high water spring to hilltop limit using the NIWA river environment classification v2 (REC2) GIS layer in the current study (Figure 3.2).

Table 3.1. Major estuarine systems of Waikato Region. Estuaries are organised by major coastal area as per the Waikato Regional Coastal Plan (Waikato Regional Council 2011), with attributes presented after the national inventory by Hume et al. (2016). Geomorphic class codes: 6B tidal river mouth, spit enclosed (sand/mud); 7A tidal lagoon, permanently open; 8 shallow drowned valleys; 9 deep drowned valleys.

Major zones	Estuary	Geomorphic class	Surface area, spring high tide (km ²)	Intertidal area (% of high tide area)	Mean depth at spring high tide (m)	Spring tidal prism (million m ³)	Uphill catchment area (km ²)	Tidal river inflow 12.4hr (million m ³)
East coast estuaries.	Whangamata.	7A	4.4	78	1	4.6	50	0.2
	Wharekawa.	7A	1.9	86	1	1.9	83	0.3
	Tairua.	7A	6	51	1	7.7	282	1
	Whitianga.	7A	15.5	72	1	17.1	450	1.4
	Whangapoua.	7A	13	80	1	14.9	107	0.3
	Kennedy Bay.	7A	0.5	91	1	0.5	51	0.1
	Colville.	8	4.6	5	3	11.7	43	0.1
	Coromandel.	8	25.4	21	5	62.8	60	0.2
	Manaia.	8	6.3	76	3	11.1	59	0.2
Hauraki Gulf / Firth of								
Thames.	Firth of Thames.	9	717	15	3	1890	544	1.1
West coast estuaries.	Raglan.	8	31.9	69	1	60.9	523	1.2
	Aotea.	8	31.9	74	3	59.2	185	0.4
	Kawhia.	8	67.6	74	2	126	499	1.4
	Marakopa.	6B	0.7	14	5	1.8	367	1.1
	Awakino.	6B	0.3	0	5	1	382	1.3
	Mokau.	6B	1.1	0	5	3.3	1452	3.9

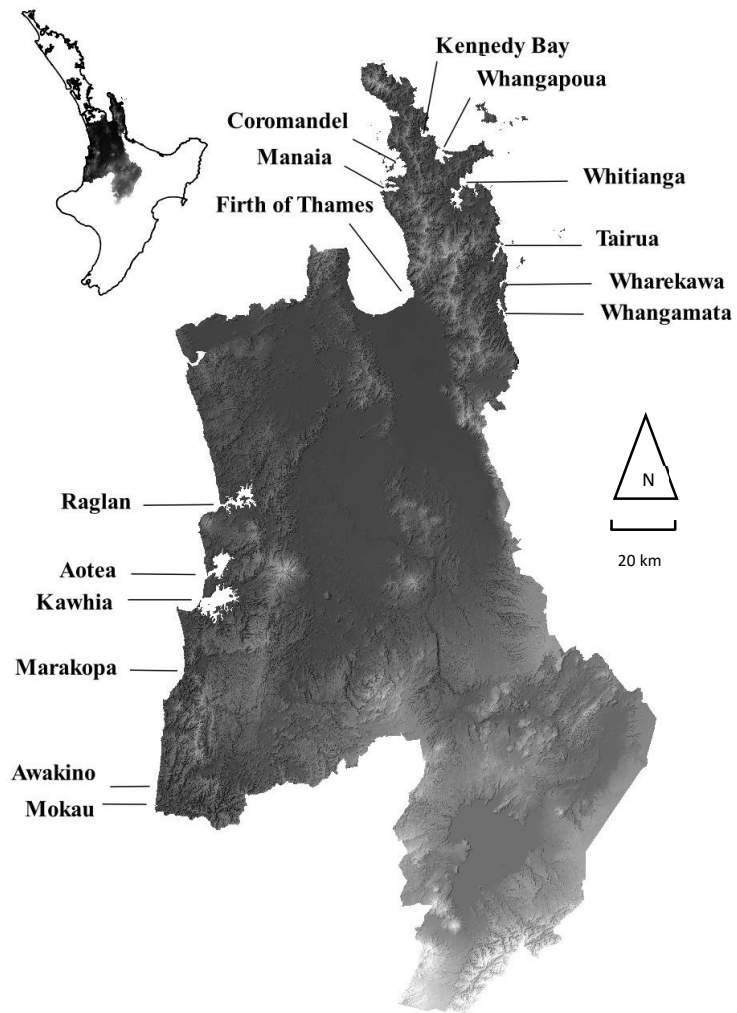


Figure 3.1. Wharekawa Harbour position with respect to major estuaries (as presented in Table 3.1) and terrain of Waikato Region (greyscale altitude, black to white as low to high altitude).

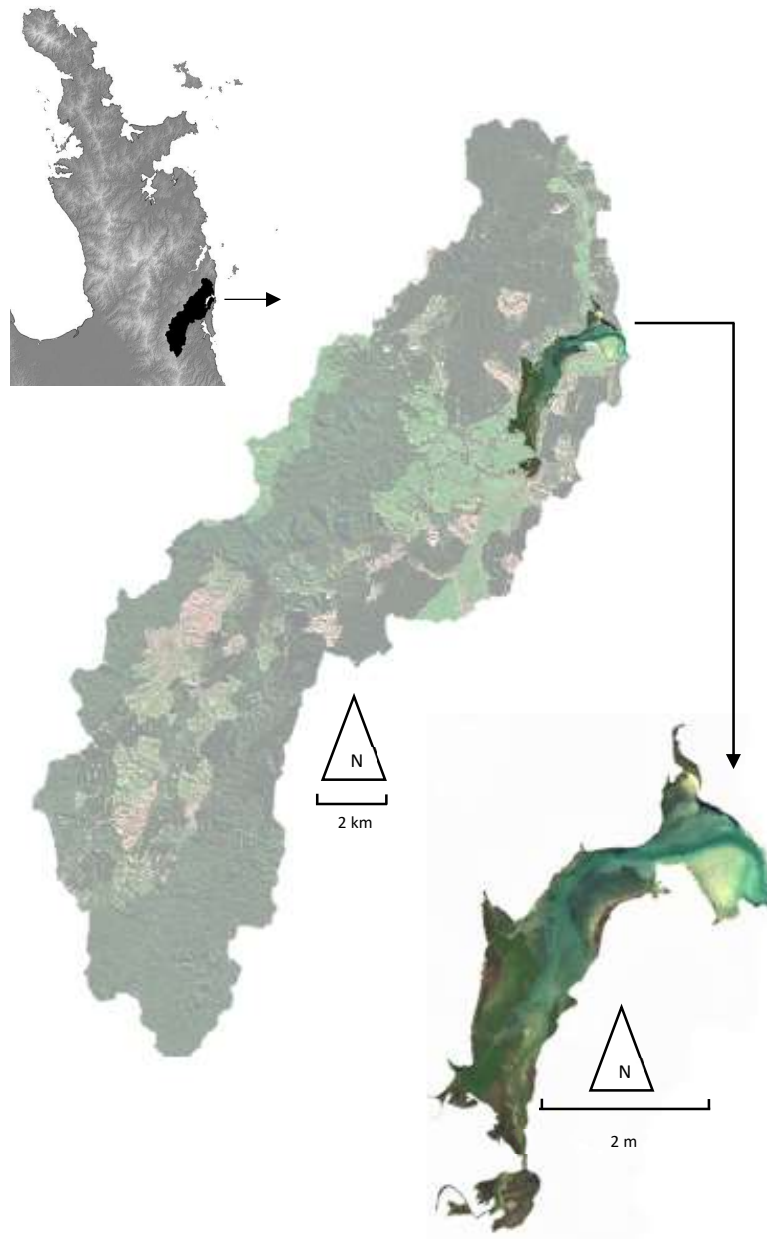


Figure 3.2. Wharekawa Harbour and surrounding drainage catchment (background – copyright Bing Maps).

The geology and landforms of the topographic surrounds to Wharekawa Harbour are strongly influenced by historical fault activity and volcanic land formation, in particular a system of volcanic domes and caldera-collapse features, as well as minor basaltic flow structures (Aldrich 1995; Malengreau et al., 2000). Current day soils making up the terrain of the catchment are predominated by brown, allophanic and pumice soils (Landcare Research 2010; Figure 3.3) on moderate or steep slopes of poor water retention and/or prone to sheet and/or slip erosion (O'Donnell 2009).

Intensive land use in the catchment largely comprises farming and plantation forestry (Graeme 2008; and Figure 3.3). The catchment comprises land-use of forestry (50%), farming (12%), negligible horticulture (0.3%), with much of the remainder land area being indigenous vegetation (38%). This is based on the calculated catchment area of 91 ha and using the New Zealand Landcover Database v4 (LCDB4) as a year 2012 snapshot. Equivalent statistics presented by O'Donnell et al. (2009) were forestry (52%), farming (12%), and horticulture (0.13%) based on the 2002 snapshot indicating negligible coarse land use change over a decade.

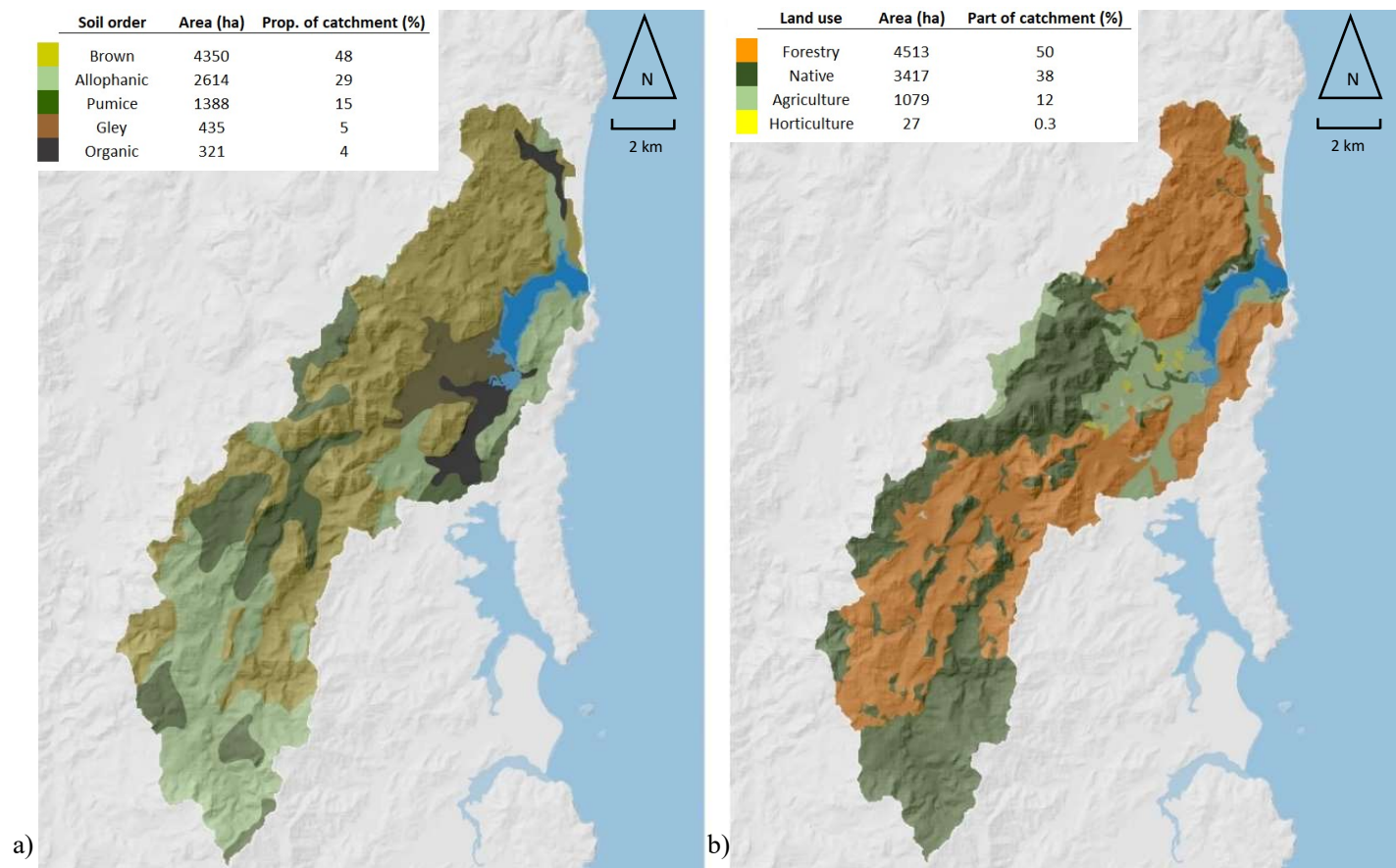


Figure 3.3. a) Soil composition and b) land use, within the Wharekawa Harbour catchment. Statistics are based on area and proportion within the catchment boundary and to the high tide line.

3.3 Estuary values

Wharekawa Harbour has high recreational value, aesthetic and cultural value to its community and visitors. The estuary provides food resources and generally good water quality (O'Donnell 2009). Within and surrounding the estuary are historical and archaeological sites relating to early Maori colonisation, and later European and Maori land-conversion from native ground cover to agriculture and plantation forestry. There remains in several parts of the estuary catchment an intact sequence of vegetation linking marine and terrestrial communities via saltmarsh, coastal wetland and coastal forest intermediate communities. Enhancement of this linkage is recognised as an area for improvement under catchment management (Graeme 1997; O'Donnell 2009). Relatively low intensity of human development compared to other estuaries raises the profile of the Wharekawa Harbour as a conservation area under natural heritage and species protection mandate and warranting the highest level of protection possible under the relevant statutory framework (Dowding 2012).

The estuary is situated within the coastal marine area as defined by s 2 of the Resource Management Act 1991 and is subject to statutory protection by regional government under the Act and is regulated by the Regional Coastal Plan (Resource Management Act 1991, Waikato Regional Council 2011). The estuary and surrounds are designated as an area of significant conservation value (Lundquist et al., 2004; Waikato Regional Council 2011) on the basis of: i) importance to local Maori; ii) high wildlife habitat value; iii) significant population of dotterel; iv) high abundance of threatened waders and other notable bird species; v) significant areas of salt marsh, seagrass and mangrove; vi) abundant shellfish; and vii) areas protected by a wildlife refuge and surrounding significant natural area parcels.

The coastal margin adjoining the estuary has ecologically intact estuarine vegetation communities which include salt-marsh (including rush/sedge, manuka/ribbonwood and sea-meadow sub-types), mangrove and seagrass community types, using the class system of Graeme (2008). Community types can be found in spatially distinct patches or in blended extents (Graeme 2008). Large growth of intertidal mangrove forest has been present on the estuary since early survey work on the estuary (Graeme 1997) and can be seen in early aerial photography (see section 3.5).

Wharekawa Harbour is a site of high importance for many estuarine birds (Dowding 2012, Dowding 2013). In particular, observations have been made on Wharekawa Harbour of species designated under the New Zealand Threat Classification system (Townsend et al., 2008), as per the following, and based on lists by Dowding (2013):

Threatened and nationally critical: - black stilt *Himantopus novaehollandiae*;
Nationally endangered: - Australasian bittern *Botaurus poiciloptilus*; Nationally
vulnerable: - Pied shag *Phalacrocorax venus*; reef heron *Egretta sacra*; New Zealand
dotterel *Charadrius obscurus aquilonius*; banded dotterel *Charadrius bicinctus*; wrybill
Anarhynchus frontalis, red-billed gull *Larus novaehollandiae*; Caspian tern *Hydroprogne
caspia*; North Island kaka *Nestor meridionalis septentrionalis*; or

At risk: - North Island fernbird *Bowdleria punctata vealeae*; little penguin
Eudyptula minor; little shag *Phalacrocorax melanoleucos*; black shag *Phalacrocorax
carbo*; South Island pied oystercatcher *Haematopus finschi*; banded rail *Gallirallus
philippensis*; variable oystercatcher *Haematopus unicolor*; pied stilt *Himantopus
himantopus*; white-fronted tern *Sterna striata* (refer to Dowding 2013 for source).

Within this inventory, dotterels, godwits, herons, variable oystercatchers and black-
backed and red-billed gulls are frequent users of the major seagrass meadows on the
estuary when the tide is out (Graeme 1997; Graeme 2008, and Figure 3.4).

Mangroves may provide habitat for banded rail (Bell and Blayney 2017). At least
one bittern is still present within the saltmarsh and mangroves of the upper reaches of the
Wharekawa River in-flow (personal observation 5 May 2017). Godwits have been
reported in flocks as large as 200 in number (Graeme 1997). Wharekawa Harbour is
designated a priority 1 site of importance to estuarine birds (Dowding 2013). The main
feeding area is the lower estuary which also coincides with several large long-term
seagrass meadows, and numerous birds spanning multiple species can be seen feeding
together (Figure 3.4).

Estuarine intertidal substrate can be rich with shellfish, predominantly featuring the
bivalve cockle (*Austrovenus stutchburyi*), pipi (*Paphies australis*), and wedge shell
(*Macomona liliana*), and gastropods (*Cominella sp.*, *Zeacumantus sp.* and *Diloma sp.*)
(Graeme and Giles 2013).



Figure 3.4. Wharekawa Harbour at low tide, with herons, oystercatchers, godwits, seagulls and dotterels feeding together on the same meadow. Canadian goose and swans can be seen in the background.

3.4 Pressures

Graeme (2008) identified four key threats to Wharekawa estuarine vegetation: stock damage, sediment accretion, illegal mangrove removal and expansion of saltwater paspalum.

3.4.1 Stock damage

Stock damage has been addressed in part under actions of the operational Wharekawa Harbour Catchment and Management Plan (O'Donnell 2009) by way of fencing and maintenance of riparian vegetation margins alongside the tributary streams that run past farmlands into the estuary.

3.4.2 Mangroves

Mangroves have been widespread in the estuary for several decades but were rare in 1945 and possibly up to the 1970's. A long-term sequence of historical aerial imagery provides an indication that the large mangrove forests of the mid-inner estuary are relatively recent formations. The first major stand of mangroves appeared behind the Opoutere Road causeway in a 1971 image. In 1945-dated imagery, the intertidal area behind the causeway appeared to be dominated by sediment with no mangrove-like clusters visible. By time of the 1983 image, the mangroves had thickened to a young forest, and at high density by the time of the 2017 field work under the current study.

Other areas of current-day mangrove forest distribution on the estuary coincide coarsely with apparent stream sediment deposition points that are visible in the 1945 and 1971 imagery. The original stream channel and flood-spill directions are not evident in recent imagery (e.g., looking backward to 2001 which is the earliest imagery in the Google Earth time-series). This is due to the recent channelization and stream redirection that came about after the mangrove forests established and the weed-grass saltwater paspalum (*Paspalum vaginatum*) infested and hardened many channel margins. Many of the new mangrove seedling patches likewise appear to be positioned on or near to likely deposition points for sediment from tributary stream water flow, observations in the current day support a hypothesis of earlier stream sediment influencing current day mangrove distribution.

Mangrove removal has been attempted in places on the estuary (Graeme 1997; Bouma et al., 2016). The most significant removal visible in the Google Earth image time-series imagery took place between 2004-2007, amounting to three areas of size ~0.5, 1.5 and 3.9 Ha of mangrove. Two of these areas, which are distant from other tracts of

mangrove forest, remain largely mangrove-free in the current day. However, one area (0.5 Ha), positioned in a gap between large tracts of high canopy dense mangrove forest, has significant mangrove regrowth, with dense mid-height mangrove saplings visible during a May 2017 field inspection. This patch will likely revert to dense canopy mangrove forest in coming years. Overall there was a reduction in Mangrove extent from 49 to 43 ha from 1997 to 2012 respectively, and this reduction can largely be attributed to the earlier mangrove clearance (WRC 2014 dataset to WRC 2012 dataset spatial difference).

There is ongoing debate in the science community concerning whether the mangrove expansion is an acceptable natural process, or a human induced environmental impact requiring intervention (Morrisey et al., 2007; Lundquist et al., 2014; Dencer-Brown et al., 2018; Pham et al., 2019). In New Zealand mangroves are a recognised valuable species that is important to coastal ecology (Dencer-Brown et al., 2018), but there are some locations where stakeholders regard mangroves as a pest species for which removal is justified (e.g., Dencer-Brown et al., 2018; Alfaro 2010). Yet mangrove removal also poses a risk of ecological damage to the estuary (Stokes 2010). For Wharekawa Harbour there are elements of a case visible in historical imagery suggesting that expansive dense mangrove forests are a recent phenomenon for Wharekawa Harbour and that current day mangrove distribution is associated with the location of historical sediment deposition. This also acknowledges the limitations of early black-and-white aerial photo interpretation, and lack of accessible imagery captured prior to 1945, at the time of writing.

3.4.3 Sediment

Sedimentation is a common pressure upon estuaries in New Zealand (Ministry for the Environment 2016). Sedimentation arises from slope soil failure (either gradually or from land slip), slope erosion or stream bank erosion, flocculation (aggregation and binding of particles within waterbody transport), or from forestry soil manipulation, scraping and other transport during harvest (Mead and Moores 2005; Jones 2008). Soil is transported into streams by gravity, wind, surface water flow, and during harvest and following timber mobilisation down a topography (Phillips et al., 2007; Jones 2008).

The impact of sedimentation depends on the rate of inflowing sediment and suspended particles compared to outflow. Impacts of sediment and particulate suspension can be considered in terms of chronic (due to continuous delivery of sediment to the estuary) and catastrophic disturbance effects (rapid delivery during rainfall events) (Thrush et al., 2004). Impacts relate to burial depth, timeframe until exposure and

sediment size. For example, research by Benham et al. (2019) demonstrates in a microcosm experiment that *Zostera muelleri* can tolerate burial to 5 mm depth for 28 days, with substantial reduction in rhizome growth and shoot density at 10 mm depth, and with impacts increasing with reducing grain size. The source and type of impact from sedimentation can vary from estuary to estuary depending on surrounding geology, coastal morphology, land use, and the number, size and catchment of streams entering the estuary.

Wharekawa Harbour has relatively high vulnerability for sediment infilling as a consequence of a relatively small tidal prism to estuary area ratio (Jones 2008). This ratio provides a simple indicator of the ability of an estuary to transport inflowing sediment out of the estuary, where a low ratio indicates poor flushing potential. Sedimentation threat to Wharekawa Harbour has been noted by Graeme (1997, 2008) and O'Donnell (2009). Sedimentation in the Northern arms of the estuary was also noted by Needham et al. (2013). There is also indication of sedimentation impact as early as 1945 as can be seen in 1945 historical aerial photography. Possibly the most significant sediment event for Wharekawa Harbour was the initial clearance-logging of mature native forest that mostly took place between the late 1890s and the 1920's (O'Donnell 2009; Barton 2017).

Native timber logging in the catchment included transport of logs downstream to the estuary by way of stream flood-inundation after release of large constructed stream dams. O'Donnell (2009) records that up to 35 dams may have been present on tributaries of the estuary. Logs were transported across the estuary in large tied rafts, on route to Auckland for timber processing. Transport of logs down the catchment to the estuary likely exacerbated sediment transport downstream. In some regions of the Coromandel Peninsula, clear-felling of native forestry was followed by repeated scrub vegetation burn-off relating to gold mining and extraction activities (King 1993; Figure 3.5). Plantation forestry had begun by the late 1940s (Barton 2017) and has continued throughout the catchment to the present day.



Figure 3.5. Early (1889) photography of the ‘Lucky at Last’ Whangamata Gold Corporation stamper battery, illustrating the denuded landscape within the Wharekawa Catchment following native forest clearance. Reproduced with permission acknowledging Sir George Grey Special Collections, Auckland Libraries, AWNS-18990630-5-2.

The change in rate of sediment accretion onto the estuary, from prehistoric times to the current day, has been estimated as 0.09–0.12 mm/year prior to Polynesian settlement, 3.6-7.2 mm/year during catchment deforestation of native forest (1880-1945), and 5.0-8.0 mm/year during the recent decades of plantation forestry in the catchment (Swales and Hume, 1995 as cited by Mead and Moores, 2005). Sediment core measurements indicate sediment deposition in the range 183-252 tonnes per km² per year (O'Donnell 2009). Sediment of the estuary is dominated by sand of varying density (Graeme and Giles 2010).

The origin of current-day sediment deposition into Wharekawa Harbour was examined by Gibbs and Bremner (2008). These authors determined that sediment originated from pine forestry (1-23%), pasture (<1-10%), native forest (<1-3%) and slip (<1-13%) sources, with a high proportion of flood-plain derived sediment likely from silt transport and stream bank erosion (29-95%) depending on storm/rain history (Gibbs and Bremner 2008).

High rainfall events can exacerbate the effects of post-forestry soil transport through landslide and stream debris-dam failure. For example, Marden and Rowan (2015) determined that transported soil was predominantly derived from forestry debris avalanche originating from plantation forestry clearance, where higher soil volumes were derived from slopes clear-felled three years previously rather than slope that had just been cleared. A similar avalanche event was observed in the current study on Wharekawa Harbour during the field data collection of early 2017. Two substantial rain systems “The Tasman Tempest” and “Tropical cyclone Cook” impacted Coromandel peninsula with sustained heavy rainfall during autumn 2017 (Moreton 2017, Parker 2017; Figure 3.6).

The outcome for the estuary was substantial soil and debris avalanches occurring nearby to the estuary margin with observable soil mass entering the estuary (Figure 3.7). Frequent land slips were visible in the recently cleared plantation forestry areas (e.g., Figure 3.7a). Singleton (2017) observed significant stream bank erosion in reaches within the Wharekawa catchment that run through pastoral areas into the estuary.

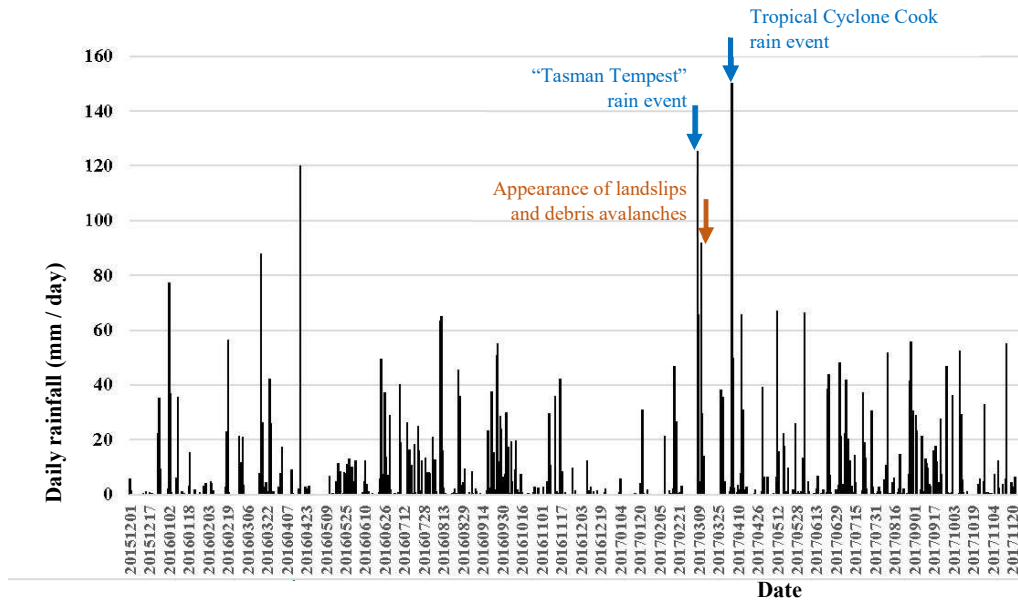


Figure 3.6. Study area two-year rainfall profile to end of 2017 field work period. Source NIWA CliFlo database download for Tairua rain gauge.

Most of the visible sediment deposited on the estuary in the weeks following these rain events appears as either deep drifts of orange/brown coarse sediment with good drainage of tidal waters, or very fine smothering mud-forming brown silt (Figure 3.8). The silt had largely dispersed by ~ 4-6 weeks after the storms, but the coarse sediment was still conspicuously present one year later. In addition to the orange/brown stream derived sediment, there was also significant transport of existing sandy sediment (grey hued sediment rich with shells) by surging flood waters. Both types of storm sediment caused notable smothering or burial of seagrass in thick layers, at depths of >200 mm at deepest observed level where there was filling of the existing estuary drainage microtopography (Figure 3.9).

The Tasman Tempest rain event induced a major landslide filling then damming a stream which formed a significant sediment release spilling across a bounding road into a salt marsh at the margin of the estuary (Figure 3.10). Significant coarse sediment from the flow was still abundant on the marsh 12 months after the event, with extensive fine orange brown silt depositing across the marsh.



Figure 3.7. Major slips and sediment/debris entering Wharekawa Harbour at the time of the Tasman Tempest and Tropical Cyclone Cook rainfall events: - a) landslide avalanche across a salt-marsh with extensive deposition of forestry derived logs and slash; and b) sediment avalanche onto low-lying pastoral land adjacent to the estuary.



Figure 3.8. Sediment accreting in large piles upon the estuary inflow from a tributary stream which drains an area of significant slope failure and landslip resulting from the ‘Tasman Tempest’ rain event, 7-12 March 2017. Sediment here formed a large wide mound that buried parts of a significant seagrass meadow with >200 mm depth of coarse-grain (fine gravel) persistent sediment. Image date 16 March 2017.

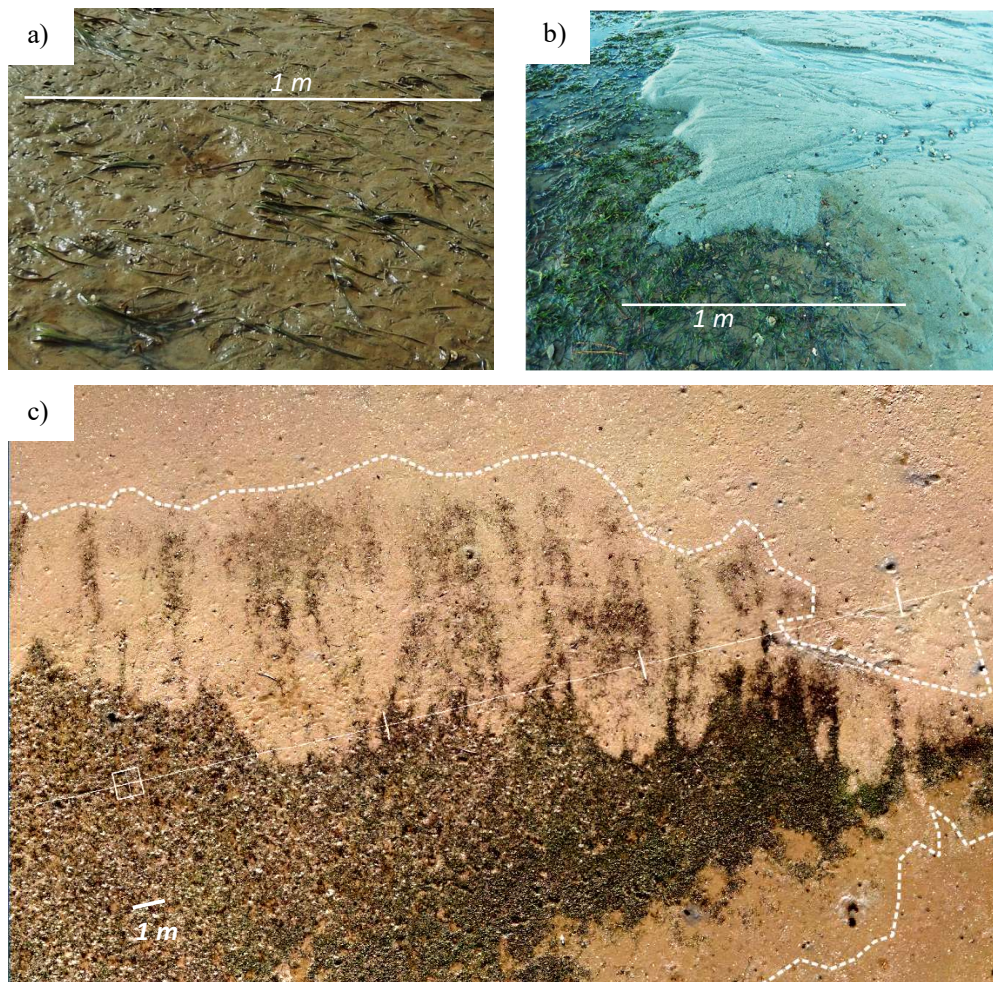


Figure 3.9. Examples of sediment incursion upon seagrass; a) orange/brown mud typical of stream particulate inflow deposition from slope failure in the catchment, b) grey sandy sediment consistent with high flood-current displacement of existing sand/shell sediment and, c) large-scale burial of a seagrass meadow with white-dashed line indicating true seagrass extent as per ground-level GNSS measurement.

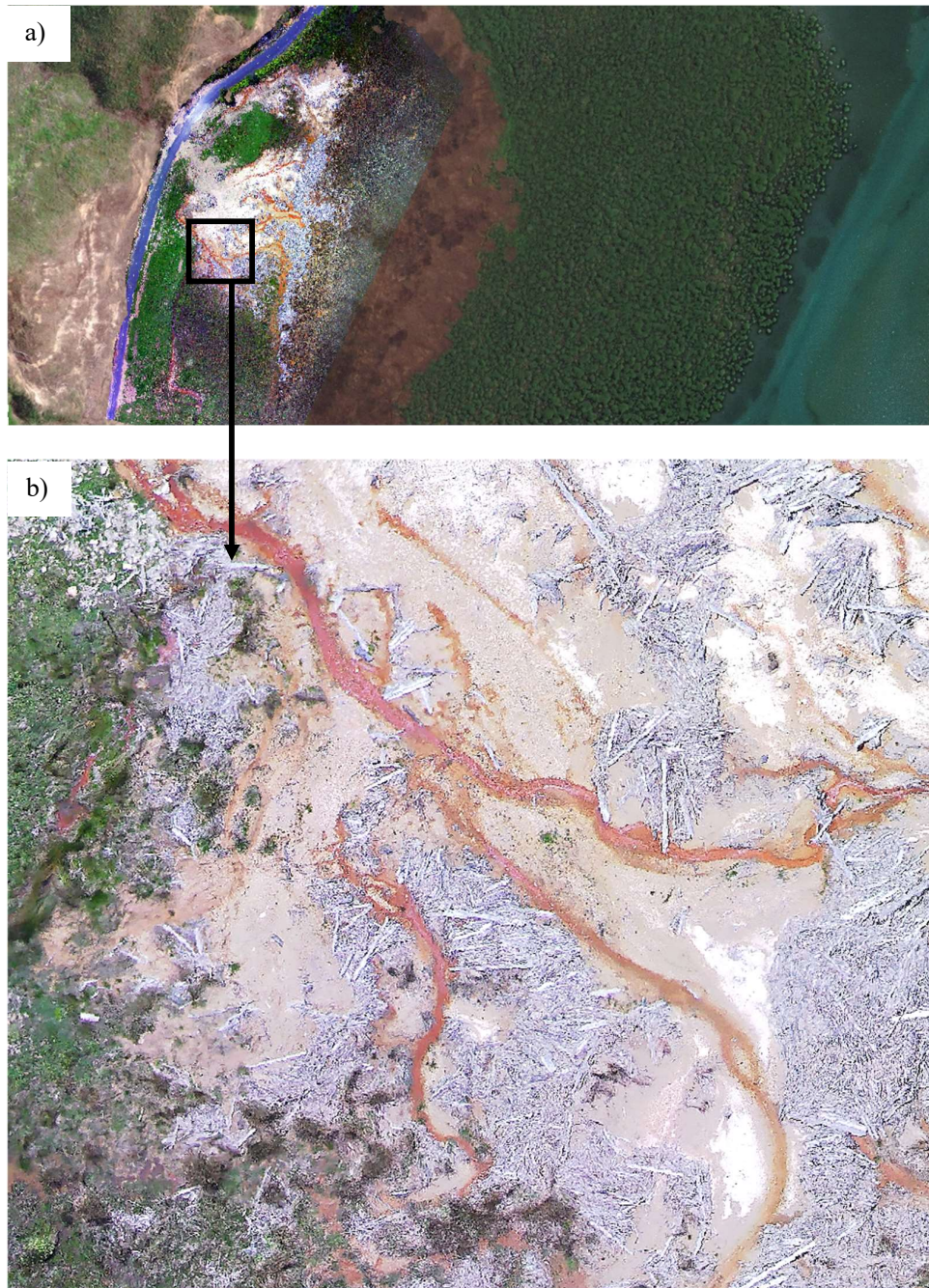


Figure 3.10. Forestry-derived landslide avalanche and sedimentation event spilling from steep slopes onto Wharekawa Harbour marginal salt-marsh, arising from the Tasman Tempest heavy rainfall event 7-12 March 2017: (a) top view as RPA imagery overlain onto Bing Maps background; and b) enlargement showing sediment forming deep deposits (>1m in places) on top of vegetation and eroding into new flow channels). These images are the nadir-view of Figure 3.7a, captured by remotely piloted aircraft on 23 March 2017.

3.4.4 Saltwater paspalum

Saltwater paspalum (*Paspalum vaginatum*) is an invasive introduced weed in New Zealand, and generally found at sub-tropical latitudes of the upper North Island (Graeme and Kendall 2001; Shaw and Allen 2003). The weed is distributed throughout much of coastal Coromandel Peninsula (Graeme and Kendall 2001; Graeme 2008; Lewis and Britton 2015). There is no clear record of when saltwater paspalum was introduced to Coromandel, however Graeme and Kendall (2001) report an instance of a herbarium observation of *P. vaginatum* near to the Coromandel in Mercer in 1877.

Saltwater paspalum was already prevalent in patches throughout Wharekawa Harbour by the time of the 1997 estuarine vegetation inventory (Graeme 1997). Saltwater paspalum has been reported as a substantial ongoing issue for Wharekawa Harbour for several decades (Graeme 1997, Graeme 2008, O'Donnell 2009). The weed is typically found on the estuary verge (Shaw and Allen 2003), and the largest paspalum infestations on Wharekawa Harbour are associated with sea rush (*Juncus spp.*) communities and lining the channelised upper reaches of the inner estuary and upstream into tributary streams (Graeme 2008). Large swards of paspalum grow in extensive swards along the inflowing margin or Wharekawa River, which trap sediment flowing downstream further increasing channelization and accelerating rates of sediment infilling and loss of sand/mud flat habitat (Graeme 2008; Figure 3.11).

The surveyed extent of saltwater paspalum on the estuary increased from 4.5 to 9.4 ha in the period from 1997 to 2008 (calculated using dataset Waikato Regional Council 2014, with spatial dataset clipped to a common extent between years, from estuary body to tributary entry points). Current day imagery (e.g., Google Earth time-series) indicates these historical infestations have further expanded over the past decade since the last ground survey, such that channel infestations are over 1 km in length and penetrating hundreds of meters into the large marginal coastal marsh and sea rush communities (Figure 3.11).

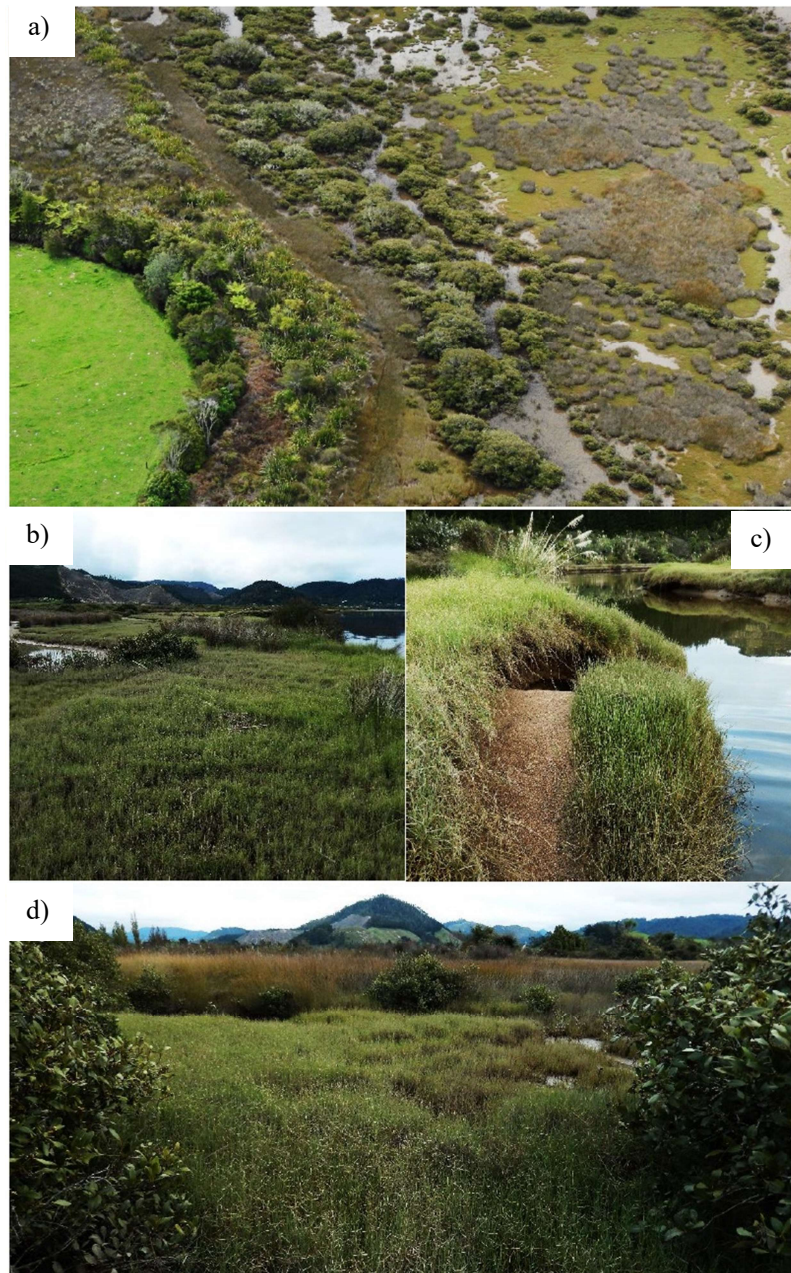


Figure 3.11. Various presentations of saltwater paspalum infestation of marsh, rush and mangrove communities, Wharekawa Harbour. Image a) shows aerial view of paspalum encroaching inward from the channel edge (top left of photo) towards the terrestrial limit of coastal vegetation and pastoral grassland (lower right of photo); b) deep swards of paspalum (e.g., ~1 m deep can be common) growing on banks of sediment deposition, with c) erosion of sediment banks at sites of flood water erosion; d) paspalum spanning gaps between mangrove and sea rush community, i.e., extending from channel edge up to near the mean high water spring tidal limit.

3.4.5 Other threats

Other threats to the estuary health include possible nutrient run-off effects from pastoral and forestry land (O'Donnell 2009), and the general effects of climate change and associated extreme weather events, ocean acidification and species intolerance to warming (Ministry for the Environment 2016). Wilding pines and willow are a potential threat for the saltmarsh community on the estuary margins (Graeme 1997; O'Donnell 2009). Seagrass may be impacted from grazing by large numbers of swans and Canada Goose that can be seen feeding on seagrass on Wharekawa Harbour (Figure 3.12).



Figure 3.12. Seagrass on Wharekawa Harbour can be subjected to intensive grazing from swans (a) and Canada goose (b).

3.5 Seagrass extent on Wharekawa Harbour - analysis

Wharekawa Harbour is one of several sites listed as being data deficient for evidence of seagrass decline (Morrison et al., 2014). The historical image time-series in Google Earth indicates that there has been significant seagrass loss comparing current day imagery to the earliest Google Earth imagery (dated 2001). This decline can be quantified in part by comparing two Waikato Regional Council vegetation surveys (Graeme 1997, 2008) with the sum of all seagrass-containing patches mapped in these surveys reducing from 50 to 45 ha between these survey times. Inspection of long-term Google Earth time-series (spanning 2001- present day) imagery, shows some areas with > decade long seagrass patch-persistence, but many parts of the estuary exhibit transient distribution over that time.

Authors Suykerbuyk et al. (2016) described similar patterns for *Zostera noltii* in the Netherlands, identifying ‘hot spots’ where seagrass was present in all map extents, and ‘cold spots’ being areas with variable extent. Within these sites, high density seagrass was believed to stabilise its substrate under a positive feedback process, and conversely once seagrass dropped below a certain density, negative feedback promoted decline.

Wharekawa Harbour seagrass has high potential for growth and spread compared to other estuaries on the same coastline (Turner 2007). The estuary also has great potential for rapid seagrass loss due to sedimentation associated with high prevalence of plantation forestry and agricultural land disturbance within its catchment, and multiple stream networks draining this land into the estuary. The current-day plantation forest tracts are the third or fourth planting since the forestry was established in the 1930s. There has been no comprehensive seagrass mapping on the estuary since the 2008 ground survey by Graeme (2008). Consequently, updated measurement of seagrass extent on Wharekawa Harbour was justified.

In order to construct a long-term time-series for seagrass extent, two high precision datasets were generated providing accurate seagrass extent data representing status of seagrass extent at the time of the current study. Likewise, estimates were made for seagrass extent prior to the 1997 ground survey, by photointerpretation on available historical imagery.

3.5.1 Survey Methods

3.5.1.1 Current day seagrass extent

A seagrass census was conducted by walking systematically around all parts of the estuary, tracing the location using one of two global positioning standards. A high precision global navigation satellite system (GNSS) survey instrument (Trimble R8

receiver with TSC3 controller) receiving real time corrections via a wide area cellular virtual reference system (VRS, Geosystems i-base) was used where cellular radio reception was available. Measurements were taken under ground control with respect to a Land Environment New Zealand (LINZ) geodetic survey mark situated nearby (LINZ mark 'EB2U'). In parts of the estuary where cellular reception was insufficient for reliable GNSS position correction, two multi-constellation handheld GPS receivers were used for mapping, a Garmin GPS64 for mapping seagrass patch exterior boundaries and a Garmin Etrex20 for mapping interior holes i.e., gaps or sand patches within the seagrass patches. Holes were captured because some were large areas of seagrass absence (e.g., 1940 m²), and many were sites of erosion to the seagrass bed.

All three GPS units were set to capture locations at 2 second intervals, and mapping was conducted at a walking speed achieving approx. 0.5 - 2 m vertex spacing on resulting seagrass polygons depending on the detail required to depict the true shape of the patch. All three receivers were mounted on a 2 m mast. This is normal operation for the Trimble GNSS equipment, and the handheld GPS units were similarly mounted so as to maximise satellite signal reception, reduce possible multipath interference, reduce interference from the observers, and maintain consistent orientation.

Seagrass extent was captured by walking slowly with the receiver elevated above the outside limit of the patches. Seagrass grows by way of extension of long underground rhizomes with emergent shoots, so the meadow margin can be dendritic in presentation and ambiguous. The measured boundary was formed by emulating on the ground a concave polygon construction method used in geographical information systems (GIS), the 'alpha shape' (Edelsbrunner et al., 1983; Van Kreveld et al., 2011), applying a gap-threshold of ~0.5 to 1.0 m by eye (Figure 3.13).

Mapping done with the GNSS instrument captured boundaries and holes on the same instrument, using automatic feature-labelling functions on board the TSC3 controller to track holes, boundaries and corrections made during capture. Mapping done by handheld GPS required capture of boundaries and holes on separate receivers so as manage shapes and avoid confusion within the limited feature-labelling of the consumer GPS units. Holes were subtracted from boundaries later in a GIS software environment using one of two procedures. The first was direct topological subtraction of polygon holes from boundaries as recorded in the field (noting the potential for GPS-signal drift resulting in the hole moving partly or completely outside of the boundary). The second involved only numerical subtraction of hole-area from boundary-area within attributes of the polygon (but functionally the same as manually shifting the hole to ensure it is contained inside of the boundary).

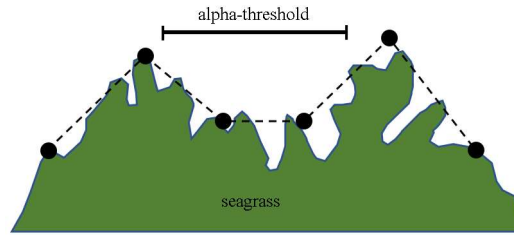


Figure 3.13. Schematic example of capture of a polygon boundary representing the seagrass edge (black dashed line) using a concave-hull approach built around GPS/GNSS survey points with alpha threshold in the range 0.5-1 m as judged by eye during ground mapping.

3.5.1.2 1997 and 2008 seagrass extent

Seagrass extents were extracted from the Waikato Regional Council Estuarine Vegetation GIS layer (Waikato Regional Council 2014 dataset) after selecting seagrass-containing features at Wharekawa Harbour and grouping by survey year 1997 or 2008. There was a systematic error present in the 1997 polygon set where all features were offset by a similar amount, consistent with a GPS projection error or image orthorectification error at time of creation. Translation and rescaling were applied to the polygon features (QGIS Vector Bender QGIS 2018) to rectify features as close as possible to likely ground position using physical reference features (n=120) observable in both aerial photography (i.e., unambiguous static shoreline and constructed features).

3.5.1.3 Recent and historical imagery

Aerial photography datasets (1945, 1954, 1959, 1966, 1971 and 1983) and three recent image datasets (Aerial photography 2002, Bing Maps 2015 imagery and Waikato Regional Council 2012a regional aerial imagery) were displayed in QGIS software, and visible seagrass patches traced on screen using polygon digitising tools (Appendix 3.9.1). Vertex spacing was approx. 0.5 - 2 m, to match as far as possible the geometry style of seagrass captured in the 2017 and 2018 GPS/GNSS ground survey.

Imagery from 1945 to 1971 comprised grey scale aerial photography, originally captured under an overlapping survey design, and orthorectified by the supplier. Historical imagery are sourced from Retrolens (www.retrolens.nz) licensed for use under creative commons (<https://creativecommons.org/licenses/by/3.0/nz/>). Most seagrass was clearly identifiable, but some patches were faint or confounded by the similar appearance of wet sand at the line of the tidal water level. To aid image interpretation, a set of low altitude (1000 ft) aerial imagery captured near to the time of the 2017 ground seagrass census were converted to single-band greyscale imagery by averaging red + green + blue

digital numbers, and the resulting image was contrast-adjusted until it appeared tonally similar to the 1945 and 1971 mosaics (Appendix 3.9.2). The content of the estuary was known at this time due to ground survey work and additional data collected concurrently. Therefore, this reference provided some textural indication on the appearance of known seagrass presence and absence in the historical imagery. Ambiguous edges to the seagrass were estimates based on the middle of a tonal change, and these were labelled with elevated uncertainty attribute values, for use in the error calculation that follows.

3.5.2 Error estimation

2017 and 2018 seagrass census

In the previous section, the total seagrass was calculated from the different image sources, with varying precision levels for the respective polygon line work for each year. Understanding the significance of between-year difference in seagrass area requires a measure of the uncertainty in geometry placement on the ground. The most precise surveys should be the 2017 and 2018 seagrass estimates due to the high precision of the GNSS survey instrument and ground-level assessment of seagrass presence. The Trimble instrument, under VRS correction, has horizontal positional error of approximately 2-5 cm when braced on a mount, but greater error when mobile under the conditions of a rapid survey. The Garmin handheld GPS receivers are rated as being accurate to 5-10 meters with respect to global latitude/longitude coordinates. Needham et al. (2013) measured agreement between aerial photography and trace-lines from an older single constellation handheld GPS receiver model Garmin GPSMAP 78SC, and determined that there was <2 m error between position estimates on nearby Tairua Estuary. However, the authors did not mention how the 2 m positional error was also related to the 2.5 m positional root mean square error (RMSE) of the aerial photography from true location. The authors later conducted GPS consistency tests (Needham et al., 2013) to assess the deviation in location-estimate for two receivers of the same receiver model measuring locations at the same time (n=8 measurements) and determined consistency of 3.5 m ($\sigma = 1.5$ m) on Wharekawa Harbour and a range of 1.5-7.4 m across all estuaries surveys on Coromandel Peninsula (various n, σ were reported; refer to Needham et al. (2013) for detail). These findings were based on low sample size without consideration of shift in constellation with time and using an older low precision receiver limited to single constellation GPS signal. Receiver positional uncertainty is unknown for the purpose of a sustained seagrass mapping survey, for polygon-area determination using a modern multi-constellation GPS receiver.

In order to quantify this error, ten shapes of varying size (mock-seagrass patches) were drawn in the sand near to the main Wharekawa seagrass study area (Figure 3.14). Use of real seagrass patches wasn't viable due to the need to minimise seagrass trampling on the primary remote sensing study area.

The shapes were surveyed at high levels of precision using the Trimble R8 with firm ground placement, on a stabilised upright mast (spirit-levelled), with < 2 cm horizontal dilution of precision reported by the control unit. The shapes were surveyed with ~0.5 m point spacing. With this high precision survey reference in place, three rapid-survey regimes were tested: i) using the Trimble R8/ TCS3 combination on a 2 m mast applied with a 'topological survey' mode of data collection, i.e., the mast is mobile with minor sway from motion; with ii) and iii) being two replications of this survey for the Garmin GPS64 and Etrex 20 GPS receivers respectively, each also on 2 m masts.

In each session, boundaries were captured first, with the polygon holes surveyed ~15-20 minutes later once the boundaries were complete: this sequence was necessary to avoid capture confusion when sorting data later due to close proximity. Valid polygon areas were calculated subtracting holes from boundaries under two regimes, by i) topological subtraction; and ii) aspatial numerical subtraction of areas within the attribute table. This was important as due to GPS uncertainty at small scale, some holes (although drawn correctly) were positioned outside of the polygon boundary, resulting in another source of error.

Three replicate captures were made for each of the three sessions, with 1 hour between replicates. Thus, the sampling design had 3 receivers x 3 repeat measures on 4\each receiver, with sufficient time in between replications to ensure a different GNSS satellite geometry overhead (more time was not possible due to the tidal window and the timeframe for incoming tidal flood) with survey conditions were otherwise near-identical such that only difference between sets should be the receiver model and satellite constellation geometry.

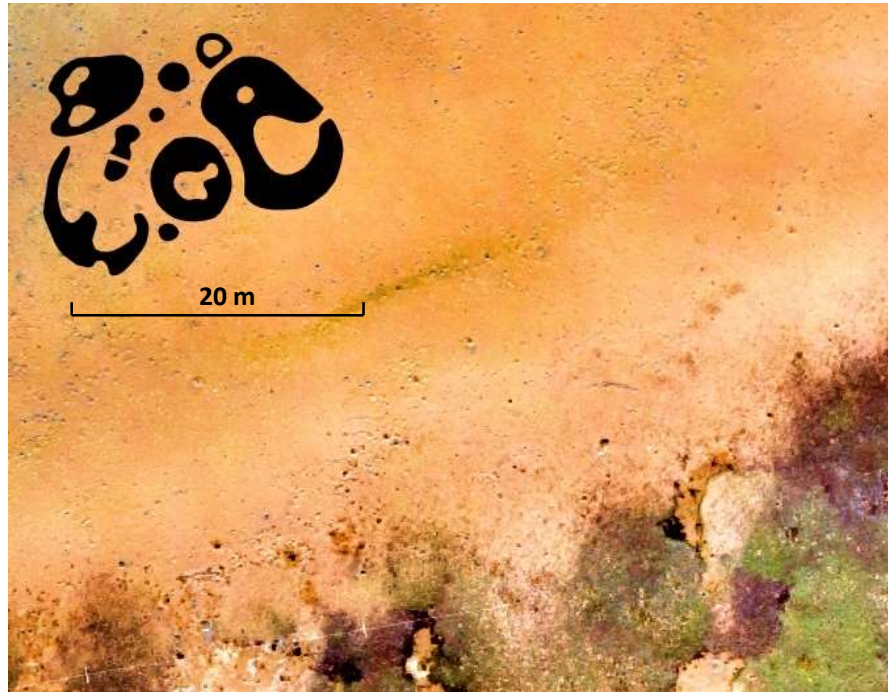


Figure 3.14. Layout of GNSS/GPS accuracy assessment, where black polygons show reference shape-locations drawn into the sand/mud, which were surveyed by high precision GNSS static capture for reference, then surveyed by rapid mobile capture (‘tracing’) using the three different receivers.

Deviation from reference, and difference between area estimate for each shape were calculated for each session. The mean deviation obtained for each model was used in the 2017 and 2018 census for error calculation.

The significance of differences between the GNSS and GPS receivers was assessed by analysis of variance (ANOVA function, The R Project 3.4) with Tukey’s pairwise comparison invoked to assess pairwise contrasts.

2008 and 1997 seagrass mapping

Seagrass polygons derived from the Waikato Regional Council 2014 spatial dataset for Wharekawa seagrass (2008 field survey) were captured by the authors using early Bluetooth GPS technology linked to an IPAQ field tablet (Waikato Regional Council 2014 metadata notes), for which accuracy was likely ~2 - 5 meters (Wing 2005; Zhang et al., 2014).

The 1997 seagrass dataset was described by the author as being captured using printed laminated aerial photos with acetate overlay carried out into the field for drawing and verifying species extents. A GPS was used in the field by the researchers for locating

position, and to map seagrass not visible in the aerial imagery. Polygons were later digitised from the acetate overlays and geo registered in a GIS system. There is no information available in associated documentation describing the precision of the line-work (Graeme 1997; Waikato Regional Council 2014 metadata notes).

As a conservative estimate, a 5m positional error was ascribed to polygon geometry in the 1997 and 2008 datasets.

Seagrass measurement for 1945, 1954, 1959, 1966, 1971, 1983, 2002, 2012, and 2015.

Seagrass visible in these image sets (Appendix 3.9.1) was traced on screen within QGIS software. Positional error is therefore related to image interpretation and ability to detect seagrass from the imagery while avoiding non-seagrass features, and the clarity of sparse seagrass patch boundaries. The ground-survey by GNSS/GPS above, had the advantage of absolute identification of seagrass presence or absence. Absolute identification was not possible for this selection of image mosaics due to lack of historical ground reference data at the time the imagery was flown. Visual interpretation is based on comparison to the greyscale 2017 reference mentioned above, along with some cross-referencing between image sets where seagrass patterns are clearly persistent between adjacent datasets.

Digitising was done at ~1:500 screen scale for most capture, but with increased magnification where ambiguity required closer inspection. Polygon line-work was ascribed a 1 m positional error as an estimated vertex placement error. There is no ground-level data available to information construction of actual positional error.

3.5.3 Uncertainties on area calculations

The estimated error for each year's total seagrass area was constructed by applying a positional uncertainty to polygon geometry line-work. This was estimated by constructing positive (expanding) and negative (eroding) buffers around the polygon geometry scaled by the respective error factor. Total area was then summed for the adjusted and original polygons, and these statistics plotted for each survey year as actual, upper and lower total area estimates, yielding a long-term time-series for seagrass extent with uncertainty. Several ambiguous areas of potential seagrass were excluded from the dataset, or included where there was textural indication of seagrass, with both of these uncertainties factored into the uncertainty estimates (error bars) for the respective years' imagery.

3.5.4 Persistence of seagrass

Understanding the significance of the current trend in seagrass extent, after decades of fluctuation, would be aided by examining how subsets of seagrass have persisted over time. In order to provide a coarse indication of seagrass persistence over the time-series, and in particular to identify highly stable patches throughout the 1945-2018 span of the time-series, analysis was undertaken tracking the presence of seagrass backward in time from the current day to the time when the seagrass was not present in the imagery. The persistence of a seagrass record would be estimated as the number of years visible continuously through the time-series. The 2018 seagrass extent was used as a reference, and this polygon-set was overlain on all other layers to compare seagrass distribution.

Due to the differences in positional accuracy between image sets (potentially >5 meters or greater uncertainty, as discussed above), a direct overlay of polygons was not valid. Therefore, in order to have tolerance for slight positional difference in location of the seagrass, a 2m grid was created as a raster, and the presence or absence of seagrass in each grid cell noted as a binary class in rasters for each year's seagrass. The number of years of continuous persistence (i.e., seagrass being present without a break in the time-series) was counted. A second measure was made that counted all years of seagrass presence across all datasets irrespective of whether there was a break in the presence time-series. This second measure provides a display similar to a hotspot analysis.

3.6 Results

3.6.1 GNSS/GPS error calculation

There was a significant difference between receivers in the deviation of rapid survey polygon line-work from the high-precision reference line-work ($F=553.78$, $df = 2$, $p < 0.001$; Tables 3.2 and 3.3). The Trimble R8/TSC3 GNSS setup had significantly better accuracy than the two handheld receivers, and the GPS64 receiver (helical antenna) had significantly higher precision than the Etrex20 (patch antenna).

Mean overall deviation for the three receivers amounted to $1.56 + 0.04$ m, $0.96 + 0.04$ m and $0.11 + 0.006$ m respectively for the Etrex20, GPS64 and Trimble R8 receivers under conditions of rapid survey (Figure 3.15; Table 3.4). The range of mean deviation values for each receiver across the three replicate sets (i.e., where each set represents a different satellite configuration) was 1.29-1.77 m, 0.8-1.16 and 0.10-0.11, and overall minimum-maximum deviation range was 0.22-2.84, 0.04-2.31 and 0.0001-0.41 for Etrex20, GPS64 and Trimble R8 receivers respectively (Table 3.4).

Table 3.2. Significance of differences between the mean deviation from reference shape for GPS/GNSS units used for rapid seagrass mapping.

GPS/GNSS device	df	SS	MS	F	P
GPS type.	2	164.19	82.10	533.78	<0.001
Replicate set.	2	6.07	3.04	19.73	<0.001
Residuals.	454	72.89	0.161		

Table 3.3. Significance of pairwise comparison of differences in the performance of GPS/GNSS units for rapid seagrass mapping in terms of deviation from reference shape. ‘Difference’ refers to the difference between mean deviation values for each GPS/GNSS device. A negative ‘difference’ value indicates that the first device in the pair had lower deviation from reference (i.e., is more accurate) than the second.

Tukey comparison	Difference (m)	95% CL		P
		Lower	Upper	
GPS64-Etrex20.	-0.61	-0.71	-0.50	<0.001
Trimble GNSS-Etrex20.	-1.46	-1.56	-1.35	<0.001
Trimble GNSS -GPS64.	-0.85	-0.96	-0.74	<0.001

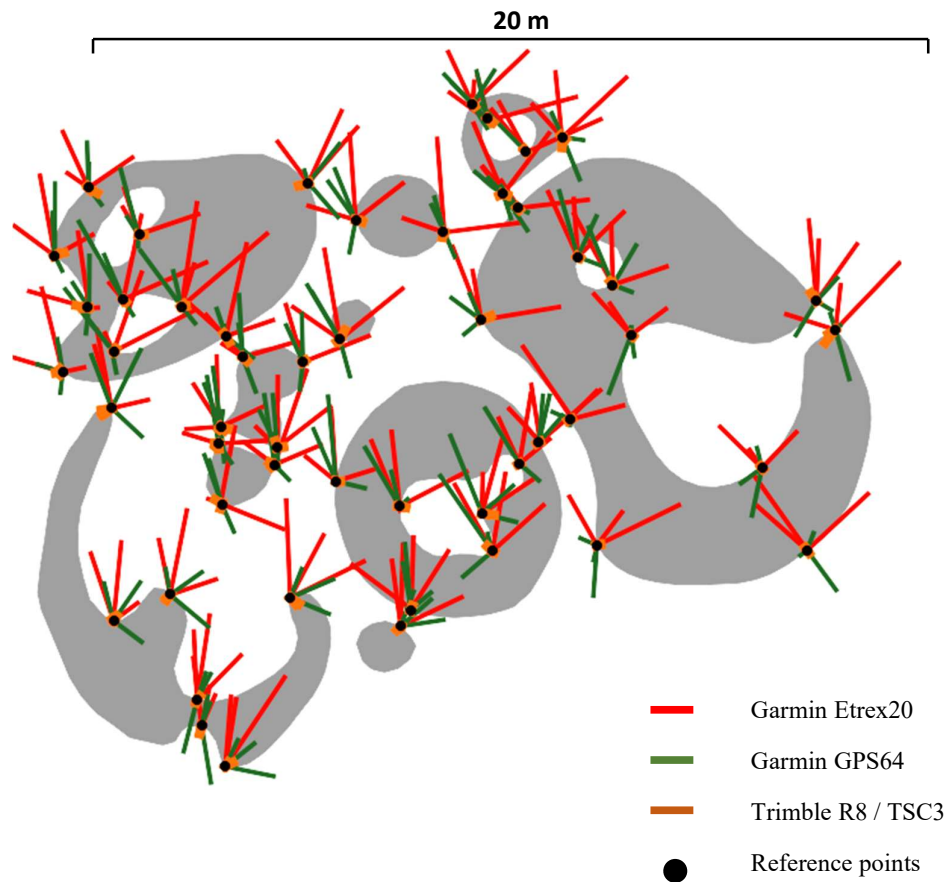


Figure 3.15. Spatial layout of the reference shapes (grey) with deviation lines from reference points for the Etrex20, GPS64, and Trimble receivers. There are three lines per receiver x point combination, being the three replicates across time.

Table 3.4. Mean deviation of rapid survey lines derived from two consumer multi-constellation GPS units (Garmin Etrex 20 and Garmin GPS64) and rapid survey capture using a Trimble survey instrument as compared to a high-precision reference capture of a simulated seagrass meadow drawn into the sand.

Source	Set	Per set		Per GPS unit	
		mean	stderr	mean	stderr
Garmin Etrex20.	1	1.77	0.05	1.56	0.04
	2	1.29	0.08		
	3	1.64	0.08		
Garmin GPS64.	1	1.16	0.08	0.96	0.04
	2	0.80	0.05		
	3	0.91	0.05		
Trimble GNSS.	1	0.10	0.01	0.11	0.006
	2	0.10	0.01		
	3	0.11	0.01		

The deviation from reference area was calculated for each GNSS/GPS model and replicate combination. Total shape-area estimated by the Trimble R8 receiver setup was more similar to the reference area than for the two consumer grade receivers (Table 3.5). For the rapid survey, the Trimble GNSS receiver underestimated total reference polygon area by 3%, and the two consumer GPS units overestimated area by 5 and 14 % for the Etrex20 and GPS64 respectively.

Uncertainty in total area estimate was most influenced by the larger shapes. Smaller shapes varied greatly in boundary positioning and estimated area (Figure 3.16), however did not contribute significantly to total error in calculated area (Figure 3.17). There was little overall bias in direction of error (i.e., over or under estimation) with respect to shape area, as illustrated by variability spread evenly about the $x=0$ line (Figure 3.17; gradient $m \sim$ zero).

Table 3.5. Mean deviation of measured total shape area compared to actual area of high-precision reference shapes (simulated seagrass reference areas), based on the rapid survey lines derived from walking the shape boundaries using two consumer multi-constellation GPS units (Garmin Etrex 20 and Garmin GPS64) and rapid survey capture using a Trimble R8+TSC3 survey instrument. Subtraction of holes was assessed for i) topological subtraction of hole from boundary in the spatial domain; and ii) subtraction of hole area from boundary area in in the attribute domain. The total area of all reference shapes was 135.5 m², after removal of 11.5m² of holes.

GPS/GNSS device used.	Measured area of holes (m²).	Resulting shape area (m²) (topological subtraction of holes).	Resulting shape area (m²) (attribute subtraction of holes).
Etrex 20.	12.7	141.9	141.1
GPS64.	13.6	154.4	153.2
Trimble R8.	10.9	131.4	131.4

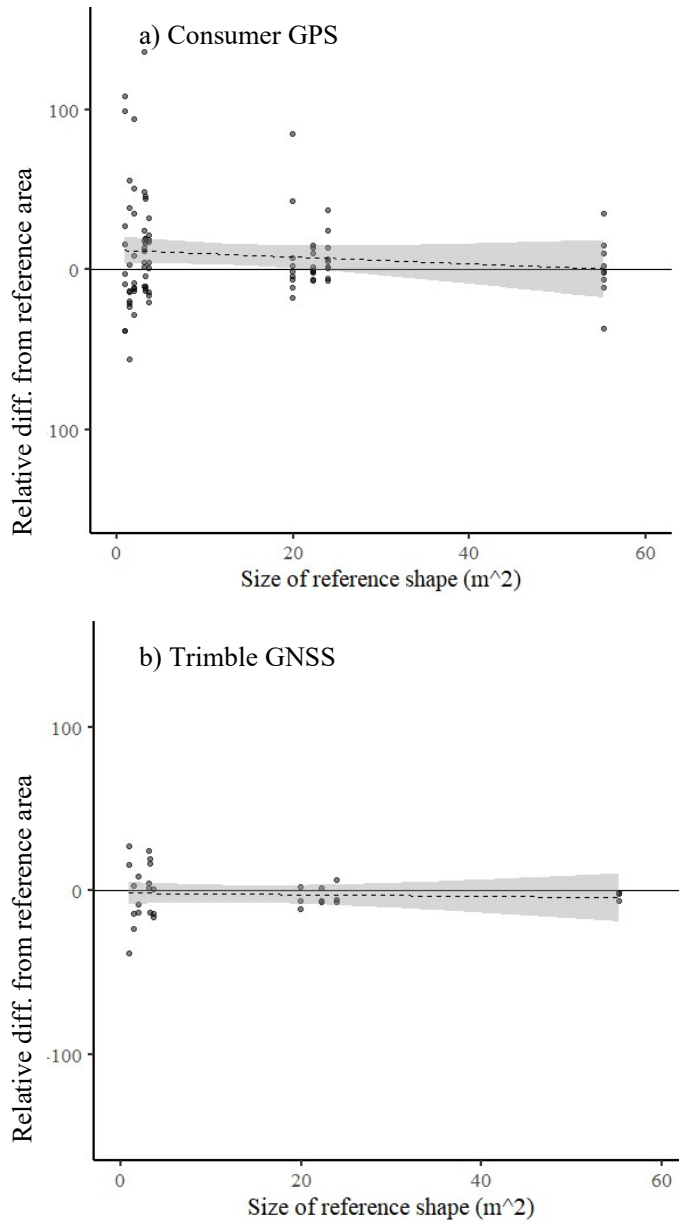


Figure 3.16. Plot of percent difference between the measured area of simulated seagrass shapes mapped using a) the Garmin consumer GPS units (data from two GPS receivers pooled) and b) Trimble GNSS survey instrument, as compared to reference shapes mapped at high precision. Dashed line is the regression line of linear fit and the grey area indicates the 95% confidence limit on the line.

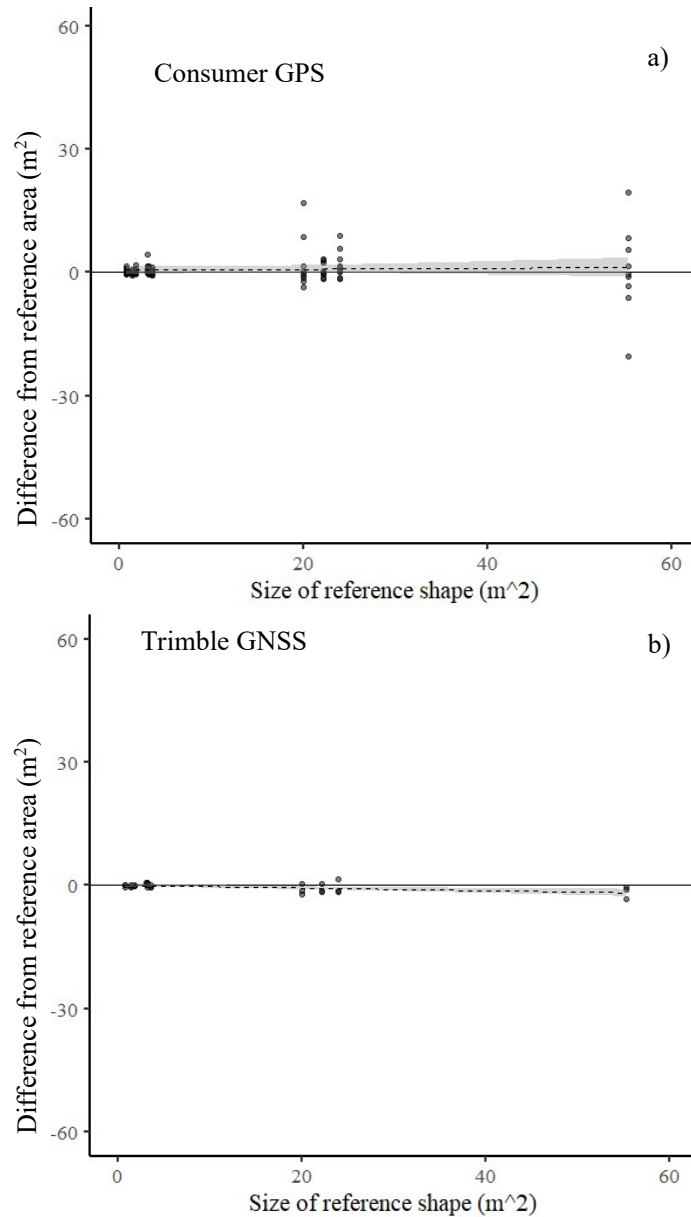


Figure 3.17. Plot of numerical difference between area of simulated seagrass shape mapped using the Garmin consumer GPS units (data from two receivers pooled) and a Trimble GNSS survey instrument (a and b respectively) as compared to reference shapes mapped at high precision. Hole-features were captured along with boundaries, and the holes were either cut into the boundaries automatically without adjustment, or where holes were manually moved to be wholly contained within the boundary. Dashed line is the regression line of linear fit and the grey area indicates the 95% confidence limit on the line.

3.6.2 Polygon placement error, and feedback into mapping methods

The results above indicate that for rapid survey using the Trimble GNSS receiver, polygon line placement uncertainty of 0.1 m should be applied when forming error estimates, and 1.6 m and 1.0 m for polygons surveyed using Etrex20 and GPS64 respectively. These uncertainty values were applied to the mapping polygons of the 2017 and 2018 seagrass census surveys.

3.6.3 Long term seagrass trend

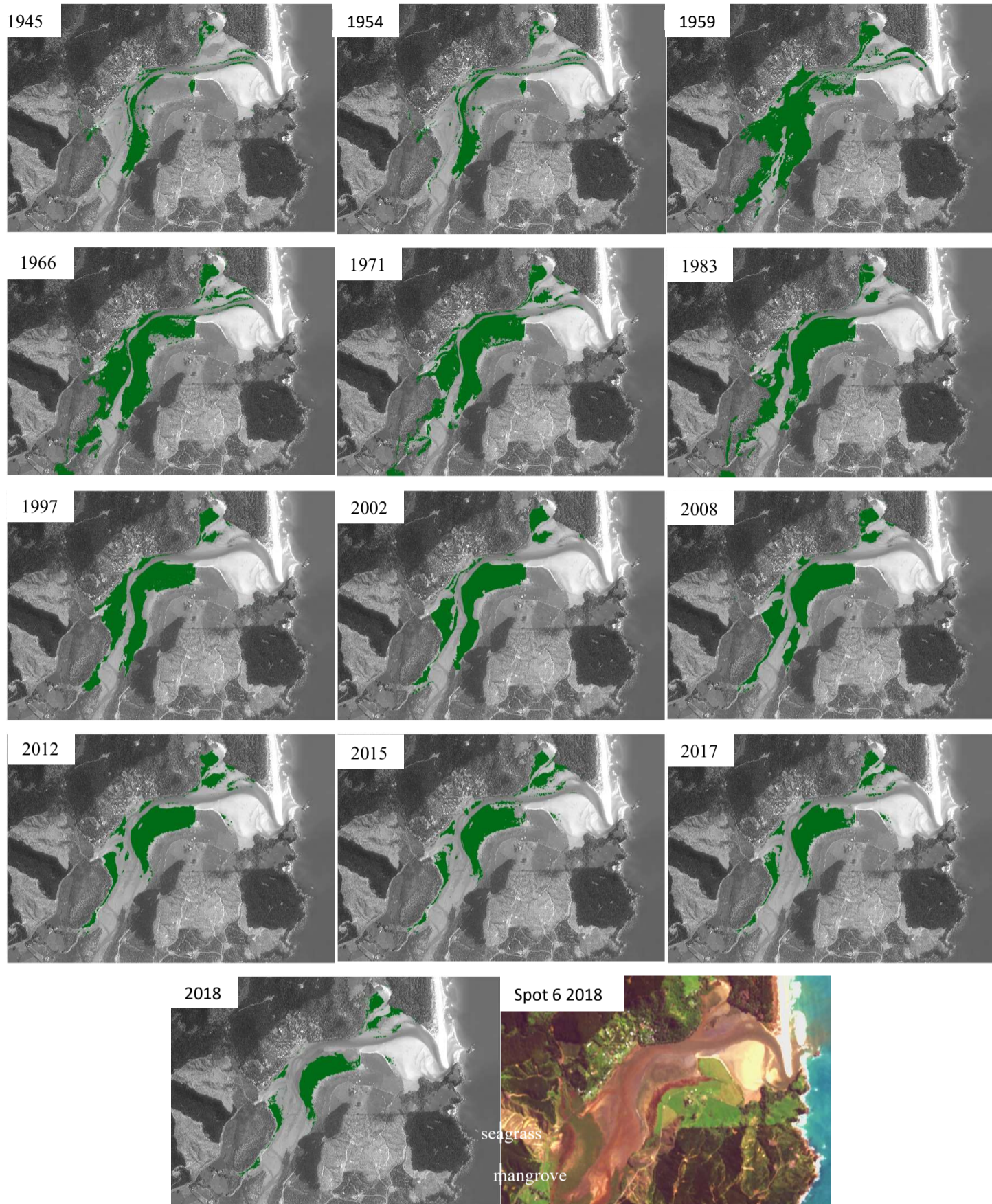
Total calculated seagrass extent with estimated uncertainty-bounds for each historical imagery year (Figure 3.18) indicate an increase in seagrass from 1945 to a maximum in 1959, then a slow decline to the present day (Figure 3.19). There was insufficient information available to quantify uncertainty under a statistical model, and the error bars presented in Figure 3.18 indicate the positional uncertainty and addition/subtraction of ambiguous areas calculated above.

The lowest seagrass area in this multi-year time-series was observed in 1945. Current day decline in seagrass is approaching the 1945 low, or possibly already equivalent to this low value (when considering the uncertainty range). There was a high-confidence 22% reduction in seagrass on the estuary from March 2017 to March 2018 (Figure 3.19), with areas of loss corresponding to parts of the estuary where there was notable observable sediment deposition and/or high sustained turbidity during the weeks that followed the two autumn 2017 storm events. It is interesting to note that although comparison of the 2017 and 2018 seagrass inventories show clear reduction in seagrass, there were several patches lost (probably buried) several years earlier, that became exposed during the course of the year, sprouting new fine seagrass.

The long-term persistence of current day seagrass was estimated by tracing back in time to when seagrass present in the 2018 extent, first appeared in the earlier imagery (Figure 3.20). Within the area of seagrass mapped in the 2018 imagery, and considering the proportion that was also visible continuously through historical imagery sets, 7 % of the 2018 seagrass was visible in all imagery going back to the 1945 historical photography (73 years prior to 2018), 53% to 1971 (47 years prior), 59% to 1983 (35 years prior), 65% to 1997 (21 years prior) and 78% to 2008 (ten years prior).

The total seagrass aggregation across all years amounted 107 ha. This equates to 47% of the 226 ha total area of the estuary calculated in this analysis. Therefore, seagrass was never detected on 53% of the estuary in 73 years, within the detection limits of the methods used. The amount of seagrass present in 2018 is 24% of the total seagrass detected across all years.

Sixteen percent of this total aggregated seagrass occupancy across all years has dense mangrove forest cover in the current day. Seagrass is present in some areas within the mangroves, but examples are rare and situated at the margins of the new mangrove forest.



↑ **Figure 3.18.** Seagrass extents (green polygons) as visible in imagery from 1945 to the present day (grey scale frames) with reference colour image (Spot 6 satellite imagery at March 2018).

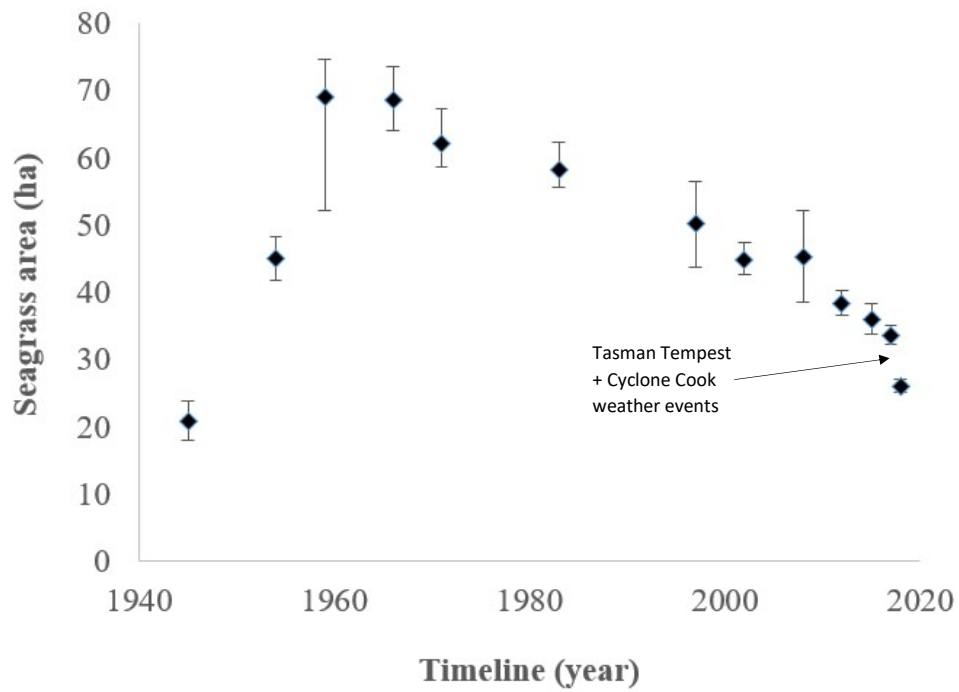


Figure 3.19. Change in calculated area of seagrass on the estuary determined from imagery or survey data. Error bars depict the maximum and minimum possible aggregated areas calculated by factoring geometry uncertainty and adjustment for ambiguous seagrass areas.

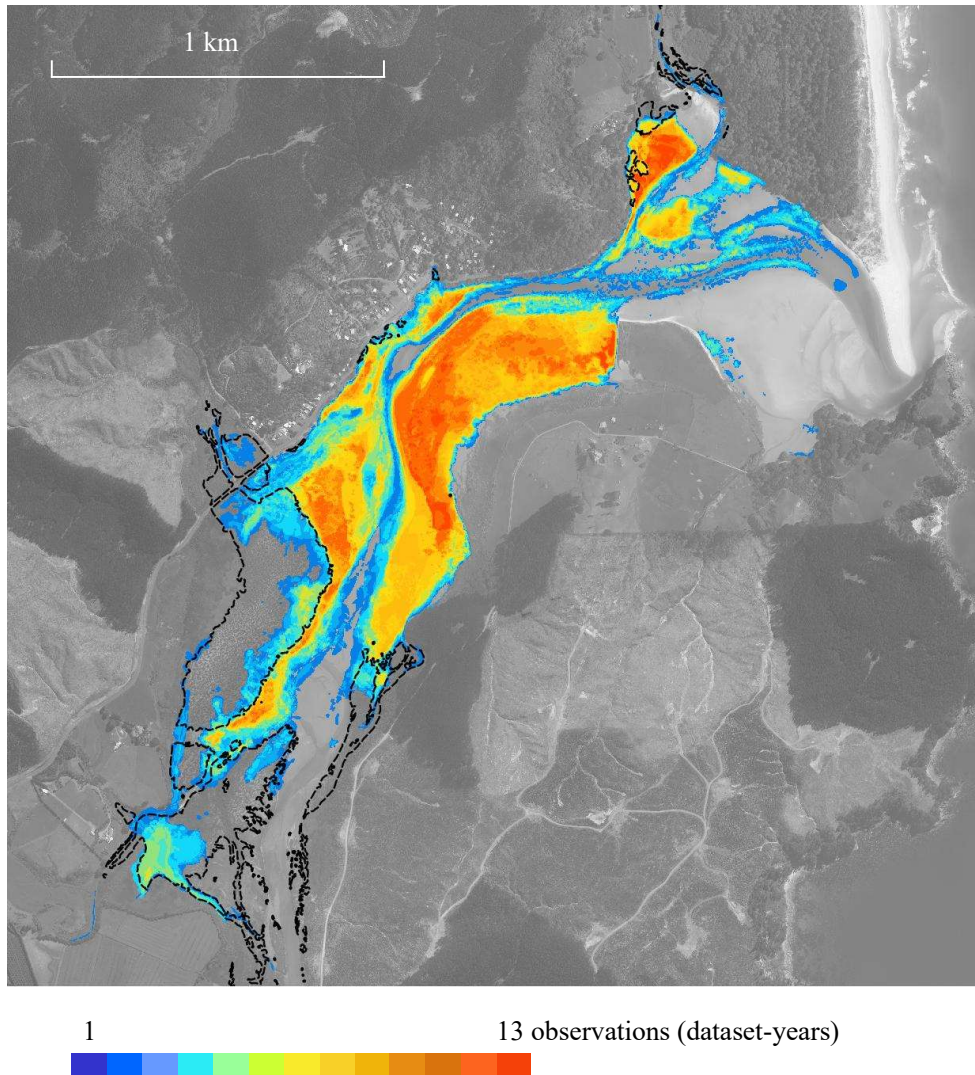
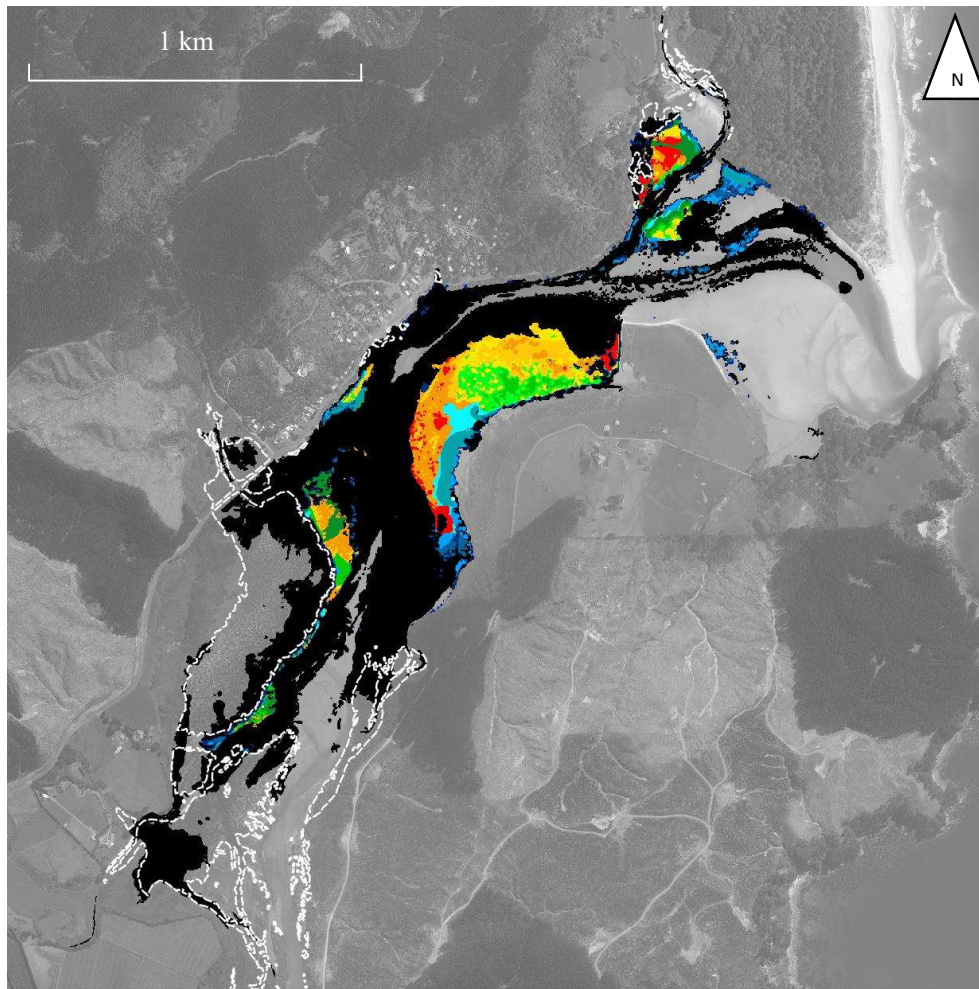


Figure 3.20. Occurrence of seagrass tallied across the thirteen datasets from 1945 to 2018, i.e., a score of 13 (red) indicates seagrass was present in all 13 datasets. Absence of colour on this scale indicates absence of seagrass in these datasets.



Key: Seagrass persistent within the periods:

■ 1945 to 2018	■ 1954 to 2018	■ 1959 to 2018	■ 1966 to 2018
■ 1971 to 2018	■ 1983 to 2018	■ 1997 to 2018	■ 2002 to 2018
■ 2008 to 2018	■ 2015 to 2018	■ 2017 to 2018	■ 2018 only
■ All other seagrass pooled	White dash line = current mangrove		

Figure 3.21. Distribution of seagrass that is found in the present day and persistent back through the time-series, colour-coded to indicate how long it has been continuously present back in time from 2018 to the respective historical dataset. Black areas show all remaining estuary areas where there has been other transient seagrass at times. The sum of all 13 colours (red through blue) depicts all seagrass from all datasets (i.e., an absence of these classes indicates where seagrass has never been detected in any dataset). The white dashed line shows current-day mangrove distribution. These data are overlain upon aerial photography (Waikato Regional Council 2012a converted to grey scale).

3.7 Discussion

In this chapter, the characteristics and history of Wharekawa Harbour and catchment were summarised. Current extent was assessed in comparison to historical extent estimates. These provide a basis of selection of Wharekawa Harbour as a study area and case-example for new method development. Wharekawa Harbour is currently subject to rapid change. This estuary faces a similar set of pressures to other estuaries in the region so remote sensing methods developed later will be relevant for application to a wide range of estuaries.

Long term change in seagrass

Previous seagrass quantities were calculated by photointerpretation of available historical imagery. From these estimates, it was determined that seagrass within Wharekawa Harbour is in decline compared to medium term patterns. Census surveys in 2017 and 2018 indicate a 22% measured reduction in seagrass across a 12-month period, where observed sediment effects were likely exacerbated by two heavy rainfall events at the start of this period. The short-term reduction is consistent with a longer-term trend in declining seagrass since 1959, when the largest seagrass extent was observed within the image data analysed under this study.

The lowest of all seagrass estimates in the time-series was observed in 1945. The 1945 extent may not show the full impact of sedimentation from the native forestry clearance, and there are signs in the patch-layout of the 1945 imagery that seagrass may have been in lower coverage in years prior to this time: some of the seagrass visible in the 1945 imagery is consistent in appearance with new seagrass, either colonised from mobile rhizome/shoot fragments or recolonised from seed bank germination, appearing as small radial patches of seagrass.

Although recent seagrass area estimates since 1959 are greater than the 1945 estimate, the most recent (2018) seagrass area measure is almost reduced to this historically low total seagrass extent of 1945. If the current rate of decline continues unabated, then local seagrass extinction may be a possibility sometime in the 2020's (extending the data-trend of Figure 3.19 to $y=0$), acknowledging that the full process and timeframe of local seagrass extinction is unknown and likely complex. However, the persistence of seagrass in some parts of the estuary, spanning all of 1945 to 2018 datasets suggests that seagrass loss may instead reach an equilibrium low-level with survival in areas less prone to sedimentation, followed by regrowth when conditions improve.

The 2017 and 2018 seagrass extents were captured by exhaustive systematic seagrass survey using high precision GNSS or GPS equipment. The other seagrass estimates in this time-series were based on seagrass capture data which had no assurance

of exhaustive detection. Some less conspicuous seagrass may have been missed. There was no ground-validation or other information available associated with these earlier datasets to indicate the density of seagrass below which seagrass is not detectable in the dataset, so these years' seagrass statistics may under-estimate total seagrass area. The occurrence of widely spanning featureless tonal gradients from high density to no seagrass, present in all of the image-sets, indicates that interpretation of seagrass from aerial photography has potential for misplacement of seagrass boundaries and error in area estimation. This deficiency justifies the research in subsequent chapters to integrate ground level survey, RPA based image capture (low altitude and spatial high resolution) and computer based feature extraction using derived information not readily visible to the observer.

Factors in the observed decline

The catchment of the estuary is large relative to its tidal water flow, compared to this ratio for other estuaries on the Coromandel Peninsula. The catchment has a high proportion of its area in forestry or agricultural land-use, and consequently is prone to high episodic sedimentation. Wharekawa Harbour has high intrinsic biodiversity and community value in the current day. There is no clear growth of mangroves on the estuary in the 1945 imagery, and there is a clear mangrove colonisation sequence from 1971 to the current day (Appendix 3.9.1 and 3.9.2). Graeme (1997) reported that there was a significant escalation of mangrove expansion in the decade leading up to the first major Wharekawa estuarine vegetation survey in 1997. Historical photography assessed in the current study is consistent with Graeme's report. The estuary is under pressure from sediment deposition originating from upstream land-use effects, in particular riparian erosion in grazing areas, and episodic sedimentation from forestry land-clearance. Although there are indications of sedimentation impacting the estuary visible in aerial photography and Google Earth time-series imagery, there is no data available to establish whether there has been recent change in the sediment heights on the estuary.

Wharekawa Harbour has been under pressure from sediment since before the earliest historical photography that was available, and seagrass has been present on the estuary in large meadows across all of this time. The 1945 imagery suggests that seagrass on the estuary was in recovery following significant loss. The pattern of seagrass distribution collated across the time-series supports an assumption that prior to native timber extraction there would likely have been substantial seagrass across much of the estuary. Parts of the estuary retained seagrass throughout all 73 years in the time-series. Nearly half of the current day extent was present ~ fifty years ago, during which there were 2-3 cycles of forestry harvest land-clearance within the catchment. These data indicate a degree of resilience in the seagrass metapopulation of Wharekawa Harbour

against the current rate of anthropogenic sedimentation arising from intensive land-use upstream. There has been some permanent loss of seagrass, some of which has been replaced by mangrove forest, but so far only a minor proportion compared to the total cumulative seagrass area mapped over the decades.

A substantial amount of the seagrass observed on Wharekawa Harbour during the 2017 and 2018 census surveys grew sparsely such that most of these scenes comprised sediment with scattered shell and/or detritus interspersed with the seagrass. Sparse seagrass with large mature leaves was highly visible at ground level. However sparse young seagrass (leaves presenting as fine short needles) was difficult to perceive even at ground level unless standing directly overhead. There are many locations where the transition from high to low visibility spans the seagrass patch or meadow. For the varying aerial or satellite image sensors there will likely be a detection limit beyond which seagrass cannot be accurately discerned from substrate. Without prior calibration of image-based seagrass extent mapping, there is potential for sparse seagrass to be missed, or patch-edges to be misinterpreted (e.g., Figure 3.22). These issues have been reported in the literature. Ismail 2001 encountered misclassification between medium and sparse classes of *Zostera muelleri*. Authors Lathrop et al. (2006) encountered omission of sparse seagrass beds due to confusion with substrate. Similarly, Pu et al. (2012) encountered misclassification between sparse seagrass and bottom substrate type. Baumstark et al. (2016) experienced poor classification of sparse seagrass due to lack of clear boundary with substrate, with some sparse seagrass remaining unmapped due to being smaller than their minimum mapping area.

It is therefore important to determine the detection characteristics for any sensor applied to seagrass mapping, to understand potential mapping uncertainty. In cases when the sensor is to be used in an automated image classification project, the detection limits also relate to image processing, derived layers included in the model, and the classification approach adopted. Calibration of the sensor's detection limits would therefore require the full image classification process-chain to be fitted concurrently. This requirement is addressed by subsequent chapters.

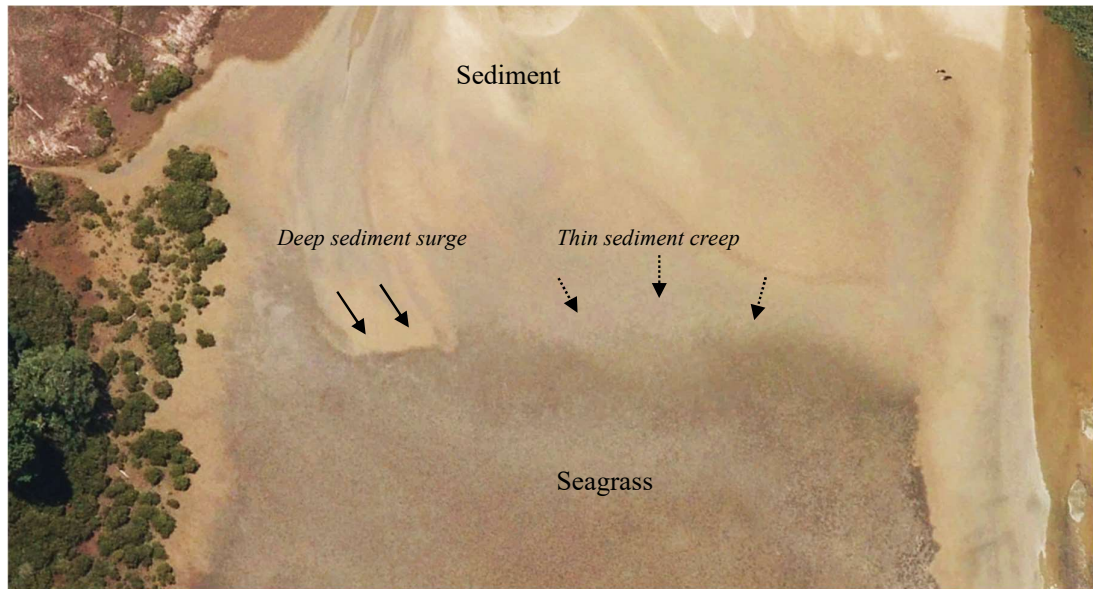


Figure 3.22. An example of a diffuse gradient between seagrass and sediment where true edge is difficult to establish and scale dependent. Image from Google Earth. Also see Figure 3.9.

3.8 Conclusion

Wharekawa Harbour provides a relevant site for the purpose of assembling and testing a seagrass feature extraction method. The estuary hosts a range of seagrass environments in confined areas, which is ideal for camera survey calibration under a limited scope and resourcing-level for ground validation. The estuary has a history of pressure from sedimentation with fluctuation in seagrass extent and distribution over the decades. Seagrass appears to be in decline based on analysis of available data and factoring the limitations of datasets captured under a range of methods.

At the time of the study Wharekawa Harbour was subject to a substantial period of rain that mobilised sediment creating areas of covering or complete burial of seagrass by sediment and detritus. This presented an uncommon opportunity to assess seagrass feature extraction amid potentially confounding factors.

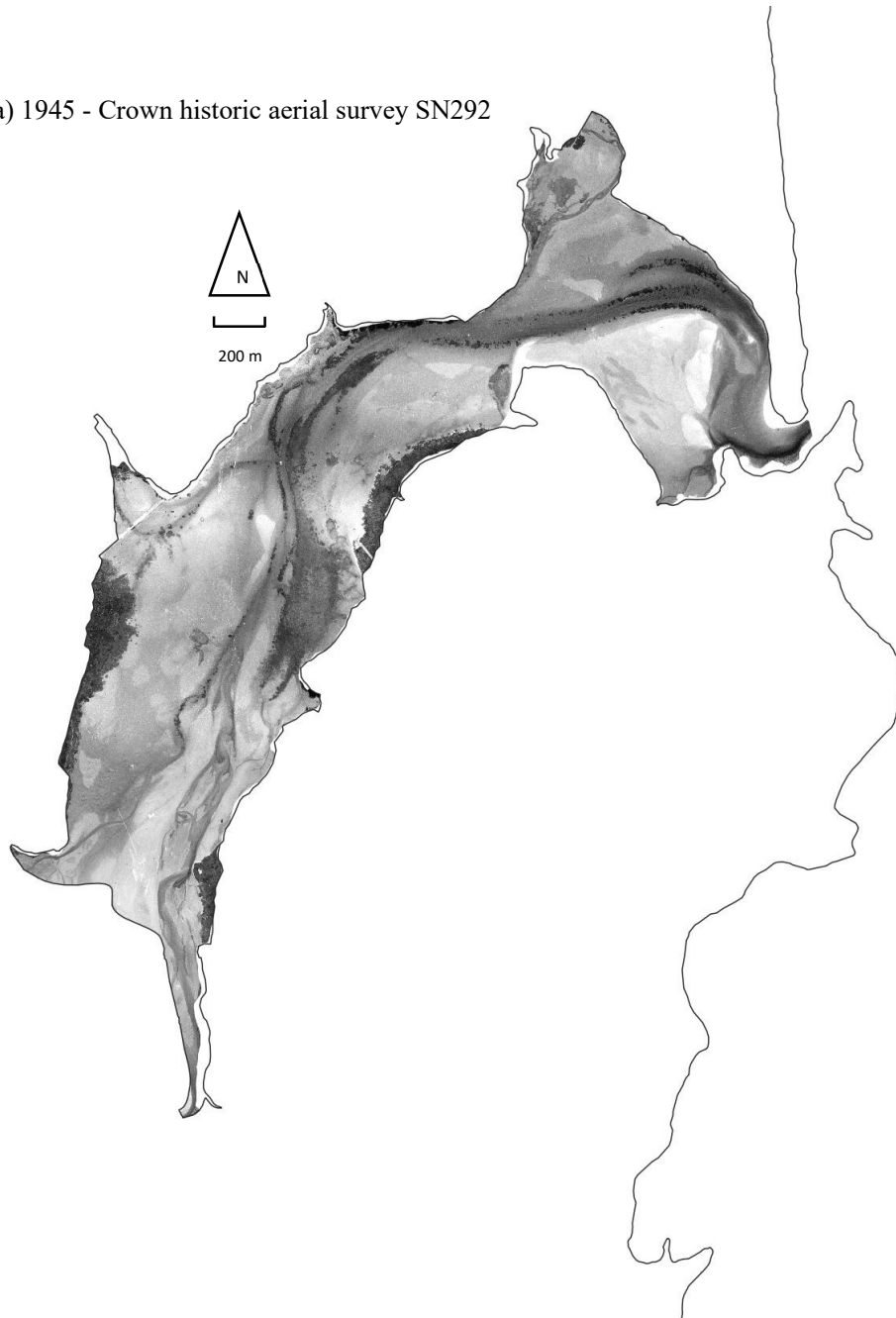
The process of mapping seagrass using aerial photography interpretation in this study highlights some key issues, that i) accurate seagrass-capture requires assessment of detection limits of the sensor and imagery; ii) accurate ground validation is required to know, at least some of the time, what low density seagrass looks like for low density patch-edges; and iii) that greater information is required than available in cartographic aerial imagery and using photo interpretation methods. Experiences during the mapping process in this chapter justify the research in the following chapters, to automate mapping

via computer learning techniques, using imagery with high spectral and spatial resolution and high precision ground referencing. As such, Chapter 4 provides classification of aerial imagery using a seagrass density-class structure that addresses some of these issues. The chapter also examines whether the state of residual water drainage during the ebb tidal phase, affects the performance of image classification.

3.9 Chapter appendices

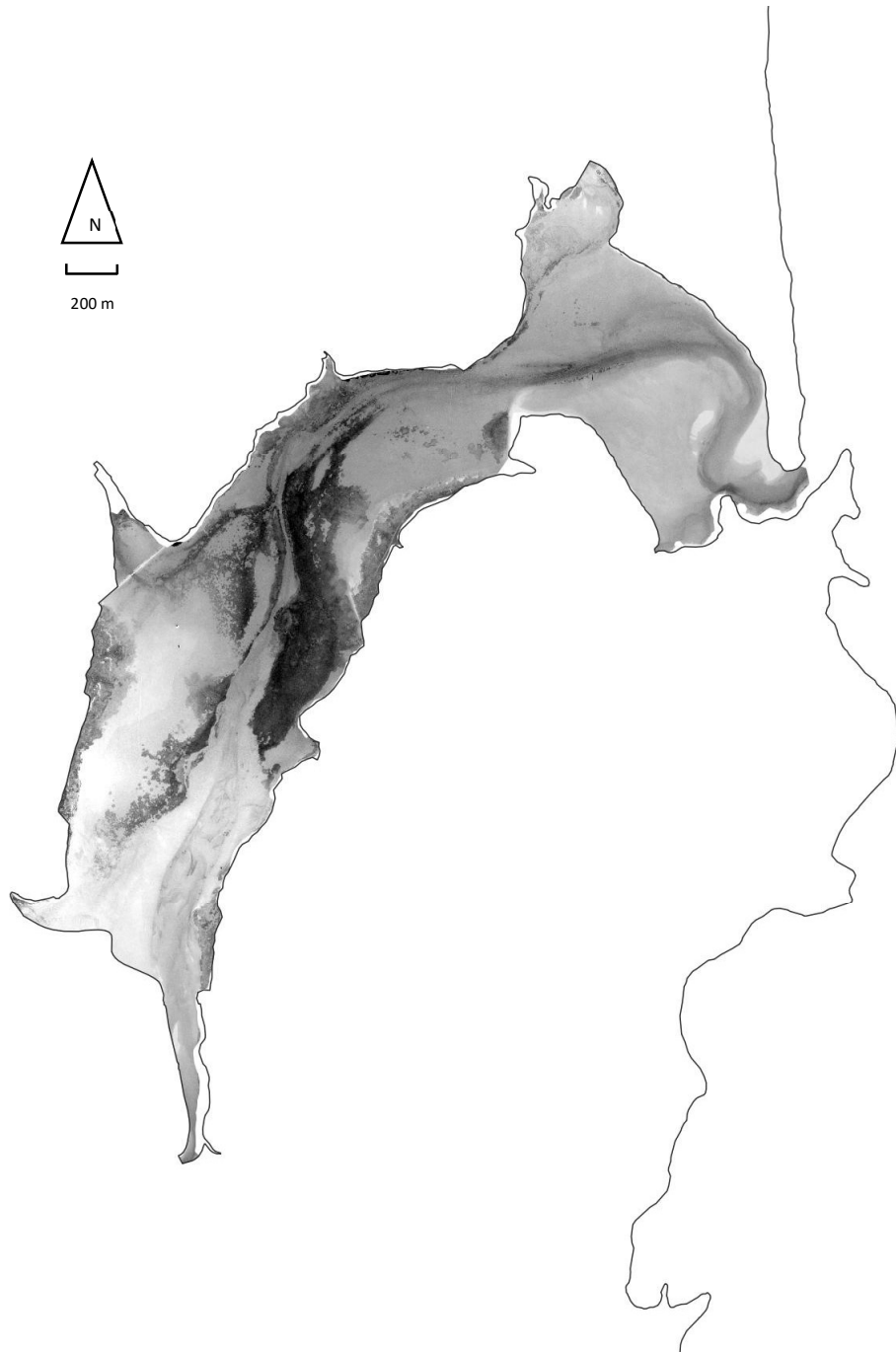
Appendix 3.9.1. Historical imagery clipped to estuary margin for 1945, 1954, 1959, 1966, 1971, and 1983 (a-f). Current-day coastline is provided for common reference.

a) 1945 - Crown historic aerial survey SN292



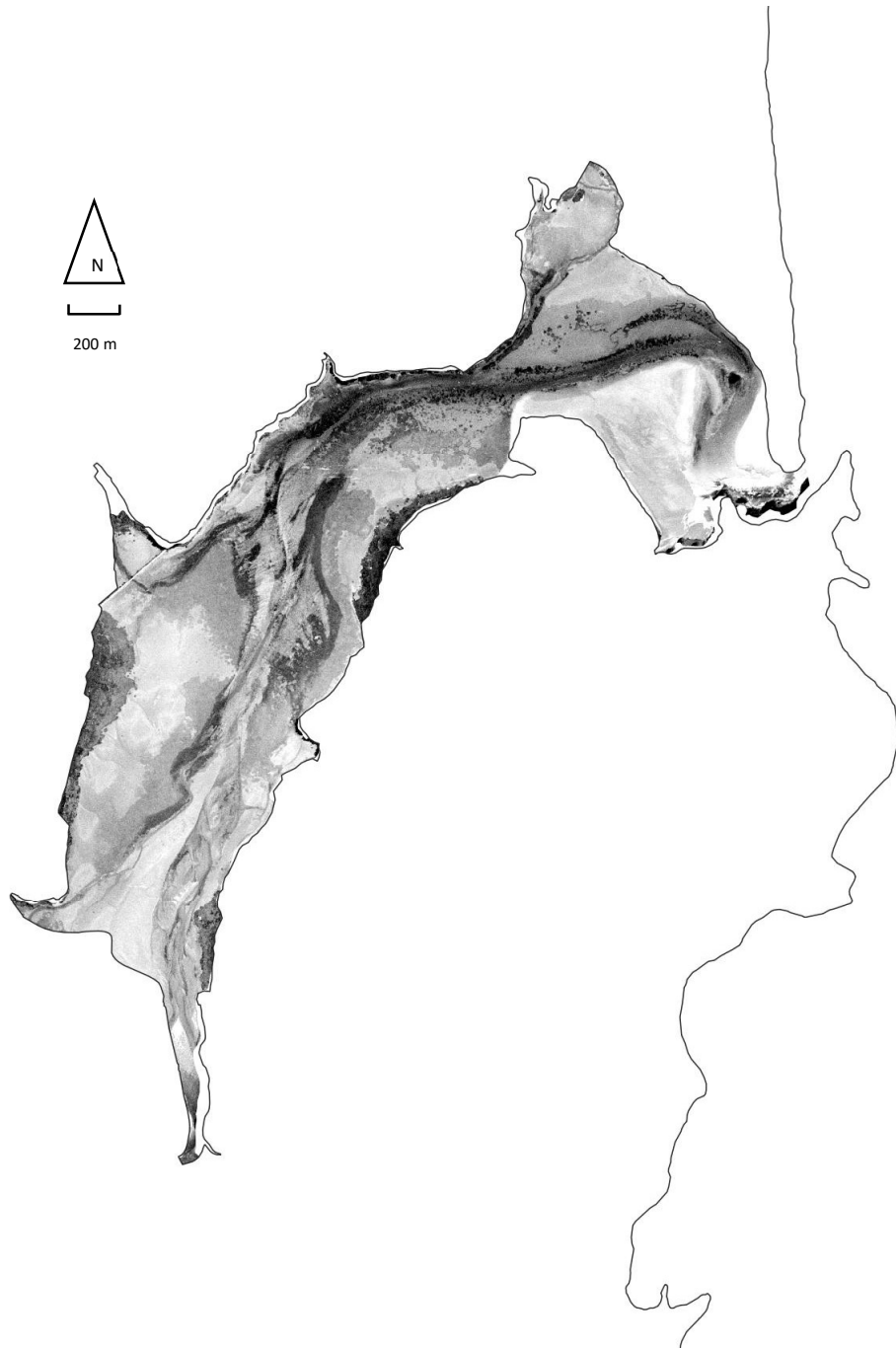
Appendix 3.9.1 ctd.

b) 1954 - Crown historic aerial survey S854



Appendix 3.9.1 ctd.

c) 1959 - Crown historic aerial survey S1210



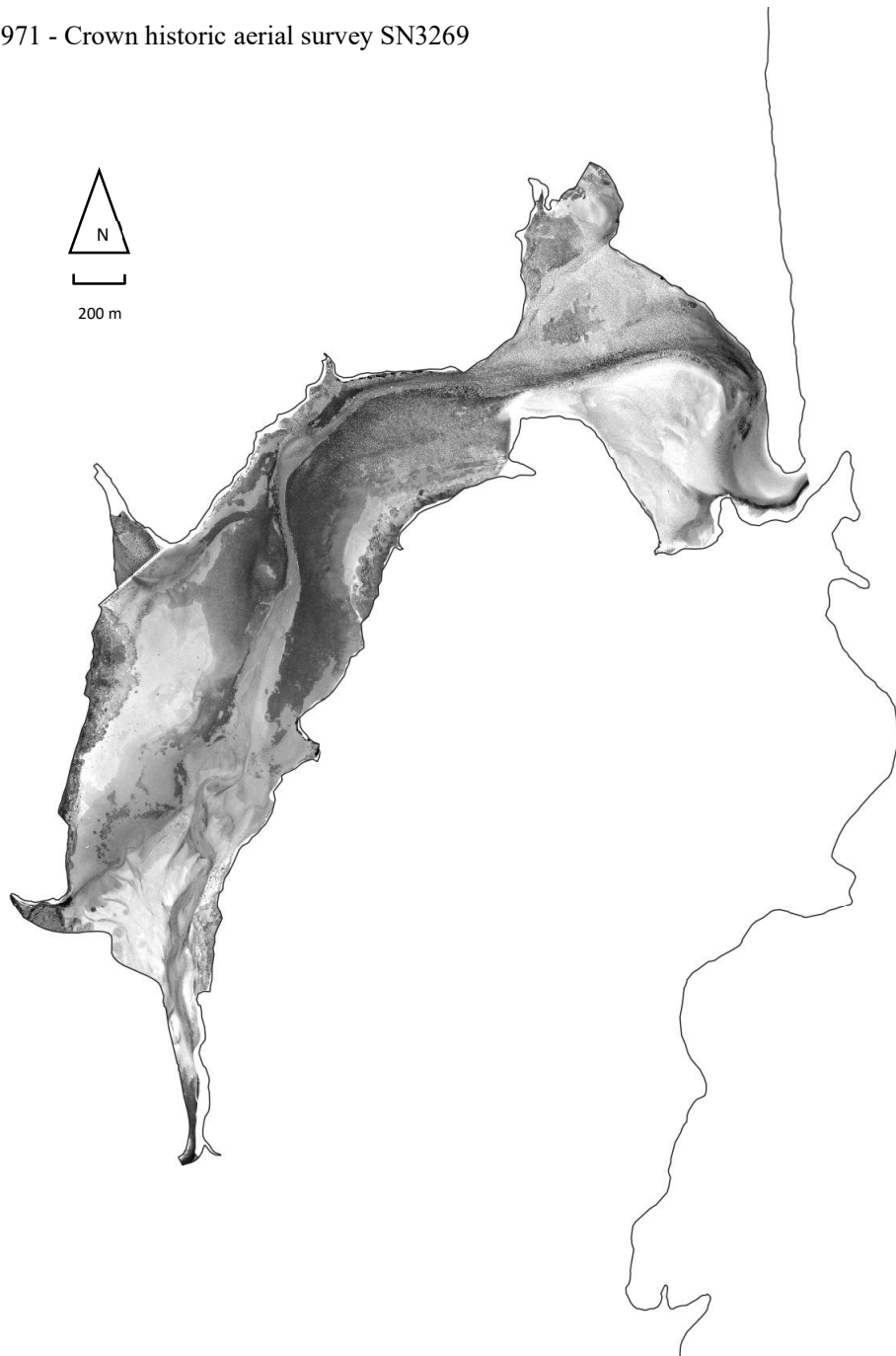
Appendix 3.9.1 ctd.

d) 1966 - Crown historic aerial survey S1894



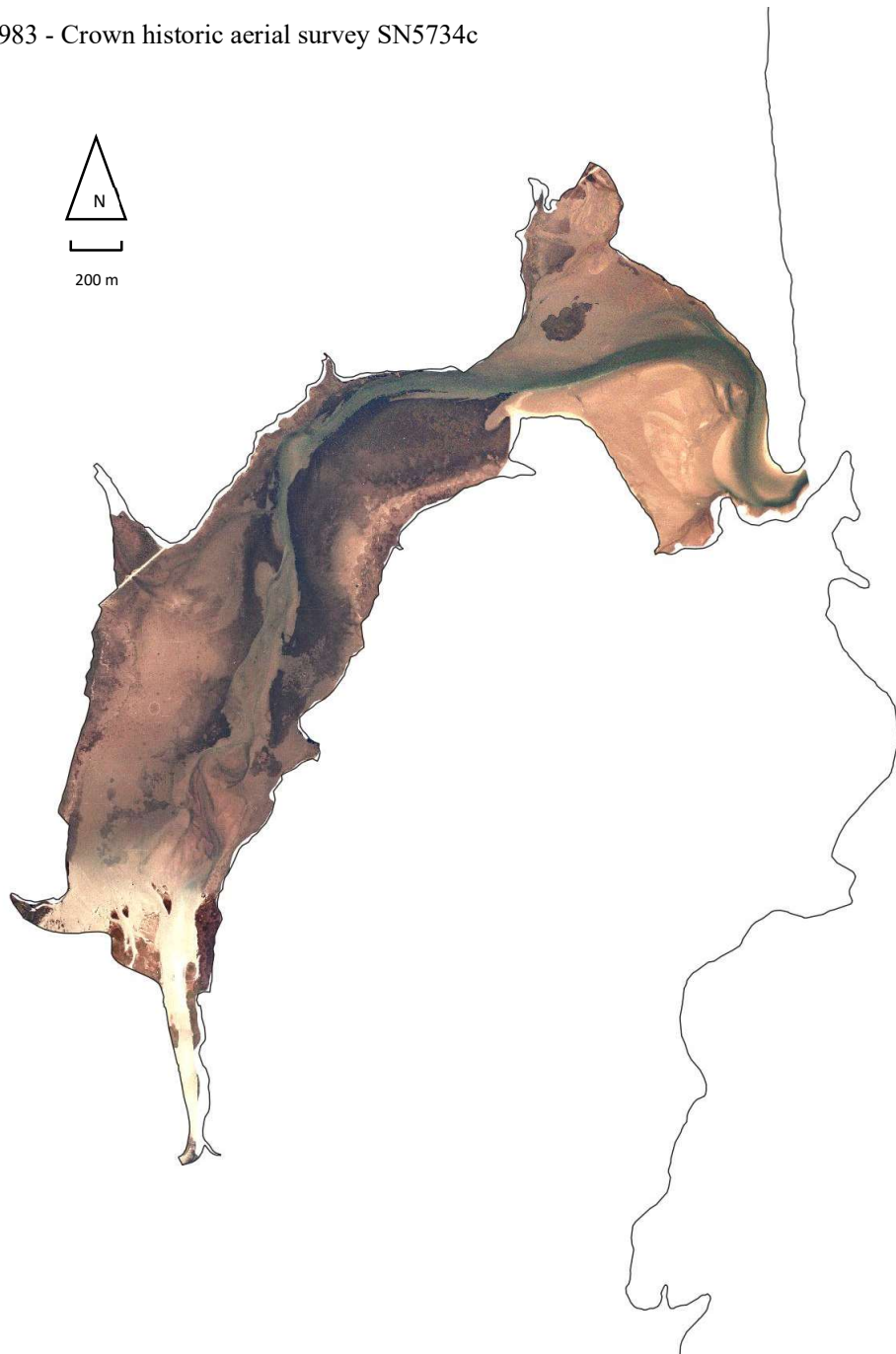
Appendix 3.9.1 ctd.

e) 1971 - Crown historic aerial survey SN3269

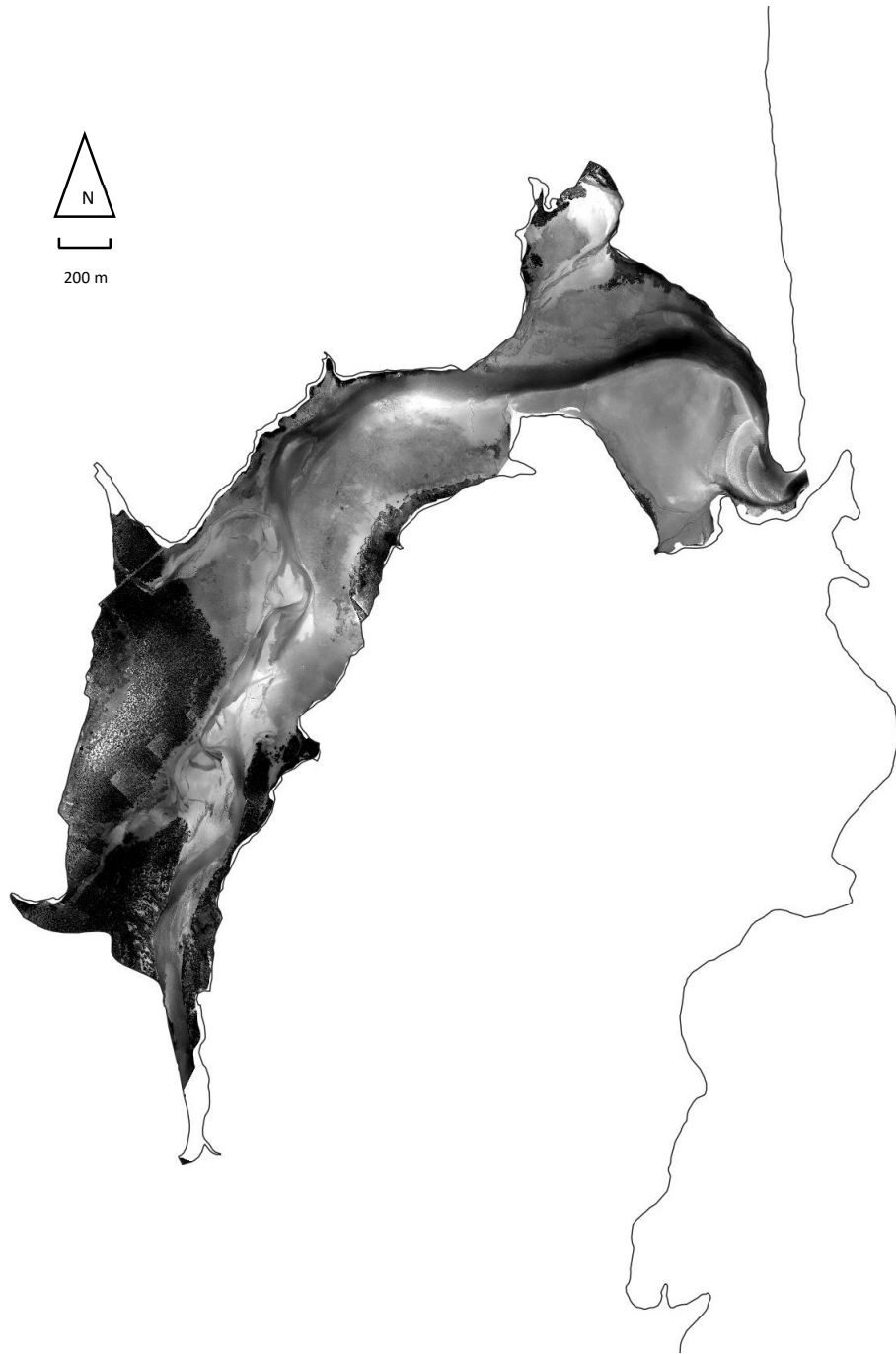


Appendix 3.9.1 ctd.

f) 1983 - Crown historic aerial survey SN5734c



3.9.1 Appendix 3.9.2. Aerial photography (2017) converted to greyscale for textural reference during photointerpretation of 1945 and 1971 imagery.



CHAPTER 4

Chapter 4. The influence of residual low-tide water on the ability to differentiate seagrass from associated scene content

4.1 Introduction

Seagrass is an important natural resource and component of coastal ecology (Chapter 1). Effective management of a seagrass resource requires monitoring methods that are accurate and cost-efficient - remote sensing has potential to provide such monitoring capability (Chapter 2). Seagrass condition can decline due to a variety of destructive or competitive pressures and on a range of timescales (Chapter 3).

4.1.1 Seagrass monitoring

Various methods have been applied to measure components of seagrass population status (e.g., Kirkman 1996; Wood and Lavery 2000; Short and Coles 2001; Marbà et al., 2013; Mejia et al., 2016). In some instances, seagrass condition has been inferred by monitoring meadow extent and change (e.g., Graeme 2008; Park 2016). Many of these methods involve manual inspection and collection of material at a seagrass site to generate detailed data for point locations, such as cores, quadrats and/or positions on transects (e.g., Burdick and Kendrick 2001; Fonseca et al., 2002; Turner and Schwartz 2006b; Dos Santos 2011; Neckles et al., 2012; Irving et al., 2013). Remote sensing methods can potentially reduce labour, with time-investment on the ground yielding greater survey extents than possible by manual mapping alone.

Remote sensing techniques have been applied to seagrass coverage analysis using imagery from both satellite and aircraft mounted sensors (Klemas 2013; Roelfsema et al., 2013; Pu et al., 2014; Barrell et al., 2015; Valle et al., 2015). Calculated contrast indices derived from empirical or standardised image spectral bands, can provide statistical predictors that enhance the information available compared to just the sensor bands (Tucker et al., 1985; Huete 1988). The Normalised Difference Vegetation Index (NDVI, Tucker 1979) correlates with biomass, chlorophyll, and other photosynthetic factors (Carlson and Ripley 1997; Xu et al., 2012; Kuzucu and Balcik 2017; Xue and Su 2017). The NVDI and similar vegetation indices enables seagrass biomass estimation (Bargain et al., 2012, 2013).

Remotely piloted aircraft (RPA) enable new survey options due to their ability to fly close to the ground at known heights, at controlled speeds and/or following

programmed flight paths under global positioning system (GPS) guidance (Chapter 2). This enables spatially explicit surveying in high detail that is ideally suited to estuarine process investigations (e.g., Jaud et al., 2016; Ventura et al., 2018). Integrating an RPA with a narrow-band spectral sensor enables optical measurement of the vegetation character and condition.

4.1.2 Survey over a drained estuary

Multispectral sensors small enough for practical deployment upon RPA are generally configured for terrestrial crop or landscape vegetation surveys (Raeva et al., 2018; Guan et al., 2019). Their application to marine vegetation species in a partially or fully submerged estuarine environment remains poorly understood. Solar light components are attenuated differentially by water, suspended particulate material, coloured dissolved organic matter (CDOM) and photosynthesising phytoplankton (Pegau et al., 1997; Fyfe 2003; Lesser and Mobley 2007; Dekker et al., 2011; Lu and Cho 2011; Cho et al., 2014; Hill et al., 2014; Röttgers et al., 2014; Shi and Wang 2014).

New multispectral RPA camera sensors require calibration for use on an estuary, to establish consistency in spectral measurement and associated feature extraction when seawater coverage or substrate wetness varies. Optical remote sensing over an estuary with the tide out may be spared much of the light attenuation by the water column when the tide is flooded. For example, Casal et al. (2012) found, using hyperspectral imaging of multiple macroalgal species, that the highest degree of spectral separability occurs at complete low tide and that spectral contrast decreased with increasing water depth. Lu and Cho (2011) found that correcting attenuation in the red-IR region of the spectrum in water depths of up to 40 cm, enabled increasing contrast against sediment and restoring NDVI values for seagrass mapping.

During a low tide event, substantial residual wetness and pooling can occur due to slow draining channels and saturated flats or closed depressions. Consequently, the surface reflectance of a drainage estuary may be variable. Literature measuring the attenuation of IR frequencies in shallow sea water (e.g., from 0-20 cm as might be found in an estuarine pool) was not available at this time. An approximation, the attenuation coefficient for light through seawater at 800 nm is given by Smith and Baker (1981), and a relationship described by Kirk (2010) (Equation 4.1). This indicates that the intensity of NIR light through residual water would be expected to drop by $\sim 1\% \text{ cm}^{-1}$ in clear sea water, equating to $\sim 18\%$ reduction at 20 cm depth in clear estuarine residual waters and increasing with turbidity.

$$D=0.4343ar \text{ (from Kirk 2010)}$$

(Equation 4.1)

Where D = absorbance, a = absorbance coefficient, r= water column depth

Aerial surveys for seagrass mapping have been conducted at low tide in New Zealand (Ismail 2001; Alexander et al., 2008). The local time of low tide in the upper reaches of the estuary may differ substantially from the gazetted time of low tide associated with the propagation and recession of the flood and ebb tides (e.g., Alexander et al., 2008). The degree to which low-tide residual waters might result in attenuation in the IR bands and complicate seagrass mapping remains largely unknown. In an estuary with the tide out, bulk water depth is eliminated but residual pooling and substrate-saturation has the potential to differentially absorb IR wavelengths and confound vegetation condition indices. This is particularly problematic with water in final stages of tide drainage, as well as in static pools or in the early stages of the return flood, which can retain suspended particles resulting in high turbidity.

In general, the intertidal seagrass species in NZ can be categorised as: i) small in observable structure; ii) present on the ground in both complex and uniform substrate environments; and iii) in scenes with highly variable non-seagrass organic content. This creates a challenge for extracting seagrass image features, that therefore requires both: a) high spatial resolution to quantify the geometry of seagrass objects in scenes with adjacent material or substrate; and b) high spectral resolution to distinguish mixed pixels containing seagrass from pixels that don't contain seagrass. The spatial and spectral resolution capabilities of imaging devices typically involve a specification trade-off, as both escalate data-traffic across a finite data bus and within the finite data-storage write-speed limits. Consequently, increasing spectral resolution demands a smaller sensor resolution, which inflates the number of overflight-passes to achieve ground coverage.

Analysis that is seasonally and/or tidally sensitive, may require specific scheduling of image capture, and will therefore be limited by satellite pass-over, or service availability when using commissioned air-charters. These scheduling requirements are compounded by weather for the optical imaging approach used here. Estuarine seagrass scenes can also be highly mobile, especially when high levels of floating wrack or detritus are present. This mobility together with spectral characteristics that vary between species and with meadow age (Dierssen et al., 2015; Tuominen and Lipping 2016), further confound classification. These factors therefore also imply that ground referencing (to support and test image classification) requires sampling that occurs very near in time to image capture, potentially within the same tide cycle or two (e.g., Alexander 2008). Thus, the complexity of tidal water pooling on outgoing and incoming tides may interfere with image capture and classification of intertidal seagrass condition.

This chapter describes preliminary research that aims to provide a first stage in disentangling the complex relationship between classification outcome and: i) variable scene content-mixing of the major ground cover groups (classified herein as seagrass, detritus, shell and sediment); ii) the role of spectral bands in predictability; and iii) drainage of residual low-tide wetness. It provides a foundational basis for the research chapters that follow.

4.1.3 Chapter objectives

This chapter aims to assess whether differentiation of seagrass from its surrounding substrate and other low-tide scene-content is affected by low tide drainage and residual pooling.

To achieve this, two specific objectives are addressed:

1. Quantify the effect of advancing residual water drainage on seagrass classification accuracy; and
2. Quantify consistency in predicted map outcome with residual water drainage.

The research context is limited to an autumn midday sun angle, with uniform overcast lighting conditions.

4.2 Method

4.2.1 Study Area

Research was conducted on Wharekawa Harbour, Coromandel Peninsula, on the New Zealand North Island (Lat. 37° 6' 30" S, Long, 175° 52' 51" E). Background and rationale for site selection is given in Chapter 3. Sampling occurred on a wide sand flat extending seawards into the sand/mud substrate (Figure 4.1). At time of sampling, this location was under pressure from sedimentation and accumulations of organic debris with tidal and river flows covering or eroding seagrass from both sides of the meadow (Figure 4.1d).

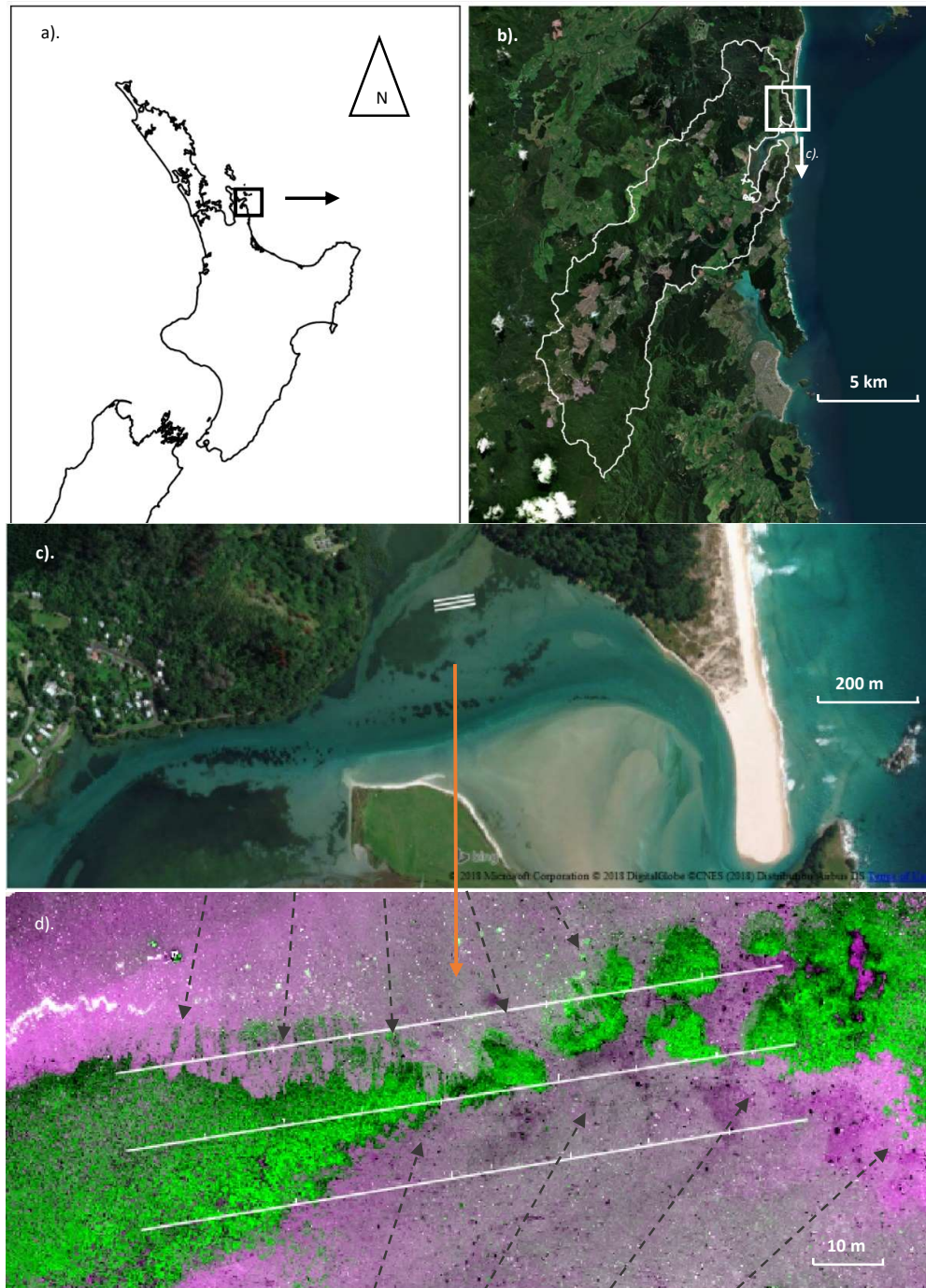


Figure 4.1. Layout of study area with respect to: a) North Island New Zealand location; b) catchment source area; c) main body of estuary; and d) the focal seagrass meadow (multi-spectral false-colour to contrast seagrass in bright green) - note incursion of sediment mass from river surge/deposit areas in d; dotted arrows).

The focal area of interest is a ~400 x 200 m subset of the northern arm of Wharekawa Harbour, comprising sand/mudflats with permanent pooling and drainage pathways of varying wetness at low tide, and a substantial seagrass meadow (~2.6 ha). Seagrass at this site varies in density from continuous dense coverage with no visible sediment, to sparse seagrass such that a nadir perspective is dominated by sediment between disparate plants, or dense seagrass coverage that appears sparse in a scene due to sediment burial. This focal area was selected due to the wide range of seagrass density levels, variable sediment incursion, and the high detritus content. The detritus predominantly comprised native broadleaf tree foliage, pine needles, sticks, wood fragments, and pinecones. The meadow was also covered in places with sparse or dense accretions of dead cockle shells. These meadow attributes were sought so as to make available, in one compact survey-scene, a diverse seagrass presentation with potentially confounding image classification factors.

4.2.2 Research approach and overview

This chapter's research addresses the postulation that the spectral character of a seagrass meadow changes during low-tide drainage and drying. A further postulation examined, is whether the classification outcome differs in wet compared to dry substrate. To achieve this, analyses of imagery from surveys taken above a seagrass scene at intervals during the timespan of low-tide water drainage occurred. As mentioned in Chapter 3, the execution of this survey was a reaction to the opportunity provided by the rain event 'Tasmin Tempest' which had a major impact on the site through the delivery of upstream forestry sediment and debris onto the site (Parker 2017; see Figures 3.6, 3.7). As a consequence, an abnormally diverse range of surface detritus content, shell exposure and partial burial of seagrass was available for assessing image analysis.

During the field survey (9 April 2017), three aerial photography flights were conducted using an RPA carrying a payload comprising an imaging sensor (four narrow multispectral bands and a conventional colour "scouting" camera sensor), synchronised on the same shutter control. The first flight started shortly after the bulk-water had cleared from a seagrass meadow (i.e., the seagrass meadow was largely exposed to air, but still saturated), the second flight one hour later, and the third flight aiming to coincide with the maximum drained state just before the incoming tidal flood (Table 4.1).

Three parallel transects, 85 m in length and spaced 10 m apart, were set out using fine white cord marked every 5 meters with tags visible in the imagery as a spatial reference for the RPA imagery and to highlight subsequent ground-photography photo-centres. Detailed ground-level photographs were acquired at each of the tagged marker

points and georeferenced to enable alignment to the RPA imagery in geographical information system (GIS) environment. Random points were set within each of these photographs and visually classified with a seagrass density class according to Table 4.2, as well as secondary ground attributes, then overlain onto the imagery to retrieve image values for each point location, and subsequently used to train a classification model. The same pixel locations were matched across image-sets such that the points contain repeat-measures on the same absolute locations. In this way, the change in spectral coordinates of sample points can be observed with respect to the changing wetness conditions. The specific workflow is summarised below (Figure 4.2). Change in classification outcome with wetness was also mapped, and the difference between prediction maps assessed.

Table 4.1. Timing of the three low-tide drainage states sampled in surveys conducted on 9 April 2018 (2 days prior to full moon / spring tide), at northern arm, Wharekawa Harbour. Published low tide was 11:25am (National Institute of Water and Atmospheric Research- tide forecast data). Time between first and last flight was 2 hours.

Flight	Flight start time	Time relative to gazetted low tide (11:25am) h:mm	Sun Angle*	Sun azimuth*	Tide state description
1	11:00	-0:25	42	27	Bulk tide cleared from meadow, exposed to air but all areas still highly wet and waterlogged; much of the seagrass sits underneath a meniscus of water; pools are full. Scene dominated by specular reflection.
2	12:01	+0:46	45	15	Much of previous waterlogging was largely drained but still glassy-wet appearance on seagrass areas, with mixture of moist and wet/saturated areas. Upper sandy areas drying, and lower sand still wet. Conditions are more like the early state than the late state.
<i>Ground photos</i>	<i>12:42</i>	<i>+1:17</i>	<i>45</i>	<i>352</i>	
3	13:01	1:36 (0:49)	45	345	The upper sandbank, emergent sand mounds and some mud now appearing near-dry (but moist to touch) with predominant diffuse reflection over non-pooled areas; most of seagrass meadow appearing moist-dry but well exposed from background which is still largely wet; many previously wet parts of pooled area are exposed and near-dry; many permanent pools or flow-constricted plains remain saturated or deep (e.g. up to 50 mm deep, and occasional stingray feeding holes up to ~ 200 mm depth).

* NOAA sun angle calculator - <https://www.esrl.noaa.gov/gmd/grad/solcalc/> ; Location centre 175.879717,37.108495.

Table 4.2. Classification variables and their definition based on content of each pixel selected by random sampling.

Attribute name	Code	Attribute	Definition	Indicators
Seagrass cover.	0	Absent.	No seagrass.	No seagrass leaves visible.
	1	Sparse.	Seagrass visible < 33% cover.	Visual estimate.
	2	Moderate.	33 to 67% cover.	Visual estimate.
	3	Dense.	67 to <100% cover.	Visual estimate.
	4	Only seagrass.	100%.	Only seagrass visible.
Seagrass hue.	1	Green.	Predominantly green leaves.	>67% of seagrass leaves green.
	2	Mixed.	Mixed.	Intermediate mix of leaf colours.
	3	Brown.	Predominantly red/brown leaves.	>67% of seagrass leaves red/brown.
Detritus cover.	0	Absent.	No detritus.	No detritus visible.
	1	Sparse.	Detritus visible <33%.	Visual estimate.
	2	Moderate.	33 to 67% cover.	Visual estimate.
	3	Dense.	67 to <100% cover.	Visual estimate.
	4	Only detritus.	100%.	Only detritus visible.
Shell cover.	0	Absent.	No shell.	No shell visible.
	1	Sparse.	Shell visible <33%.	Visual estimate.
	2	Moderate.	33 to 67% cover.	Visual estimate.
	3	Dense.	67 to <100% cover.	Visual estimate.
	4	Only shell.	100%.	Only shell visible.

(Table 4.2 ctd.)

Attribute name		Attribute	Definition	Indicators
Sediment cover.	0	Absent.	No sediment.	No sediment visible.
	1	Sparse.	Sediment visible <33%.	Visual estimate.
	2	Moderate.	33 to 67% cover.	Visual estimate.
	3	Dense.	67 to <100% cover.	Visual estimate.
	4	Only sediment.	100%.	Only sediment visible.
Sediment type.	0	Not applicable.	No sediment.	Class 0 in Sediment cover.
	1	Sand.	Predominantly sand surface.	Particulates visible, varied.
	2	Mud.	Predominantly mud surface.	Particulates not visible, uniform.
	3	Clay-silt.	Predominantly clay sit surface.	Orange fine covering over sediment.
	4	Gravel.	Predominantly gravel.	Large particles, small stones mainly.
Wetness at late drainage.	0	Well drained.	Dry appearance.	Diffusely reflective appearance.
	1	Wet.	Waterlogged.	Specular reflective appearance.
	2	Pool.	Underwater.	Water surface reflection, meniscus, emergent objects.

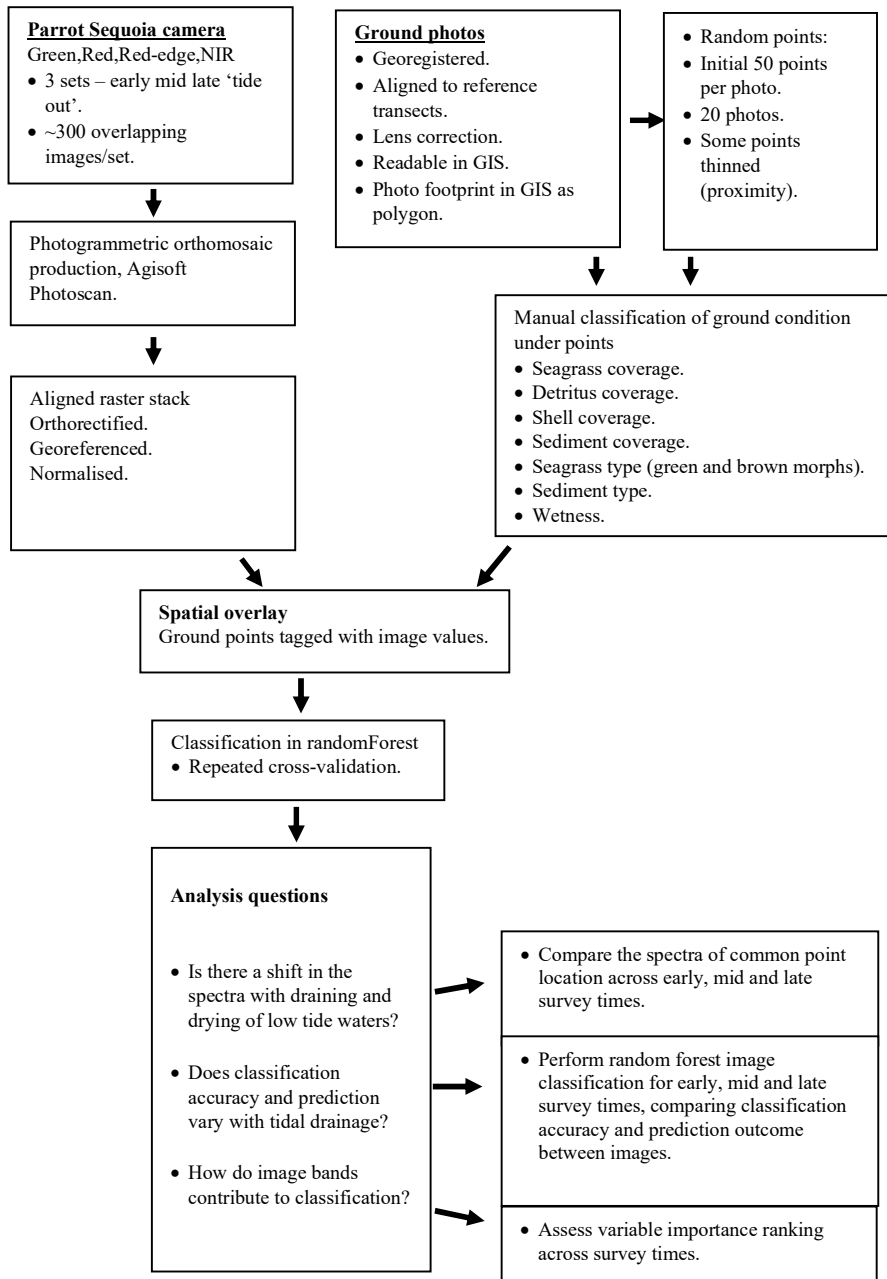


Figure 4.2. Processing flow for development of classification models and performance assessment relating to key research questions.

4.2.3 Aerial imagery capture

Imagery was collected using a Parrot Sequoia narrow-band multispectral camera (Appendix 4.6.1) mounted to an autonomous quadcopter (the RPA; 600 mm quadcopter with PX4 flight controller and multi-constellation GPS). The Sequoia comprises four independent 10-bit narrow band sensors as well as a conventional high-resolution camera (Table 4.3).

Table 4.3. Summary of camera specifications for the Parrot Sequoia imagery

Band	Band centre wavelength	Band width	Bit depth	Shutter	Field of view (w x h)	Resolution (MP)
Green.	550 nm.	40 nm.	10 bit.	Global.	62 x 49°	1.2
Red.	660 nm.	40 nm.	10 bit.	Global.	62 x 49°	1.2
Red-edge.	735 nm.	10 nm.	10 bit.	Global.	62 x 49°	1.2
Near IR.	790 nm.	40 nm.	10 bit.	Global.	62 x 49°	1.2
Colour (RGB).		Wide band.	3 x 8 bit.	Rolling.	64 x 50°	16

The RPA was programmed to follow a pre-set flight grid using Ardupilot Mission Planner software (<http://ardupilot.org>) (Figure 2.10). The survey comprised overlapping flight-swaths with the survey extent set to capture quality imagery 30 m beyond the ground sampling extent (i.e., the transects). This approach ensured contiguous imagery across all parts of the target area. All three replicate flights used the same flight program. The camera was fixed at the front-underside of the aircraft on vibration reduction grommets mounted on a short narrow boom (Figure 4.3). Flight speed was set to 5 ms⁻¹, swath spacing to 8 m and the image sampling rate equivalent to 8 m forward spacing. These parameters were maintained for each flight and equate to ~75-85% image overlap depending on GPS error and minor wind drift. Multispectral and conventional camera images were collected on the same camera trigger ensuring the same scene and flight conditions as a basis for direct comparison between cameras.

The time of day and month chosen for this flight was based on achieving capture when the low tide coincides with sun angles ~40-45° above the horizon. This coincides with the sampling occurring with the time of highest possible daily radiance incident on the scene (Robledo and Soler 2000), but not so much angle that direct sunlight reflection

from the wet sand/mud flat surface would contaminate the image. Early flight trials detected problematic reflection at $>45^\circ$ sun angle (pers. obs.).

The exact moment of low tide on an estuary depends on location on the estuary with respect to its microtopography (e.g., Alexander 2008), or relative to a local or nearby tide-gauge time-series average if available. For much of this estuary, drainage is continuous right up until the point that the return flood-line rolls over the relatively dry sediment. For the purpose of this study, the time of interest for survey was narrowed to ‘around low tide’, which includes the late stage of ebb and early-mid stage of tidal flow. This is generally described in the chapter as ‘low tide drainage state’, which varies between parts of the estuarine topographic structure at any one time.

RPA flight-path accuracy accrues a trade-off between maintaining airframe-heading, upright orientation and ensuring near-vertical downward) camera orientation. A vertically oriented camera gimbal was not an option due to air frame weight limits and because the downwelling sunlight sensor of the camera needed to remain in the same plane as the camera, which could not be attached to a gimbal with a clear view of the sky. Increased positional control confers an increase in automatic course and attitude adjustment. The flight controller was programmed with a 2 m positional tolerance with respect to the GPS-programmed flight plan. Absolute positional error was therefore a combination of three random factors: drift in the GPS solution, impact from light-moderate wind over the estuary and waypoint tolerance for reaching the target GPS coordinate. Consequently, 1-2 m of flight path variation was typically observed (up to 5 m with wind gusts). Wind speed was usually <5 kn with up to 10 kn occasional gusts.



Figure 4.3. Camera drone in flight over seagrass meadow; multispectral camera with downwelling sunlight sensor mounted at front.

4.2.4 Ground reference data collection

Spatial reference was provided across the scene by way of three 90 m transects (using a highly visible white 2 mm nylon cord) deployed on the ground and spaced at 10 m parallel separation and aligned to <100 mm deviation from dead-straight (Figure 4.4). Major markers were placed at 20 m intervals along the transect (white 20 mm diameter plastic pipes 1 m length), and minor markers (black zip ties) at 5 m increments alternating with the pipes (Figure 4.5). Transects were straightened on the ground such that the line of the cord was no more than ~0.1 m from the sightline between the transect end-pegs. The transects and markers were deployed to serve the following functions: i) to align the RPA imagery to a common extent and georeferencing for analysis in a GIS environment; ii) to allow the inherent error to be quantified within the imagery that results from the drones onboard GPS; iii) to provide a spatial reference frame for photo observations taken at ground level to identify ground features with accurate position relative to the common reference frame; and iv) to observe linear dimensional distortion manifest in the resulting photogrammetric mosaic images.

Transect end points were spatially positioned by track using a Garmin GPS65 global positioning (GPS) receiver set to record locations every two seconds for a 20-minute period at each peg. Track points were averaged, excluding outliers, in a GIS environment.

Ground observations were recorded by standardised photo capture using a Nikon S9500 with GPS geotagging enabled. Nadir-oriented images were taken at a consistent height above a 1 m visual reference marker (white tube) placed on the ground, with photos centred on the mid-point of where the transect cord and white marker cross, and with orientation set on the bearing of the transect. Images were corrected for lens distortion (Agisoft 'lens' application) then affine transformed and georeferenced from GPS data, bearing and the pixel ground sampling distance of the corrected images.



Figure 4.4. Seagrass on the study area (overcast sky conditions), 9 April 2017, showing transect and marker layout.

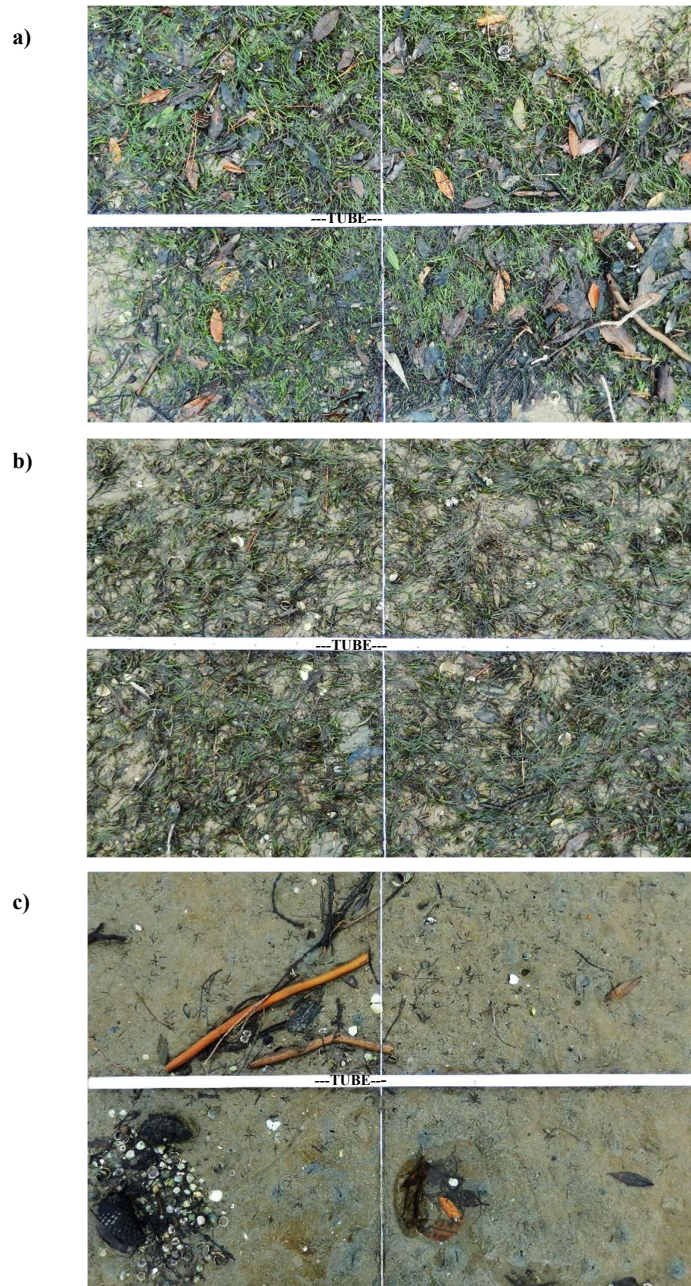


Figure 4.5. Example of nadir ground photography showing 1 m wide reference tube and transect line for: a) high density green seagrass with detritus (leaves and stick); b) medium density seagrass (green + brown mix) with detritus (fine stick, needle and wood fragment); and c) a sediment scene (mud with clay-silt) with detritus and shell, no seagrass.

Twenty randomly positioned points were selected within each of 50 corrected ground images (“random points within polygon” function, with the QGIS 2.18 software), with points less than 2-pixel separation distance removed, totalling 981 points across the

entire (n = 49) available photo set. Point locations were inspected on the RGB images and scored for a range of attributes quantifying seagrass density, detritus content, sediment content and type, and visible pooling (Table 4.2).

Seagrass density was scored using a modified Braun Blanquet (BB) coverage scale (Braun-Blanquet 1965) that was assessed at a coarser class-division. The five-tier scale of the BB system was replaced with a coarser three-tier scale due to earlier testing of observer consistency during method development. This indicated that five levels were unreliable for this pixel scale judgement but was consistent when simplified to three levels. Coverage was assessed at the pixel scale, as a component of the greater scene (rather at the full quadrat scale of the BB system). The scale applied (three tiers, plus special attention to the extremes) was according to the follow list: 0 (absent); 1 (sparse, less than 33% coverage); 2 (moderate, 33-66% coverage); 3 (dense, >66% coverage); and 4 (complete, 100% coverage).

Values 0 and 4 were recorded as extreme cases of 1 and 3 to observe pure and absent pixel locations (Table 4.2). Class 4 was merged into class 3 for the classification analysis.

Detritus and sediment pixel-content were quantified on the same coverage scale. Sediment type was classified nominally by surface appearance (sand, mud, silt, gravel) as a substrate background to vegetative ground cover (no relation to subsurface sediment is implied). Pooling of water was quantified as being present/absent for a target pixel by close inspection of specular versus diffuse reflection patterns and meniscus visible in the ground photography.

True seagrass location across the whole site was spatially quantified as per the workflow in Chapter 3 (refer to 3.5.2). This provides a distinction between areas containing seagrass (at one of the three density levels tested) and areas verified as having no seagrass present.

4.2.5 Photogrammetry and data compilation

Multispectral and conventional camera image-sets collected during RPA sorties were orthorectified using Agisoft Photoscan Pro 1.4 (<http://www.agisoft.com>) using the normal program workflow (Table 4.4).

Table 4.4. Orthomosaic production steps using the Agisoft Photoscan normal workflow.

Production step.	Description.	Parameters.
Align photos.	Coarse alignment of the overlapping images by way of triangulation of common features found in the images.	Align photo accuracy = 'highest'.
Dense point cloud.	Pixel depth estimation and reconstruction of 3D point cloud scene.	Quality = 'ultra-high'; depth filtering = 'moderate'; calculate point colours = 'yes'.
Triangulated mesh.	Tessellation of the point cloud and reconstruction of polygonal surface model.	param. surface type = 'height field'; source data = 'dense cloud'; face count = 'high'; interpolation = 'enabled'; calc. vertex colours = 'yes'.
Surface texture.	Calculation of colour of faces of the triangulated mesh model.	Mapping mode = 'orthophoto'; blending mode = 'mosaic'; texture count = '8192'; enable hole filling = 'yes'.
Orthomosaic.	Orthorectification and mosaicking of component images into single-image product in orthographic projection under geographic coordinate system.	Surface = 'mesh'; blending mode = 'mosaic'; pixel size = default estimate.

Single image mosaics for the three tide-stages were clipped to a 20 m buffer around the transect extent and georeferenced to each other in a GIS software environment to within one or two pixels of separation. The normalised difference vegetation index (NDVI) was calculated from red (R) and near-infra-red (NIR) bands using Equation 4.2 (Tucker 1979). All image bands were then normalised to a scale of 0 to 1 using Equation 4.3.

$$\text{NDVI} = (\text{NIR}-\text{R})/(\text{NIR}+\text{R}) \quad (\text{Equation 4.2})$$

$$\text{Normalise}(x) = (x - x_{\min}) / (x_{\max} - x_{\min}) \quad (\text{Equation 4.3})$$

where x is the pixel value, x_{\max} and x_{\min} are image maximum and minimum values.

Some random sampling points were manually moved by one or two pixels in distance to ensure the exact pixel locations remain matched across all three (early, mid, late) tidal drainage images (there was minor distortion of the multispectral images at pixel-scale that required correction in places). Effectively the point-locations were consistently placed upon the same material object across the three survey times. Sun angle spanned a 3-degree range across the time of surveys, and cloud cover was consistently overcast.

The spatial point dataset containing ground classification attributes for the 49 reference quadrats, were spatially overlain upon the respective early, mid and late survey images, with corresponding band numbers retrieved as new dataset attributes. Image classification was based on the contents of this analysis dataset. These 981 points were limited in location to the photo reference sites positioned on the three transects. A further 1000 fixed location points were randomly deployed across the greater scene out to 20 m maximum distance from the transects creating second analysis dataset for assessment of spectral shift.

4.2.6 Spectral shift across the tidal sequence

Change in the spectra of objects within the aerial survey scene were measured by determining fixed reference points and calculating change in spectra at those points over time. The difference in image number between survey times was calculated per ground sampling point, allowing comparison on early-late and mid-late spectral and classification change. Seagrass extents captured by precision GNSS survey near to the time of the survey-day (refer to Chapter 3 for details) provided a spatial reference for coarse seagrass presence and absence and for classifying points as being within seagrass areas or on ground explicitly devoid of seagrass. This distinction was used to compare spectral change with time, inside and outside of the seagrass patches. Overall consistency in spectra was measured by applying Pearson's correlation to pairs of image values (early to late and mid to late).

A subset of the photo reference data was additionally filtered to select points of high density for seagrass, detritus, shell and sediment sets, eliminating sparse or highly

mixed classes for this particular analysis. This was used to compare spectral shift per ground-class for moderately pure signals.

The flights were made across a short total timeframe spanning midday with respect to sun movement, with only minor sun-angle variation across the timeframe of survey. Likewise, the uniform, thinly overcast cloud conditions appeared constant during the survey. However, there was no measure of absolute solar (diffuse) brightness at the image-band wavelengths available on site during the survey. Consequently, a radiometrically corrected or controlled measure of spectral change with respect to residual drainage and drying was not possible.

4.2.7 Change in classification outcome with tidal drainage

The three mosaic images were classified using a common ground-observation point dataset, to train a classifier using the randomForest algorithm within the *rminer* data mining package (R-Project 3.5). The model was constructed with a 100-repetition 5-fold cross validation, and tuning parameters set in the range $mtry = (3,4,5)$ and $ntree = (800, 1000, 1200)$. Classification accuracy statistics (overall, and per class) were collated for each cross-validation iteration and image-set, and mean classification per tide-stage calculated. Variable importance was extracted from the model using the importance function of randomForest (accessed via the *rminer* interface) under 1-D sensitivity analysis setting with absolute deviation from model median as importance metric.

Consistency in classification with advancing low-tide drainage state was assessed for the 1000-point dataset across the full image extent as these were independent from data used to train the model. Agreement in classification response was calculated with respect to i) class attribution; and ii) whether seagrass was present/absent.

The agreement of predicted classification response was further examined at a greater aggregated scale. Square tile grids were constructed (0.5 x 0.5 m and 1 x 1 m tile size). The area of seagrass per seagrass-class was calculated per tile. Correlation in these tile-area sums between survey times, early to late and mid to late, were calculated as a measure of agreement at these summary scales.

4.2.8 Comparison of multispectral and scouting cameras

The Parrot Sequoia camera includes a 16 MP red-green-blue conventional ‘scouting’ camera model mounted alongside of the four 1.2 megapixel narrow-band multispectral camera modules, and is actuated under the same trigger event whereby the cameras sample the same survey-space. However, in addition to the band differences

between cameras, the multispectral camera operates on a global shutter (i.e., instant capture of sensor lines at once) as compared to the scouting camera on a rolling shutter (sequential capture of sensor lines). In low light levels image error artefacts can arise under a rolling shutter during RPA flight across a scene (less so in bright sun light). The RPA surveys in this study were conducted in overcast conditions, so the rolling shutter had significance. When considered at the same spatial resolution, the multispectral camera should yield higher classification performance than the scouting camera due to the narrow spectral bands and global shutter. However, the scouting camera operates with significantly higher resolution than the multispectral modules which may confer advantage in detecting and classifying seagrass structure. This section tests the assumption that the multispectral camera provides classification benefit over a conventional camera sensor.

The random forest classification procedure above was replicated using imagery derived from the red-green-blue scouting camera captured concurrently to the multispectral imagery. The image-set captured during flight was rendered into a single orthorectified mosaic using Agisoft Photoscan following the previous procedure. The resulting image was georeferenced to objects visible in the multispectral image so that the images were in alignment, and both multispectral and scouting camera images were in alignment with the ground-level photography.

The ground sampling points used for the multispectral classification were also used to train and test the scouting camera image under random 5-fold cross-validation. The random forest model structure was matched between cameras with the exception that the model predictors differed due to the difference in source bands: - normalised green, red, red-edge, NIR and NDVI for the multispectral camera and normalised red-green-blue for the scouting camera. Calculation of NDVI for the scouting camera was not possible due to there being no NIR band.

4.3 Results

4.3.1 General observations

Seagrass at this site typically comprised uniform seagrass patches, or sand/mud areas with seagrass spreading from the 'bare' patches (Figure 4.5). Many seagrass patches, either existing or recently degraded, had raised firm, often dense edges compared to the patch-centres (Figure 4.6). Seagrass density ranged in character from thick mats comprised entirely of 'long-leaved' seagrass, to solitary needle-like leaves emerging from sediment, often difficult to see by eye unless crouching low directly above the substrate.

There were distinct green and brown colour variants of the seagrasses. At the location of the transects, green and brown seagrass were distinct but difficult to demarcate exactly. In other parts of the estuary, the green/brown patterning occurred in clearly definable patches which in places blended like a Euler diagram, suggesting there may be distinct morphs of the seagrass growing radially into neighbouring patches (Figure 4.6). Detritus was commonly associated with seagrass and appeared upon inspection to be caught-up or associated with the surface textural roughness of the seagrass at prominent patch-edges or deposited in small blow-out pools within the seagrass extent. Some detritus was present away from the meadow, accumulated in stingray feeding holes up to 20 cm deep.

In general, there was clear spectral separation of the seagrass from its sediment background (Figure 4.7). However, the spectral range of shell and detritus content overlapped with that of seagrass and sediment (Figure 4.7). This indicates that in mixed seagrass/shell/detritus scenes there may be some confusion of image classification without additional predictor information to contrast the classes.



Figure 4.6. Apparent radial growth pattern of seagrass expansion as seen by drone at 60 m meters above ground level (exaggerated contrast applied). Aerial imagery captured April 26 2017 in sunny cloudless conditions.

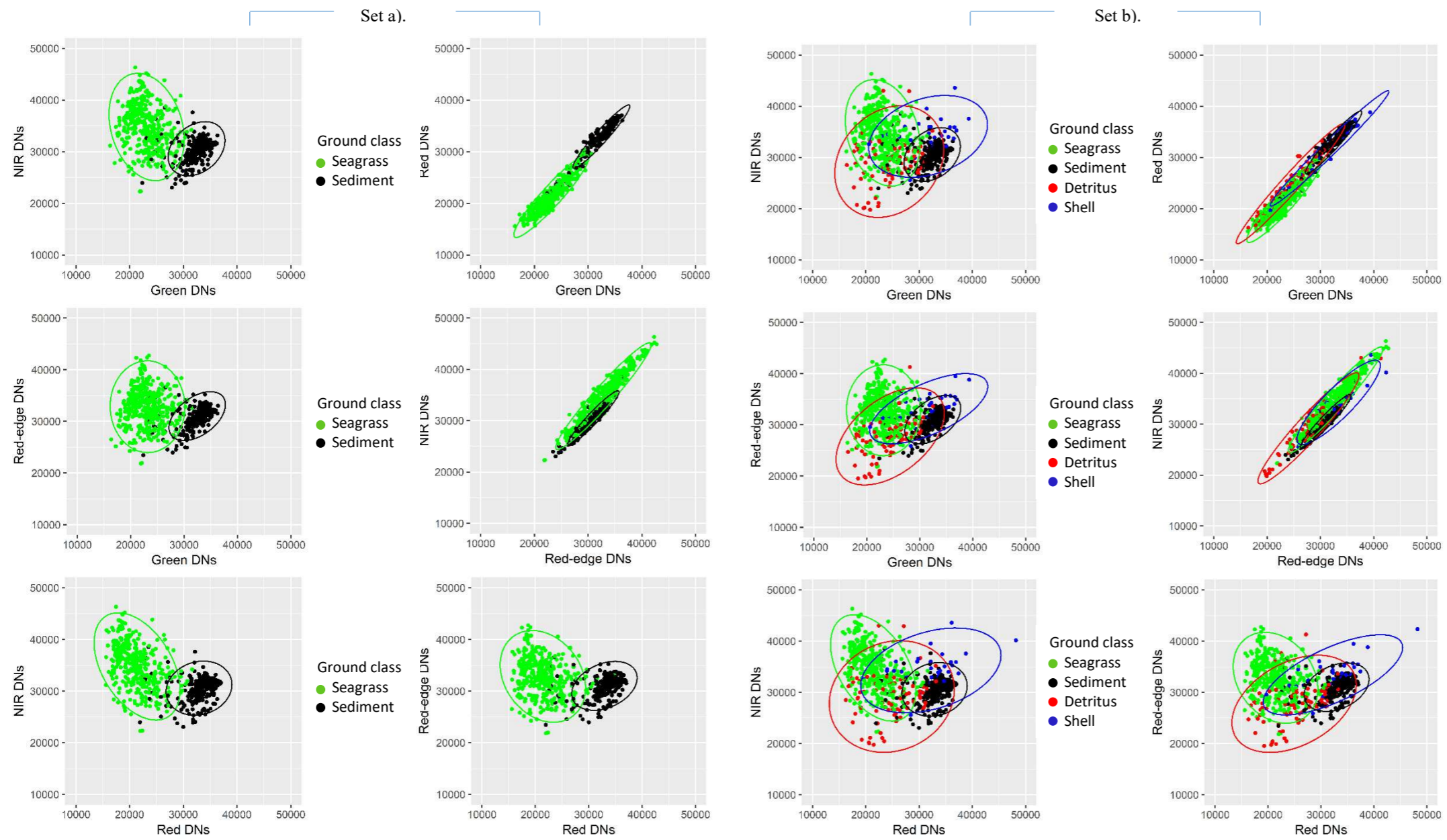


Figure 4.7. Spectral coordinate plot of raw image digital numbers in pairwise combinations of image bands for: a) seagrass and sediment; and b) seagrass, sediment, detritus and shell content. Ellipses show 95% quantile estimates.

4.3.2 Spectral shift across the tidal sequence

Spectral shift was calculated as late-minus-early or late-minus-mid survey image band values, where a negative number corresponds to reduced image intensity with advancing drainage state (Figures 4.8 and 4.9).

In most cases objects became darker in the four camera bands within the measured seagrass areas, as compared to outside of the seagrass area for which the camera bands were closer to remaining constant (Figure 4.8). Overall dimming across the camera bands reduced with time across the material types (Figure 4.9). Cloud cover appeared to remain the same during the time spanning the survey sequence. However, absolute solar irradiance wasn't measured on site, so change in cloud condition can't be eliminated as a factor in the observed change in image values with time. There was also change in sun aspect during the timeframe spanning the surveys (Table 4.1). The general reduction in image intensity across time may be due to subtle cloud thickening or change in aspect.

However, several observations have relevance to the task of seagrass feature extraction. There was negligible change in NDVI values with changing drainage when comparing between inside and outside of the measured seagrass extents (Figure 4.8). Across the material types (Figure 4.9) NDVI, values were closer to remaining constant (i.e., nearer to zero spectral shift) than the four camera bands. These observations indicate the stability of NDVI with changing conditions. The NDVI values for seagrass, both exposed and in pools, increased with time (i.e., positive shift). This indicates possible enhanced feature contrast with drainage and drying whereby seagrass becomes brighter compared to the surrounding materials.

The change in intensity levels were minor with respect to total intensity (Figure 4.10). The variation in mean spectral band intensity was in the range of 2-5% for the four camera bands, and close to zero change overall for the NDVI band. In all four camera bands there was high correlation in image-value across drainage states for the reference objects for all the bands and ground-cover types, except in the case of sediment, for which there was lesser correlation in the green and red bands (Table 4.5). Pooling reduced the correlation between the images of early and late low-tide drainage state, compared to exposed substrate that drained and dried with time (Table 4.5).

The following section assesses the consistency of classification outcome with time. This assessment is made in the context of the above 2-5% shift in spectra between the early and late surveys.

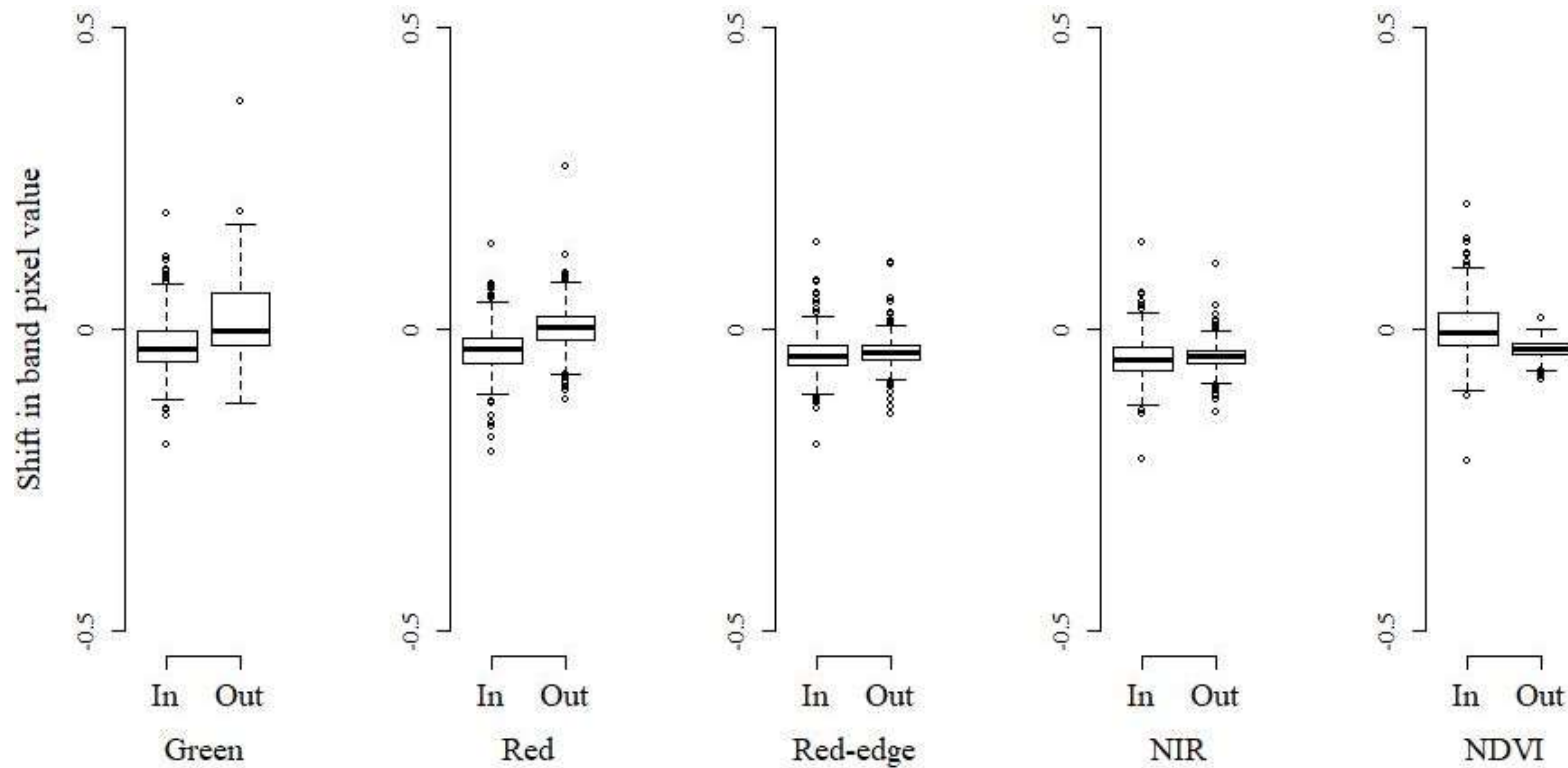


Figure 4.8 Spectral shift in normalised image value within each band (units of reflectance in range 0-1), after advancing from the earliest to latest (driest) low-tide drainage state, and grouped by whether the points are inside or outside of the GNSS-surveyed seagrass extent; n=1000 random points. A negative value indicates that the image-value is brighter earlier in the timeframe of low-tide water drainage.

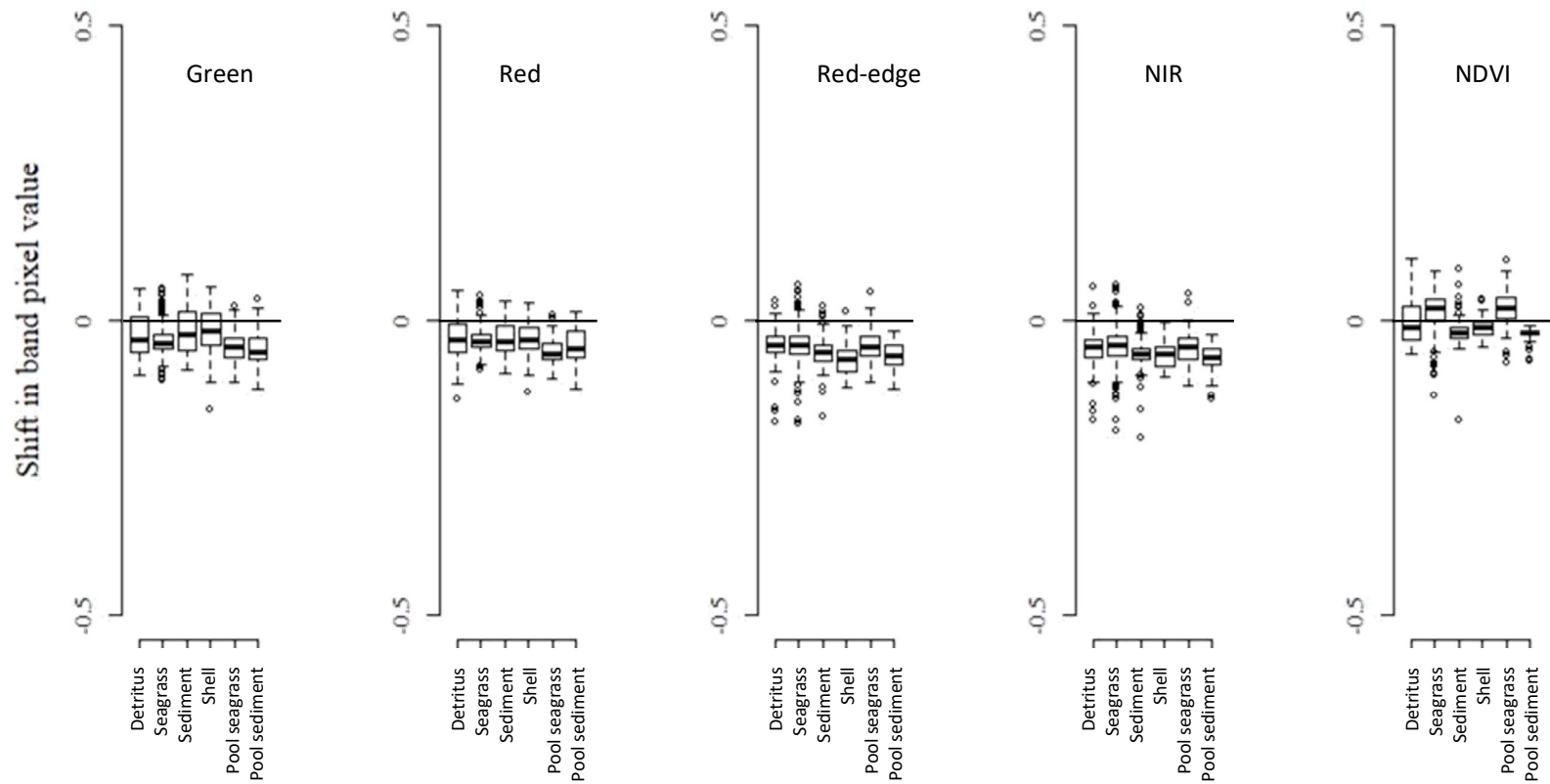


Figure 4.9. Spectral shift in normalised image value within each band (units of reflectance in range 0-1), when advancing from the earliest to latest (driest) low-tide drainage state and grouped by ground cover class. A negative value indicates a higher image-value earlier. The box-and-whisker plot indicates median value (centre line), interquartile range (box), 1.5x the interquartile range (the whisker), and outliers (circles).

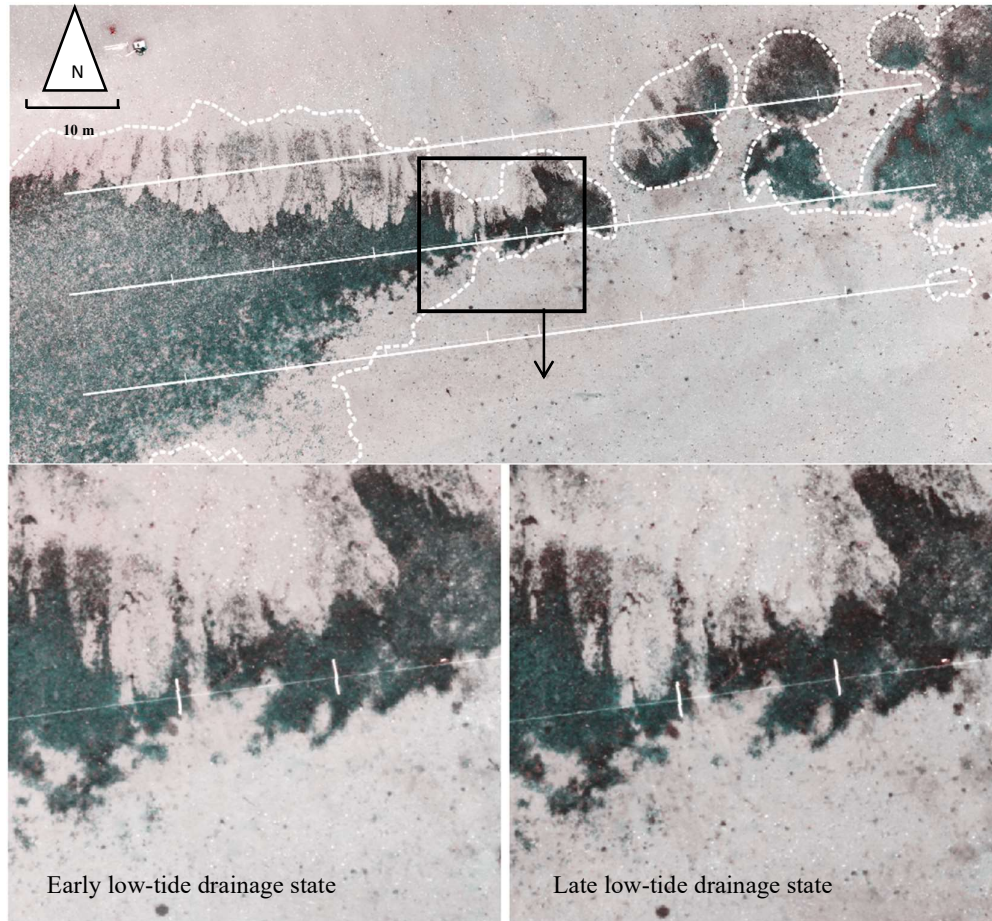


Figure 4.10. Spectral shift with changing low-tide drainage state (in pseudo colour of multispectral image bands). Transect positions (solid white lines) and GNSS-measured seagrass meadow boundaries (dotted white lines).

Table 4.5. Correlation by image band between the image numbers going from early to late low-tide drainage states for each ground cover group (n=804).

Set	Green	Red	Red-edge	NIR	NDVI
Seagrass.	0.87	0.94	0.91	0.93	0.96
Seagrass in pool.	0.78	0.88	0.91	0.89	0.93
Detritus.	0.88	0.93	0.90	0.92	0.96
Shell.	0.89	0.95	0.90	0.93	0.97
Sediment.	0.69	0.88	0.83	0.86	0.92
Sediment in pool.	0.52	0.58	0.80	0.81	0.96

4.3.3 Change in classification outcome with tidal drainage

In terms of extracting the seagrass feature from the imagery, an important measure of performance is whether the images can consistently be classified into target ground classes with a similar level of accuracy and class attribution. The classification accuracy results for the three drainage states were within 1% accuracy variation, for the overall accuracy (Figure 4.11a), and accuracy by seagrass class in terms of the classification sensitivity (true positive rate) and specificity (true negative rates) based on random forest model classification metrics (Figure 4.11b). The model was effective in detecting high density seagrass and establishing the absence of seagrass. Classification sensitivity was poor for the mid-density seagrass classes. Classification specificity was high for all classes indicating that seagrass presence is distinct from seagrass absence, and the individual class error-rates likely relate to misclassification between the seagrass classes.

These results relate to the 981 reference points identified within the ground photography. However, misclassification can be seen outside of the verified seagrass area and away from the transects that was not captured by the ground sampling (Figure 4.12). An area of dark wet sediment with sun-glare was mistaken for a low-density seagrass in the image of the early survey time (Figure 4.12, upper right of frame), with no such issue in the two later survey images. There was 75% agreement on class seagrass density attribution between predicted images between early and late times (Figure 4.13), equating to 82% agreement on attribution of seagrass presence absence between times. The equivalent agreement rates for the mid-late comparison were 87 and 92% for class and pres./absence measures respectively. Much of the disagreement between early and late surveys sourced to an inclined area of sediment uphill from the seagrass which may have caught reflected sun glare or polarised reflection upon the wet sloping surface: the specific type of interference could not be established from available information.

Agreement in seagrass class estimation at the scale of aggregated 0.5 m and 1 m tiles was poor (low correlation coefficient) for the low and medium density classes when comparing early to late drainage-state images, but high in agreement for the high-density class (Table 4.6). Correlation coefficients were markedly higher in the mid to late image comparison than the early to late comparison. There was no improvement in the degree of agreement on class attribution with increasing aggregated tile scale, i.e., tile size made little difference to the class agreement between tide states (Table 4.6).

The importance of the model predictors varied with survey (Figure 4.14). In general red had notably high classification importance, and green notably low importance.

4.3.4 Comparison of multispectral and scouting cameras

Classification accuracy was greater for the multispectral camera as compared to the red-green-blue scouting camera, by up to 5-7 accuracy percentage units, or an improvement of 7-10% is gained from using the multispectral camera, above the accuracy of the scouting camera, when compared under a common random forest model structure (Table 4.7). Classification accuracy was high for high density and absent seagrass classes, and this was consistent across the three residual water drainage states (Table 4.8). In general, the maps derived from the red-green-blue scouting camera indicated the location and density of seagrass at a moderate level of accuracy overall but with substantial noise. Much of this noise appeared outside of the boundary of the GNSS-measured seagrass meadow extent (Figure 4.15). The classified map derived from the multispectral image exhibited substantially less false seagrass presence in non-seagrass areas.

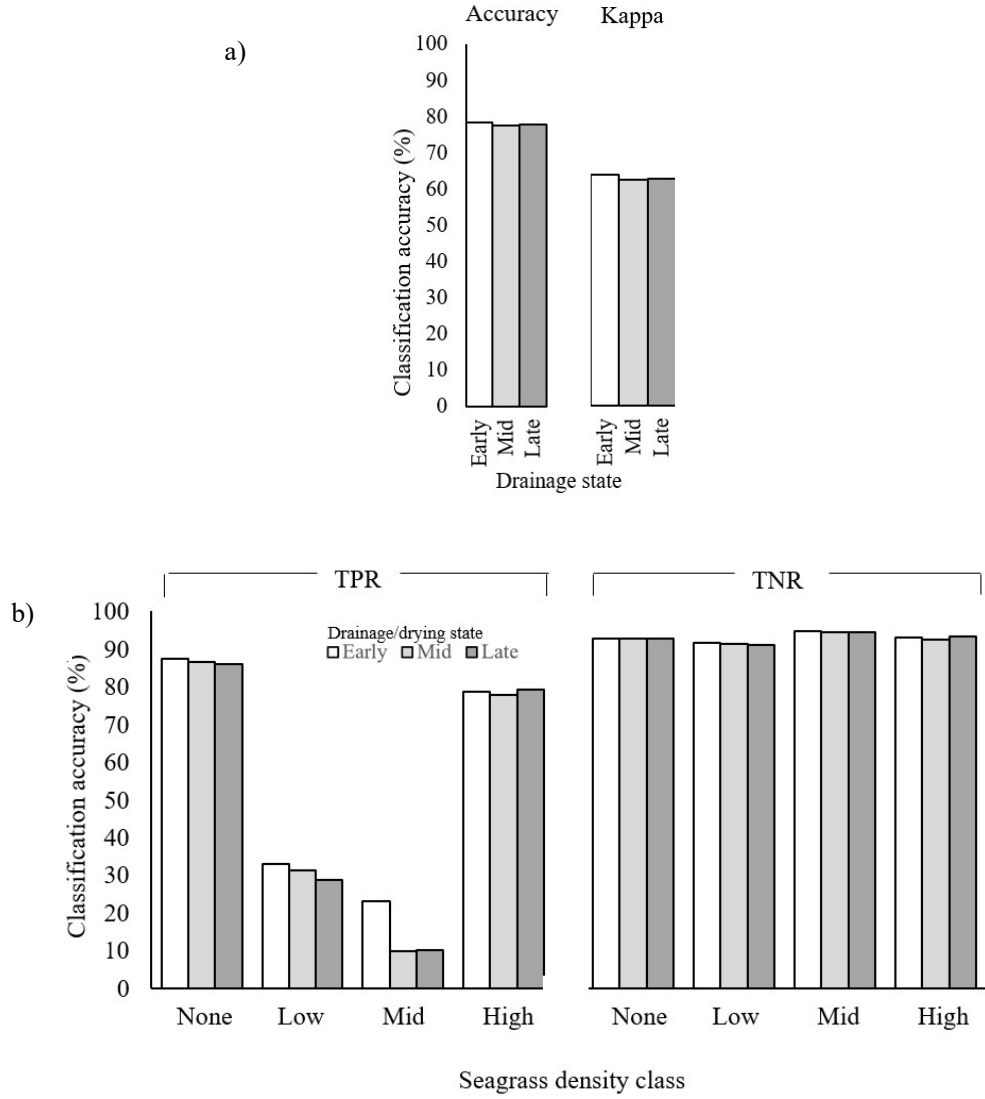


Figure 4.11. Change in mean classification (iterated with 1000 repeats) for a) overall accuracy and b) true positive rate (TPR) and true negative rate (TNR) classification accuracy statistics per seagrass density class.

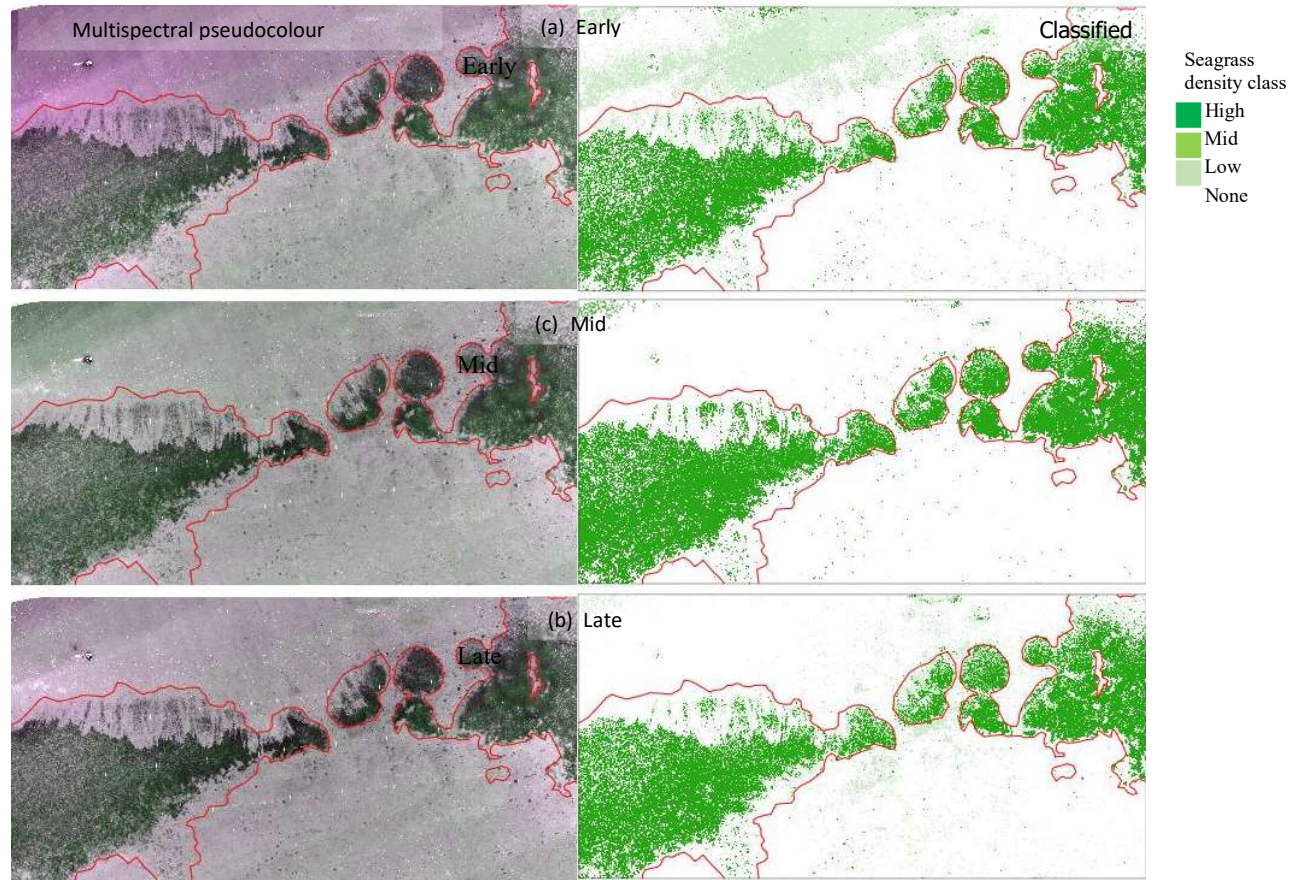


Figure 4.12. Classified seagrass maps (right frames) for (a) early, (b) mid and (c) late low-tide drainage/drying states, with seagrass meadow boundaries (solid red line), and multispectral pseudo colour images for each survey time (left frames).

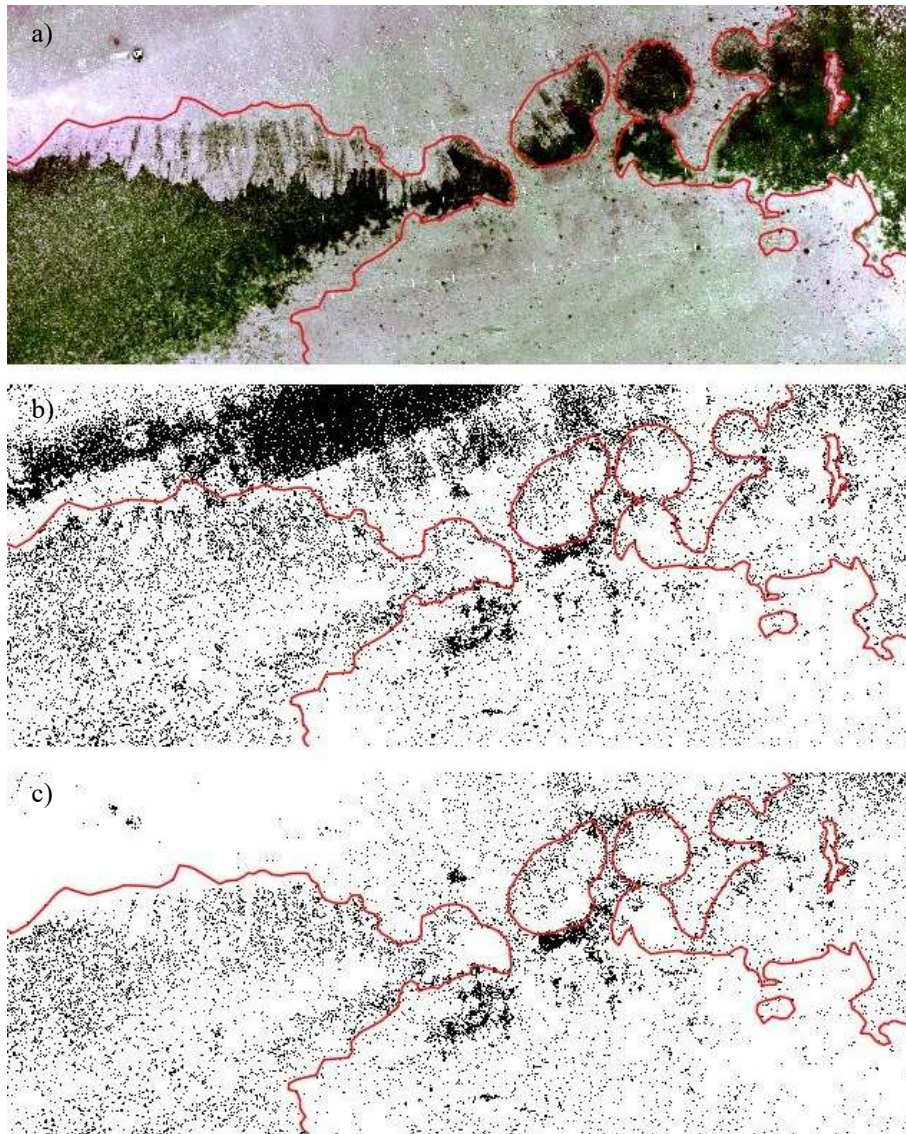


Figure 4.13. The calculated difference maps for agreement on predicted seagrass density class for mid-late comparison (b) and early-late comparison (c). Actual seagrass meadow extent shown by red line. Areas of class-agreement (white pixels) and class-disagreement (black pixels) relate to the extent shown in the multispectral pseudocolour map (a).

Table 4.6. Correlation between predicted map seagrass class attribution for two summary grid scales (0.5x0.5m and 1x1 m). Seagrass density figures are correlation coefficients.

Seagrass density					
Grid size					
Comparison	(m)	Absent	Low	Medium	High
Early-late.	0.5	0.76	0.06	0.37	0.98
Early-late.	1	0.76	0.04	0.43	0.99
Mid-late.	0.5	0.97	0.50	0.75	0.99
Mid-late.	1	0.98	0.55	0.81	0.99

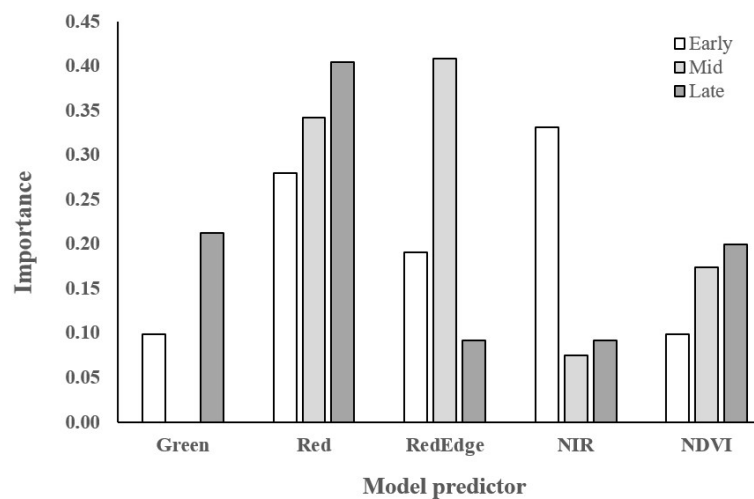


Figure 4.14. Relative importance of predictors contributing to the classification model for each of the three surveys, early, mid and late.

Table 4.7. Comparison of classification accuracy between co-mounted multispectral and colour scouting cameras. Both cameras capture upon the same trigger event so exposed to the same survey and flight environment but noting that the multispectral and scouting cameras comprise a global (instant) and rolling (sequential) line scanning capture, respectively. Note the difference in ground sampling distance (GSD), frame size in megapixels and band set for each camera.

	Camera module.	
	Multispectral.	Scouting.
Megapixels	1.2	16
GSD as rendered	2.7 cm	0.8 cm
Spectra.	Green, red, red-edge, NIR*	Red, green, blue
Band width	Narrow-band	Wide-band
Shutter type.	Global	Rolling
Drainage state.	Overall accuracy.	
Early.	78.3	71.3
Mid.	77.5	72.6
Late.	77.8	72.0

* Green: 530-570 nm ; Red: 640-680 nm;
Red Edge: 730-740 nm; Near Infrared: 770-810 nm

Table 4.8. Comparison between camera types of classification accuracy values per seagrass density class under random forest classification, for early, mid and late stages in low-tide residual water drainage.

Scouting camera.

		Early.	Mid.	Late.
Seagrass density.	Absent.	84	86	86
	Low.	21	16	10
	Medium.	2	14	2
	High.	80	82	83

Multispectral camera.

		Early.	Mid.	Late.
Seagrass density.	Absent.	87	87	86
	Low.	33	31	29
	Medium.	23	10	10
	High.	79	78	79

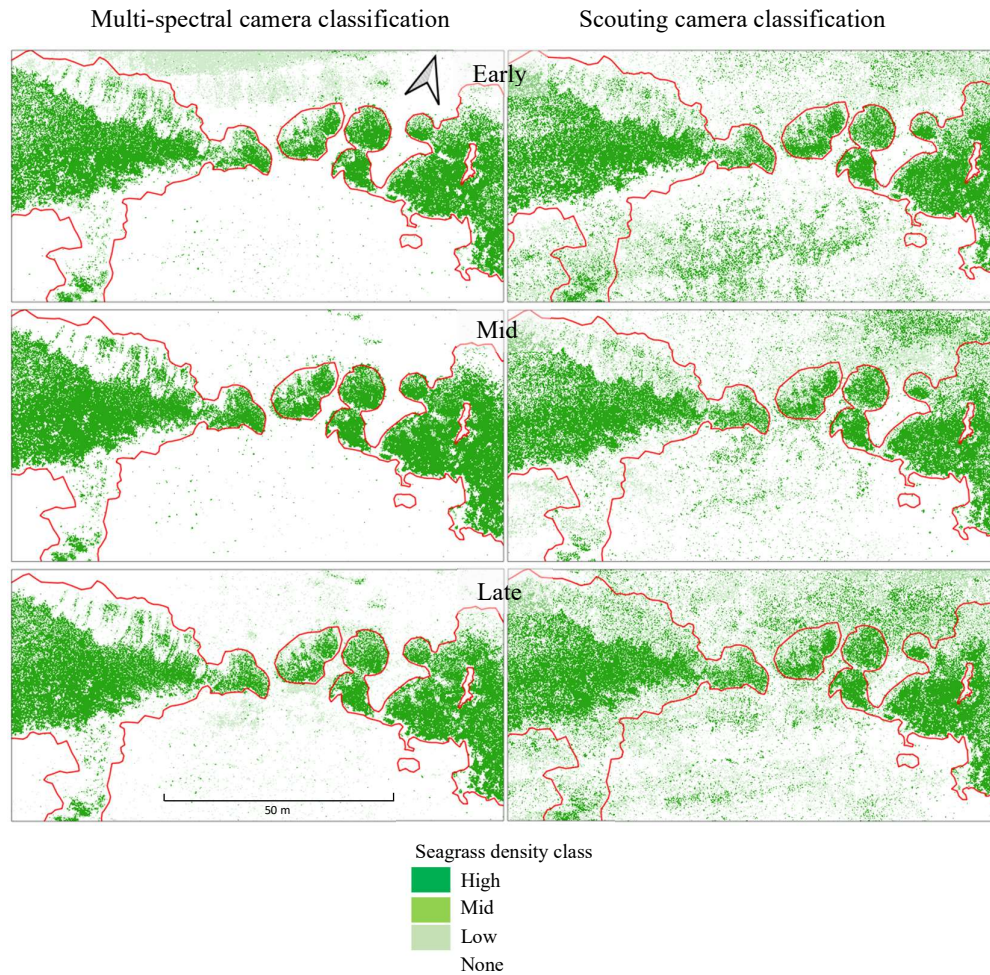


Figure 4.15. Comparison of multispectral image classification (left set) with equivalent classification using the red-green-blue scouting camera (right set) for early, mid and late stages in low-tide residual water drainage (top to bottom). Red lines denote the boundary of measured seagrass meadow extent outside of which seagrass is confirmed as absent.

4.4 Discussion

In this chapter, seagrass was surveyed with a remotely piloted aircraft carrying a multispectral camera to detect differences in the spectral characterization of a scene containing seagrass at a range of density levels and spanning a range of drainage conditions. The aim of this chapter was to assess whether differentiation of seagrass from its surrounding substrate and other low-tide scene content is affected by the progression of low-tide drainage and residual pooling. Results indicate that although minor shift in

spectral coordinates of seagrass and other materials was observed, there was no discernible impact on image classification performance or classification outcome. In general, it is possible to generate valid seagrass density mapping across the whole window of time that the tide is out. However, during the early stage of residual water drainage (i.e., immediately after the water column has ebbed), areas at the periphery of the photogrammetric image grid are susceptible to glint or glare interference that creates false surface feature-identification.

Although a number of studies captured imagery at low tide (Young et al., 2010; Kim et al., 2015; Gade et al., 2018), there was no other literature found that documents consistency or change in seagrass in feature extraction outcome with changing low-tide residual water clearance and drying of substrate. Therefore, the current research is a novel contribution. For macroalgae, Casal et al. (2012) determined that reflectance-difference between species-groups in hyperspectral bands decreases with increasing water depth, with the best separability at low tide when targets are emerged. The current research examines the change in separability of seagrass from substrate, during low-tide water clearance from the substrate, in terms of classification accuracy.

4.4.1 Spectral change across the tidal sequence

The magnitude of shift in spectra between the earliest and latest ebb times equated to only 2-5% in normalised image units (Figures 4.8 and 4.9). This change may be due to some degree of final drying of the scene, change in overcast cloud thickness, or from pixel-scale misalignment of images at time of object detection. The classification outcome differed when considering the greater scene which included a different sediment topography and situation (e.g., out to 20 m from transects) as compared to information contained nearby to the transects and reference photos.

4.4.2 Change in classification outcome with tidal drainage

Results here suggest that seagrass feature extraction can be achieved at a moderate level of classification accuracy (Figure 4.11), and that there is consistency between survey times in classification output during the hours of low tide when seagrass is emergent. Immediately following bulk water clearance from the ground there is potential for erroneous inclusion of low-density seagrass due to confounding by wet sediment that attracts glare (Figure 4.12). High density seagrass, and seagrass absence, can immediately be extracted with high confidence, however mid and low-density seagrass are classified with some error (Figure 4.11). Agreement between classified maps is also lowest for

these sparse seagrass classes (Table 4.6). This was also the case in one study classifying *Sargassum sp.* wrack, where 20-30% or higher ground coverage was required to achieve discrimination using spectra detail available in their airborne hyperspectral sensor bands (Hu et al., 2015).

Predictor importance varies with the time after low-tide ground exposure (Figure 4.14). Red, red-edge and NDVI bands are generally important. No particular rule is evident for inclusion or exclusion of bands at this stage. NDVI is relatively stable to changing drainage state and distinguishes seagrass from its surroundings (Figure 4.9). This may be the case for other vegetation indices also. Utilisation of the red-edge band within contrast ratios in place of, or in addition to, NIR may add further classification benefits. Assessment of classification factoring vegetation indices and texture layers are an important extension to the research based on prevalence in the literature (Khatami et al., 2016; Xue and Su 2017), which is investigated in subsequent chapters.

4.4.3 Comparison of multispectral and scouting cameras

Results (Section 4.3.4) verify that the multispectral camera yields higher classification accuracy than the red-green-blue scouting camera by 7-10% across the three tidal drainage states tested. The scouting camera however did yield classification results at accuracy levels that may still be useful depending on the precision of mapping required. Some seagrass mapping may be successful with low-cost camera investment, e.g., sites with good seagrass contrast against sediment with minimal shell and detritus. Aerial photography using a consumer grade (RGB) camera has been used in remote sensing of seagrass yielding useful seagrass distribution maps (Barrell and Grant 2015; Ventura et al., 2016; Li 2018; Ventura et al., 2018; Nahirnick et al., 2019b). Nebiker et al. (2016) compared NDVI values from and modified consumer RGB camera (with NIR channel exposed) and a multispectral camera mounted upon an RPA each with the ground-reference value from a field spectrometer. In this study in a terrestrial turf setting, the multispectral camera yielded NDVI values with lower spectral deviation from reference than the consumer camera. No literature could be found comparing concurrently captured consumer and multispectral imagery over seagrass. Therefore, results from the current study contribute by identifying improved methodology by using a multispectral rather than consumer camera for mapping seagrass in a drained estuary and verifying that consumer camera sensors can yield seagrass maps in the case of *Zoster muelleri* in New Zealand.

4.4.4 Applicability and limitations

The results of this chapter indicate that seagrass feature extraction is achievable but with some potential limitations. Low and mid density seagrass were difficult to classify correctly, although successful in terms of establishing seagrass presence/absence. Notable change in spectral coordinates was detected where there was permanent pooling during the low tide. Seagrass reflectance spectra were found to be clearly distinct from those associated with sediment. However, there was considerable overlap in seagrass and sediment spectra with that of detritus and shell in the same scene. Applications of the method for quantifying seagrass condition could be compromised where these are prevalent.

Shell and detritus are spectrally confounding to seagrass feature extraction. For the purpose of mapping change of seagrass density across a time-series (e.g., annual monitoring), consideration of detritus and shell surface content may be required to avoid or standardise the contaminating effect between survey times e.g., by avoiding time immediately following high disturbance events such as floods and storms if these are the primary cause of surface shell accumulation. Seagrass density classification would benefit from increased statistical explanatory power, by adding additional predictors to the image stack such as vegetation indices and texture layers.

Change in solar incident intensity was not measured across the survey timeframe, so this trial cannot eliminate the observed spectral shift being influenced by subtle change in overcast cloud cover. However, there was little difference in classification accuracy between survey times. Difference in prediction outcome between the latter two tidal states was minor in the vicinity of the seagrass meadow and transects. There was some variation in predicted seagrass density class per pixel between early and late surveys with glare on some wet inclined parts of that scene confusing classification. Here some sediment appeared as sparse seagrass, depending on sun angle and aspect of slope.

Generally, these results suggest that flight operations need not be constricted to a narrow window of opportunity but would benefit from avoiding the times up to an hour after bulk tidal water clears from the ground, thereby allowing initial draining and drying of the sand topography to minimise interference from glare. Operational planning for an RPA field survey might use the time, between clearance of tidal water and initial draining, to establish positional referencing and collect ground observations.

4.5 Conclusion

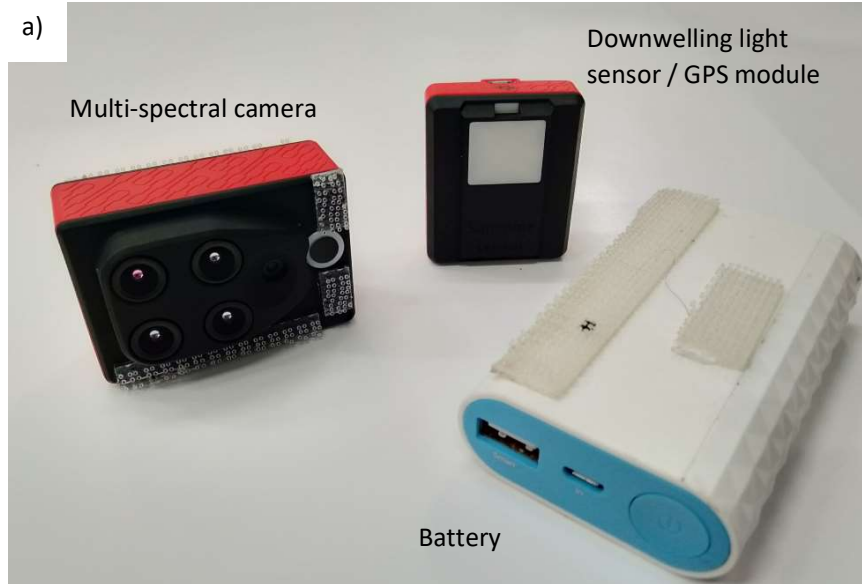
In this chapter, the objectives were met by demonstrating that although there is a minor shift in the spectral coordinates of materials with advancing drainage and drying, it is not sufficient to affect classification accuracy. The results indicate that seagrass contrasts moderately well against the non-target classes, particularly at high density, and classification outcome generally remains consistent, with some inconsistency for sparse seagrass. Feature extraction for high-density seagrass is immediately feasible. There is potential for enhanced seagrass feature extraction, and improved density class assignment for mid and low-density seagrass, by building-in additional predictors into the classification model.

In this autumn study, undertaken on an overcast day, drainage did not substantially affect classification outcomes. There is little evidence that residual water on the estuary is a critical confounding influence, with the exception that some estuary topography may attract glare that confuses the model when the ground is still saturated. During hot summer months there may be greater contrast between drainage states due to the more aggressive drying of zenith sun angles and salt crystal accretion on the surface of ground materials. This is an area for future research.

This chapter assessed the impact of tidal drainage on classification outcome, with analysis focused on the pixel-scale of information. The next chapter will systematically assess an object-based image analysis (OBIA) framework to test and contrast several published predictors and classifiers, on the task of seagrass feature extraction and mapping.

4.6 Chapter appendices

4.6.1 Appendix 4.6.1. Parrot Sequoia camera and downwelling sunshine light sensor / GPS module (a); and mounted upon the RPA (b).



CHAPTER 5

Chapter 5. Assessment of object-based image analysis for seagrass feature extraction

5.1 Introduction

Pixel-based image analysis (PBIA) of multispectral imagery collected at 30 m altitude above a seagrass scene yields classification of seagrass density class and non-target substrate-type with good model and per-class accuracy (Chapter 4). Object-based image analysis (OBIA) has potential to improve classification performance over that of PBIA (Blaschke et al., 2014; Myint et al., 2011). In general, OBIA has been shown to yield superior classification performance compared to pixel-based classification due to increased information aggregated within the object components, and greater potential contrast between endmember groups (Benfield et al., 2007; Frohn et al., 2011; Whiteside 2011; Ursani et al., 2012; Cai and Liu 2013; Blaschke et al., 2014; Wahidin et al., 2015; Khatami et al., 2016; Ventura et al., 2016; Ma et al., 2017). Frohn et al. (2011) showed substantial gains in accuracy using OBIA over PBIA for a wetland habitat mapping project using a pairwise sequential colour-based region-merging image segmentation. Meneguzzo et al. (2013) demonstrated that OBIA better represented land-cover patterns than PBIA when using independent components analysis for pixel classification and an unspecified classifier for object-based image analysis. Sevara et al. 2016 found OBIA performance exceeded that of the pixel-scale for feature extractions from a terrestrial digital terrain model (DEM). Elsewhere, Ghosh and Joshi (2014) demonstrated OBIA benefits over PBIA when using support vector machine to map bamboo patches when using Worldview2 satellite imagery.

There are reported exceptions though where PBIA either equalled or exceeded the classification performance of OBIA (Dingle Robertson and King 2011; Duffy et al. 2018). Poursanidis et al., 2018 established that the relative performance of PBIA and OBIA for mapping seagrass varied with the classifier used and the type of radiometric correction applied to the imagery.

Consequently, there is no evident rule that can be applied for development of seagrass image analysis in the present study. Comparative assessment of both PBIA and OBIA are justified for *Zostera muelleri*.

The basis for OBIA is the segmentation (partitioning) of the subject imagery into objects (patches of contiguous pixels) under a clustering, region-growing or other pattern recognition rule (Dronova 2015). Segmentation results are assessed according to a supervised reference or unsupervised metric, then segments classified using reference data (see Appendix 5.7.1 for summary of components). Segmentation and subsequent classification outcomes can be dependent on the spatial and spectral resolution of the input imagery relative to the physical object-size and spectral separability of the ground-objects and materials that make up the visual scene (Johnson and Xie 2011; Dronova et al., 2012; Troya-Galvis et al., 2015; Chen et al., 2019; Räsänen and Virtanen 2019; Yang et al., 2019). At some scale of segmentation, small objects (i.e., smaller than the resulting segment size) can become absorbed into the surrounding segment pixel-set leading to information loss (e.g., Dingle Robertson and King 2011) or other dilution of spectral character of the segment. These sources of classification error are relevant to seagrass feature extraction (see Section 2.4.2 and Appendix 2.8.2). Optimal segmentation parameters are not available for seagrass on a post-storm heterogeneous estuarine seagrass scene. Therefore, assessment of optimal OBIA image segmentation scale is required for the seagrass survey method developed in this chapter.

Numerous classifiers (algorithms) are applicable to image classification (see Appendix 5.7.1.5). The three classifiers: Linear Discriminant Analysis (LDA); Support Vector Machine (SVM); and Random Forest (RF); are strong candidate classifiers for seagrass feature extraction (Pal and Mather 2005; Lin et al., 2010; Khatami et al., 2016; Yang et al., 2019). Variable selection and collinearity reduction within the classifier implementation have potential to improve classification (Appendix 5.7.1.7) but this needs to be established for seagrass feature extraction by multispectral camera.

5.2 Chapter objectives

The goal of this chapter is to test a semi-automated, object-based image analysis workflow that can be applied to RPA-sourced multispectral imagery and achieve moderate to high classification accuracy for quantifying seagrass ground coverage under a discrete interval range. Towards this overall goal, this chapter aims also to evaluate the effect of segmentation scale, classification algorithm choice and variable selection on the accuracy of seagrass detection and coverage estimates. The five specific objectives of this chapter are:

1. Selection of a small subset of object-based image analysis workflow components that are indicated to yield moderate to high classification accuracy in a range of vegetation mapping cases;
2. Assemble a semi-automated process-chain that ingests RPA imagery, ground observations and spatial referencing data to yield spatially explicit classification results;
3. Compare segmentation scale, classification algorithm and variable selection in terms of seagrass detection and classification accuracy;
4. Assess a range of spectral bands, indices and texture layers for contribution to classification outcome;
5. Select a classifier, segmentation scale and variable-selection method for subsequent testing on repeat surveys; and
6. Verify the method for mapping of seagrass in repeat surveys undertaken in the following year.

5.3 Method

5.3.1 Study area

RPA flights were undertaken on 9th April 2017 at 30 m above ground level, over the general study area described in Chapter 3 and the specific site used in Chapter 4 (Section 4.2.1). Subsequent flights were also made 2nd Feb 2018 and 28th March 2018.

5.3.2 Aerial imagery capture

The imagery used for this analysis was the same as the third set of imagery from Chapter 4, corresponding to the ‘late’ low-tide residual drainage state (detailed description in Section 4.2.3).

This multispectral camera imagery was captured above a seagrass meadow using an autonomous RPA flown at sufficient velocity and height to achieve moderate spatial coverage (~100 x 200 m extent), but low and slow enough to resolve scene detail for content identification. The imagery was aero-triangulated and radiometrically calibrated within the photogrammetry software to derive a single orthorectified mosaic of the scene with all four spectral bands (R, G, RE, NIR) in alignment (Figure 5.1, and see Section 4.2.5 for the detailed description), from which additional layers were derived below.

5.3.3 Ground reference data collection

The ground reference data collection strategies are described extensively in Chapter 4 (Section 4.2.4). Detailed ground-level photos (1 m height above ground level)

allowed regions of the image to be associated accurately with seagrass density and other scene components. Training-sample polygons, selected from the segmentation step described below were inspected in a Geographical Information System (GIS) environment, and overlain on the high-resolution ground photography. Polygons were ascribed to one class from a classification typology that represents the range of seagrass conditions, shell, detritus and sediment presented in Table 5.1. This class-set differs slightly from that of Chapter 4, using instead a univariate class typology factoring classes of seagrass mixed with detritus and shell to cover the range of seagrass presentations and model more variability in image spectral information than was achieved in Chapter 4.

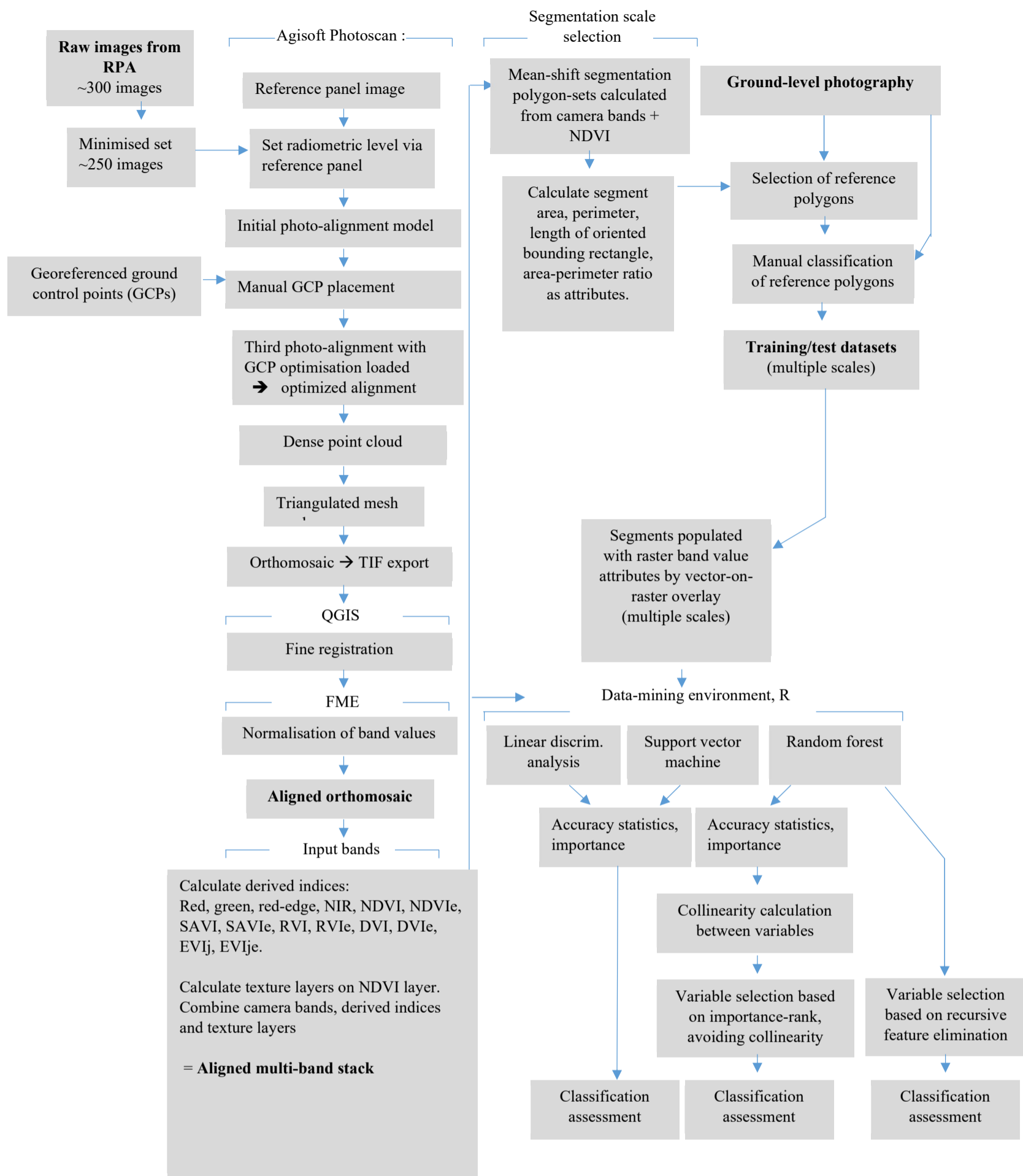





Figure 5.1. Analysis workflow for data preparation, segmentation assessment and comparison of classifier and variable selection variants.

Table 5.1. Ground cover classes applied to seagrass meadow image classification.

Class	Description	Example
<i>Single material on sediment</i>		
Seagrass		
High density.	Two thirds to full cover.	
Mid density.	One-third to two-thirds cover.	
Low density.	Trace to one-third cover.	
Sediment.	Full sediment cover, negligible other objects.	
Detritus		
High density.	Full detritus cover, negligible other material.	
Low density.	Less than two thirds cover.	
Shell		
High density.	Shell cover, minor other material.	
Low density.	Less than two thirds cover.	
<i>Mixes</i>		
Seagrass + detritus.	Mixed seagrass + detritus.	
Seagrass + shell.	Mixed seagrass + shell.	
Seagrass + detritus + shell.	Mixed seagrass + detritus + shell.	
Shell + detritus.	Mixed shell + detritus.	

5.3.4 Photogrammetry and data compilation

A calibrated reflectance panel was placed in the scene at the time of flight. The raw bands (green, red, red-edge and near infra-red) were radiometrically adjusted using ‘calibrate to reflectance panel’ and ‘use onboard downwelling light meter’ settings after entering the panel’s pre-calibrated reflectance values (Agisoft Photoscan version 1.5). This process adjusts and rescales digital numbers to provide estimated reflectance values. These features were not available in Photoscan during the period of research resulting in Chapter 4, but the inclusion of this calibration step here now permits the calculation of a wide range of formal vegetation indices.

Band calculations were determined following the rules described in Table 5.2 and implemented using FME Workbench 2017 (SAFE Software) to combine bands into a single raster stack for use in segmentation, classification and the final mapping. Indices were calculated using multispectral image bands in calibrated units of reflectance.

A selection of spectral band ratio or contrast indices (i.e., ‘vegetation’ indices) were calculated from spectral bands corresponding to published formulas provided for normalised difference vegetation index (NDVI, Tucker 1979), soil-adjusted vegetation index (SAVI, Huete 1988), difference vegetation index (DVI, Richardson and Wiegand 1977), ratio vegetation index (RVI, Jordan 1969) and a version of the enhanced vegetation index using the bands available within the camera band-set of the present study (EVI_j, Jiang et al., 2008).

These vegetation indices were selected due to their prevalence in the literature for vegetation condition assessment (see Chapter 2). The vegetation indices are conventionally calculated including the near infra-red (NIR) band. A second exploratory variant of each vegetation index was calculated substituting the red-edge band for the red band, to determine any predictive improvement yielded by red-edge reflectance (Table 5.2).

Table 5.2. Spectral and derived bands calculated and compiled into the analysis layer package, used for segmentation and classification.

Short band Name	Full band name	Formula	Literature link
Green.	Green (550nm centre, 40nm width).	Green.	
Red.	Red (660nm centre, 40nm width).	Red.	
RedE.	Red edge (735nm, 10nm width).	RedE.	
NIR.	Near infra-red (790nm, 40nm width).	NIR.	
NDVI.	Normalised difference vegetation index (Red, NIR).	$(\text{NIR}-\text{Red})/(\text{NIR}+\text{Red})$	Tucker 1979.
NDVIe.	Normalised difference vegetation index (Red, Red-edge).	$(\text{NIR}-\text{RedE})/(\text{NIR}+\text{RedE})$	<i>Red-edge variant of above.</i>
SAVI.	Soil adjusted vegetation index (Red, NIR).	$(1+L)(\text{NIR}-\text{Red})/(\text{NIR}+\text{Red}+L)$	Huete 1988.
SAVIe.	Soil adjusted vegetation index (Red, Red-edge).	$(1+L)(\text{NIR}-\text{RedE})/(\text{NIR}+\text{RedE}+L)$	<i>Red-edge variant of above.</i>
DVI.	Difference vegetation index (Red, NIR).	$\text{NIR} - \text{Red}$	Richardson and Wiegand 1977.
DVIe.	Difference vegetation index (Red, Red-edge).	$\text{NIR} - \text{RedE}$	<i>Red-edge variant of above.</i>
RVI.	Ratio vegetation index (Red, NIR).	NIR/Red	Jordan 1969.
RVIe.	Ratio vegetation index (Red, Red-edge).	NIR/RedE	<i>Red-edge variant of above.</i>
EVIJ.	Enhanced vegetation index by Jiang (Red, NIR).	$2.5*(\text{NIR}-\text{Red})/(\text{NIR}+2.4*\text{Red}+1)$	Jiang et al., 2008.
EVIJe.	Enhanced vegetation index by Jiang (Red, Red-edge).	$2.5*(\text{NIR}-\text{RedE})/(\text{NIR}+2.4*\text{RedE}+1)$	<i>Red-edge variant of above.</i>

In addition to spectral layers and derived vegetation indices, a set of texture layers describing the spatial complexity/variance of the imagery locally, were derived from the NDVI band. These were calculated using the HaralickTextureExtraction function of the Orfeo Toolbox which generates a wide range of texture models (see Table 5.2). This tool brings together algorithms that calculate up to 29 kernel statistics which the tool-developers reference to Haralick et al. (1973). The Haralick's texture layers are varied in statistical approach, and include a range of grey level kernel pattern measures. The resulting texture extractions were screened visually. Texture layers resembling unstructured noise with respect to seagrass patterns were eliminated. The resulting set of Haralick's texture layers were then used to support subsequent image analysis (Figure 5.2).

The polygon-set derived at each segmentation scale was overlain on the 28 bands (14 spectral plus 14 texture layers) and summary statistics calculated for each polygon. Five further geometric attributes were also derived for each polygon (e.g., segment perimeter, area) and these together with the derived spectral and texture attributes form the basis for the information set for image classification (Table 5.3).

5.3.5 Image segmentation

Image segmentation was performed with the Orfeo toolbox software using python scripts to implement the mean-shift segmentation algorithm described in Section 2.3. Segmentation was made using the four camera bands plus NDVI layer as input rasters. The algorithm was set with parameters to enhance the sensitivity to small spectral differences at small spatial scales resulting in a very fine scale of segmentation. Specifically, the parameter spectral range-radius was set to 0.0005 (in units of normalised reflectance) after observing that there was very little additional segmentation by further reducing this parameter.

The initial minimum segment size parameter used was 5-pixels, resulting in 'super-pixels' of similar colour at the scale of individual seagrass plants. This parameter controls the smallest allowable segment size by merging smaller segments into the most similar adjacent segment, merging in order of increasing size. Iterations of the algorithm were then run applying a range of minimum segment size parameter values (5, 10, 20, 40, 80, 160, 320 and 640 pixels). This resulted in eight segmentation polygon-sets available for optimal scale assessment.

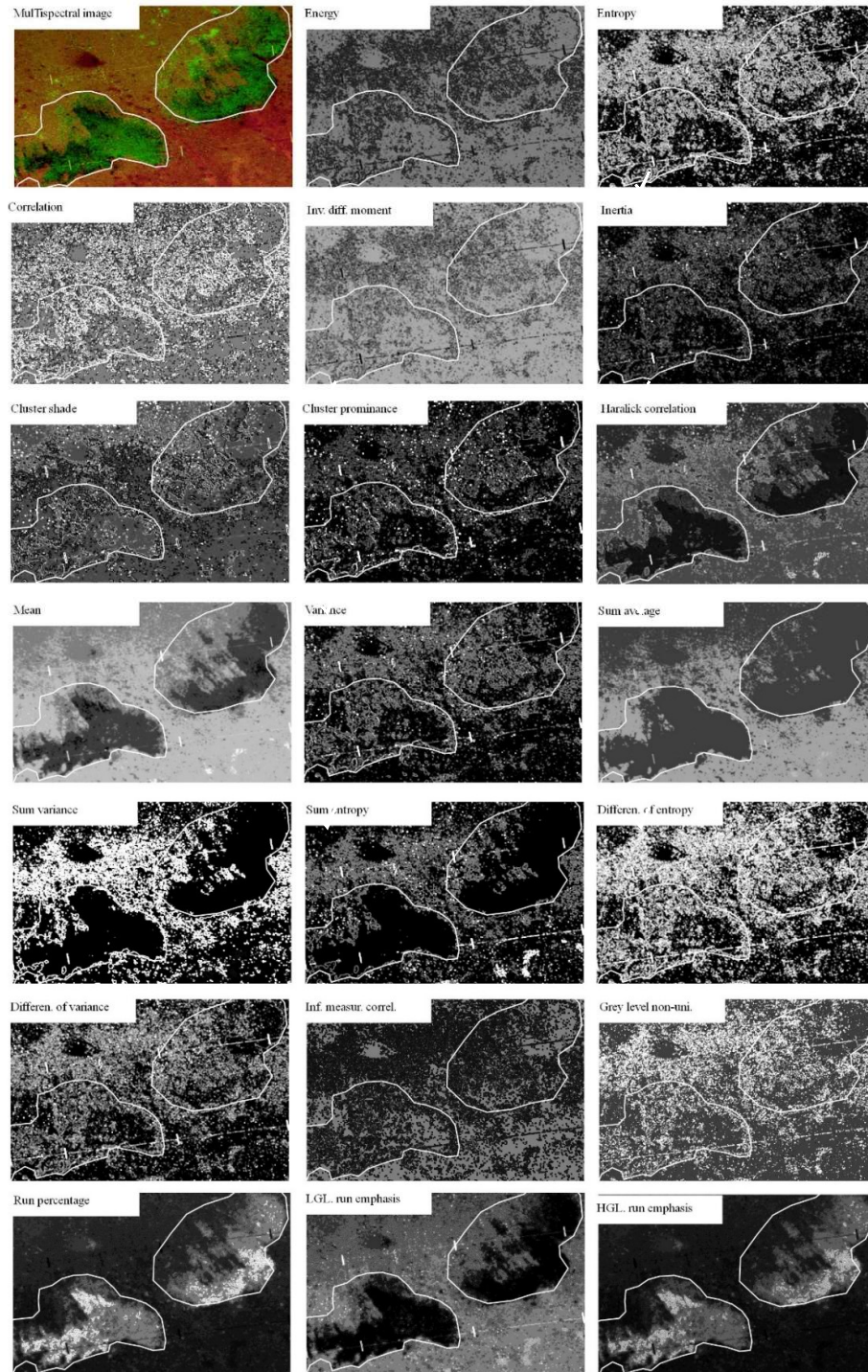


Figure 5.2. A seagrass scene (~30 m wide) within the main study area showing the respective Haralick's texture depictions with a grey-scale colour-ramp running from low (black) to high (white). Grey-scale contrast in these frames have been enhanced to expose detail for illustration, and with respect to the true measured seagrass extent (white polygon line).

Table 5.3. List of predictors available in the analysis image prior to feature selection (see Table 5.2). Haralick’s texture layers are denoted with “H.” Geometry attributes are based on calculated segment characteristics.

Band no.	Predictor name.	Range.	Band no.	Predictor name.	Range.
<i>Spectral attributes</i>			<i>Texture attributes</i>		
1	Green.	0-1	15	H. Energy.	0-1
2	Red.	0-1	16	H. Entropy.	0-1
3	Red-edge.	0-1	17	H. Correlation.	0-1
4	NIR.	0-1	18	H. Inv. diff. moment.	0-1
5	NDVI.	0-1	19	H. Inertia.	0-1
6	NDVIe.	0-1	20	H. Cluster shade.	0-1
7	SAVI.	0-1	21	H. Cluster prominence.	0-1
8	SAVIe.	0-1	22	H. ‘Haralick correlation’.	0-1
9	DVI.	0-1	23	H. Mean.	0-1
10	DVIe.	0-1	24	H. Variance.	0-1
11	RVI.	0-1	25	H. Information Correlation.	0-1
12	RVIe.	0-1	26	H. Grey-level non-uniformity.	0-1
13	EVI _j .	0-1	27	H. Low grey-level run emphasis.	0-1
14	EVI _j e.	0-1	28	H. High grey-level run emphasis.	0-1
			<i>Geometry attributes.</i>		
			29	Segment area.	(m ²)
			30	Perimeter.	(m)
			31	Length of bounding rectangle.	(m)
			32	Length/width bounding rectangle.	(m/m)
			33	Area-perimeter ratio.	(m ² /m)

5.3.6 Optimal segmentation scale

The resulting segmentation patterns were analysed following the approach described by Johnson and Xie (2011). This method combines inter- and intra-segment variance scores to form a global fit index. Inter-segment scores are based on Moran's Index (Equation. 5.1), a common measure of spatial autocorrelation (Li et al., 2007). Here this was applied to the NDVI band due to its demonstrated influence on pixel classification outcomes as discussed in Chapter 4.

$$\text{Moran's Index (MI)} = \frac{n \sum_{i=1}^n \sum_{j=1}^n w_{ij} (y_i - \bar{y})(y_j - \bar{y})}{\sum_{i=1}^n (y_i - \bar{y})^2 \sum_i \sum_j w_{ij}} \quad (\text{Equation 5.1})$$

where y_i and y_j are the mean segment image intensity values for each pair of segments being compared, \bar{y} is the mean intensity value across the whole image, and n is the number of compared pairs. The spatial weighting, w_{ij} of each comparison is assumed to be unity for adjacent segments. Intra-segments scores were calculated using the area-weighted variance index (Equation 5.2) as again applied by Johnson and Xie (2011):

$$\text{Area-weighted variance index} = \frac{\sum_{i=1}^n v_i * a}{\sum_{i=1}^n a} \quad (\text{Equation 5.2})$$

where v_i is the variance of pixel values within each segment and a is the segment area in square meters.

Inter- and intra-segment scores were then normalised according to Equation 5.3:

$$\text{Normalised value} = \frac{(x - x_{min})}{(x_{max} - x_{min})} \quad (\text{Equation 5.3})$$

where x is the segment score value, and x_{max} and x_{min} the overall maximum and minimum value across all segments. Finally, normalised Moran's Index and area-weighted variance scores were then combined into global score using Equation 5.4:

$$\text{Global score} = v_{norm} + MI_{norm} \quad (\text{Equation 5.4})$$

The approach of Johnson and Xie (2011) was selected as this method provides an unsupervised, objective measure of segment heterogeneity without the having to draw, *a priori*, the training polygons required to assess segment fit, which would potentially introduce user bias. The approach defines segmentation as being effective when there is a low average per-segment variance score (i.e., segment pixels are internally similar) and the Moran's Index score for autocorrelation is also low (i.e., segments are different from their neighbours), where the lowest global score out of a range of tested segmentation scales indicates an optimal segmentation.

In addition to Moran's Index, area-weighted variance and their global score, an additional index of intersegment variance difference, was calculated as root mean square error between the target the variance x_{seg} and adjacent segment variance x_{adj} of adjacent segment pairs (Equation 5.5). A high root mean square error between each segment and

its neighbours would indicate segmentation that has high difference between spectral character of adjacent segments.

$$\text{Root mean square error} = \sqrt{\sum(x_{seg} - x_{adj})^2} \quad (\text{Equation 5.5})$$

Johnson and Xie (2011) define the optimal segmentation scale as the output with the lowest global score. Here, additional measures of segmentation (root-mean-square error and signal to noise ratio) were used to provide additional measures of segmentation fit to contrast with primary global score and highlight any obvious anomalies. The resulting polygon-set with the lowest global score and associated measures, would signal an optimal scale.

The global score approach of Johnson and Xie (2011) was developed for a different target vegetation species and imaging regime and may not, therefore, be directly transferrable to seagrass. As such, rather than adopt the single optimum segmentation scale, a simple sensitivity analysis was undertaken to assess the effect of segmentation scales on the resulting classification accuracy. The reference ground photography ultimately limits the range of classification scales to a *minimum segment size* of 40 pixels. Larger scale segments were too large, in many cases, to be contained within the ground-footprint of the reference photos.

5.3.7 Model training and test data

Polygons were selected from image segmentation feature-sets to form training polygon objects. Selection was made by manual inspection of polygons overlain on the aligned ground-level (high-resolution) photography where:

- i) the polygons were wholly within the extent of the ground photographs;
- ii) the scene content of the polygons was clearly visible as uniform unambiguous examples of the target classes; and
- iii) the polygons were positioned with some tolerance for minor (1-2 pixel) potential misalignment between ground photography and the multispectral drone imagery.

Polygons were then attributed to a single class from the full list of categories (Table 5.1) based on content observable in the ground photographs. In turn, polygons were then intersected with the underlying multiband-band analysis image and mean band values calculated for pixel-centres within the polygon geometry. Additional attributes were calculated quantifying perimeter, area, perimeter/area ratio, oriented bounding box length and length width ratio as morphological attributes of the segment geometry. All

measures were joined to the polygon feature set as attribute columns and saved as a shapefile for subsequent analysis (hereby termed ‘the analysis dataset’).

A separate fixed test-data subset was not used, as classification modelling was conducted using k-fold resampling with replication, whereby all reference data potentially participate as training or test data across multiple instances during model iteration.

5.3.8 Classifier comparison and predictor importance

Image polygon sets (or the point-set in the case of PBIA) containing attributes for the image band values along with actual ground cover class information based on the visual interpretation described above, were imported into R Project for subsequent classification modelling.

The three linear classifiers (linear discriminant analysis, support vector machine and random forest) were assessed for classification performance with respect to seagrass detection and density estimation. An iterative classification model was constructed to assess classifier performance over a range of segmentation scales, and the relative classification accuracy achieved under a particular segmentation scale.

Each classifier was applied using the *rminer* package (The R Project v 3.6) for linear discriminant analysis and support vector machine classifiers (LDA and SVM methods), and *randomForest* package for the random forest (RF) classifier (*rminer* can access this package as a meta-method, but the *randomForest* package was used directly in this case). LDA and SVM classifications were made under repeated 5-fold cross-validation, with results reported as the average of 100 repeats of each cross-validation set. Cross validation wasn’t applied external to the *randomForest* routine as this method includes resampling components within its internal structure. The random forest *ntree* parameter was tuned by running a range of values (*ntree* = 50 to 1200) for each iteration of segment size dataset, and observing the minimum out-of-bag (OOB) error rate within each set.

Classifier performance for seagrass was assessed by examining: i) overall classification accuracy and kappa statistic; ii) the user and producer accuracy for each target class as extracted from the model confusion matrix; and iii) the rate of successful seagrass detection (seagrass presence pooled across density classes).

The classifier comparison procedure was repeated for the four segmentation scales of minimum size threshold 5, 10, 20 and 40 pixels, and for pixel-based analysis. Training of polygons was made for each individual scale due to difference in location and extent. Some class assignment changed with increasing scale as pure class types within a small

segment mixed with other contents at the large segment scale. Assessment of larger sized segmentation (e.g., the 80, 160, 320 and 640 pixel segmentation scales of Section 5.3.4) was not reliably feasible because the size of these segments extended beyond the edge of reference photos (1m x 1.2m footprint in ground units) such that predominant segment class could not be determined in many cases. Training of segments at this scale would require a more extensive ground referencing system (e.g., 2 or 5 m quadrats).

5.3.9 Variable importance and feature selection

The importance of variables contributing to the LDA and SVM methods, was quantified using the *importance* method within the *rminer* package (Cortez and Embrechts 2013). Model variance was set as the importance metric (method = *sensv* parameter). Variable importance within the RF method was exposed using the *importance* function set to units of mean decrease in accuracy. Visual comparison of variable importance between classifiers was made by normalising on a relative scale of 0 (lowest importance) to 100 (highest importance).

The effect of feature selection on classification outcome was assessed using the optimal classifier defined from the analyses made in Section 5.3.4 (random forest in this case). The selected classifier was then subjected to three sub-setting regimes: i) no variable filtering; ii) variable filtering based on dropping collinear variables in sequence by decreasing rank of variable importance; and iii) feature selection using a recursive feature elimination (RFE) algorithm. The effect of feature selection was quantified in terms of change in classification outcome compared to no feature selection.

Variable importance and feature selection methods were based on random forest parameters *ntree* = 1000 (number of trees), *mtry*=6 (number of variables sampled), and all models replicated and averaged 100 times.

The relative performance of red-edge and near infra-red spectra, both directly as sensor bands and within derived indices, was estimated by collating rank position within each variable importance list and then comparing mean rank value across segmentation scales and band or index type. The relative value of texture layers in comparison to spectral layers, derived indices and segment geometry attributes, was estimated by comparing the average importance-value observed, on the relative-scale within each classification model with predictors aggregated as general type 'band' (e.g., green), 'index' (e.g., NDVI), 'texture' (e.g., entropy) or segment 'geometry' (e.g., perimeter/area ratio). Segment geometry attributes were not relevant to the individual points under the PBIA pathway.

Spectral and texture layers may potentially encode similar descriptions of the scene content resulting in multi-collinearity within the resulting layer set that might require procedural adjustment. Additionally, the derived indices NDVI, SAVI, DVI, EVIj and RVI were determined with two versions (red-edge or near infra-red) between which some similarity can be expected. Collinearity was determined by calculating correlation between all predictor layer pair combinations in a correlation matrix (R Project v3.6, *cor* function). Collinearity between predictors was considered significant in cases where Pearson's correlation coefficient was 0.7 or greater. A candidate variable list with reduced collinearity was formed by systematically selecting variables in sequence of descending importance but dropping variables where there was collinearity with any previously selected variable as indicated from pairwise tests.

Determination of an optimal classification method thus incorporated the evaluation of which segmentation scale, classifier and feature selection regime yielded the greatest accuracy for ascribing seagrass presence/absence and seagrass density class, as well as considering the benefit of using red-edge band and texture elements in the classification.

5.3.10 Seagrass mapping and replication

Additional survey flights were undertaken one year after the previous survey, on the dates 02/02/2018 and 28/3/2018. The February survey was set for a time of year considered likely to be near to the annual maxima for seagrass growth disturbance, based upon indications in the literature (Turner and Schwartz 2006b; Turner 2007), monthly visual inspections on site, and weather observation (no storm events). The March 28 survey was an attempt to survey exactly one calendar year following the 9 April 2017 survey but prior to autumn storm activity. Sky cloud cover, sun angle and tide state were consistent across the three capture times (Appendix 5.7.2). The transect for the two repeat surveys was widened from 10 m to 20 m spacing between rows, extending the survey area downhill to sample more seagrass environment in an area where there was seagrass present in previous years (Figure 5.3).

The RPA was programmed with an adjusted flight plan for the February survey (compared to April 2017), but the same flight programme was loaded into the RPA for the March survey for exact course-replication within the limits of the GPS sensor-precision. Forwards overlap and side-lap, flight speed and flying height were consistent for all three surveys. Ground photography was also consistent in method and scale across the three surveys.

The image processing, band collation and classification was replicated using the same scripts as was used for applying random forest at pixel scale, with no variable selection. As before, all analysis image-stacks consisted of spectral, vegetation index or texture layers derived from reflectance values. The random forest programme parameters were also applied ($mtry = 6$, and $ntree = 1000$, with 5-fold cross validation). Ground-level photography was repeated as per the previous class system. The April 2017 survey polygons were freshly re-classified at the same time as the ground-reference classification for the two 2018 surveys, to ensure consistency in human judgement one year later. In this case, non-homogeneous/ambiguous samples were deleted from the reference dataset to improve the purity of the sample.

The significance of difference between the accuracy statistics for each survey was measured by applying analysis of variance (ANOVA) to the accuracy statistics, grouped by survey time and invoking Tukey's pairwise comparison function to compare survey times for mean accuracy level. The resulting classifier was used to ascribe predicted class membership across all pixels of the image. This was repeated for the three survey times, resulting in three georeferenced prediction maps.

The efficacy of the method was also assessed by comparing the mapped (predicted) seagrass extent to the actual location of the seagrass meadow as measured by high precision GNSS survey instrument (see Chapter 3). These plotted seagrass meadow boundaries have ~110 mm (i.e., ~ 4 pixels) of positional accuracy with respect to the common geographic reference datum used in this study (New Zealand Transverse Mercator coordinate system, referenced to LINZ geodetic marker EB2U).

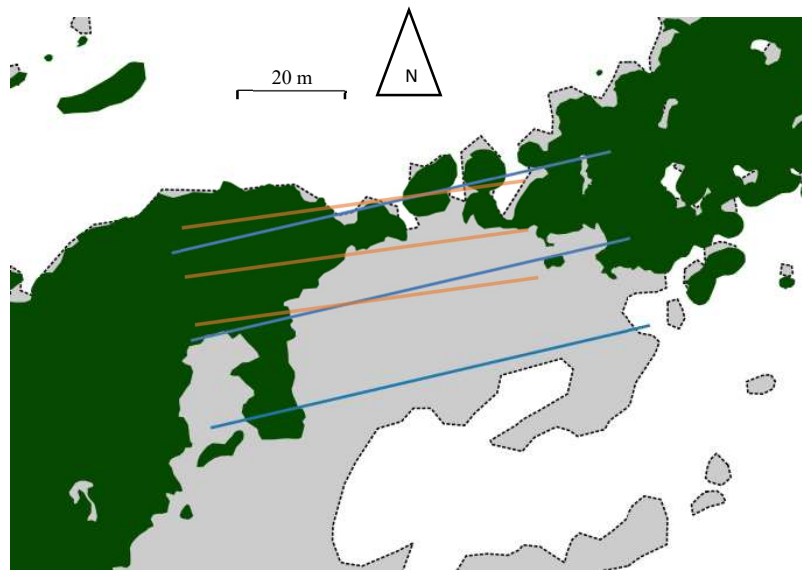


Figure 5.3. Survey site showing the transects used for the original transect of April 2017 of Chapter 4 (orange, transect pattern 1) and the early February and late March 2018 surveys (blue, transect pattern 2) and held consistent between these latter sets. Green area denotes the seagrass survey mapped using a precision global satellite navigation system (GNSS). The grey area shows the seagrass extent visible in 2015-dated Bing Maps imagery but currently absent.

5.4 Results

5.4.1 Image preparation and segmentation

Normalised spectral bands, their derived indices and Haralick's textural layers were calculated and stacked into a multi-band georeferenced raster. For this particular image of size of 6100 x 4200 pixels (columns x rows) and using memory-optimised processing in FME Workbench (SAFE software), peak memory usage was ~24 GB of RAM with processing and memory demands decreasing with increasing segment size.

5.4.2 Segmentation and assessment

Image segmentation was iterated across the range of minimum segment size parameters including 5, 10, 20, 40, 80, 160, 320 and 640-pixel threshold values (Figure 5.4). The number of segments generated increased linearly with minimum segment size (Figure 5.5). Numbers of segments for this 130 m x 70 m image mosaic footprint ranged from 7,901-1,043,000 segments (Appendix 5.7.3).

Moran's Index score and corresponding area weighted variance value for each segmentation scale increased with minimum segment size (Figure 5.5). These combined to yield an unsupervised global segmentation score that similarly increased with minimum segment size threshold (Figure 5.5). Root mean square error (Figure 5.5), an alternative to intra-segment variance, yielded a curve consistent with area-weighted variance, with low intra-segment variance at the lowest segment scales. The signal-noise ratio similarly reflects the same tendency for low deviation from neighbours in smaller sized segments. All score-types indicate effective segmentation at small segment scale.

At the minimum segment size threshold, segments were on average 17 pixels in size (Appendix 5.7.3) corresponding to an object-space dimension of ~0.01 m². At this size, segments effectively function as 'super-pixels' below the physical scale of seagrass meadows (see Figure 5.4) but are sufficiently small in scale to isolate objects like shells and elements of detritus (which are only a few pixels in size). Segments at intermediate and large scales by contrast, increasingly incorporated non-target objects like shells and sticks.

There was no specific optimal segmentation scale elucidated by the scale-assessment using Moran's Index and intra-segment variance measures, except the tendency that small segments are better under this aerial survey specification, and pixels are best.

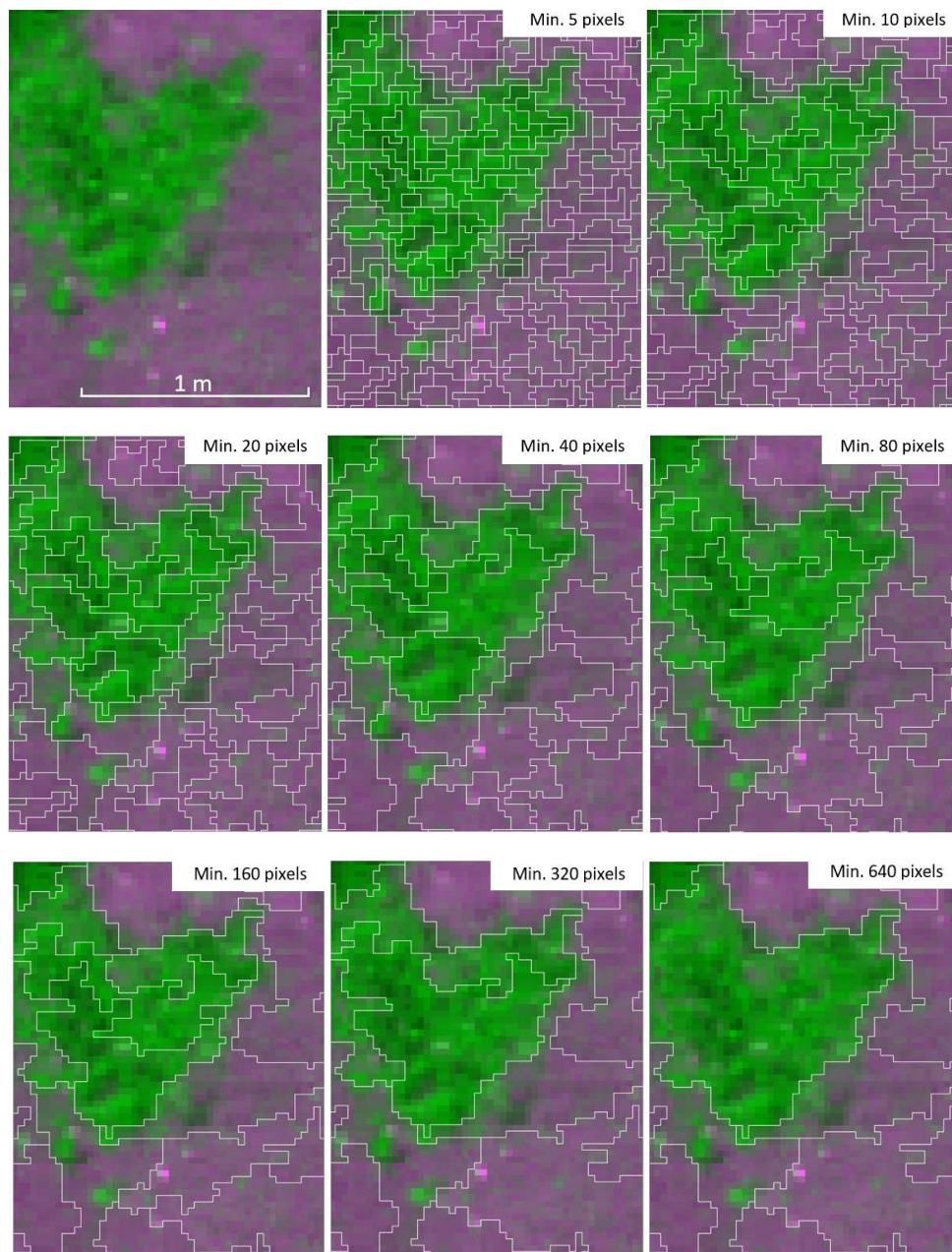


Figure 5.4. Example of the segmentation size-range resulting from an increase in the segment size threshold parameter. Segments are overlain on actual seagrass position as visible in the false-colour enhanced image sample shown here. In this colour scheme, bright green hues denote seagrass, purple denotes sediment, pink to white hues are shell, and blended grey hue is detritus.

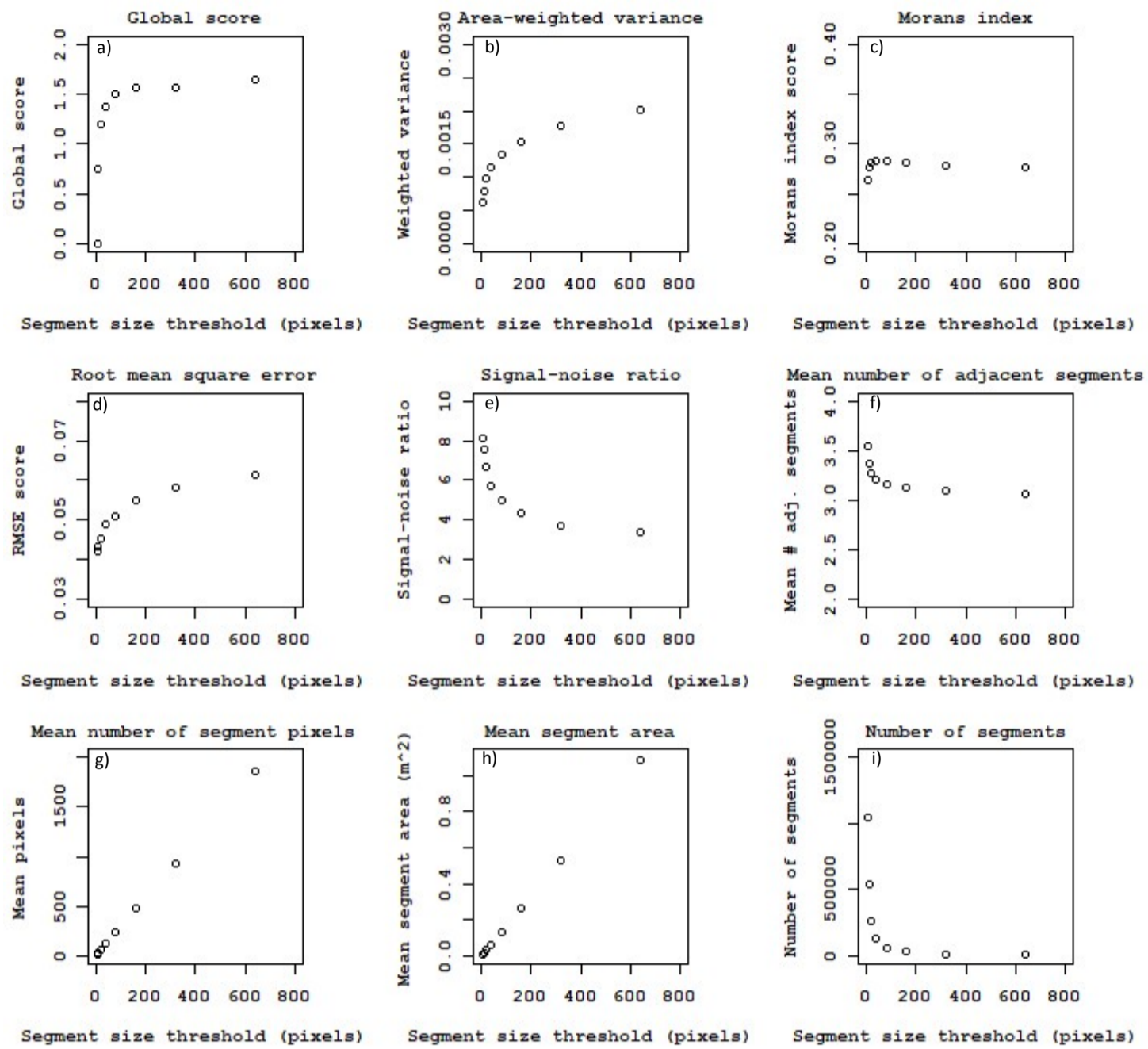


Figure 5.5. Measures used in the unsupervised assessment of segmentation fit where: a) low global score indicates contrast between adjacent segments; b) low area weighted variance indicates segments have predominantly similar values; c) low Moran’s Index value indicates low evidence of autocorrelation between adjacent segments; d) and e) low root mean square and high signal-noise ratio indicate that pixel-values are similar to the segment mean. Other reference attributes include f) mean number of adjacent segments to each segment in the set; g) mean number of segment pixels for each minimum segment size; h) mean area of segments; and i) number of segments across whole image.

5.4.3 Classification and assessment

Three classifiers, linear discriminant analysis, random forest and support vector machine were applied to each of the ground-validated polygon datasets representing a range of segmentation scales. Selection of these classifiers is discussed in Appendix section 5.7.1.5.

Sensitivity analysis on the random forest *ntree* parameter (i.e., the number decision-trees used for averaging) indicated only minor gain in accuracy with *ntree* > 500, and negligible additional benefit with *ntree* > 1000 (Figure 5.6). Computation time was acceptable for *ntree* = 1000, therefore this parameter value was applied for all subsequent use of random forest in this chapter.

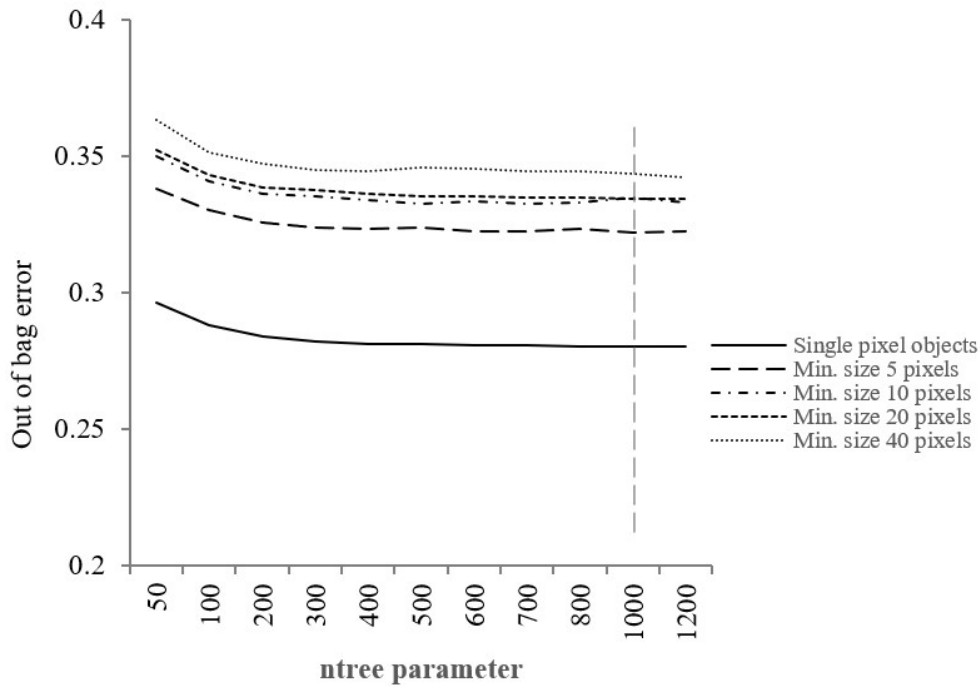


Figure 5.6. Sensitivity analysis on the *ntree* parameter, comparing out of bag error rates across a range of *ntree* values for different image segmentation scales. The vertical line indicates *ntree*=1000, which was used for subsequent testing using the random forest method.

Classification of high-density seagrass was accurate in most cases, with producer accuracy levels of up to 90% and user accuracy up to 84% for this class (Appendix 5.7.4). However, the classification was confused for lower density seagrass classes with accuracy values spanning poor to moderate accuracy levels (Figure 5.7, Appendix 5.7.4).

Detection of seagrass generally decreased with increasing minimum segment polygon size. Seagrass/detritus and seagrass/shell mixtures were poorly classified.

Classification accuracy across all classes was greatest at pixel-scale and accuracy generally decreased with increasing minimum segment size (Figure 5.8). Random Forest generally yielded higher classification accuracy than LDA and SVM. At small segment size SVM classified better than LDA in terms of producer accuracy and overall accuracy, although achieved higher levels of non-target exclusion than the other classifiers with respect to user accuracy (Appendix 5.7.4). The highest overall classification rate across all ground classes was pixel-based classification using the random forest classifier, achieving an overall accuracy of 71%. Seagrass detection rates were highest with the random forest classifier and decreasing segment size (Figure 5.8).

While the classification accuracy peaked at 71%, classification based on the more straight-forward measure of seagrass presence/absence extracted from these same classes (i.e., with ground-class recoded to binomial ‘seagrass’ or ‘no seagrass’) yielded a detection rate as high as 98% for the pixel-scale classification using the random forest classifier. In other words, 98% of actual seagrass-containing segments were ascribed one of the target seagrass classes, even though there was misclassification in the exact seagrass density/mixture class.

Sediment classified at high accuracy level when unmixed with other material (pure sediment; Figure 5.7). However, when mixed with seagrass, detritus and shell, there was poor class separability in terms of the low observed user and producer accuracy (Figure 5.7).

The key predictor variables differed between classifiers (Figure 5.9, Appendix 5.7.5). For example, classification using LDA was influenced heavily by the texture variables, which were less influential in the RF model. The relative influence of predictors also varied with segmentation scale (Appendix 5.7.5). Although there were some highly influential predictors for specific iterations, there was no clear common set of influential predictors that suggest preferential inclusion in future models (Figure 5.10). It is worth noting, however, that *red*, *green*, the texture band *Haralick's correlation* and several red-edge based vegetation indices were consistently important predictors across classifiers (Figure 5.10).

The basic spectral information available is contained in the camera bands (green, red, red-edge, NIR). Vegetation indices add contrast to differences in spectral information. Texture information models the spatial distribution of spectral information. Classification using only the camera bands yielded weaker classification than models including vegetation indices and textural information (Appendix 5.7.6). The best

classification results were achieved factoring all predictors. Camera bands combined with texture layers also yielded among the better of classification outcomes (Appendix 5.7.7). For models containing all possible layers, the predictors of type ‘band’ and vegetation ‘index’ were most important within the models, then ‘texture’, and segment ‘geometry’ was least important (Table 5.4).

Table 5.4. Variable importance, as mean decrease in accuracy across iterated replicates, for each segmentation scale, aggregated by the type of predictor as one of the class-set ‘band’ (green, red, red-edge, NIR), ‘index’ (e.g., NDVI), ‘texture’ (e.g., entropy) or segment ‘geometry’ (e.g., perimeter/area ratio).

Attribute	Single pixel	5	10	20	40
Band	6.3	5.2	4.5	4.7	4.0
Index	5.2	6.0	5.0	3.7	4.0
Texture	3.3	2.7	2.4	1.3	1.9
Geometry	<i>n/a</i>	0.2	0.2	0.1	0.1

The optimal subset of predictors, based on feature selection by recursive feature elimination, varied between classifiers (Figure 5.9 and Appendix 5.7.5). Overall there was little or no demonstrable change in classification model accuracy by sub-setting variables within the model using recursive feature elimination (Figure 5.11). Feature-selection based only on eliminating collinear variables reduced the overall classification accuracy in the range of 2-4% in accuracy units (Figure 5.11). There was varied effect of collinear or RFE feature selection on classification of individual seagrass density classes across the range of segmentation-scales tested (Figure 5.12). For high density seagrass, user accuracy was generally highest when there was no feature elimination, and producer accuracy was highest when RFE reduction was applied.

Comparing red-edge and NIR bands as alternatives for use in derived index calculations, indices that were calculated with red-edge consistently yielded higher rank (i.e., lower mean rank position) than when NIR was used (Figure 5.13). However, considering these as individual predictors, NIR was a marginally better predictor than red-edge for small segment sizes.

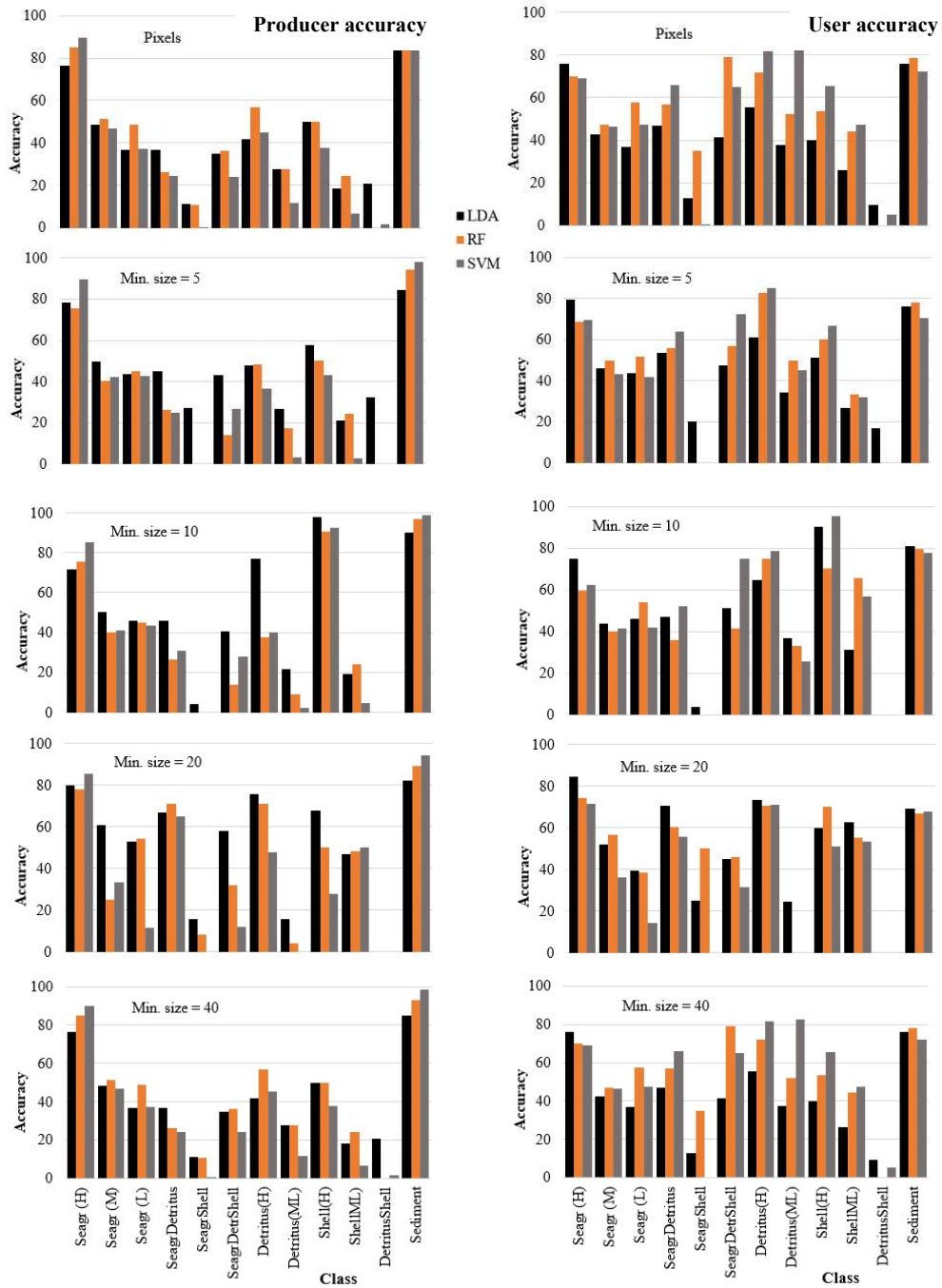


Figure 5.7. User and producer accuracy for target ground classes, in each of the five segmentation scales assessed, and comparing classifiers. User accuracy (right stack) of charts organised by increasing minimum segment size) and producer accuracy results (left stack) are organised with the respective linear discriminant analysis (LDA), random forest (RF), and support vector machine (SVM) results contrasted for each ground class result.

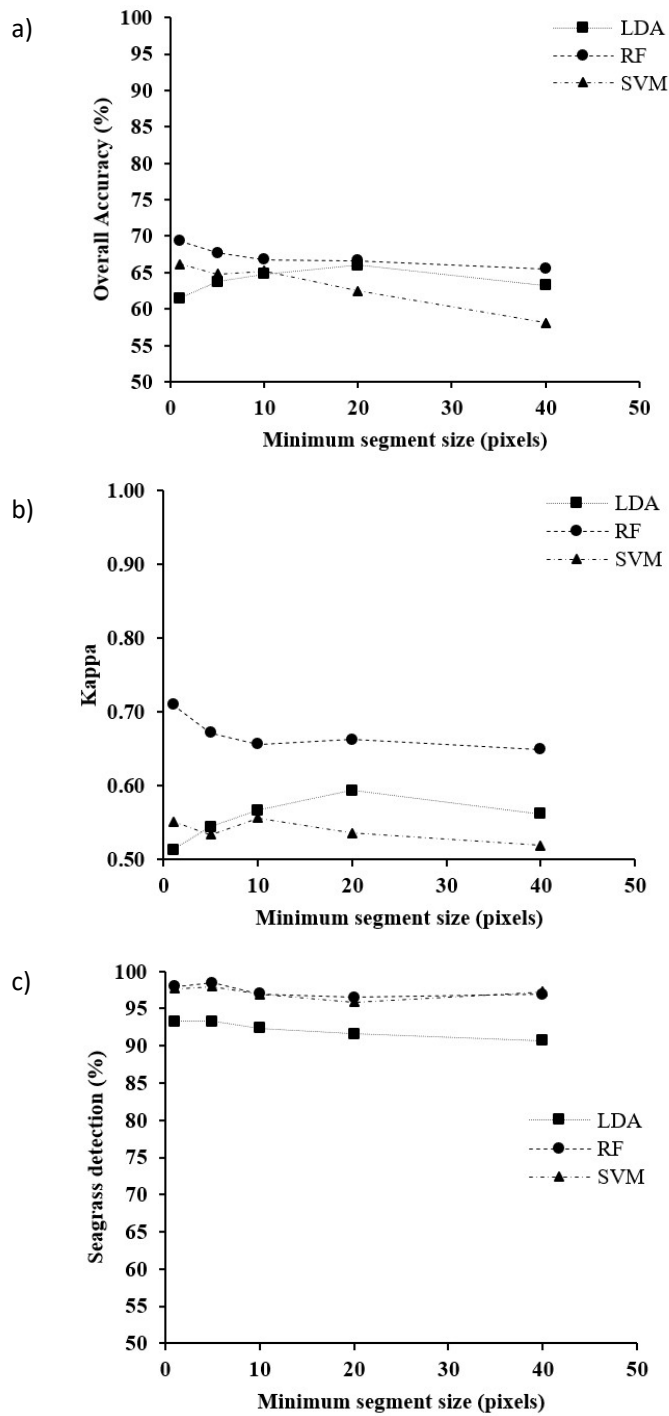


Figure 5.8. Accuracy statistics across all ground cover and density classes: a) overall accuracy (total rate of correct classification outcomes); b) kappa statistic (classification accuracy relative to a random chance outcome); and c) seagrass detection (the proportion of actual seagrass from any density class that was classified as seagrass by the model).

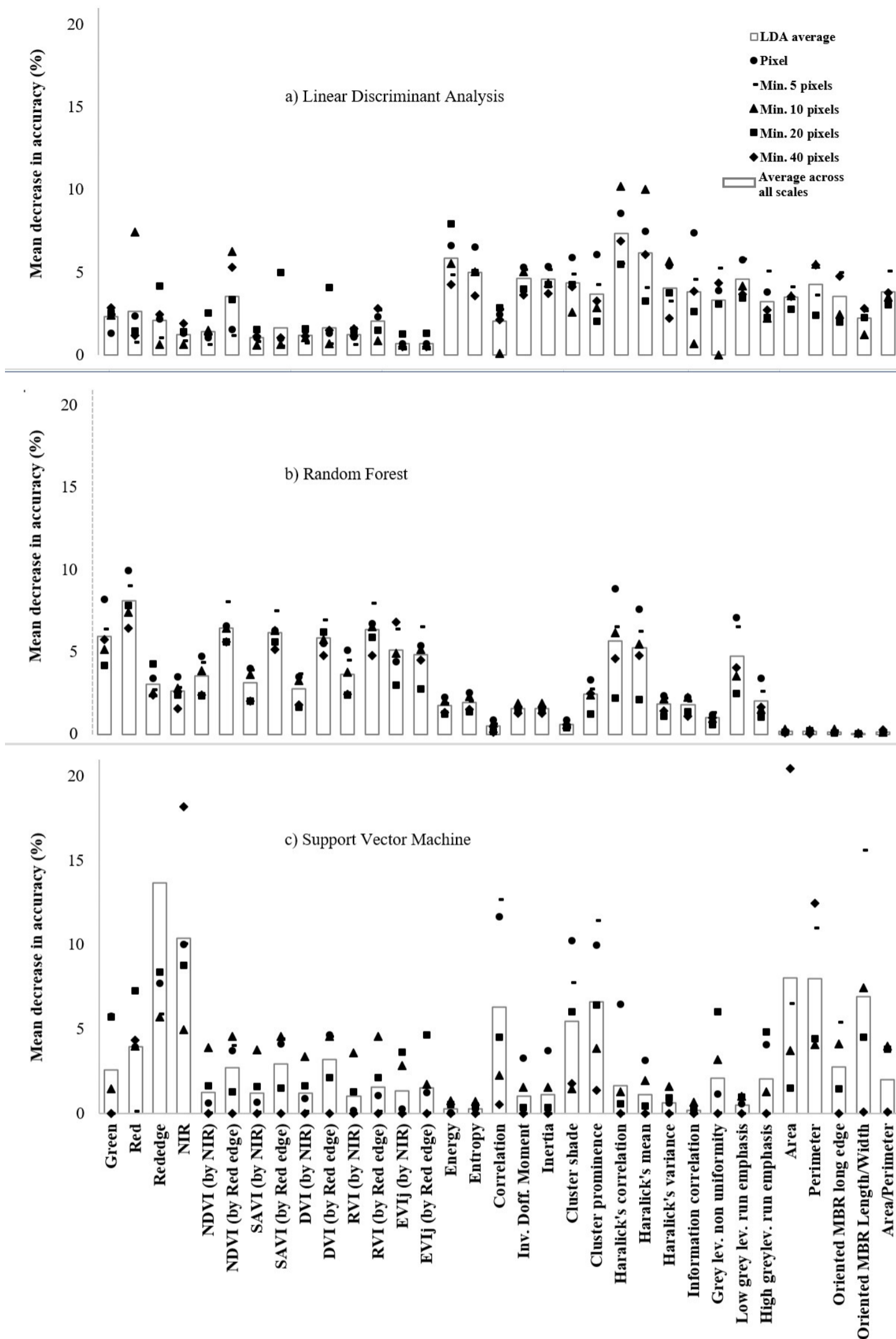


Figure 5.9. Relative predictor importance for spectral, texture and segment geometry predictors across the range of segmentation scales and the three classifiers tested: a) Linear Discriminant Analysis; b) Random Forest; and c) Support Vector Machine. Point symbols show the relative contribution value from the variable importance function within each classifier respectively, contrasting the values attained at each segmentation scale. This point plot is arranged to illustrate the general tendency in predictor impact for each classifier. Columns show the average across all segmentation scales for each classifier.

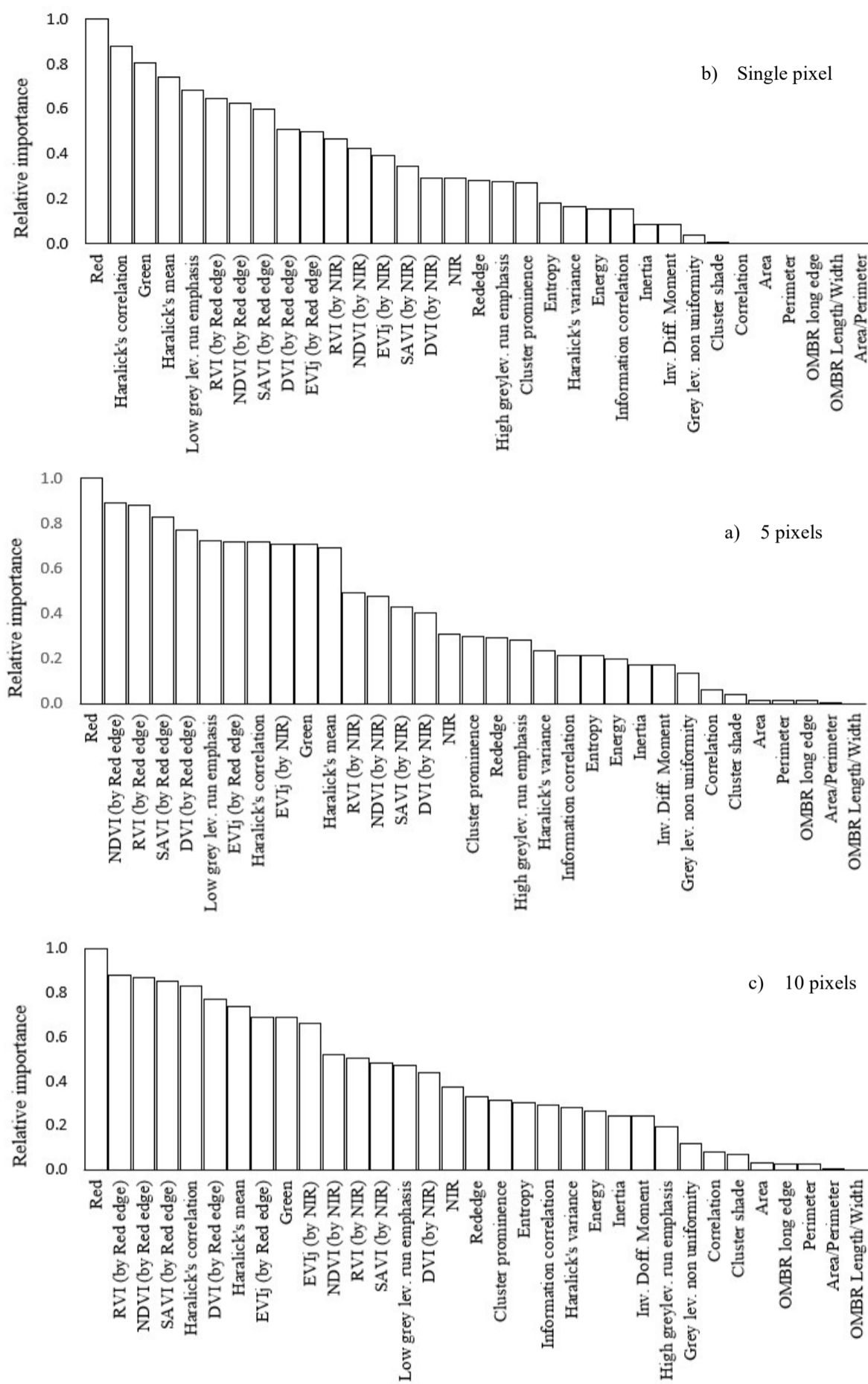
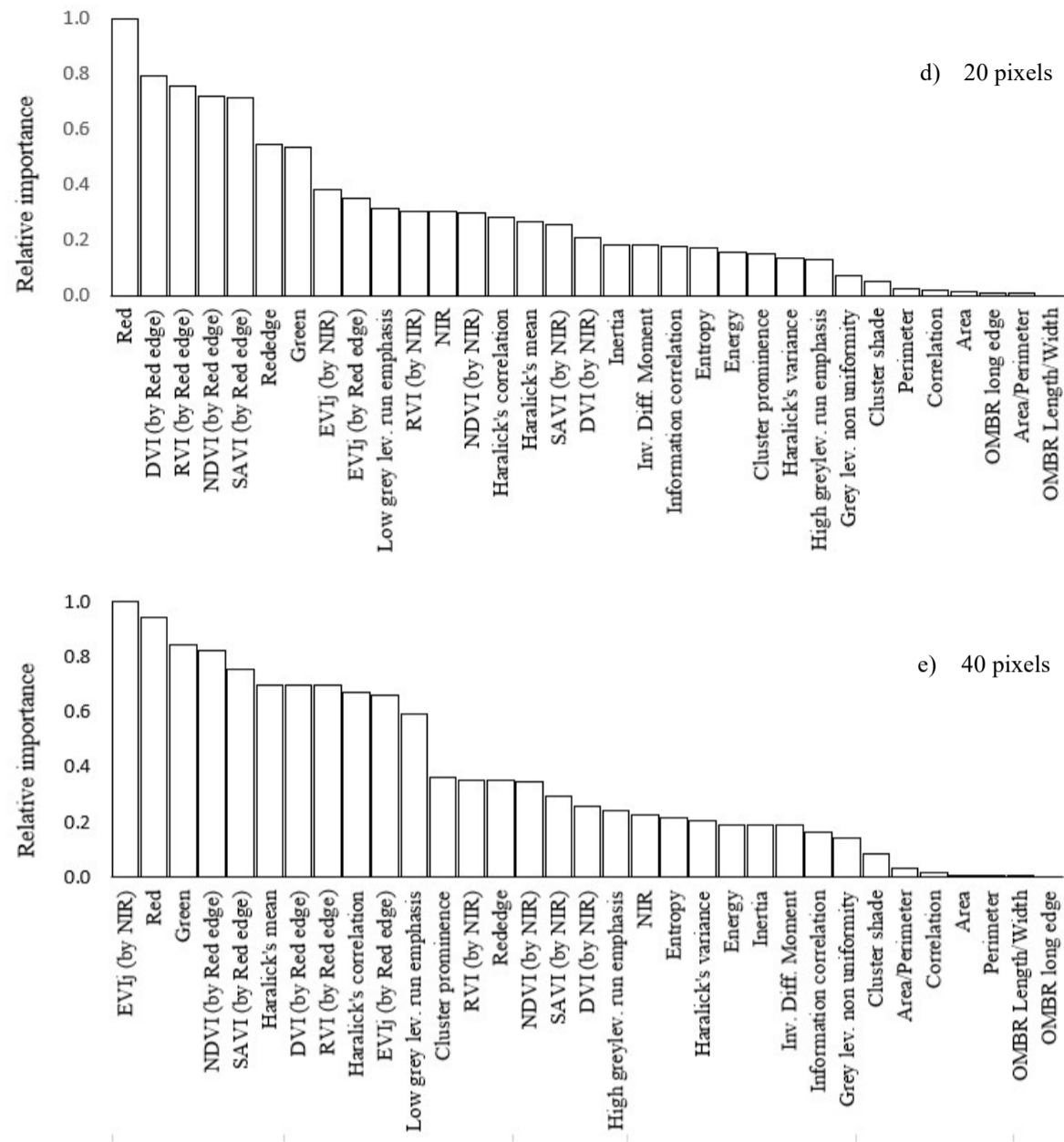


Figure 5.10. Predictor importance in decreasing order of relative influence (least influential on the right) for the five segment scales test under the random forest classifiers tested. Units are normalised relative importance on a scale where 0 is least important and 1 is most important. The five charts relate ((a) to e)) respectively to each of the five segmentation scales tested (single pixel, and minimum size 5, 10, 20 and 40 pixels). Ctd. next page.

(Figure 5.10 ctd.)



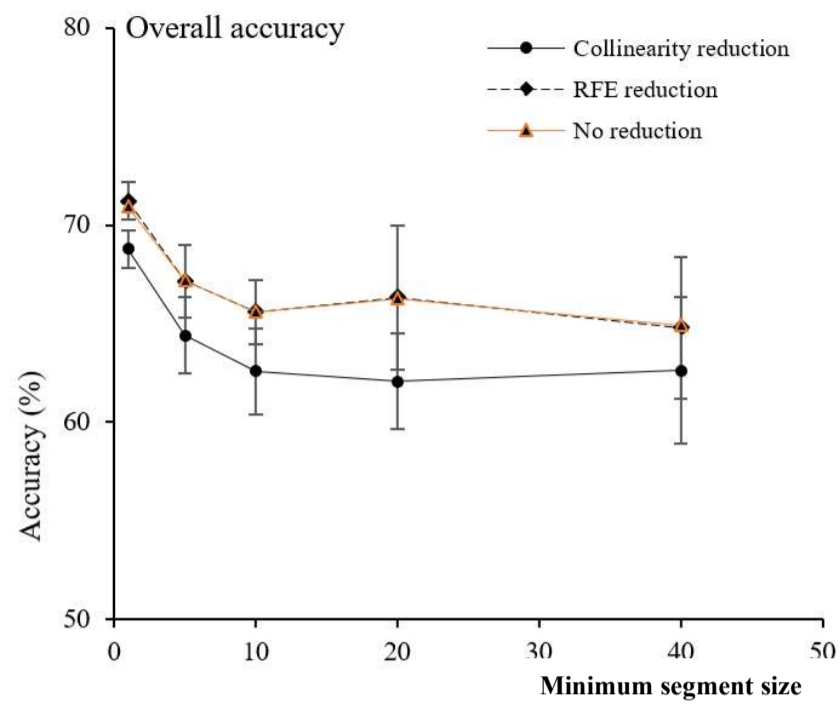


Figure 5.11. Mean overall accuracy of random forest classification models under three variable-selection regimes: no reduction (all predictors present); collinear reduction (elimination of similar predictors in descending order of importance); and recursive feature elimination (automatic selection eliminating variables of low variance contribution), for all segmentation scales pooled. Error bars are standard deviation about the mean of 100 model iterations.

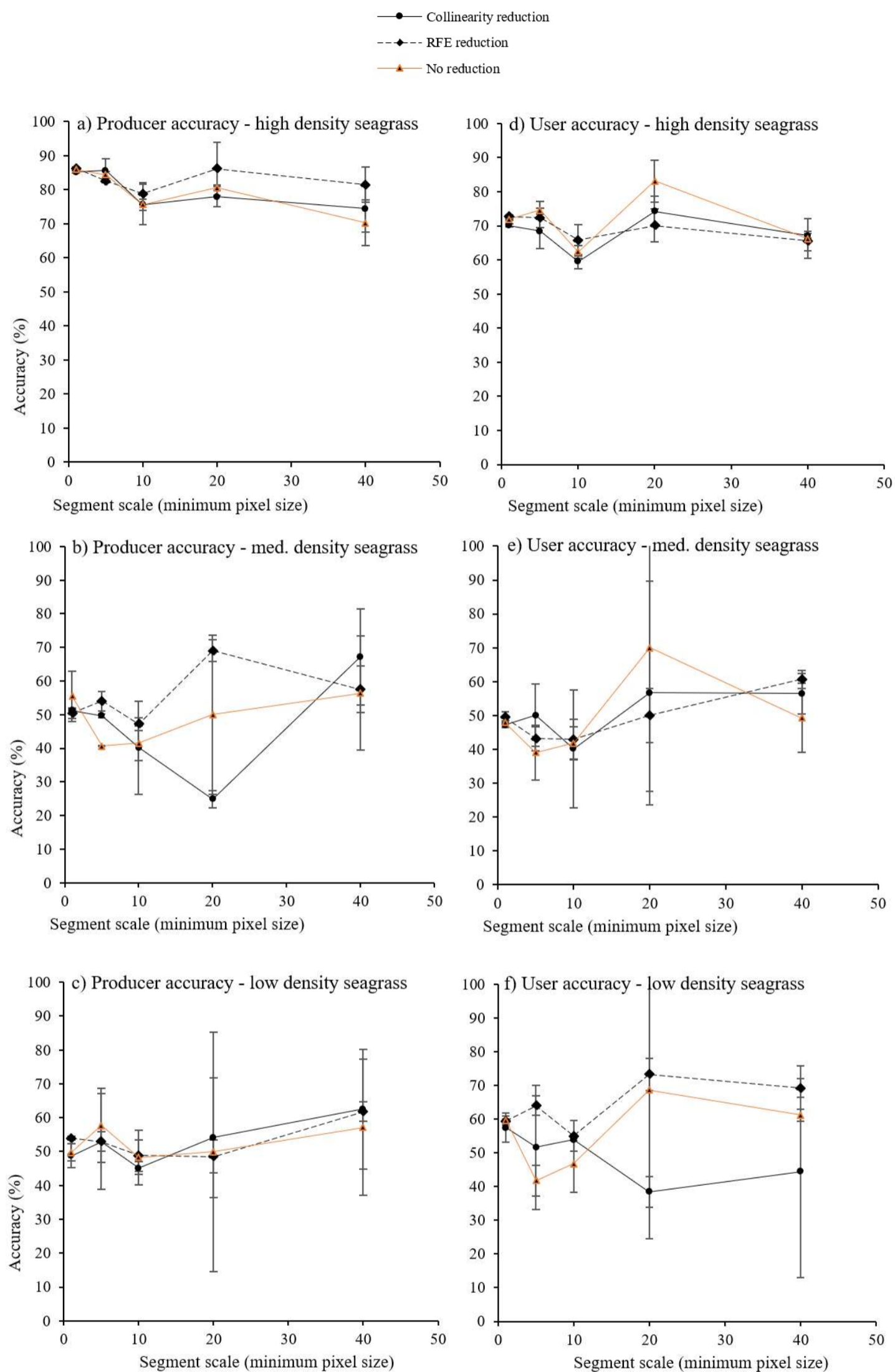


Figure 5.12. Mean accuracy of classification models under three variable-selection regimes in terms of producer accuracy (a-c) and user accuracy (d-f), and by seagrass density class, iterated across the separate segmentation scales. Note that classes for non-mixed high, med. and low seagrass coverage are presented here, i.e., mixed detritus and shell classes are not shown. Error bars are standard deviation about the mean of 100 model iterations.

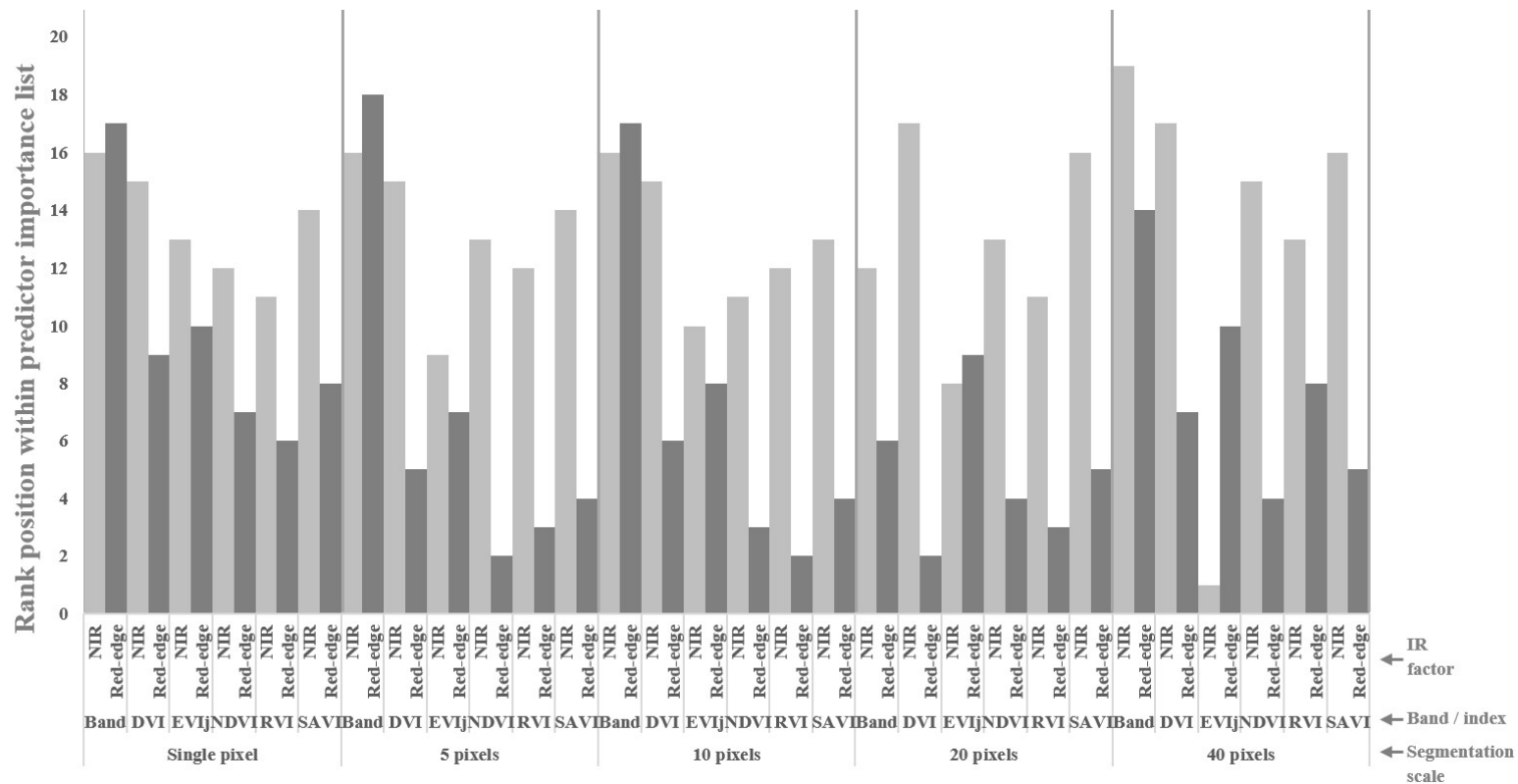


Figure 5.13. Comparison of the performance of near infra-red and red-edge directly as predictors, and indirectly as alternative components of the respective vegetation index calculation (NIR-light grey, red-edge dark grey). Of these, NIR is the conventional factor used in published vegetation indices, and red-edge is a possible predictor that may have value for contrast to red reflectance in a data-mining context. In this chart, *lower* mean rank values indicate *greater* influence (i.e., small is good).

5.4.4 Seagrass mapping and replication

The mean accuracy level was lower in April 2017 (76%) as compared to accuracy attained in February and March 2018 (84 and 83% respectively) (Figure 5.14). Overall there was a significant difference between mean accuracy levels when comparing pairwise between survey times ($F_{[2,2992]}=92113$, $p < 0.001$; Tukey's pairwise comparison $p < 0.001$ in all cases). Per-class seagrass classification accuracy was high in the two 2018 survey as compared to the 2017 at a similar time of year (Appendix 5.7.8).

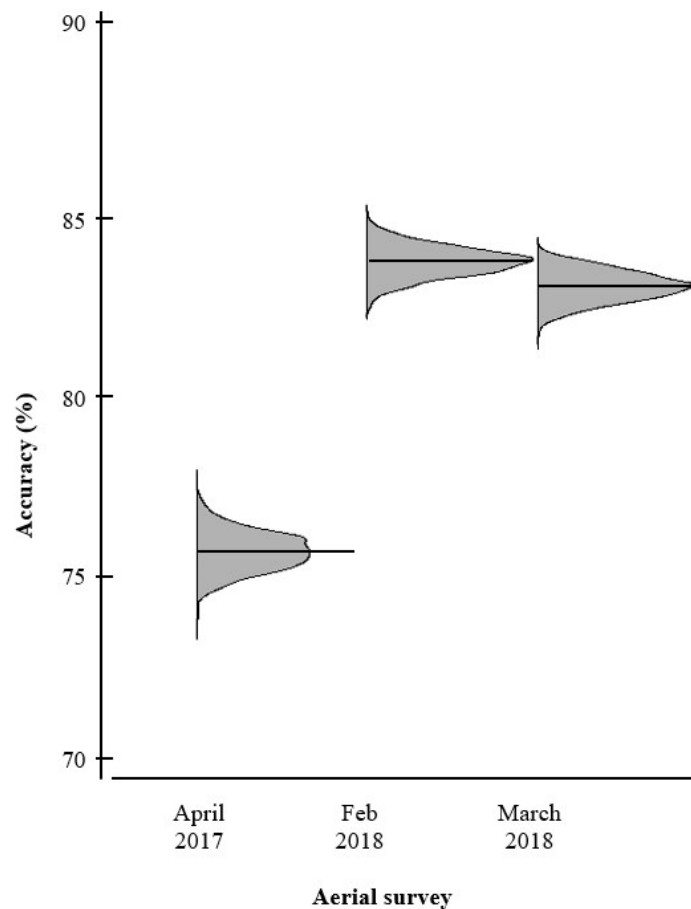


Figure 5.14. Comparison of accuracy outcome across three sample periods. Distribution plots depict median accuracy levels and the frequency distribution around the median, for each of the three aerial surveys. Data relate to classification accuracy values from $n=1000$ cross-validated classification iterations per survey.

The predicted seagrass maps located most seagrass as being within actual ground-survey plots of distribution (Figure 5.15). This was the case for all three surveys. There was notably more detritus present during the April 2017 survey as compared to both 2018 surveys (Table 5.5) for which detritus was present only in trace amounts (Figures 5.15 and 5.16), Seagrass was erroneously predicted in areas outside of the ground-surveyed seagrass meadow extent equivalent to an 8-17% overestimation of total seagrass (Table 5.6).

Some areas of erroneous mapping were observed as being associated with expansive mats of microphytobenthos or suspended loose (tidal) green plant material in pools and at the low tide extent (e.g., accretion of seagrass leaf, mangrove leaf and pod, and green leaf of terrestrial origin) (Figure 5.17). However, these areas were outside of the extent of the ground-level photography so can't be quantified. Some established cockle (*Austrovenus stutchburyi*) shell accumulations, with green algal staining, were also falsely classified as seagrass.

There was a notable contraction of the seagrass meadow boundaries between the 2017 ground census and the 2018 census (see Figure 5.16 for example, and Chapter 3 Section 3.6.3 and Figure 3.19 for census). This reduction in seagrass was detected by the classification and mapping method tested here (Figure 5.15).

Table 5.5. Estimated detritus and shell content for each of the three surveys, to illustrate the difference in detritus contamination between surveys. Proportion relates to the focus area (bounding rectangle) of 11360 m².

	Detritus		Shell	
	Predicted area containing detritus (m²).	Proportion of the focus area (%).	Predicted area containing shell (m²).	Proportion of the focus area (%).
April 2017.	1645	14	1219	11
Feb 2018.	26	< 1	970	9
March 2018.	134	1	1772	16

Table 5.6. Proportion of predicted seagrass within and outside of the actual ground-surveyed seagrass meadow zone as depicted in Figures 5.15 and 5.16. Error refers to the extent of erroneously classified seagrass situated in the area verified by ground survey as not containing seagrass, as a proportion of total estimated seagrass.

	Predicted seagrass outside of actual seagrass zone (m²)	Predicted seagrass within actual seagrass zone (m²)	Error (overestimation) (%)
April 2017.	287	3365	8
Feb 2018.	652	3259	17
March 2018.	609	3239	16

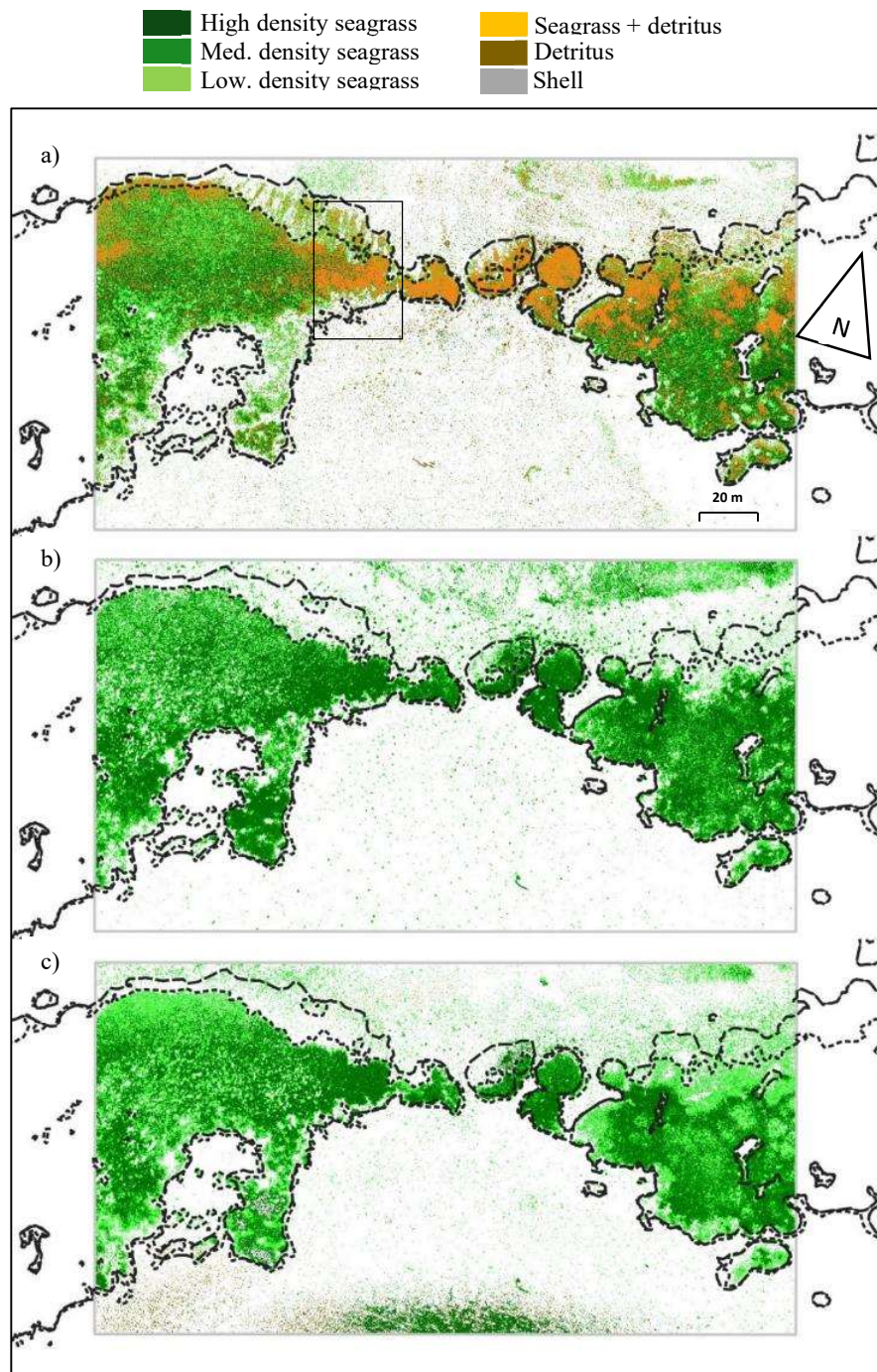


Figure 5.15. Ground cover and seagrass density estimate as generated from the random forest classification model for each of the three surveys: a) 9th April 2017; b) 2nd Feb 2018; and c) 28th Mar 2018. The light grey box provides a common focus area across the three surveys. The small black box in (a) shows the position of the enlargement given in Figure 5.16.

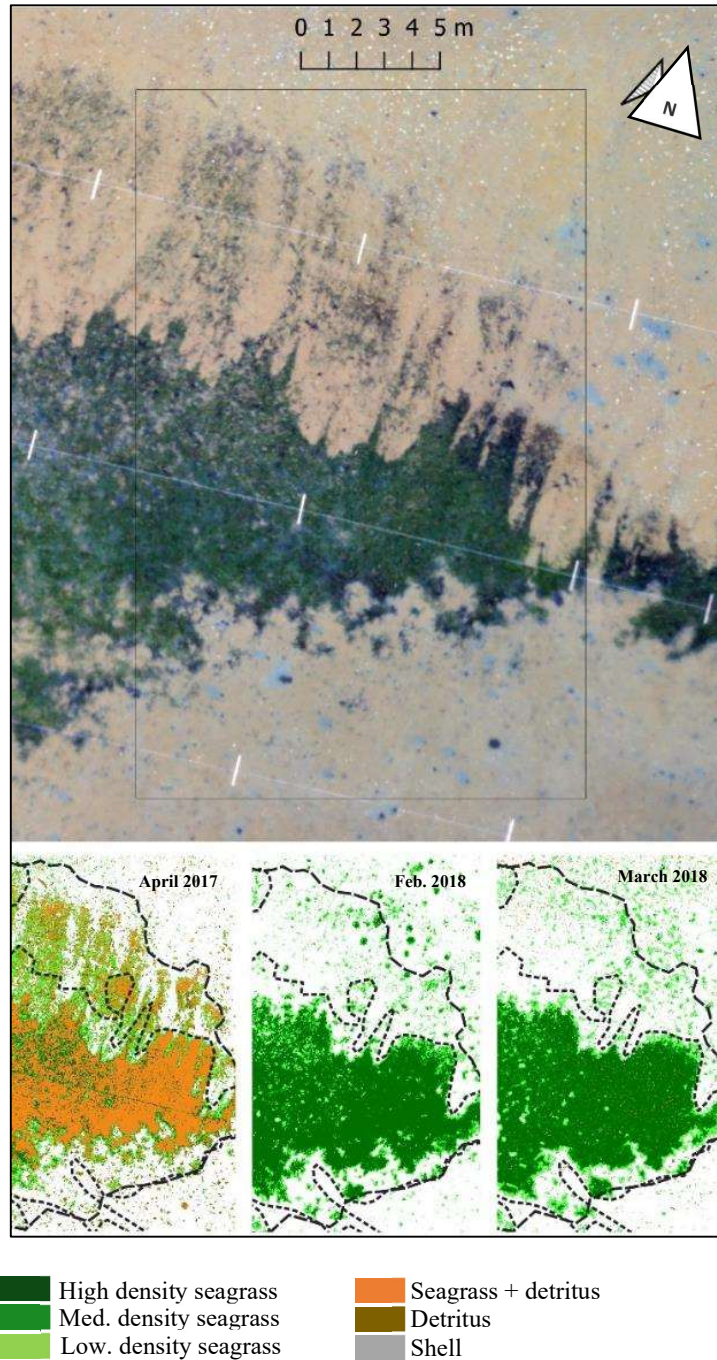


Figure 5.16. Enlargement of an area of seagrass under pressure from sediment inundation. Precision ground-survey (GNSS-tracks) are shown for the April 2017 seagrass census (long-dash) and April 2018 census (short dash). The colour RPA photography (upper pane) shows for reference, the seagrass scene taken during the April 2017 RPA survey. The lower three frames show predicted groundcover for the three surveys (April 2017, February 2018 and March 2018).

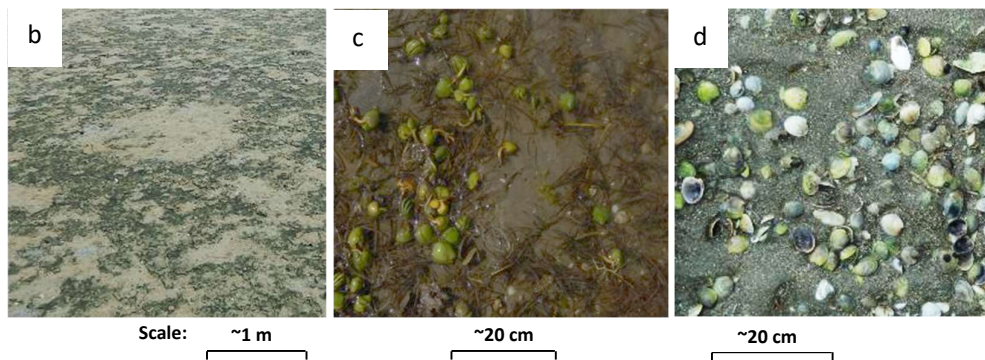
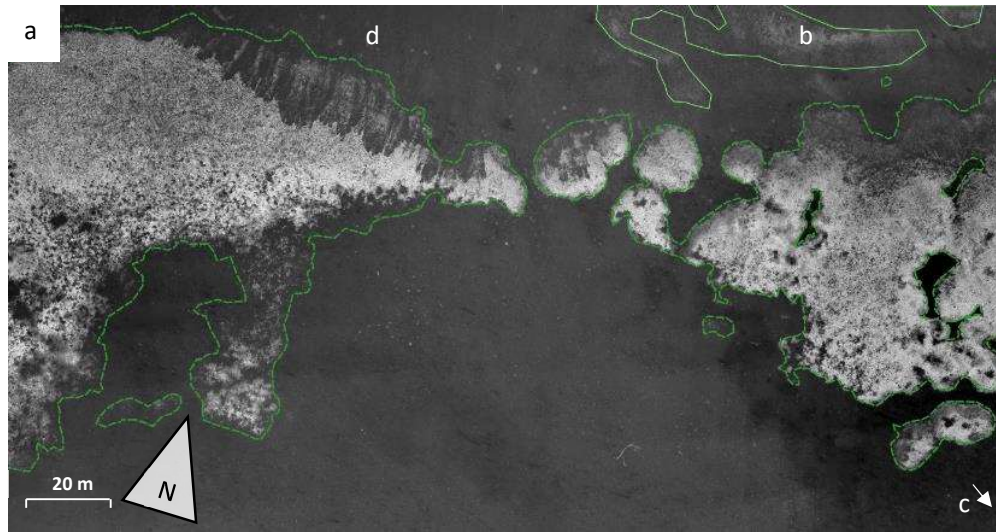


Figure 5.17. Examples of non-seagrass surface content that can be mis-classified as seagrass. The upper frame (a) shows the normalised difference vegetation index NDVI layer (i.e., denoting photosynthetic activity) marked with surveyed seagrass extent (long dashed line) and approximate microphytobenthos (MPB) extent (solid green line). Lower frames include: ground level photograph of MPB (b); loose seagrass and other green plant material accumulate in pools (c); and green stained shells that can also overlap in appearance with sparse seagrass (d). Approximate locations of (b-d) are shown by white letters in (a).

5.5 Discussion

In this chapter, pixel-based image analysis was compared to object-based analysis at a range of segmentation scales to determine the optimal scale, classifier, variable selection approach, and to assess the value of vegetation indices and texture layers. A classification process was developed that ingests RPA imagery, ground observations and spatial referencing data to yield spatially explicit classification results. The method is viable at multiple survey epochs (Section 5.4.4). Classification improves with decreasing segmentation scale and highest classification accuracy is attained at pixel scale (Section 5.4.2). The classification algorithms Random Forest and Support Vector Machine provide superior classification outcome for seagrass coverage estimation compared to Linear Discriminant Analysis: of these Random Forest is marginally better for mapping (Section 5.4.3).

Under the Random Forest workflow, there is no appreciable benefit to performing collinearity reduction and feature elimination. Vegetation index and texture layers improve classification accuracy levels with greater influence than the spectral bands alone. For the Random Forest classifier, models classified seagrass with highest overall accuracy when fitted with all predictors, or spectral bands + texture, depending on segmentation scale (Section 5.4.3).

The goal of the above assessment was to recommend a single classification workflow: in this case data indicates the greatest classification accuracy is attained with pixel-based classification using the Random Forest algorithm upon all predictors (no feature selection) and setting the number of decision trees (ntree parameter) to ≥ 1000 .

The closest study to the current research was reported by Duffy et al. (2018). In that study, image acquisition occurred using a quadcopter RPA flown over meadows of the seagrass *Zostera noltii* using a consumer camera. The imagery, along with ground reference observations, were then used to support three classification regimes: two unsupervised classification pathways (the first with red, green and blue, and the second adding texture from the green band) and an OBIA pathway with colour bands and texture (Duffy et al., 2018). Their research concluded that unsupervised classification performed better than their OBIA approach.

Reducing segment size down to the individual pixel scale improved the classification model. There was no literature available at time of writing with methods consistent with those applied here for an estuarine seagrass subject. Similar research into the effect of segmentation scale, for other ecosystem types, varies in the observed response. Dronova et al., 2012 determined for 30 m GSD Landsat satellite imagery over a wetland landscape, that coarser scales of segmentation resulted in greater classification

accuracy that fine scales. Räsänen and Virtanen (2019) determined for a fen ecosystem, that classification accuracy improved with reducing segmentation scale for RPA, aircraft and satellite derived aerial photography at various image resolutions. Johnson and Xie (2011) determined for an urban study area, that intermediate segment scale delivered greatest inter-segment difference with lowest intra-segment variance, as combined in their global score. Yang et al. (2019) determined for a cropland region that intermediate segmentation scales of analysis yielded the highest information gain ratio. Neither of the latter two reported effect of segmentation scale with respect to classification accuracy. Li et al. (2016) determined for an agricultural setting that classification accuracy generally reduced with decreasing segmentation size under SVM, adaboost and naïve Bayes classifiers, but increased under the random forest classifier. Li et al. (2016) also noted that classifier response to change in segmentation scale differed between their two study areas. This result highlights that projects may not have a single optimum design for remote sensing across a whole site, and hence assessment of optimal scale could vary on and estuary section by section or temporally.

The approach of Lathrop et al. 2006 - dividing a seagrass landscape into sections at multiple scales based on character then classifying sections separately using OBIA could be suitable for larger scale application. Image analysis in this chapter (and Chapter 4) sample one of a number of discrete hydro morphological seagrass situations on Wharekawa Harbour (e.g. upper tidal seagrass patches on sand, seagrass on permanently saturated mud-fields, subtidal seagrass in estuarine channels).

Seagrass can present as objects that are as small as just a few centimetres in size, and in scenes mixed with similar sized non-target objects including shells, twigs, pinecones, leaves, and macroalgal fragments (discussed in Chapter 2). Thus, the lower limit of scale assessed under this investigation inevitably targeted this small scale of detail. Much of the study area comprised heterogeneous mixed scenes with shell and detritus scattered variably, although detritus content reduced dramatically by the following year. Larger segmentation scales absorbed small shell and detritus objects into the polygon geometry. Segmentation polygons may increasingly be drawn erroneously as the segmentation scale increases, due to sub-pixel mixing and blend of spectra across adjacent pixels. In smaller segments the contaminating objects sit in isolated segments. This difference may in part explain the observed improvement in classification accuracy, intra-segment variance, and segment dissimilarity with decreasing segment scale.

Of the three classifiers, random forest yielded the greatest classification accuracy for seagrass density classes and detection, and there was little gain from feature-set

reduction using random forest. Given the additional computer run-time (hours) for the recursive iterations under random forest, there is little gain to be made by including this step in the processing pipeline. The results therefore indicate that a strategy for further work should include all spectral, derived index and texture layers in a random forest classifier and then allow the classifier to fine-tune the optimal classification using the internal decision tree process and associated resampling aggregations.

The feature selection scenarios explored in this analysis indicate that the derived indices and texture layers have predictive value that is worth the additional cost in processing time. The segment geometry attributes added little to classification accuracy under this scale of survey. The red, green, Haralick's correlation and several red-edge based vegetation indices were generally the most influential predictors across the range of classifiers and scale tested. However, the specific importance varied with scale and classifier. Recursive feature elimination did not yield a significant gain in classification accuracy. Reduction of the feature-set based on reducing collinearity did not result in accuracy gains. Consequently, recursive feature elimination and collinearity reduction are not of benefit to seagrass classification with this camera and survey scale.

Other studies, however, establish classification improvement from recursive feature selection. For example, for an image classification using Worldview 2 satellite imagery over bamboo habitat, Ghosh and Joshi 2013 applied RFE to find a set of predictors to optimise classification. Their classification was iterated comparing the best 5 and 10 predictors derived from RFE, as well as all 32 predictors: the subset of best 10 yielded the highest classification accuracy. This result may be particular to the monotonic bamboo habitat.

Seagrass density class attribution in the 2017 survey was moderate to poor, except at high seagrass density due to the confounding influence of detritus and shell. Class accuracy for seagrass was better in the two 2018 surveys that were not affected by storm debris. Seagrass survey and mapping may therefore be confounded if undertaken following storm damage or where partial sediment burial or high detritus/shell deposition is present. Annual monitoring of seagrass extent retaining sensitivity at low seagrass density may require survey times that avoid post-storm interference, excepting cases where the storm or related damage is the subject of the survey.

Seagrass features were extracted using a class typology based on the dominant presentations of seagrass found in the estuary, and quantifying apparent density of seagrass coverage within sediment, shell and/or detritus background components. Factoring the mixed classes was important because these confounded classes became evident and the source of classification problems could therefore be better understood

(e.g., seagrass/shell and detritus/shell were problematic classes as visible in Figure 5.7). The results here indicate that setting the timing of the survey to the time of year of high seagrass density but avoiding periods immediately following high turbulence and stream-inflow, results in better classification and mapping at a time of weather disturbance.

The high rate of seagrass detection does, nonetheless, indicate that the method is suitable for binary seagrass mapping. However, an observation made on site at the time of the survey, was that algae and/or microphytobenthos (MPB) formed dense mats near to the flying site. These were not incorporated within the study site directly but may well present a potential confounding effect if they overlap both spectrally and spatially with seagrass area of interest. It should also be recognized that the results obtained here are likely to exhibit some further dependency to flying height and associated difference in pixel ground sampling distance. Further verification of seagrass detection and class separation red at higher flying heights may allow the survey area per flight battery to be expanded.

The class attribute was based on visual interpretation of ground-level photography including a 3-tier seagrass coverage indicator. Consequently, this method captures the judgement of the observer in ascribing the training dataset classes and so there is potential for user bias. This issue is examined in Chapter 6.

Based upon the outcomes of this chapter, the recommended method arising from this chapter for seagrass mapping is single pixel segmentation scale for classification, using a random forest classifier, with no feature selection and class breakdown of seagrass presentation within the ground reference dataset. This method is suitable for detection and mapping of seagrass at 30 m flying altitude using a 4-band multispectral camera, utilising both spectral and textural information.

5.6 Conclusion

In conclusion, this chapter reports on an assessment of candidate classification methods based on a review of image analysis workflow components relevant to seagrass feature extraction (Appendix 5.7.1). The approach includes examination of segmentation methods (with scale selection determined via and unsupervised inter- and intra- variance method) followed by a range of classifiers that include linear discriminant analysis, random forest and support vector machine. Results demonstrated that all three classifiers were capable of yielding moderate-high classification accuracy with replicability. Random Forest and Support Vector Machine stood out as the most effective in detecting and classifying seagrass. A range of segmentation scales was assessed, from the single-

pixel scale upwards, and the single-pixel scale was found to generate optimal performance.

The most effective classification regime tested here was the random forest method applied to pixel classification using all predictors available. The suitability of the approaches used do, however, require further testing across all possible seagrass environments. This would require a range of contrasting scenes to be assessed together.

The workflow developed is semi-automated providing opportunities for sequential quality assurance and performance assessments. However, by using FME and R programming with python process control, the script components could be re-formatted to provide a fully automated machine learning framework. The process receives input from RPA imagery, ground observations and spatial referencing to yield a classifier that can be applied to a subject image. The classification method applied here resulted in maps that accurately described the presence/absence of seagrass, and spatial distribution of the seagrass meadow across three surveys spanning a year of seagrass change. Immediately following a storm, the classification was confounded in part by the presence of high levels of detritus and shell. Classification was more accurate one year later in similar seasonal conditions, but without the recent storm disturbance. Classifying the non-seagrass scene content yielded information about the prevalence of disturbance-related detritus on the scene.

There was moderately good differentiation of seagrass condition in terms of the visually interpreted coarse density class-set used for classifying the training and test ground reference data. However, such perception-based classification is prone to observer subjectivity. Therefore, Chapter 6 examines classification using accurately quantified seagrass density measures for model training, and thus explores the maximum classification accuracy levels likely possible from this method and site.

5.7 Chapter appendices

5.7.1 Appendix 5.7.1. Background literature review relevant to object-based image analysis for seagrass feature extraction.

5.7.1.1 Object-based image analysis components

Numerous approaches to image classification have been developed within the remote sensing field. Lu and Weng (2007) identified groups as including per-pixel (class membership per-pixel based on endmember signature), sub-pixel (proportional membership for mixed pixel content), object-oriented (classification of pixel-cluster objects), and per-field (classification within vector areas). The relative efficacy of pixel-based image analysis (PBIA) and object-based image analysis (OBIA) have been examined (Blaschke et al., 2014; Myint et al., 2011). OBIA advances upon the pixel-scale approach by considering group-level characteristics including summary statistics for band digital numbers (e.g., mean, variability, range etc), the geometric properties of each object (e.g., area, length, perimeter, rectangularity) and the characteristics of adjacent or nearby pixels (e.g., texture, grey-level co-occurrence, contextual information).

A potential success factor for OBIA is that additional data about the spectral or physical structure of a landscape (as additional variables in a predictive model), is available to increase clustering contrast and differentiating power. In general, OBIA has enhanced classification performance compared to pixel-based classification due to increased information aggregated within the object components, and greater potential contrast between endmember groups (Benfield et al., 2007; Frohn et al., 2011; Whiteside 2011; Ursani et al., 2012; Cai and Liu 2013; Blaschke et al., 2014; Wahadin et al., 2015; Khatami et al., 2016; Ventura et al., 2016; Ma et al., 2017). For example, Myint et al. (2011) concluded that the OBIA method tested in their research dramatically outperformed the best of pixel-based methods tested. In a review of wetland remote sensing studies, Dronova (2015) observed increased classification performance and identified the following benefits of OBIA: i) additional object characteristics and metric attributes that can be factored into the classification model; ii) smoothing of local spectral variation; and iii) the ability to quantify landscape structural hierarchies at multiple scales. Similarly, Ventura et al. (2016) successfully mapped seagrass using a range of classifiers applied to consumer drone imagery (RGB) to an accuracy level of 93% with highest feature extraction accuracy found using object-based methods based on eCognition software. Object-based image analysis also allows for segmentation and classification in an ecologically relevant context (e.g., vegetation patches and structural features), which are not necessarily captured by a pixel approach (Dronova, 2015).

For the purpose of this chapter, a process-flow for OBIA is generalised as a sequence starting with input images and training data, terminating with a feature extraction product, and containing one subset of the many available information-processing and extraction components (Figure 5.18).

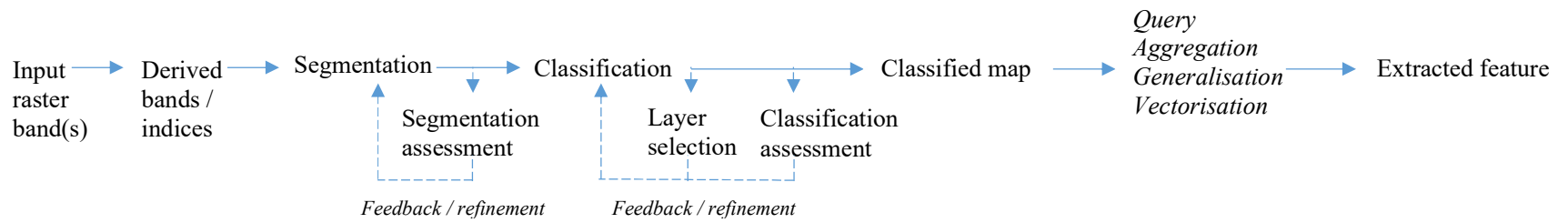


Figure 5.18. Generalised OBIA process as applied to the current study.

5.7.1.2 Input and derived bands

Input data to an OBIA-based classification model can include the raw, value-normalised or reflectance-transformed bands. The bands can also have filtering or generalising transformations applied (Gao et al., 2017). Derived contrast indices within (e.g., histogram equalisation) or between bands (e.g., vegetation indices) can expose new characterising information, reduce variance or increase sensitivity of a classification (Table 5.7). A range of indices have demonstrated improvement to classification models since quantitative satellite imagery became available in past decades (Goward et al., 1991; Roderick et al., 1996; Hao et al., 2008; Adam et al., 2010; Xue and Su 2017).

The normalised difference vegetation index (NDVI) is a commonly used index for multispectral sensors (Yengoh et al., 2015). The NDVI approximates the degree of removal of red light from incident solar radiant power as a result of photosynthesis. Assessments demonstrate that NDVI correlates well with a range of plant condition metrics such as biomass, leaf area index and photosynthetic condition depending on the vegetation scene and scale (Carlson and Ripley 1997; Bakr et al., 2010; Xu et al., 2012; Froidefond et al., 2014; Kuzucu and Balcik 2017; Potgieter et al., 2017; Xue and Su 2017).

Variants of the NDVI have been developed with additional band configurations (Bargain et al., 2012; Xu and Su 2017). For example, Li et al. (2018) demonstrated the value of red-edge-red and red-edge-green contrast-indices that are similar to the NDVI calculation. In their study, the red-edge-green was the most distinctive index for seagrass (Li et al., 2018). Liu et al. (2013) found that NDVI is only marginally affected by changes in sun angle, an observation that has important logistic benefits for drone-flown multispectral imagery (see Chapter 2). Strong et al. (2017) tested the performance of five alternative vegetation indices against the normalised difference vegetation index on grassland imagery taken from a remotely piloted aircraft. They determined that an enhanced normalised difference vegetation index, factoring blue and green bands instead of red and infra-red offered the best ability to differentiate to “grass” scene types.

There are numerous other vegetation indices that have been used to contrast vegetation from non-vegetation and characterise species membership or condition normalised difference vegetation index. These include soil-adjusted vegetation index (SAVI), difference vegetation index (DVI), ratio vegetation index (RVI) and the enhanced vegetation index (EVI) (Jordan 1969; Richardson and Wiegand 1977; Huete 1988; Jiang et al., 2008). Several of these indices have been tested in the context of seagrass mapping (Table 5.7). It’s important to note that vegetation indices can differ in

classification performance (Huete et al., 2002; Hufkens et al., 2012) and in the saturation level at high seagrass density (Bargain et al., 2013).

Enhancements to classification models can also be made by incorporating non-spectral information (Warner 2011; Kumar et al., 2012; Wang et al., 2016). For example, authors Benfield et al. (2007) used distance to land, mangroves and rivers as additional predictive layers in distinguishing coral reef community types using Landsat imagery. Image texture can add important enhancement of image classification (Zhang 2019). For example, in a study using high resolution red-green-blue-infra-red cartographic imagery at 30cm pixel size, Szantoi et al. (2013) demonstrated that classification accuracy increased from 62% to 84% by using both NDVI and texture in an OBIA classification model. Finally, in a meta-analysis of supervised pixel classification research across a range of sensor types, Khatami et al. (2016) determined that inclusion of texture information yielded a notable increase in classification accuracy compared to minor improvement by manipulating spectral information e.g., by index creation or feature enhancement. Inclusion of vegetation indices may not always result in improved analysis. For example, Kuzucu and Balcik (2017) observed reduced classification performance by including vegetation indices in 6 m resolution multispectral satellite imagery.

Table 5.7. Derived layers and indices used in studies of relevance to the multispectral high-resolution seagrass segmentation context (working examples, not originating paper).

Index name	Formula	Seagrass investigation
Normalised difference vegetation index (NDVI). NDVI band variations.	$(\text{NIR}-\text{R})/(\text{NIR}+\text{R})$	Bargain et al., 2012; Dronova et al., 2011. Guichard et al., 2000; Yang and Yang 2009; Lyons et al., 2012; Martin et al., 2014; Szantoi et al., 2013; Kuzucu and Balcik 2017. Li 2018.
Normalized difference water index (NDWI).		
Soil adjusted vegetation index (SAVI).	$(1+\text{L})(\text{NIR}-\text{R}) / (\text{NIR}+\text{R}+\text{L})$	Bargain et al., 2012; Kuzucu and Balcik 2017
Enhanced vegetation index (EVI).	$2.5*((\text{NIR}-\text{R}) / (\text{NIR} + 6\text{R}-7.5\text{B} + 1))$	Bargain et al., 2012; Lyons et al., 2012
Green NDVI.	$(\text{NIR}-\text{G}) / (\text{NIR}+\text{G})$	Yang and Yang 2009; Lu and He 2017
Blue NDVI.	$(\text{NIR}-\text{B}) / (\text{NIR}+\text{B})$	Yang and Yang 2009; Lu and He 2017
Red edge NDVI.	$(\text{R}_{\text{rs}}(700)- \text{R}_{\text{rs}}(670)) / (\text{R}_{\text{rs}}(700)+ \text{R}_{\text{rs}}(670))$	Hill et al., 2014.
Ratio vegetation index (RVI).	NIR / RED	Kuzuku and Balcik 2017.
Visible atmospherically resistant index (VARI)	$(\text{G} - \text{R}) / (\text{G} + \text{R} - \text{B})$	Chayhard et al., 2018b.

5.7.1.3 Segmentation

Segmentation has been defined as a process of partitioning an image into non-intersecting regions such that each region is homogeneous, and the union of no two adjacent regions is homogeneous (Pal and Pal 1993; Espindola et al., 2007). There are numerous algorithms based on clustering and region-growing to partition an image into object-sets (Dronova 2015; Garcia-Lamont et al., 2018). The optimal choice of algorithm may vary depending on the image-type (single versus multiband), required accuracy levels, operator capability (point-and-click software versus iterative code-assembly within an application interface), budget (commercial versus open source) and requirement for adaptive classification (e.g., fuzzy membership, Bayes classifier). Furthermore, as the performance of a remote sensing classification model is likely to vary with data and the physical context. Thus, it follows that even for a specific site there may not necessarily be a single optimal solution (e.g., de Klerk et al., 2016).

Garcia-Lamont et al. (2018) developed a typology of segmentation approaches (Table 5.8). Segmentation can generally be differentiated from clustering in that segmentation methods partition the spatial domain, using local spectral coordinates to define rules for region boundary expansion that are weighted or constrained by proximity (Haralick and Shapiro 1985). Clustering partitions the spectral space of an image. However, in common use, segmentation can be taken to refer to any means of partitioning an image (Tilton et al., 2015).

Table 5.8. Segmentation families according to Garcia-Lamont et al. (2018).

Category (sub-category)	Approach	Characteristic property
Edge detection.	Brightness discontinuity or change.	Pixel intensity relative to neighbourhood.
Threshold: -Global -Adaptive -Otsu.	Partitioning of image by about a single or several image values, or under a more complex conditional rule.	Pixel intensity relative to a rule/rule set.
Histogram-threshold.	'Meta-heuristic' computing for multi-level thresholding, based on sampling of variability in pixel intensity values within the image, band or a subset (various methods).	Pixel intensity relative to internal distribution of pixel intensities in the set.
Region based.	Region-growing or splitting from a seed or ground reference based on similarity criteria and spatial relationship of pixels.	Pixel intensity relative to neighbourhood values.
Feature clustering.	Prior grouping of pixels into observed classes based on clustering tendencies in terms of a nominal scale.	Pixel intensity relative to internal distribution of pixel intensities in the set.

(Table 5.8 ctd.)

Category (sub-category)	Approach	Characteristic property
Neural network.	Logical rapid partitioning of an image based on a network / cascade of membership rules based on prior knowledge of the system.	Pixel intensity relative to a tiered membership ruleset.
Multi-feature fusion.	Comparisons among multiple reference feature-sets.	Patterns within an image or combining predictive features.
Fuzzy approaches.	Weighted or probability-based membership criteria.	Pixel intensity relative to probabilistic rules.
Texture approaches.	Segmentation based on regional labelled according to texture reference, or measures of greyscale variability.	Patterns in the spatial distribution of pixel values.
Contrast enhancement.	Intensity transform function based on transforming the observed grey-levels to an idealised, prior-known or adaptively calculated histogram profile of intensity values.	Pixel intensity relative to internal distribution of pixel intensities in an idealised frequency dist./ histogram structure.
Model based.	Catch-all for exploratory approaches.	Various.

As discussed in the previous chapters, selection of an optimal procedure for seagrass feature extraction requires the method to differentiate the seagrass feature from its background in its various surface growth forms (fine vs. thick leaf, dense vs. sparse growth, emergent vs covered or buried). The procedure should perform consistently across a wide variation in substrate and detrital scene content within and between estuaries.

Varying scene composition may manifest as differences in object geometry and spectral representation depending on the pixel size, the footprint of material on the ground and associated mixing of spectral information across pixels (Burnett and Blaschke 2003). Hence, the optimal segmentation function is likely to be scale dependant, both in terms of the target material (i.e., seagrass) and non-target items (e.g., shells, mud, detritus etc).

For example, consider scale across four orders of magnitude of seagrass feature size as shown in Figure 5.19, which in increasing areal extent depicts i) *seagrass leaves* (e.g., 2 x 60 mm in size); ii) *uniform seagrass clumps* (e.g., 200 x 600 mm); iii). *uniform seagrass patches* (e.g., 2 x 6 m); and iv) *meadow and meadow metapopulation scales* (20 x 60 m). Image ground sampling distance relative to the size of target object and non-target materials may result in different optimal segmentation algorithms.

The published literature that reviews the application of feature extraction to terrestrial vegetated systems is large (e.g., Laliberte and Rango 2011; Dronova et al., 2012; Li et al., 2016; Ma et al., 2107; Samiappan et al., 2017). Segmentation results from these terrestrial studies may have relevance at estuarine margins where seagrass grows adjacent to or within regions of higher estuarine vegetation type (Figure 5.20) such as mangroves, saltwater marsh and sea-meadow communities (e.g., Graeme 2008). However, these precedents within the literature are not necessarily transferable to the context of an estuarine sand/mud flat without prior calibration (Diesing et al., 2016).

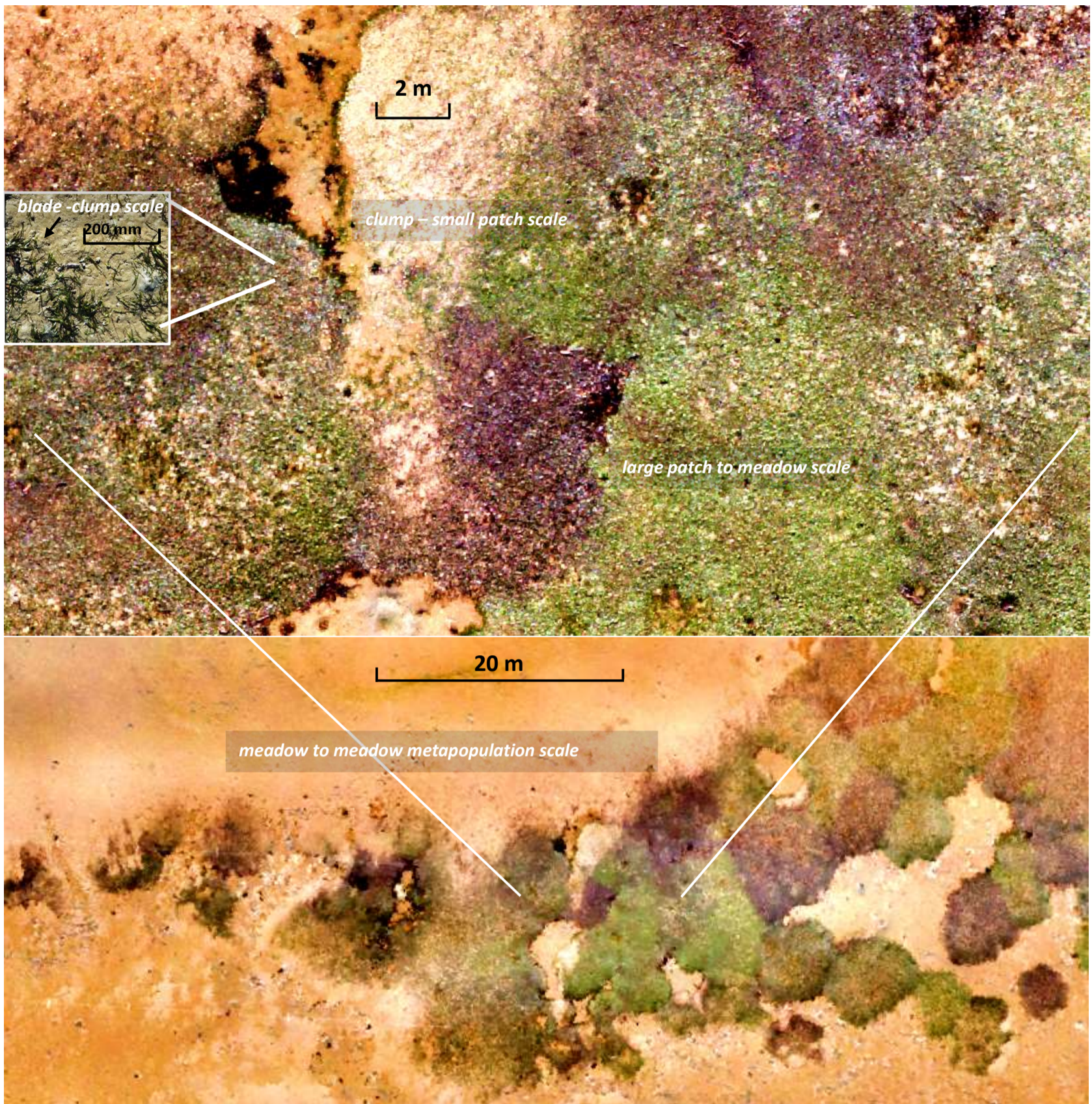


Figure 5.19. Seagrass meadow depicting various scales of interest that might be the subject of an image classification.



Figure 5.20. Point cloud model from a fixed-wing RPA photogrammetry flight near Waiponga Reserve, Wharekawa Harbour on 25 May 2017 (3-D scene perspective in Agisoft Photoscan 1.5) showing vertical structure running from high variability at the coastal margin (mangrove, marsh and saltmarsh ribbonwood / manuka, then dune grass community types running from lower left to upper middle), with dense seagrass (lower right) blending up to and into the mangrove margins.

Segmentation algorithms are numerous (e.g., Pal and Pal 1993; Trias-Sanz et al., 2008; Liu et al., 2015; Kaur and Chawla 2015). Of these, mean-shift segmentation is a commonly deployed algorithm that has been found to yield accurate segmentation in combination with a suitable classifier (Comaniciu and Meer 2002; Liu et al., 2013; Kaur and Chawla 2015; Einzmann et al., 2017; Pipaud and Lehmkuhl 2017).

This algorithm incorporates an unsupervised classification procedure that groups nearby pixels into classes based on their proximity to cluster-density centres. The procedure uses a circular processing kernel (analysis window) with a predetermined spatial radius about each pixel. The mean spectral value is calculated for the kernel pixels and is related to the nearest cluster centre. The pixel is attributed the spatial coordinates of the cluster centroid. The process iterates until a convergence criterion is met. Pixels that converge to the same point acquire a common value for cluster mean spectral value. The mean-shift algorithm incorporates a ‘*minimum segment size*’ parameter that defines the smallest allowable segment size, below which segments are merged to the most spectrally similar adjacent segment. The result is a raster with pixels attributed to the new

cluster mean spectral value, which can be converted to spatial vector features using a polygon-vector transformation.

Given its widespread use and thorough evaluation within the literature, mean-shift segmentation is a strong candidate for a segmentation of seagrass imagery in the current study. Mean shift segmentation is also more suitable than k-means segmentation as the k-means method makes *a priori* subjective assumptions about the number of classes intrinsic to the image, which may vary with different scene content. By contrast, mean shift segmentation identifies natural cluster tendencies in the colour space that should adjust with changing scene content. The approach is well-matched against the photogrammetrically acquired aerial image sets used here which exhibit minor variation in solar incidence upon the ground (e.g., varying cloud movement, or camera orientation changes during RPA flight attitude control). In this case, determination of accurate local cluster centres and segment margins under the mean-shift method would be tolerant to minor variation in spectral capture across a photogrammetrically acquired image scene above a wet estuary. The k-means method requires global consistency in the spectral response. Segmentation based on k-means may experience contamination of spectral grouping if there is variation in colour representation across the acquisition scene. However, the c-means algorithm, a fuzzy variant of k-means clustering that attributes probability of class membership, was found to classify images with lower mean squared error and higher signal to noise resolution than mean-shift segmentation (Kaur and Chawla 2015).

Relatively few published segmentation algorithms have been developed for open software environments. Some are implemented or wrapped within commercial software packages as part of integrated solutions. The following section attempts to summarise the range of software solutions available. It is noteworthy that full disclosure of an entire segmentation workflow, with documented parameter settings, could not be found in any published research. Indeed, many research papers only record coarse description of the segmentation methods used that cannot be immediately reproduced and tested without further information (e.g., Baumstark et al., 2013; Samiappan et al., 2017; Ahmed et al., 2018; Li 2018).

Trimble eCognition: The software package eCognition, is widely used in the literature and provides an implementation of a multi-resolution segmentation algorithm that has accurately delimited image-objects in several contexts (Dronova et al., 2011; Frohn et al., 2011; Laliberte and Rango 2011; Laliberte et al., 2012; Li et al., 2016; Ventura et al., 2016; Ma et al., 2018). Multi-resolution segmentation performs segmentation at several segment-scales, then combines these iterations forming a line

density topography from the combined segment-line-work, then derives final polygon boundaries from ‘centre of strongest tendency’ based on scale parameters. The specific segmentation algorithm used at each stage within each multi-resolution stack, and in combination, is not documented transparently within available literature.

IMAGINE – Objective: The *Objective* module of *ERDAS IMAGINE* software by Hexagon Geospatial is marketed as a professional-grade utility with object-based feature extraction functionality in-built, and has appeared in published research (e.g., Gibbes et al., 2010). The software was not available for direct evaluation at this time, but inspection of the published documentation indicates sub-processes run in both raster and vector space (Erdas Imagine manual, Hexagon Geospatial).

ArcGIS – Spatial Analyst extension: ArcGIS suite of software by Environmental Systems Research Institute (ESRI) provide within their *Spatial Analyst* package an implementation of the iterative self-organising data analysis technique, or ‘ISODATA’ (e.g., Dogan et al., 2009; Bakr et al., 2010) which, is similar to the k-means clustering approach, classifies all pixels within the image pixel-set into a specified number of differentiable groups (e.g., Dhanachandra et al., 2015). *Spatial Analyst* also provides a mean-shift segmentation for 3-band operations, although no publications could be found demonstrating its use for a vegetation mapping analysis.

Orfeo toolbox: Orfeo toolbox (OTB) is an open source application-set initially established to support satellite image processing but with applications relevant to general image processing (Tinel et al., 2012; Grizonnet et al., 2017). Several segmentation applications are included within the OTB package including mean-shift segmentation, connected components, watershed, k-means and other cluster or thresholding tools (e.g., Petitjean 2012; Andrés et al., 2017). The software contains a simple command line interface for scripting from the operating system console, and a Python programming language wrapper for procedural execution.

GRASS: The Geographic Resources Analysis Support System (*GRASS* or more commonly, *Grass*) is another open source geospatial analysis application set that implements both region-growing, hierarchical and mean-shift segmentation for multi-band imagery (<https://grass.osgeo.org>).

The R-Project: The open source software package *The R-Project* (<https://www.r-project.org/>) is long established user-supported statistical package (Ihaka 2009), which in addition to its core procedural libraries, also runs third-party ensemble modules (programming wrappers that call other background applications). Recent modules provide spatial analysis capabilities including ingestion of rasters into the software’s native data format from which spatial and non-spatial statistics can be computed (Kaya et al., 2018).

There are numerous segmentation options available in *R*, including cluster based and threshold-based classification once segmentation has been performed externally. Packages are available implementing mean-shift segmentation and region growing, for example packages ‘MeanShift’ (Ciollaro and Wang 2016), ‘bayesImageS (Moore 2018)’, ‘dbscan’ (Hahsler 2015), ‘EBImage’ (Oles et al., 2018), and ‘itcSegment’ (Dalponte 2018). An advantage of using The R-Project is that the entire image classification workflow can be automated within a single runtime environment through the use of the extensive library of functions and programming-wrappers suitable for classification, assessment, post-processing and result output.

QGIS: Quantum GIS (*QGIS*) is an open source geographic information system (GIS) that allows third-party programming modules to be run as tools within the GIS user interface (Dessau and Sutton 2011). At present QGIS does not have its own native image segmentation or classification capability. However, it is worth noting that as it has software interfaces for GRASS, Orfeo Toolbox, the R Project and a Python programming language interface. Thus, there are options to enable process automation using a combination of these tools.

The proprietary packages listed above (eCognition, ESRI Spatial Analyst and ERDAS Objective) are substantially more expensive than the open-source packages (see Table 5.9). The packages Spatial Analyst and Objective are modules within extensive enterprise-level GIS suite of software which need to be purchased together in order to access to the OBIA capability. Hence, the costs reflect the inclusive wide software capability. Cost-effectiveness arises from enterprise-scale adoption of the full software suite. The software eCognition only performs image classification. The open-source packages are free but require greater time investment to automate and quality-assure the many steps in an image analysis process-chain.

Table 5.9. Comparison of main software considered for segmentation and classification using object-based image analysis framework. Prices are indicative only, for a single licence with no prior subscription, representing the lowest cost pathway to achieving OBIA. Prices provided by the vendor are unofficial quotes, noting that i) Imagine and ArcGIS segmentation/OBIA options are embedded in bundles with significant other corporate functionality and support; and ii) different application contexts can yield different pricing schemes.

Software	Vendor/Origin	Segmentation	Classification	Feature selection	Accuracy assessment	Cost approx. \$NZD (student rate)
eCognition.	Trimble.	Yes.	Yes.	No.	Yes.	30,000 (7500)
IMAGINE – Objective.	Hexagon Geospatial.	Yes.	Yes.	No.	Yes.	23,000 (4400)
ArcGIS - Spatial Analyst extension.	ESRI.	Yes.	Yes.	No.	Yes.	34,000 (0)
Orfeo toolbox.	French Space Agency (CNES).	Yes.	Yes.	No.	Yes.	0
Grass.	U.S. Army Corps of Engineers.	Yes.	Yes.	No.	Yes.	0
The R-Project.	University of Auckland.	Yes.	Yes.	Yes.	Yes.	0

5.7.1.4 Segmentation assessment

Image segmentation results in boundary-geometries (as polygons or labelled regions) that depict objects within the scene based on a set of spatial and attribute contrast thresholds that control scale of image partitioning. Measurement of the accuracy of segmentation is generally uncommon (Ye et al., 2018).

Segmentation ‘scale’ is the measure of the degree of partitioning of the image, where large scale refers to coarse detail and large segments (and vice versa). The choice of segmentation scale can impact classification results (Gao et al., 2011). Liu and Xia (2010) determined that segmentation accuracy decreases with increasing segmentation scale and that there is an optimum segmentation scale in terms of effect on accuracy. Similarly, Kim et al. (2011) demonstrated higher overall classification accuracy with small-scale, high-detail objects for a forest land-cover scene. Likewise, a study using unsupervised clustering on a coastal river delta/wetland scene, found that high spectral granularity and its resulting high detail of objects within the image, yielded higher overall classification of target wetland species (Martin et al., 2014).

Under-segmentation refers to an insufficient degree of partitioning of objects while over-segmentation refers to excessive partitioning. Under- and over-segmentation have different impacts on the derived data models. Under-segmentation is regarded as problematic as it may lead to contamination by non-target materials, of similar spectral character, being erroneously included in the object (Liu and Xia 2010). However, over-segmentation may be advantageous, particularly with high dimensionality problems (Liu et al., 2018), where small units become ‘superpixels’ optimised for homogeneity and separability, with less emphasis on correctly matching segment and whole object geometry (Zhu et al., 2016; Guan et al., 2018; Liu et al., 2018). Conversely, Kim et al. (2009) observed improvement in classification accuracy with increasing segment size, although these involved different scaled vegetation and imagery than these studies.

Accurate classification has been achieved using segmentation-scale selection made upon a qualitative inspection of the resolution of target objects in the scene (Tsai et al., 2011). Computed measures of segmentation accuracy and error include both supervised methods and unsupervised methods (Zhang et al., 2008). Supervised methods compare the characteristics of segmentation objects to a human digitised or selected reference (Pham et al., 2016; Pont-Tuset and Marques 2016; Ma et al., 2018; Su et al., 2018). Unsupervised methods calculate metrics within and/or between segments to maximise fit to predetermined global criteria (Gao et al., 2011; Johnson and Xie 2011; Ahmed et al., 2018). A recent review (Ye et al., 2018), concluded that most segmentation assessment methods required pre-knowledge of the location of the target material, e.g., comparing the

polygon extent of segments with actual extent. Visible screen content is usually displayed only in red-green-blue colour space, ignoring additional bands which can contain rich information. This subjective prior interpretation of image content introduces a potential source of bias in terms of coercion of the model to the screen-view used to set the reference material.

Segmentation accuracy can be evaluated in terms of concordance between boundary position and actual location in the image scene, contrast of spectral or attribute measures between geometries, and ability to differentiate objects in a mixed scene (Espindola et al., 2007). This has also been termed segmentation optimisation (e.g., Ma et al., 2017). The degree of disagreement between segmented and actual object property is the segmentation error. Measures of concordance between segmented objects and scene content have included spatial and spectral heterogeneity in image values (Johnson and Xie 2011; Gao et al., 2017), area (Whiteside et al., 2014; Pham 2016), signal/noise ratio or Taguchi method (Chen and Sun 2000; Ahmed et al., 2018), location (Whiteside et al., 2014), and overlap in probability distribution (Liu et al., 2015). There are many more measures, and a comprehensive inventory is provided by Ye et al. (2018). Dronova et al. (2011) used consistency in NDVI segment scores as stop-criteria in region-growing based segmentation, while Ma et al. (2018) used image information content or entropy as a metric for identifying uniform training samples.

A multi-scale segmentation method proposed and tested by Johnson and Xie (2011) demonstrated an outcome where, after identifying over- and under-segmented geometries followed by correction, there was significant improvement in segmentation performance as measured by the authors' global weighted variance score. Over-segmentation can be aggregated into a merged object if an effective classifier and post-classification feature extraction is applied.

5.7.1.5 Classification

Data classification involves applying a classifier (or 'learner') to elements of a dataset to attribute membership under some grouping typology. Methods for this process date back to early thinking in statistics (Gordon, 1981; Bell 2014). Image classification methods are a subset of the much larger field of machine learning and data mining and too numerous to summarise here, though useful reviews have been developed elsewhere (see for example, Gordon 1981; Webb 2003; Larose 2015). An image is a form of data matrix so statistical machine-learning approaches are applicable to the problem of classifying content of an image.

Many data classification approaches have been implemented in spatial analysis software, e.g., ESRI ArcGIS, ERDAS Imagine, QGIS, and procedural libraries (Lu and Weng 2007; Klemas 2011; Tiner et al., 2015). A full inventory of classification methods applied across remote sensing and image analysis is beyond the scope of this chapter, and the reader is directed to several reviews that collate methods in depth (see Liu and Mason 2009; Allan 2016; Gómez et al., 2016).

Classification methods may integrate multiple approaches and/or parameter-iterations to improve performance. Examples include ‘bagging’ (iterative model averaging by bootstrap aggregation), ‘boosting’ (iterative model averaging with variable weighting for weak and strong classifiers) and other hybrid / ensemble approaches (Lemmens and Croux 2006; Bakr et al., 2010; Zaman and Hirose 2011; Du et al., 2012; Korytkowski 2016; Esmael et al., 2018).

Unsupervised and supervised classification

Unsupervised classification initiates with a cluster or global segmentation step to group pixels or objects into calculated classes based on natural clustering within the frequency distribution of pixel values. Membership is informed by an attribution rule (Rahman et al., 2013; Kulkarni 2017).

Supervised classification involves training an algorithm using a known labelled set of reference objects. A reference ‘training’ dataset (polygons, points or extents) is required under a sampling strategy that ensures representativeness and captures variability (Bell 2014). Within the classifier, training data forms a multivariate model of class separation with decision rules or functions for class attribution for new data. Image classification is enacted by applying the classifier to pixels or objects to define their membership under the class system of the training dataset.

Supervised classification methods, relevant to developing a method for seagrass, and that have been applied to coastal scenes include: thresholding (Khatami et al., 2016; Satapathy et al., 2018); regression (Xiang et al., 2012; Lu et al., 2015); maximum likelihood (Ayhan and Kansu 2012; Reshitnyk et al., 2014); discriminant analysis (Du and Nekovei 2005; Lin et al., 2010; Koukal and Atzberger 2012); support vectors (Pal and Mather 2005; Chu et al., 2012; Zhang 2013; Höhle 2015); random forest (Lu and He 2017); chain decision trees (Yang et al., 2003; Xu and Anwar 2013; Höhle 2015); decision-rules based on prior knowledge (Aitkenhead and Aalders 2011); and neural networks (Ayhan and Kansu 2012).

Hybrid approaches have also been developed that integrate unsupervised and supervised methods. For example, Kim et al. (2011) used majority class-membership derived from a maximum-likelihood pixel-based classification to determine membership

of segmented objects. Zanotta et al. (2018) classified segmentation objects using maximum likelihood classified image pixels based on continued increase in a ‘confidence’ scoring factor. Similarly, Ma et al. (2018) used a hybrid method where image-segments scoring zero entropy (i.e., pure spectra) were queried from the set to provide optimised training samples for main classification using the random forest algorithm.

The relative performance of classifiers can vary with data and class structure and no one classifier is immediately optimal for all applications (e.g., Guo et al., 2010). Thus, assessment of optimal classifier for seagrass application is justified in the present study.

Candidate classifiers

Three linear classifiers were selected for this study for the purpose of seagrass detection and density measurement: i) linear discriminant analysis; ii) support vector machine; and iii) random forest. These were chosen due to prevalence in the literature for successful image classification and due to their common goal to maximise class separability.

In linear discriminant analysis, a decision function is calculated based on pre-classified training data so as to separate groups with a training dataset and the feature-space re-projected so as to maximise class mean separability. The function and re-projection is then applied to the subject new data. The method assumes linear, quadratic or polynomial separability within the re-projected feature space.

The random forest applies an iterative decision-tree ensemble algorithm whereby possible class separation rules (attribute thresholds) that separate classes are iteratively assessed, and an optimal solution reported based on one of several impurity measures; typically using Shannon’s entropy or the Gini index metrics (Louppe 2014). The optimal decision rule-set forms a classifier that can be applied to targets of the same scheme.

Support vector machine calculates a linear, polynomial or radial hyperplane in feature-space that maximises class separability, with the hyperplane then applied as a classifier. Support vector machine classifiers rank among the highest accuracy approaches in a comparison run by Wahidin et al. (2015) using 30 m multispectral Landsat imagery.

Class typology

The class-nomenclature is an important determinant of a remote sensing outcome, and often the class-breakdown arises as a subjective framework developed under the expert knowledge of the researcher (Forestier et al., 2012; Arvor et al., 2013; Blaschke et al., 2014). Arvor et al. 2013 argue that remote sensing would benefit from advances in

ontology design and communication. In land-cover classifications for example, the class set needs to break down important parts of the scene and characteristics of the parts according to the research objectives, scale and variability of occurrence (either present or absent). Classification may operate at multiple spatial scales corresponding to the hierarchy of patches and constituent objects that comprise the natural system (Burnett and Blaschke 2003; Hay et al., 2003; Forestier et al., 2012). Therefore, it may be appropriate to have sequential tiers of class (e.g., fine and coarse) in a classification system.

The literature on land-cover classification has strong emphasis on partitioning of data into spatially discrete patches of only a single category. Natural vegetated systems, however, more typically occur as blended classes, particularly around their margins, especially when the underlying environment gradients are gradual. For example, in the context of a seagrass scene, although hard edge classifications have relevance at the interface of a disturbance or sharp environmental gradient (e.g., at the edge of a sediment burial mass or scoured pool), seagrass is also likely to present as a mosaic of overlapping or integrating patches of differing density and substrate (e.g., see Figure 5.19). The transition between overlapping zones may be ecologically meaningful spatially, but under a hard classification system such overlap might present as uncertainty or error (Rocchini et al., 2013). Fuzzy classification is an alternative approach that allows a relaxed approach to classification that ascribes objects (pixels or segments) with a degree of membership across multiple potential classes rather than single membership to one class (Amo et al., 2004; Gomez and Montero 2008). This approach can yield accuracy benefits for image classification as all information is captured in the classification (Shi et al., 2011). Selection of a classification depends on project objectives, spectral distinctiveness, variability in spectral and attribute characteristics and the level of classification accuracy sought from the analysis. However, in comparative studies, there is a general tendency for classification by support vector machine to yield greater classification accuracy than other tested algorithms, with Random Forest also yielding high relative performance (Schwert et al., 2013; Abe et al., 2014; Khatami et al., 2016; Phan and Kappas 2018).

5.7.1.6 Classification assessment

Classification assessment is a critical part of robust image classification and mapping (Rocchini et al., 2013). Classification performance depends on the interaction between scene object content, spectral dissimilarity of target object, information contained within the image, representativeness of the training dataset, quality of knowledge underlying design, the classifier algorithm used and generalising functions applied to the classified result (Liu and Mason 2009; Canty 2014). The basis for many

accuracy measures is the confusion matrix (Congalton 1991). The confusion matrix contrasts the calculated membership made within each class with respect to reference (training) dataset of known accurate class membership. This enables per-class and overall accuracy statistics to be calculated and spectral or classification overlap between classes to be visualised.

Common accuracy measures include: overall accuracy and user/producer accuracy derived from a confusion matrix (Bakr et al., 2010; Gao et al., 2011; Reshitnyk et al., 2014; Höhle 2015; Lu and He 2017); kappa statistic (Bakr et al., 2010; Gao et al., 2011; Höhle 2015) and kappa significance (Congalton and Green 2009); independent sample accuracy test (Foody 2004; Aitkenhead and Aalders 2011); tau statistic (Reshitnyk et al., 2014); mean spectral error (Khatami et al., 2017); area under receiver-operating-curve (ROC); and area under curve for short (AUC) e.g., Ahmed et al. (2018).

Confusion matrices (the tabulation of actual vs. predicted classification frequencies) provide overall and between-class accuracy metrics representing for the dataset. Overall accuracy (OA) measures the number of correctly classified pixels across all classes. Producer and user accuracy provide per-class measures of correctly classified actual ground features (producer accuracy) and correctly classified map features (user accuracy) within the class. In other words, producer accuracy provides a detection rate and user accuracy provides the mapping accuracy for each class. The relative importance of producer and user statistics depend on the project objectives. The kappa statistic measures accuracy across the whole dataset in terms of how different the observed row and column frequencies differ from those expected under a random model.

The confusion matrix approach is useful. However, there are several drawbacks: i) correct accuracy assessment is dependent on correct co-registration of training features on the image; ii) training of the classification model requires random and representative training samples deployed so as to capture the variance of content across the image avoiding undue autocorrelation; and iii) accuracy statistics relate to the whole dataset without any measure of variation in spatial error distribution across the image (Foody 2002; Hsiao and Cheng 2013).

There are currently no established conventions on how best to assess classification accuracy and the optimal method may depend on the data composition (e.g., variance, class frequencies), sample design and the classifier used (Stehman and Czaplewski 1998). The kappa statistic has also been critiqued, particularly in terms of its reliability. Kappa values are dependent on the number of classes used, and with large sample size significance can be found leading to rejection of the null hypothesis even when differences are minor (Stehman 1997; Pontius and Millones 2011). The user, producer

and total accuracy statistics are recommended for classification accuracy assessment under United Nations land-cover mapping guidelines (United Nations 2016), which also recommends against use of the kappa statistics. Consequently, these metrics are used in this analysis, with the method limitations addressed by applying semi-random sample selection and a survey design sampling representatively across the extent of the study area.

5.7.1.7 Collinearity and feature selection

Collinearity in statistical modelling refers to the case where variables are numerically related (Dormann et al., 2012). Collinearity between variables can lead to redundant information describing the same process, bias of effects, failure to identify individual (collinear) variable-contribution to a model, and/or masking of the impact of missing data (Belsley 1980; Dormann et al., 2012; Wildi 2013; Marsman et al., 2017). In geospatial data mining, collinearity between layers is to be expected when systematically mining a predictive solution from multiple derivative layers based on just a few core layers. Many of the indices and ratios between image bands are derived from slight variations using the same underlying data. Feature extraction by image analysis is therefore prone to collinearity. Reduction of collinearity should be considered in developing a predictive remote sensing model. Collinear variable combinations can be removed according to inclusion or exclusion criteria (e.g., by dropping predictors that have the greatest influence in the model or highest relevance to the underlying real-world process), by dimensionality reduction (e.g., principal component reduction) or by forming orthogonal combinations of the collinear variables. Collinearity reduction may not improve the overall fit of a predictive model if predictive information is greater than the collinear redundancy of information or if bias is introduced through the variable selection (Freckleton 2011; Dormann et al., 2012).

A robust classification model should select significant or influential variables while eliminating non-significant factors and minimising collinearity. Robust layer selection has previously been shown to improve image classification accuracy and is recognized as an important selection step in any classification workflow (Chu et al., 2012; Diesing et al., 2016). Diesing et al. (2016) propose that dimensionality reduction should be an integral part of image classification.

Layer selection or feature selection can be approached from two classical approaches: i) *Wrapper*, where all possible combinations of input variables (or a sequential/heuristic subset) are computed within the target model and the predictor-set of highest influence/fit adopted as optimal; and ii) *Filter*, where a pre-processing step other

than the planned model, ranks variables based on fitness criteria and eliminates non-influential predictors prior to model execution (Kohavi and John 1997; Choi et al., 2012; Chandrashekar and Sahin 2014).

An advantage of the *wrapper* approach is that predictors are tested in the context of the target classification model and optimisation can be measured in terms of the accuracy and/or fit of classification outcomes. However, these methods can become computationally intensive when the number of predictors is large. As the dimensionality of the model increases, *filter*-based selection methods may be preferred to enable analyses within viable processing timeframes (Chandrashekar and Sahin 2014). One performance trade-off for implementing the pre-processing stage of a *filter* selection is that additional performance criteria (other than classification performance) need to be devised and tested for suitability, rigor, and additional sources of bias.

A range of processing algorithms are available for feature selection from the wider literature on statistics and data mining (e.g., Bolón-Canedo et al., 2015). Several popular approaches are implemented within scriptable model packages such as The R Project. This software for example incorporates a series of relevant customisable tools e.g., the packages *relief* (selection frequency), *rfe* (backwards selection), *FSelectorRcpp* (rank/weight cut-off). Within the same software environment, the *Caret* package also integrates a range of classifiers and classification assessment tools, as well as *findCorrelation* for collinearity removal and *rfe* for backward selection (Khun 2013). Finally, the *Random forest* package provides a variable *importance* function that can be used to examine relative contribution and support the elimination of redundant predictors.

[End of Appendix.5.7.1]

5.7.2 Appendix 5.7.2. Summary of seagrass, debris, cloud cover and sun angle for survey periods used in this replicated classification assessment. All three surveys were conducted at low tide approx. 60 minutes before returning tidal flood.

Survey session	Transect pattern	Seagrass state Characteristic	Estuary debris	Cloud cover	Sun Angle
9 April 2017.	1	Seagrass meadow under autumn degradation, and immediately following a significant high-rainfall weather system.	Significant debris and shell deposition as sparse surface covering or aggregated in mats and piles.	Overcast	45
2 Feb 2018.	2	Substantial regrowth and thickening of seagrass meadow and patches.	Little debris / detritus visible on the study area.	Overcast	44
28 Mar. 2018.	2	Autumn seagrass extent, similar to April 2017 extent / state but without any storm damage or debris.	Little debris / detritus visible on the study area.	Overcast	47

5.7.3 Appendix 5.7.3. Attributes resulting from iterations upon increasing *minimum segments size*, the parameter within the segmentation process that controls the smallest allowable segment size.

Min, segment size.	No. segments.	Mean no. neighbours.	Mean no. pixels per segment.	Mean segment area (m ²).	Moran' s Index.	Area-weighted variance.	Global score.	RMSE.	SNR.
5	1,043,264	3.6	17	0.01	0.264	0.0006	~0.00	0.042	8.16
10	542,413	3.4	33	0.02	0.276	0.0008	0.75	0.044	7.54
20	268,073	3.3	65	0.03	0.282	0.0010	1.20	0.046	6.64
40	131,703	3.2	127	0.07	0.283	0.0011	1.37	0.049	5.72
80	66,604	3.2	242	0.13	0.283	0.0013	1.51	0.051	5.03
160	32,277	3.1	481	0.27	0.281	0.0015	1.56	0.055	4.33
320	16,239	3.1	927	0.53	0.278	0.0018	1.57	0.058	3.75
640	7,901	3.1	1855	1.09	0.276	0.0020	1.64	0.061	3.38

5.7.4 Appendix 5.7.4. Per-class user and producer accuracy levels for the three classifiers tested. High, medium and low classes are indicated by H, M, and L respectively.

	Class	Producer accuracy			User accuracy		
		LDA	RF	SVM	LDA	RF	SVM
Single pixel	Seagrass (H)	76	85	90	76	70	69
	Seagrass (M)	48	51	47	43	47	47
	Seagrass (L)	37	49	37	37	58	47
	Seagrass/Detritus	37	26	24	47	57	66
	Seagrass/Shell	11	11	0	13	35	0
	Seagr/Detr/Shell	35	36	24	41	79	65
	Detritus (H)	42	57	45	55	72	82
	Detritus (ML)	28	28	12	38	52	83
	Shell (H)	50	50	38	40	54	65
	Shell (ML)	18	24	7	26	44	47
	Detritus/Shell	21	0	1	9	0	5
	Sediment	85	93	99	76	78	72
	Min. 5 pixels	Seagrass (H)	78	76	90	79	68
Seagrass (M)		50	40	42	46	50	43
Seagrass (L)		44	45	43	44	52	42
Seagrass/Detritus		45	26	25	54	56	64
Seagrass/Shell		27	0	0	20	0	0
Seagr/Detr/Shell		43	14	27	47	57	72
Detritus (H)		48	48	37	61	83	85
Detritus (ML)		27	18	3	34	50	45
Shell (H)		58	50	43	51	60	67
Shell (ML)		21	24	3	27	33	32
Detritus/Shell		32	0	0	17	0	0
Sediment		84	94	98	76	78	70
Min. 10 pixels		Seagrass (H)	71	76	85	75	60
	Seagrass(M)	50	40	41	44	40	42
	Seagrass(L)	46	45	44	46	54	42
	Seagrass/Detritus	46	26	31	47	36	52
	SeagrassShell	4	0	0	4	0	0
	Seagr/Detr/Shell	41	14	28	51	42	75
	Detritus (H)	77	38	40	65	75	79
	Detritus (ML)	21	9	2	37	33	26
	Shell (H)	98	90	93	90	70	95
	Shell (ML)	19	24	5	31	66	57
	Detritus/Shell	0	0	0	0	0	0
	Sediment	90	97	99	81	80	78

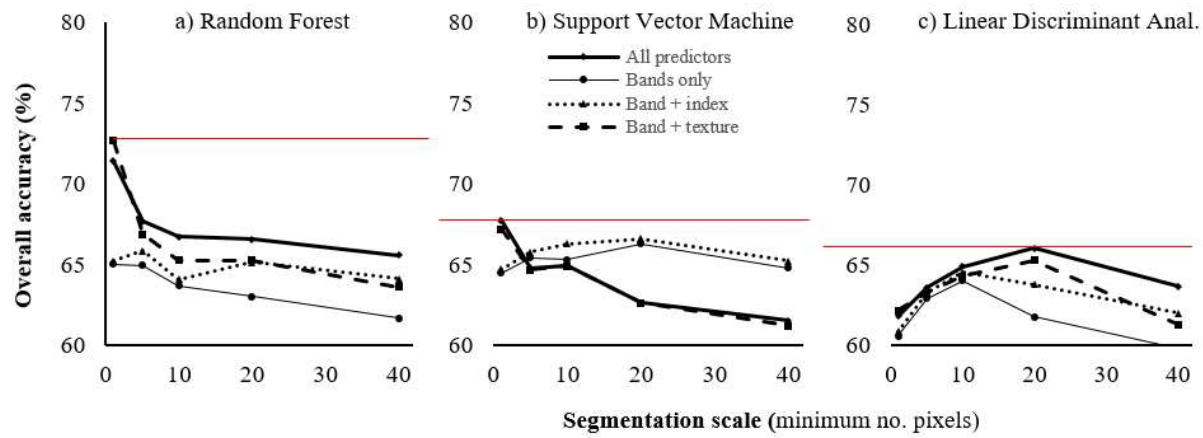
(Appendix 5.7.4 ctd.)

Class	Producer accuracy			User accuracy			
	LDA	RF	SVM	LDA	RF	SVM	
Min. 20 pixels	Seagrass (H)	80	78	85	84	74	72
	Seagrass (M)	61	25	33	52	57	36
	Seagrass (L)	53	54	12	39	39	15
	Seagrass/Detritus	67	71	65	71	60	56
	Seagrass/Shell	16	8	0	25	50	0
	Seagr/Detr/Shell	58	32	12	45	46	31
	Detritus (H)	76	71	48	74	71	71
	Detritus (ML)	15	4	0	25	0	0
	Shell (H)	68	50	28	60	70	51
	Shell (ML)	47	48	50	63	55	54
	Detritus/Shell	0	0	0	0	0	0
	Sediment	82	89	94	69	67	68
	Min. 40 pixels	Seagrass (H)	73	74	68	74	67
Seagrass (M)		60	67	71	60	56	51
Seagrass (L)		61	63	33	52	44	48
Seagrass/Detritus		53	58	57	62	51	58
Seagrass/Shell		0	0	0	0	0	0
Seagr/Detr/Shell		50	10	1	45	25	8
Detritus (H)		24	0	0	28	0	0
Detritus (ML)		0	0	0	1	0	0
Shell (H)		24	25	0	17	9	0
Shell (ML)		30	56	25	37	71	49
Detritus/Shell		27	0	0	19	0	0
Sediment		88	97	98	85	90	72

5.7.5 Appendix 5.7.5. Predictor sets obtained from collinearity reduction/ recursive feature elimination (random forest classifier), for each respective segmentation scale.

Seg. scale.	Reduced model	Reduced model - recursive feature elim.
Single pixel.	Class ~ Red + NIR + Highgreylevelrunemphasis + Clusterprominence + Entropy + Greylevelnonuniformity + Correlation + Clustershade	Class ~ Red + Green + Lowgreylevelrunemphasis + Haralickscorrelation + EVIje + Haralicksmean + NIR + RedEdge + Highgreylevelrunemphasis + Clusterprominence + EVIj + Greylevelnonuniformity + RVie + Entropy + RVI + Haralicksvariance + NDVIe + Informationcorrelation + Energy
Min size 5 pixels.	Class ~ Red + NIR + Clusterprominence + Highgreylevelrunemphasis + Energy + Greylevelnonuniformity + Correlation + Clustershade + AreaSegment_m ² + AreaPerimFraction + LengthWidthFraction	Class ~ Red + Green + EVIje + Lowgreylevelrunemphasis + Haralickscorrelation + RVie + NDVIe + RedEdge + NIR + Haralicksmean + SAVIe + EVIj + DVie + Clusterprominence + RVI + NDVI + SAVI + DVI + Highgreylevelrunemphasis + Haralicksvariance + Entropy + Greylevelnonuniformity + Energy + Correlation + Informationcorrelation + Inertia
Min size 10 pixels.	Class ~ Red + NIR + Clusterprominence + Informationcorrelation + Greylevelnonuniformity + Correlation + Clustershade + AreaSegment_m ² + AreaPerimFraction + LengthWidthFraction	Class ~ Red + RVie + NDVIe + EVIje + SAVIe + NIR + RedEdge + Green + EVIj + DVie + Haralickscorrelation + Haralicksmean + Lowgreylevelrunemphasis + NDVI + RVI + Clusterprominence + SAVI + DVI + Entropy + Greylevelnonuniformity + Haralicksvariance + Energy + Inertia
Min size 20 pixels.	Class ~ Red + RedEdge + Invdiffimoment + Clusterprominence + Highgreylevelrunemphasis + Greylevelnonuniformity + Clustershade + Perimeter_m + Correlation + AreaPerimFraction + LengthWidthFraction	Class ~ Red + RVie + NDVIe + DVie + SAVIe + RedEdge + Green + NIR + EVIje + Lowgreylevelrunemphasis + EVIj + Haralickscorrelation + Haralicksmean + NDVI + RVI + SAVI + Clusterprominence + DVI + Highgreylevelrunemphasis + Inertia + Invdiffimoment + Entropy + Informationcorrelation + Haralicksvariance + Energy + Greylevelnonuniformity + Clustershade
Min size 40 pixels.	Class ~ EVIj + Clusterprominence + RedEdge + Invdiffimoment + Greylevelnonuniformity + Clustershade + AreaPerimFraction + Correlation + AreaSegment_m ² + LengthWidthFraction	Class ~ Red + NDVIe + EVIj + RVie + SAVIe + Green + DVie + EVIje + Haralicksmean + Haralickscorrelation + Lowgreylevelrunemphasis + RVI + NDVI + RedEdge + SAVI + Clusterprominence + NIR + Highgreylevelrunemphasis + DVI + Greylevelnonuniformity + Haralicksvariance + Entropy + Inertia + Clustershade + Invdiffimoment + Informationcorrelation + Energy

5.7.6 Appendix 8.7.6. Contribution of camera-bands, derived indices and texture layers in overall classification accuracy for the three classifiers tested (random forest, support vector machine and linear discriminant analysis) and across the range of segmentation scales assessed. Red horizontal line highlights the highest accuracy attained for each classifier.



5.7.7 Appendix 5.7.7. Classification outcomes for predictor subsets comprising the camera-bands, derived indices and texture layers for the three classifiers tested (random forest, support vector machine and linear discriminant analysis) and across the range of segmentation scales assessed.

		Seg. Scale	Producer accuracy			User accuracy			
			Overall	High	Medium	Low	High	Medium	Low
Random forest	All predictors	1	71.42	87.39	55.33	55.52	73.04	54.46	62.27
		5	67.66	85.65	47.69	51.53	78.05	45.34	51.13
		10	66.74	78.18	45.55	48.97	65.52	41.79	48.61
		20	66.58	81.98	52.48	35.37	76.54	50.86	46.51
		40	65.59	72.42	65.79	49.17	83.17	55.94	52.36
	Camera bands only	1	65.03	83.88	41.31	31.86	70.60	44.91	43.59
		5	64.96	83.81	41.88	47.13	71.88	43.83	48.63
		10	63.72	75.15	34.99	43.42	63.55	36.43	45.48
		20	63.05	79.16	47.60	39.50	78.11	48.42	48.81
	Band + index	40	61.70	70.71	63.51	26.44	68.76	53.51	31.50
		1	65.23	83.35	45.14	41.08	70.44	45.99	46.93
		5	65.88	84.01	44.12	45.04	73.00	46.26	45.64
		10	64.08	73.16	38.90	44.27	63.02	38.71	47.29
		20	65.16	81.07	50.93	36.10	78.01	47.64	45.72
		40	64.14	69.17	58.83	31.75	67.21	51.30	37.48
		1	72.68	88.70	61.57	49.38	73.58	58.46	67.33
Band + texture	5	66.88	87.31	45.20	47.17	70.90	44.28	55.66	
	10	65.27	78.22	39.85	44.72	63.96	38.30	45.67	
	20	65.28	81.60	42.83	39.81	75.34	47.31	48.23	
	40	63.63	68.76	68.75	34.45	66.11	53.63	47.48	

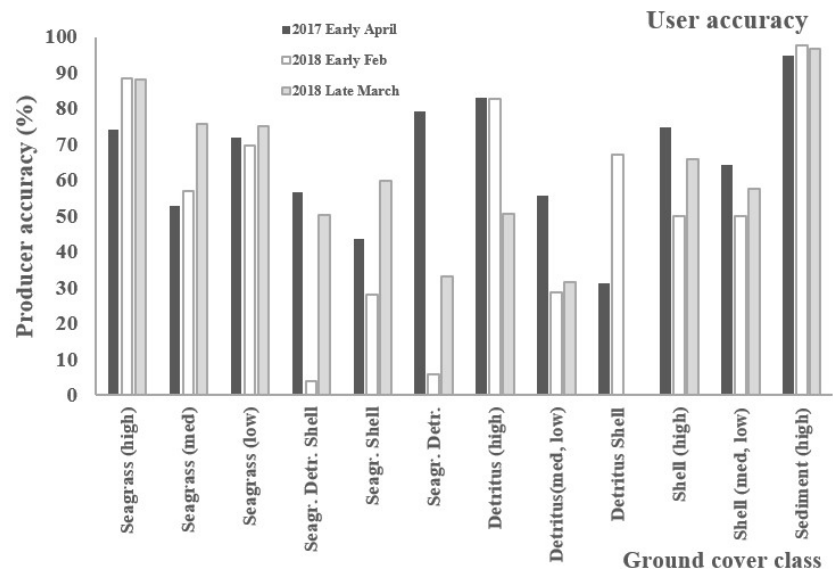
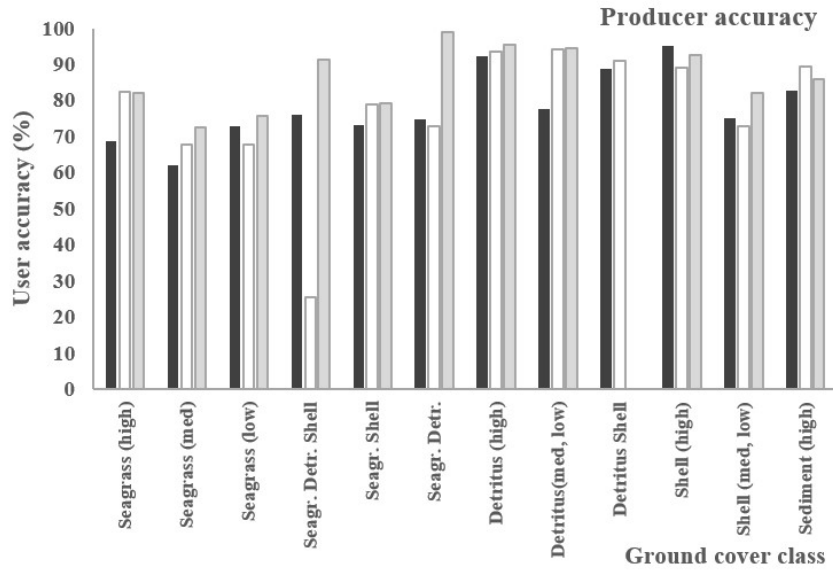
(Appendix 5.7.7 ctd.)

		Seg. Scale	Producer accuracy				User accuracy		
			Overall	High	Medium	Low	High	Medium	Low
Support vector machine	All predictors	1	67.77	89.84	52.28	39.70	70.13	49.51	54.67
		5	64.80	89.77	41.48	42.37	69.71	42.92	41.73
		10	64.97	84.90	40.83	43.06	62.09	41.53	42.41
		20	62.64	85.68	31.19	12.97	72.33	39.90	14.85
		40	61.54	68.47	70.82	35.23	64.96	51.64	48.77
	Camera bands only	1	64.50	87.71	44.14	22.36	68.35	43.06	48.05
		5	65.42	87.54	46.03	35.48	71.85	45.99	42.31
		10	65.33	83.58	40.71	38.62	63.96	41.47	42.91
		20	66.30	84.66	51.21	35.41	78.92	54.98	48.65
		40	64.80	74.60	66.76	27.77	65.98	56.02	43.90
	Band + index	1	64.73	87.24	46.34	23.02	69.11	43.14	47.75
		5	65.77	86.37	50.25	38.56	73.06	45.82	43.42
		10	66.30	83.12	48.07	39.47	64.95	42.69	46.49
		20	66.63	86.40	9.50	31.18	76.11	54.10	41.31
		40	65.22	74.85	65.03	34.18	67.58	55.15	51.10
	Band + texture	1	67.22	90.51	50.75	35.83	69.38	49.51	52.42
		5	64.70	90.60	41.92	32.43	68.19	41.41	44.38
		10	64.92	85.48	36.17	39.96	61.41	38.34	39.95
		20	62.65	82.88	34.21	17.84	71.73	35.76	25.43
		40	61.22	65.85	78.58	2.28	65.72	46.92	5.43

(Appendix 5.7.7 ctd.)

		Seg. Scale	Producer accuracy			User accuracy			
			Overall	High	Medium	Low	High	Medium	Low
Linear discriminant analysis	All predictors	1	61.81	75.31	50.01	37.88	76.16	43.99	38.62
		5	63.63	78.05	49.25	43.75	79.18	46.06	43.42
		10	64.91	71.55	49.93	46.55	74.60	43.94	46.50
		20	66.08	80.34	59.84	51.81	84.85	51.61	39.99
		40	63.68	73.32	59.65	60.80	74.05	60.18	52.43
	Camera bands only	1	60.60	84.15	36.08	4.07	70.22	40.24	31.27
		5	62.92	83.51	41.72	20.73	73.73	46.34	42.05
		10	64.06	77.93	43.65	34.49	69.79	44.93	46.76
		20	61.78	81.56	46.38	28.84	80.21	61.87	39.53
		40	59.86	76.50	62.20	30.76	73.80	59.48	44.00
	Band + index	1	60.88	75.60	47.04	24.60	74.56	42.16	33.57
		5	63.29	78.12	47.14	38.17	78.34	45.95	42.95
		10	64.55	73.70	49.76	40.54	74.39	45.10	44.14
		20	63.80	80.39	61.57	45.91	82.84	49.17	38.19
		40	62.04	75.07	63.05	42.92	74.19	60.81	50.25
	Band + texture	1	62.19	78.83	49.54	31.47	73.33	42.69	35.06
		5	63.29	79.43	47.00	36.93	75.25	43.03	41.49
		10	64.32	70.45	47.52	46.80	71.42	41.24	41.54
		20	65.31	78.77	51.20	49.14	84.31	51.43	39.54
		40	61.30	63.65	63.45	55.94	73.59	54.95	51.57

5.7.8 Appendix 5.7.8 Per-class producer and user accuracy statistics for map classification at the survey times of April 2017, Feb. 2018 and March 2018.



CHAPTER 6

Chapter 6. Mapping of seagrass leaf area and change

6.1 Introduction

Chapter 5 identified general optimisations for classification of multispectral narrow-band imagery flown by drone at 30 meters above a seagrass meadow with tidal water drained at low tide. For this scale of survey, smaller segments or even individual pixels, provided the highest classification accuracy both for the high-density class of seagrass density, and in terms of seagrass presence and absence. The random forest classifier provided the best results compared to support vector machine and linear discriminant analysis classifiers. The computation-time required to photogrammetrically render a *c.*300-photo scene, calculate and normalise the required layers then run the classifier and image, was ~8 hours run time (on Intel i7 CPU at 3.5 Ghz, 32 Gb RAM) with quality checking (i.e., same-day). There was no practical reason nor computational benefit identified for applying a feature selection or elimination, when using the random forest classifier. The method extracted medium to high density seagrass features with good classification accuracy. However, sparse seagrass classes were consistently confused, and there was some misclassification of surface macroalgal growth for low-density seagrass.

The classification method was based on visually interpreted feature-identification and density attribution from the ground photography using a generally accepted and common density-interval class approach (Braun Blanchet 1965; Schwarz et al., 2006; Short et al., 2006; Neckles et al., 2012; Pu et al., 2014). Visual interpretation can generate large volumes of reference data quickly, but can incorporate human error, subjectivity, and drift in class attribution with time and practice (Congalton and Mead 1983). This was found to be the case in the current study where reclassification of the same data yielded higher accuracy after practice and minor refinement (Chapter 4 and Chapter 5). Factoring an empirical measure of seagrass density into classification-training would require the elimination of much of this potential subjective error. There is no literature at this time demonstrating low altitude RPA-based image classification using a computed density

measure (as opposed to visual interpretation), so assessment of this potential improvement is justified.

The leaf area index is a common consideration in vegetation and canopy condition assessment (Ross 1981; Chen and Black 1991; Asner et al., 2003; Borfecchia et al., 2013b; Atzburger et al., 2015). At the canopy scale, leaf area index (LAI) is generally defined as the leaf area per unit ground area. There are variants of leaf area index that estimate total leaf surface, one-sided leaf area, horizontal planar area, solar incidence and view angle, as well as factoring leaf orientation and aggregation or overlap (Chen and Black 1991; Barclay 1998). Of these, projected horizontal leaf area to the normal is a measure that has been used to estimate the maximum amount of sunlight that can be intercepted by foliage. Therefore, this also estimates the amount of ground obscured by foliage. The response of indices can vary with vegetation geometry and degree of leaf aggregation (Lang and Yueqin 1986; Carlson and Ripley 1997; Herbert and Fownes 1997; Barclay 1998; Jonckheere et al., 2004). Horizontal leaf area has relevance to seagrass, as upon a drained estuary the leaves predominantly lay flat on the ground. High density seagrass can grow with significant overlapping leaf aggregation (Figure 6.1), so leaf area index > 1 can be expected in places.

Classification performance can depend on the number of classes. For example, authors Aitkenhead and Aalders (2011) conducted image classification for land-cover mapping that achieved 89% accuracy when based on eight classes, but 53% accuracy based on 96 classes. In a study comparing efficacy of Earth Observing-1 satellite sensors for detecting seagrass density, Pu et al. (2018) demonstrated markedly higher overall accuracy for three seagrass coverage classes as compared to five classes. Nahirnick et al. (2019b) demonstrated RPA based mapping of subtidal seagrass (*Zostera marina*) achieving class accuracy levels in the range 70-98% across four density classes *very sparse*, *sparse*, *moderate* and *dense*. Under this class granularity, the Authors noted underestimation of predicted seagrass through omission of sparse seagrass (Nahirnick et al., 2019b).



Figure 6.1. Overlapping (LAI \gg 1) and disparate (LAI = 0.6) seagrass.

Outcomes from the previous chapter are built-upon within this chapter to examine the model performance when trained using precisely measured leaf area, as compared to the visual interpretation method used in Chapter 5. Two class sets of differing granularities are assessed: i) 3-tier (high, medium and low density), and ii) 10-tier (decile) classification scales. The result from the RPA classification is used to train image classifications for: i) multispectral imagery collected by fixed wing aircraft; and ii) multispectral imagery from satellite, both acquired near to the time of the RPA survey.

6.2 Chapter objectives

The specific objectives of Chapter 6 are to:

1. Map seagrass density distribution based on measured horizontal leaf area for two replicate surveys;
2. Examine the relationship between model seagrass density estimation and measured horizontal 2-dimensional leaf area;
3. Quantify change in seagrass presence and density class;
4. Contrast the cost and benefit of visual photo interpretation versus measured seagrass density attribution; and
5. Demonstrate the use of low-altitude RPA imagery for training a subsequent classification using fixed wing aircraft imagery.

6.3 Methods

6.3.1 Study area, ground observations and aerial survey

The study area in this chapter is the same as that used for Chapters 4 and 5. Within this assessment, the adjusted transect deployment described in Section 5.4.4 was used.

The parallel transects were 100 m in length and spaced with 20 m separation. Ground reference locations were marked every 5m and were matched in location between February and March replicate surveys. The transects were placed to sample a seagrass meadow-complex with parts that are both stable and changing (Figure 6.2, and see Chapter 3). Ground reference photos were taken using a Nikon S9500 camera at nadir, 1 m above the ground and levelled using a bidirectional spirit-level. Photo centre points were surveyed using a precision GNSS instrument (Trimble R8 receiver with TSC3 controller).

Aerial surveys were conducted using a Parrot Sequoia multispectral independent-lens camera fixed to vibration-resistant mount upon a 600 mm ‘quadcopter’ rotary wing autonomous remotely piloted aircraft (RPA). A survey flight plan was programmed into the RPA for an aerial survey on 3rd February 2018, and the same flight plan applied to a follow-up survey on 29th March 2018 (Table 6.1). Both surveys targeted the late-drainage stage of low-tide just before the returning flood, aiming for 45-degree sun angle, under approximately uniform over-cast cloud conditions. The RPA flight plan was set to traverse a strafe-pattern achieving 80% image overlap across the site in both the forwards and lateral directions. Imagery were collected in green (550 nm), red (660 nm), red-edge (735 nm), and near infra-red (790 nm) spectral bands on independent sensors of 1280 x 960 pixel resolution equating to ~2.7 cm pixel ground sampling distance (GSD) at 30 m height above the ground.

6.3.2 Image-processing and data preparation

Image processing followed the same overarching workflow as previous chapters (summarised in Table 6.2 and discussed in depth in Chapter 5).

The resulting product comprised a 28-band normalised image-stack aligned to the study reference-frame (NZTM horizontal datum, NZVD2016 vertical datum referenced to LINZ geodetic mark EB2U). Bands included camera spectral bands, vegetation indices including red-edge and NIR variants, and texture layers.

Table 6.1. Summary of seagrass, debris, cloud cover and sun angle for survey periods used in this replicated classification assessment. Both survey times were low tide approx. 30 minutes before returning tidal flood.

Survey session.	Seagrass state / characteristic	Estuary debris	Cloud cover	Sun angle to horizon
3 Feb. 2018.	Substantial dense seagrass throughout meadow.	Rare.	Overcast	44
29 Mar. 2018.	Dense seagrass throughout meadow, but clear sign of thinning; inundation from sediment evident.	Rare.	Overcast	47



Figure 6.2. Seagrass upon the study area at time of 28 March 2018 survey, with transects (solid lines) and location of ground photography quadrats (the squares upon transect lines). The same transect layout and RPA flight program was used for the 2 Feb 2018 survey.

Table 6.2. Summary of data preparation stages and analysis.

Step	Detail
Field data	<p>Placement of photogrammetric markers and quadrat marker points.</p> <p>Capture of radiometric panel reference.</p> <p>Launch of RPA on pre-programmed flight plan (route replicated across Feb and March 2018 surveys).</p> <p>GNSS survey of quadrat mark-point centres.</p> <p>Collection of ground level photography (quadrat references centred on mark-points).</p>
Photogrammetric processing	<p>Align images.</p> <p>Apply radiometric corrections.</p> <p>Insert position markers for GNSS ground control points into the model.</p> <p>Optimise camera positions upon GNSS points.</p> <p>Re-align images using optimised camera positions.</p> <p>Create dense point cloud.</p> <p>Build triangle mesh.</p> <p>Calculate texture; apply colour correction.</p> <p>Generate orthomosaic → exported Tiff file (multispectral image).</p> <p>Fine georeferencing to ground control points, quadrat markers and unambiguous objects visible in both images (1-2 pixel fine alignment).</p>
Multispectral image processing	<p>Calculate vegetation indices.</p> <p>Calculate Haralick's texture layers on NDVI vegetation index layer.</p> <p>Normalise layers to 0 - 1 scale excluding extreme outliers.</p> <p>Append spectral bands, indices and texture bands to create single multiband stack.</p>
Ground reference data generation and image segmentation	<p>Georeference ground photography.</p> <p>Create set of 1000 sample segments randomly placed across quadrat extents after eliminating noise.</p> <p>Digitise leaf area, calculate proportion (%) per segment.</p> <p>Clip multi-band raster by segment and convert to points with class and band attributes.</p> <p>Digitise leaf area per test square.</p> <p>Export to text format, for import into R for classification.</p>
Image classification	<p>Apply random forest classification.</p> <p>Assess classification accuracy.</p> <p>Compare change-outcome agreement for test-squares.</p> <p>Calculate a change map on generalised grid.</p>

A set of ground-reference points was constructed from 1200 segmentation polygons (mean-shift segmentation, minimum size 10 pixels) selected from within the ground photography extents. Segments were removed that contained coloration from transect cord/markers, and further removal was made where segments were notably non-uniform or ambiguous. Segmentation polygon-sets (n=1000 after thinning) were generated for each survey image (Feb. or Mar.). Segmentation polygons were then overlain upon the respective survey image, and the contained pixels converted to points with the respective image-bands as attributes. This approach was taken to speed up the process of manually classifying a large number of points for model training, and hence to capture the variability in spectral character across ground-class types, avoiding non-uniform segments where spectral error would be introduced.

Segmentation polygons were attributed a ground-class, then the points associated with each polygon inherited the respective ground-class. The ground-referenced point-sets were used as training data to classify the multi-band survey images using the random forest classifier from within the *rminer* data-mining library of R-Project v3.6 software (parameters *ntree* = 1000, *mtry* = 6). Assessment of classification performance was made using overall accuracy and class accuracy metrics.

Two ground-referenced class-systems were assessed (expanded below): i) a three-tier class set for high, medium, and low-density seagrass, where seagrass cover is based on accurately digitised seagrass extent; and ii) a ten-tier (decile) class set, approximating a continuous density scale, again based on digitised seagrass.

6.3.3 Horizontally projected seagrass leaf-area index classification

The two-dimensional leaf area of seagrass was digitised in high detail within all polygons of the segmentation dataset used above (minimum 10-pixel size threshold segmentation set from the February and March 2018 surveys). Digitising was done at a scale of approximately 3:1 with polygon vertex spacing down to ~1 mm in object-space depending on shape. This scale was necessary due to the small seagrass leaf size and convoluted (twisted/entangled) presentation. The 2D polygon-area of the digitised seagrass, and proportion of segmentation polygon covered in seagrass, were calculated in FME Workbench. This proportion was generalised to a class on a ten-tier (decile) scale based on membership to the seagrass proportion ranges 0-0.1, 0.1-0.2, etc with zero for seagrass absence. Similarly, the seagrass proportion for each segmentation polygon was classed on a 3-tier scale (high, medium and low) based on the proportion being $> \frac{2}{3}$, $\frac{1}{3} - \frac{2}{3}$, $< \frac{1}{3}$, with background value of zero seagrass representing absence. The 10-tier and 3-

tier class-sets were each used to classify the respective February or March multi-band survey images. The purpose of repeating analyses upon two different class-sets was to examine the relative applicability of coarse and fine-scale class granularity for mapping seagrass change.

6.3.4 Analysis

6.3.4.1 Classification assessment for leaf area estimates

The training polygons above were derived from segmentation polygons. A separate set of test areas, independent from the training polygons, was used to assess classification performance in terms of the classification outcome contained in the predicted map. Locations of near-exact spatial overlay were available in the vicinity of the six transect endpoint ground-level marker pegs, around which 8 test-areas were fitted within the extent of the ground photography, 48 squares in total, each 200 mm x 200 mm in ground-size (Figure 6.3). A further set of traced seagrass extents were digitised under the same method within these test-areas. The test-areas were identical in image and ground locations spanning February and March surveys such that direct subtraction was valid. Classification performance was assessed by overlaying the test-areas onto the classified map and calculating the agreement between actual digitised seagrass class and the predicted class of the map. Classification metrics were calculated for each of the class-sets assessed (10-tier and 3-tier), as per-pixel overall and class accuracy statistics from the random forest resampling, correlation between outcome class assignment, regression of linear relationship, and percentage agreement on class assignment.

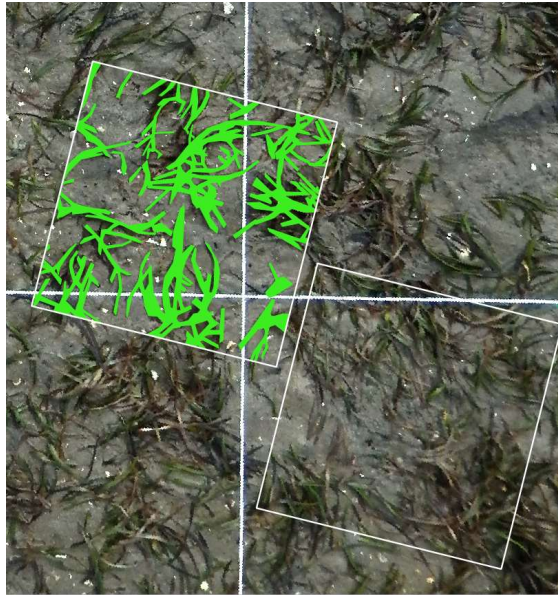


Figure 6.3. Example of digitised seagrass inside of 200 mm x 200 mm test-squares.

6.3.4.2 Measurement of change in leaf area

The applicability of the method for change detection in leaf area was assessed by comparing change in true and predicted seagrass density for exactly matched locations (the test-areas above) between the two survey times, February and March 2018, and with respect to the two class-scales, 10-tier and 3-tier for comparison. Change was calculated with sampling units being each of the 48 square test-areas. The seagrass extent was digitised per test-area, however the predicted map was heterogeneous at the scale of a test-areas. In order to provide per-test-area predicted scores to compare with traced seagrass area scores, a weighted average class score was applied using Equation 6.1, where y is the predicted class number, a is the geometric area of that class present in the test-area, and A is the area of each test-area.

$$\text{Weighted average class} = \frac{\sum y*a}{A} \dots\dots\dots \text{(Equation 6.1)}$$

The degree of agreement between actual change and the change-prediction made by the respective classification maps for the two survey times, was quantified using correlation and liner regression analysis.

6.3.4.3 Visual interpretation-based classification

Classification maps were generated using training polygons classed with a 3-tier class set assigned by visual interpretation on the three-tier scale of Section 6.3.3. Class assignment is equivalent to the encoding used in previous chapters, and comparable to the computer-calculated exact 3-tier leaf area scale tested above. Classification assessment was made by repeating the predicted and actual score comparison made above, with: i) predicted values derived from the classified map as weighted average scores per square test-area ($n=48$); and ii) actual values being the accurately traced seagrass leaf area per test-area. This comparison links classification made using accurately calculated training references back to the visual interpretation used in previous chapters. This also allows the trade-off between classification accuracy and manual timeframe to be assessed.

6.3.4.4 Classification of mid-altitude imagery using a low altitude reference

The classification procedure was repeated as before (Section 6.3.3-4), using the March 2018 multispectral image and corresponding ground reference data. The resulting classification map was used to train the classification of a secondary image captured at mid-altitude by fixed wing aircraft flying at 250 m -300 m altitude using a Micasense

Red-Edge camera, where capture was made the day prior to the RPA flights under similar overcast lighting conditions. The Red-Edge camera has similar spectral ranges of bands as the Parrot Sequoia used on the RPA, except that the Red-Edge also comprises a blue narrow-band sensor. The mid-altitude image frames collected under a photogrammetric flight design with ~70%-80% overlap, were rendered to single georeferenced orthorectified multi-band mosaic using the same procedure as applied to the 30 m altitude RPA imagery. Derived vegetation indices and texture layers were added, with the resulting multi-band image stack used for classification and analysis. The 250 m-300 m altitude analysis image-stack had the same bands as the RPA imagery, but with a blue band also factored as a classification predictor. The mid altitude image-stack was aligned to the 30 m altitude RPA image with a combination of photogrammetric reference markers visible in the imagery and distinct invariant reference features visible within the structure of the seagrass meadow.

The ground sampling distance of the Red-Edge imagery was 250 mm. The ground reference dataset was split five-fold into a training dataset (4/5 of sample) and a test dataset (1/5 of sample). The test dataset was used to assess the accuracy of predicted classification outcome for both altitudes. The ground reference data were classed on the 3-tier seagrass density scale (high, medium, or low-density seagrass, or absent) as measured by the seagrass horizontal leaf area trace described above. Additional sampling points were added to the training dataset to sample microphytobenthos (MPB) occurring at the edge of the RPA flying extent.

6.4 Results

6.4.1 Classification assessment for leaf area estimates

Classified maps for the two survey times were similar for the two class-systems used. Seagrass density difference was evident with respect to the structural elements of the seagrass meadow changing between surveys such as patch-edge contraction (Figure 6.4).

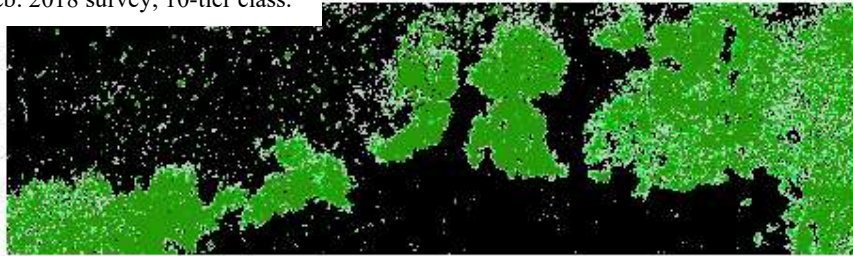
Overall classification accuracy within the random forest cross-validation was 86% and 90% for the Feb. 2018 and Mar. 2018 datasets (Table 6.3). Overall accuracy, and per-class accuracy for most classes, were higher for the Mar. 2018 data than the Feb. 2018 data, and this was the case for both the 10-tier and 3-tier class sets (Table 6.3 and Table 6.4). On the 10-tier scale, Type 1 error for seagrass presence was low (0.01) for both surveys and Type 2 error ranged between 0.1-0.14 (Table 6.3). Equivalent error values for

the 3-tier scale were 0.01-0.02 for Type 1 error and 0.08-0.11 for Type 2 error (Table 6.4). Predicted decile class and the equivalent actual measured decile class for test-areas were strongly correlated (correlation coefficients of 0.90 and 0.89, both significant at $\alpha=0.05$) for February and March surveys respectively, with linear fit (predicted vs. actual score) of $R^2 = 0.8$ and 0.8 , respectively (Figure 6.5). However, while predicted and actual measured decile density class correlated well, absolute agreement on class designation was low with 42% and 45% agreement respectively (Table 6.5). Thus, class attribution was close but not exact for the decile classification. Aggregation of classes into a measure of seagrass presence/absence, yielded agreement between actual and predicted class values at the rates 85% and 96% of the time for February and March surveys respectively.

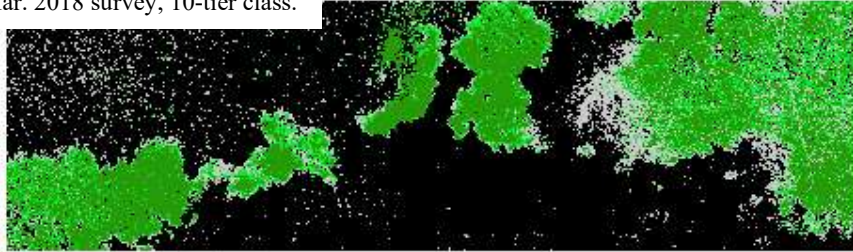
Class agreement rate on the 3-tier scale calculated with correlation coefficient values of 0.9 and 0.85, class agreement of 68% and 74%, and agreement for presence/absence was 87% and 96% for the February and March surveys respectively (Table 6.5).

Classification accuracy was higher on the 3-tier scale than the 10-tier for both the per-class and in terms of seagrass presence/absence. Consequently, use of the 3-tier scale yields more confident classification mapping than the 10-tier scale. However, the granularity of information and detail available using the 3-scale is less than the 10-tier scale (Tables 6.3, 6.4 and 6.5).

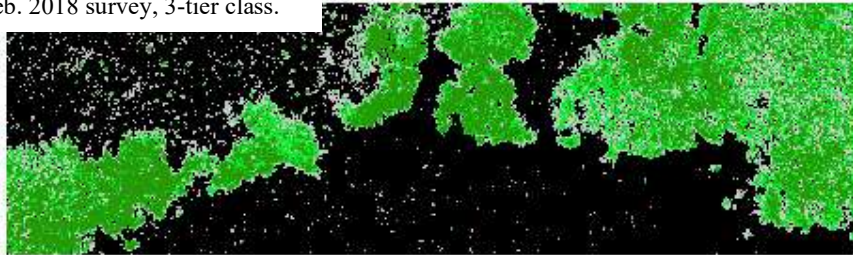
a) Feb. 2018 survey, 10-tier class.



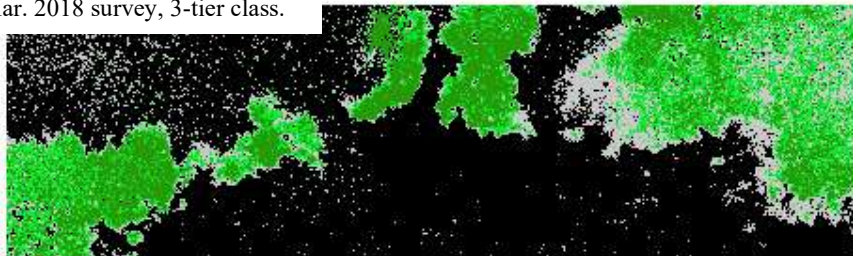
b) Mar. 2018 survey, 10-tier class.



c) Feb. 2018 survey, 3-tier class.



d) Mar. 2018 survey, 3-tier class.



e) Overview (aerial photo).



Figure 6.4. Classified seagrass-density maps for February and March 2018 surveys, and for 10- and 3-tier class sets, with aerial photography overview. Key: High density (dark green); mid-density (light green); and low-density seagrass (grey) upon seagrass absence (black). Rectangle in e) shows the extent of a)-d).

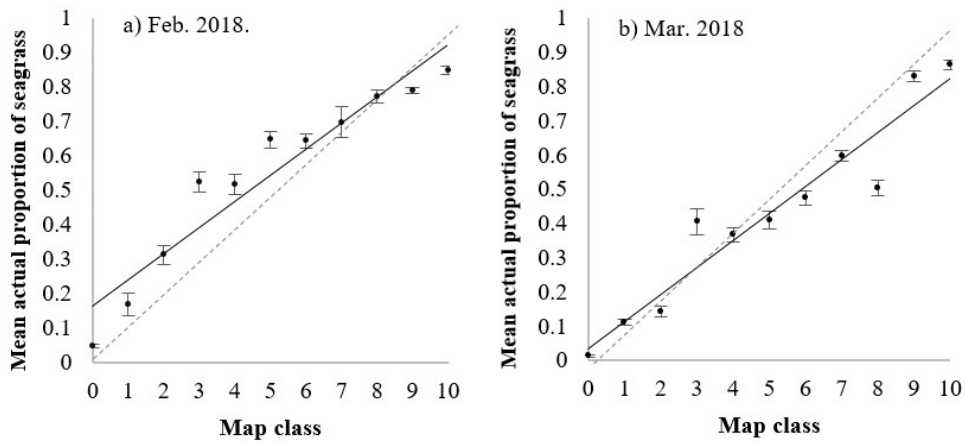


Figure 6.5. Relationship between predicted map class and actual mean seagrass leaf area of the square test-areas for the two surveys: a) February 2018; and b) March 2018. Error bars are standard error about the mean. Shown are the line of best fit (solid line) and line of unity expected under perfect class agreement. See Table 6.5 for line statistics.

6.4.2 Measurement of change in seagrass density (leaf area)

Difference-maps enable the change in seagrass density (in terms of digitised leaf area) to be visualised for each of the two class-sets tested (10- and 3-tiers of scale granularity (Figure 6.6). Both scales yielded similar maps, with growth in some areas and decline in others across the 8-week timeframe between surveys. Growth was prominent at the patch margins and hole edges and decline in many but not all central patch areas. The 10-tier set allowed fine seagrass regrowth to be detected that wasn't possible using the 3-tier class set. For example, under the 'high, med, low' model, the lowest density seagrass was at times classified as being absent of seagrass.

There was a moderate linear relationship between predicted and actual change using the 10-tier class set (Figure 6.7). The agreement in direction of change (i.e., sign) between predicted and actual change was 69% overall. Thus, 31% of test-areas were incorrectly attributed as a decline when there was gain, or gain when there is decline (Figure 6.7). This error was largely associated with subtle levels of change – but there was good coarse agreement between predicted and actual change when the change was substantial. The agreement rate was 74% when disregarding less than one class-unit of change, and 100% when disregarding up to 2 class-units of change, on the ten-class scale. The three-tier class set was less sensitive to change, with 60% agreement on change-direction for all test-areas, and 83% agreement when only considering the medium and high change.

6.4.3 Visual interpretation-based classification

Visually interpreted seagrass density class attribute on a 3-tier scale agreed with actual leaf area derived seagrass density measures (i.e., prior to classification), in 88% of the 1000 training segments. Image classification based on visual interpretation of training classes yielded marginally lower outcome class agreement statistics than the equivalent measured (3-tier) leaf area training classification (Table 6.5), in terms of correspondence of predicted map class with actual computed leaf area.

Table 6.3. Within-classifier accuracy metrics (n=5633 points) for the ten-tier decile scale. Accuracy statistics are true positive rate. Classification metrics (%) are out-of-bag accuracy statistics reported from the rminer algorithm (random forest model). Presence/absence statistics are the true positive and true negative classification rates, and corresponding Type I and II error rates, for whether seagrass was predicted as present or not.

		Feb. 2018.	March 2018.
		<i>Overall accuracy.</i>	
		86	90
		<i>User accuracy.</i>	
Seagrass class	Absent.	99	99
- decile scale.	0-10%	37	55
	10-20%	49	74
	20-30%	69	65
	30-40%	43	77
	40-50%	41	77
	50-60%	60	68
	60-70%	59	70
	70-80%	76	75
	80-90%	66	83
	100%	52	81
Seagrass presence / absence.	Presence.	86	90
	Absence.	99	99
Type 1 error.		0.01	0.01
Type 2 error.		0.14	0.10

Table 6.4. Within-classifier accuracy metrics (n=5633 points) for the 3-tier scale of high, medium and low seagrass density (proportions $> \frac{2}{3}$, $\frac{1}{3} - \frac{2}{3}$, $< \frac{1}{3}$ respectively). Accuracy statistics are true positive rate. Classification metrics (%) are out-of-bag accuracy statistics reported from rminer algorithm (random forest model). Presence/ absence statistics are the true positive and true negative classification rates, and corresponding Type I and II error rates, for whether seagrass was predicted as present or not.

		Feb. 2018.	Mar. 2018.
		<i>Overall accuracy.</i>	
		91	93
		<i>User accuracy.</i>	
Seagrass class	Absent.	98	98
- 3 tier scale.	Low.	69	74
	Medium.	62	86
	High.	88	88
Seagrass presence / absence.	Presence.	89	92
	Absence.	98	99
Type 1 error.		0.02	0.01
Type 2 error.		0.11	0.08

Table 6.5. Within-classifier accuracy metrics in terms of agreement in classification outcome between the predicted map and actual measured seagrass density class of independently measured square test-areas, for 10-tier (decile) and 3-tier (high, med. low) class sets, and human-interpreted classes.

Statistic.	Feb. 2018.	Mar. 2018.
Number of test-areas.	48	48
Number of points.	3072	3072
10-tier classification, computed seagrass density reference:		
Correlation (predicted vs. actual).	0.90	0.89
Regression coeff. (β , intercept).	0.09, 0.09	0.08, 0.02
Regression fit (R^2).	0.80	0.80
Agreement by 10 classes.	0.42	0.45
Agreement by pres./abs.	0.85	0.96
3-tier classification, computed seagrass density reference:		
Correlation (predicted vs. actual).	0.90	0.85
Regression coeff. (β , intercept).	0.26, 0.06	0.22, -0.004
Regression fit (R^2).	0.82	0.73
Agreement by 3 classes.	0.68	0.74
Agreement by pres./abs.	0.87	0.96
3-tier classification by human visual interpretation:		
Correlation (predicted vs. actual).	0.88	0.85
Regression coeff. (β , intercept).	0.23, 0.048	0.21, 0.012
Regression fit (R^2).	0.77	0.73
Agreement by 3 classes.	0.69	0.64
Agreement by pres./abs.	0.91	0.96

6.4.4 Classification of mid-altitude imagery using a low altitude reference

Classification of the mid-altitude aircraft-sourced imagery using low-altitude multispectral RPA-sourced imagery yielded low correspondence between predicted and actual classes on the 10-tier decile scale of measured seagrass density, although when generalised to presence/absence of seagrass there was high accuracy near to the ground reference transects (Table 6.6). Spatially, seagrass presence/absence estimates (with decile classes fitted to account for variability) yielded accurate seagrass extent-mapping close to the training reference, but error increased with distance away from these ground observations. There was notable error and when moving from the coarse conditions of the study site (largely sandy ‘ridge’ with water-carved microtopography) to other major substrate character (e.g., permanently waterlogged flat mud, or stream channel) (Figure 6.8.). This indicates that separate training data may be required by each major section of the estuary and warrants further investigation.

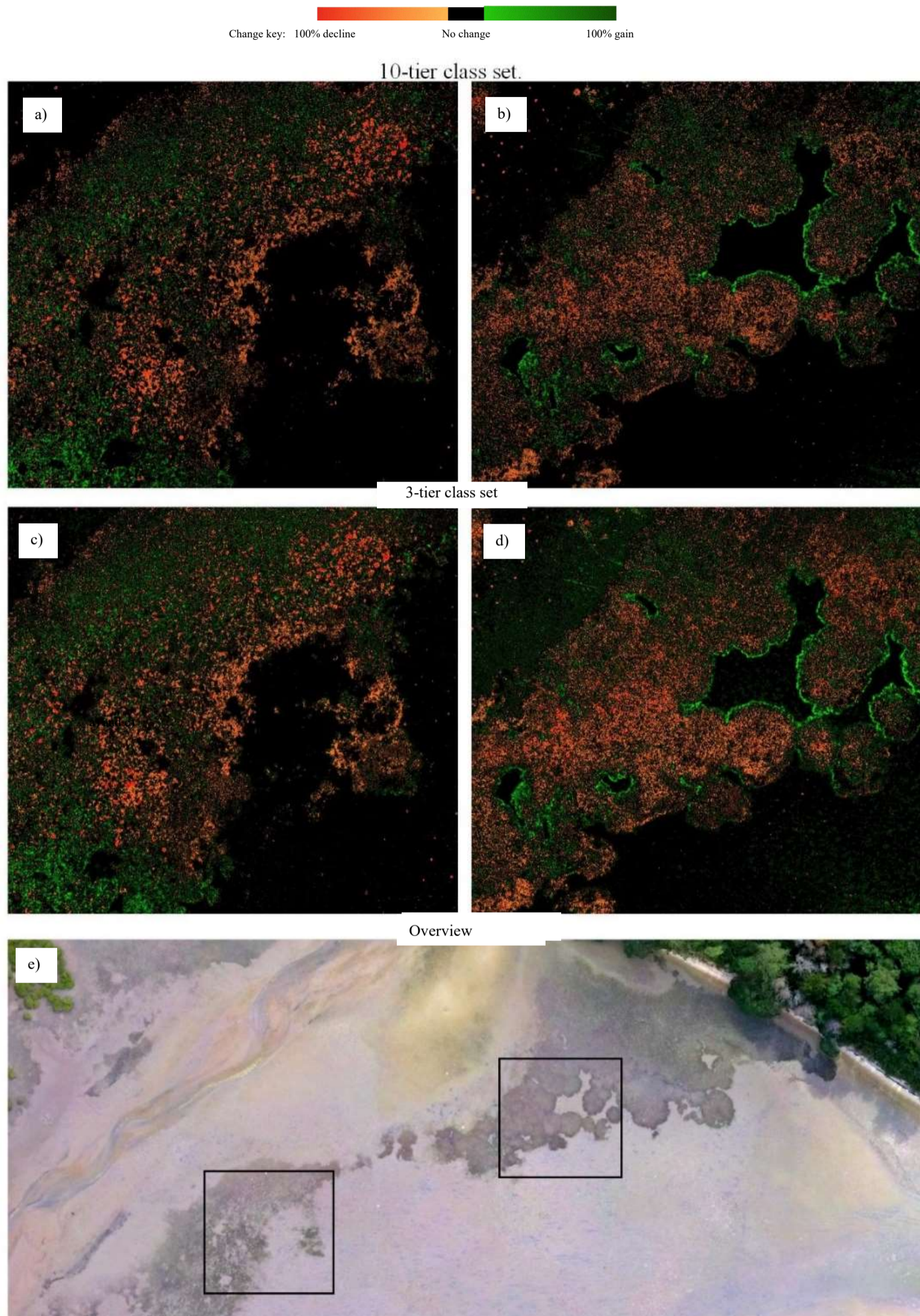


Figure 6.6. Change in seagrass density-class between February and March 2018 survey times, and for the two class-sets tested (10- and 3-tier class system). Black boxes on aerial photography overview map (e) show the locations of the enlargements above. The colours in the upper frames indicate reduction in seagrass density (reduction intensity orange → red hues) or increased density (gain intensity pale → rich green hues), with black indicating no change or absent.

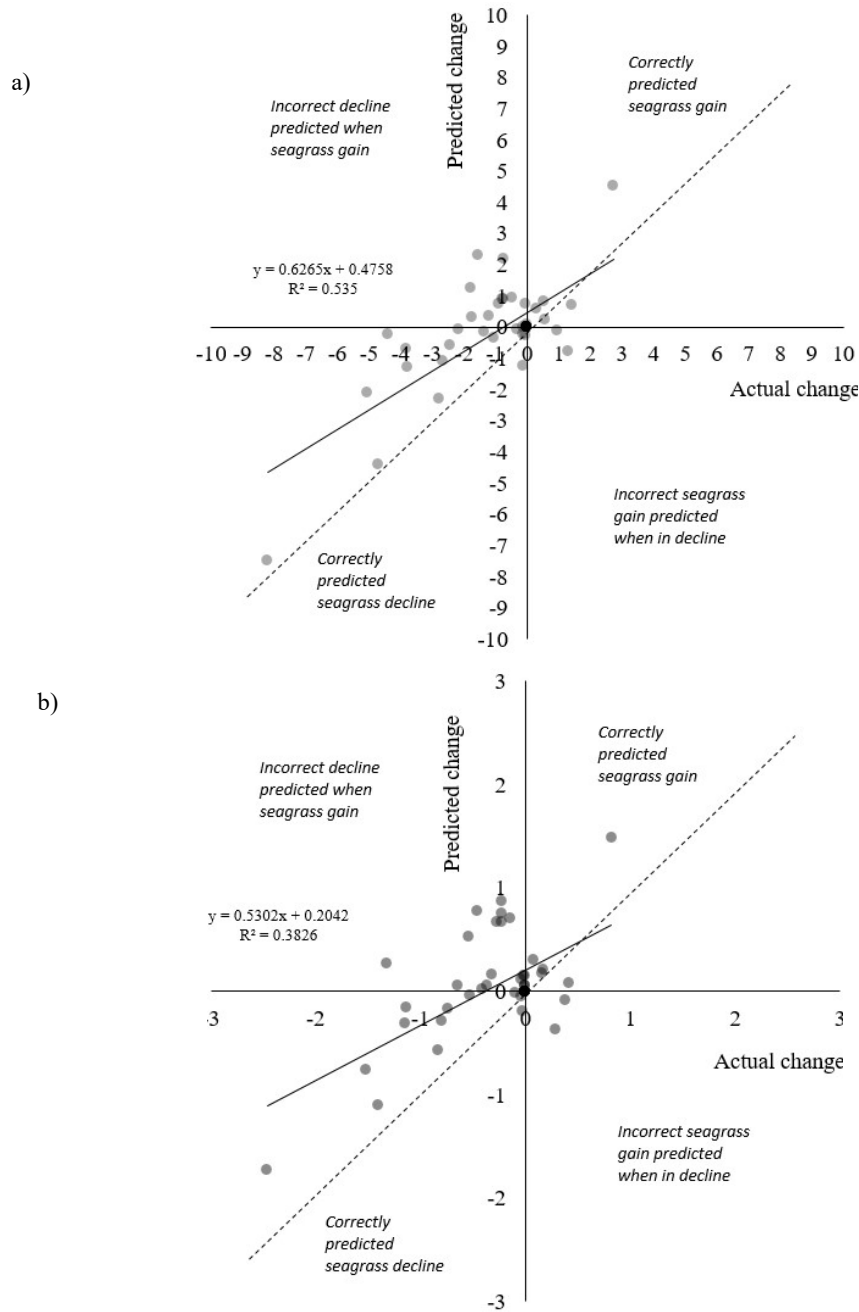


Figure 6.7. Predicted and actual change in seagrass density within 48 test-areas. Axis units are shift in density class, where a positive value indicates gain in seagrass density, and negative indicates decline. Two class-division scales were assessed: a) a 10-tier class division; and b) a 3-tier class division. Solid trend-lines show linear regression fit of data, and dotted lines show the line of perfect class agreement.

Table 6.6. Classification outcome after using the 30 m altitude multispectral classification map (Parrot Sequoia camera, 2.7cm pixel GSD) to train multispectral imagery collected at 250-300 m altitude (Micasense Red-Edge camera, 250 mm pixel GSD), where classification statistics are based on sampling points measured along the ground-reference transects, with class-observations calculated from accurately digitised horizontally projected leaf area.

	Producer		User		Producer		User	
		accuracy	accuracy		accuracy	accuracy		accuracy
		(%).	(%).		(%).	(%).		(%).
Seagrass class.	Absent	98	88	Absent.	96	88		
	1	0	0	Present.	71	93		
	2	0	0					
	3	13	20					
	4	3	5					
	5	0	0					
	6	0	0	Overall	71			
	7	5	4	accuracy				
	8	0	<i>n/a</i>	(%).				
	9	81	21					
10	26	19						

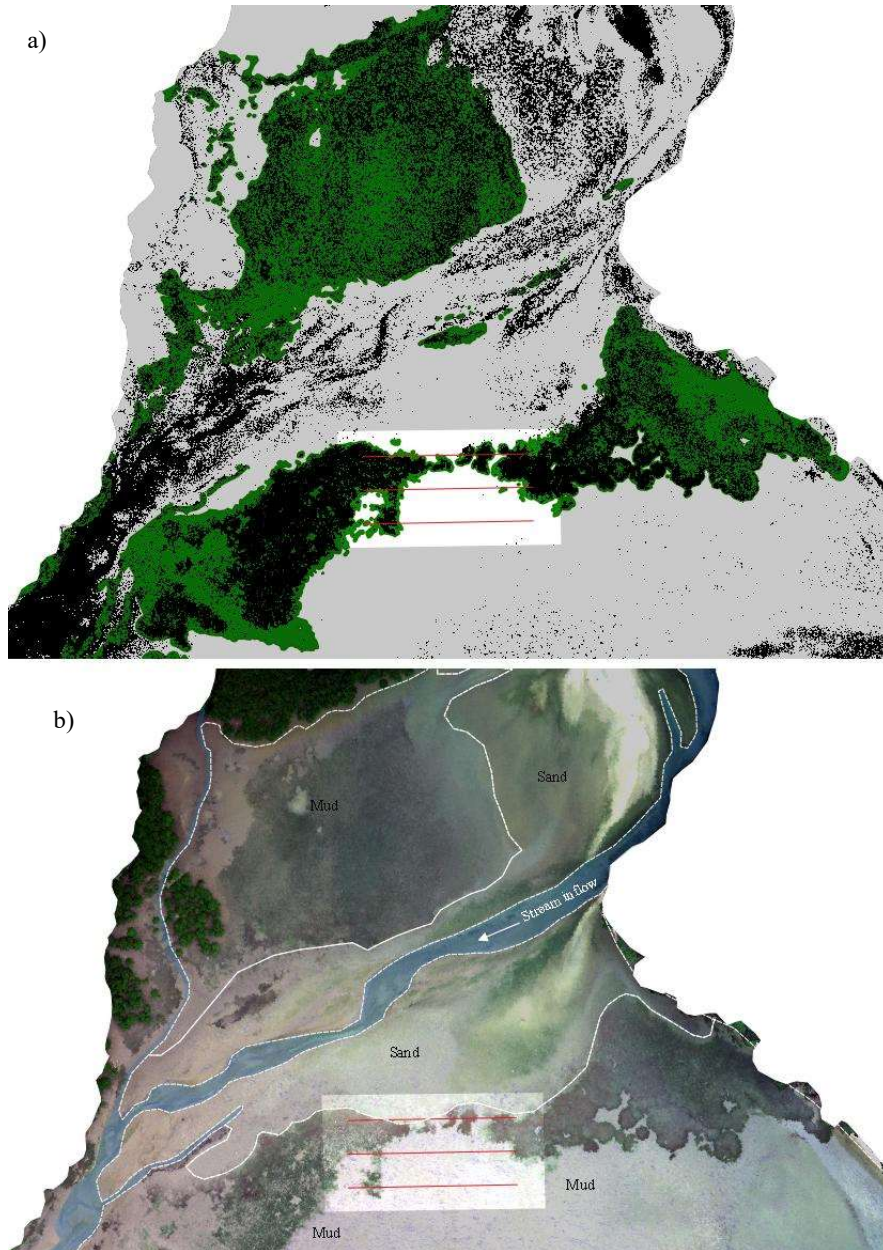


Figure 6.8. Classification outcome after using the 30 m altitude multispectral classification map (Parrot Sequoia camera, 2.7cm pixel GSD) to train multispectral imagery collected at 250 m - 300 m altitude (Micasense Red-Edge camera, 250 mm pixel GSD). Black pixels show estimated seagrass (a), and absence of black indicates predicted absence of seagrass. Green polygons in (a) show the actual presence of seagrass as measured by precision ground survey (refer to Chapter 3 for description). Red-Edge camera imagery for reference (b). Central to both frames is a rectangle showing the area of interest captured by the three ground-observation transects.

6.5 Discussion

This Chapter 6 maps seagrass coverage based on measured horizontal leaf area for two replicate surveys, February and March 2018. The relationship between predicted seagrass density class estimation and measured horizontal 2D leaf area was determined to be linear with high model fit (Figure 6.5). Change in seagrass presence and density-class was quantified using difference-maps on 3-tier (high, medium low) and 10-tier (decile) density-scales (Figure 6.6). The classification performance of a model trained by traced seagrass references is higher in accuracy than a model trained using visual interpretation references (Section 6.4.3). However, the time-cost of tracing the seagrass is substantial and suited to situations where high monitoring sensitivity is required. Classified multispectral imagery flown at 30 m altitude was used to classify multispectral imagery captured at 250 m – 300 m altitude (Section 6.4.4). The classification yields predictions with moderate classification accuracy near to the reference training samples, and error that increases with distance from the training samples (Figure 6.8).

The classified maps yielded information about seagrass meadow structure and regions of change within seagrass patches. The classification method is suitable for mapping seagrass density in terms of measured leaf area, as well as detailed presence/absence mapping. The method is reliable for extracting the seagrass feature for medium and high-density classes, with low density seagrass being confounded with areas seagrass absence. Change detection is reliable when there is moderate change, but error appears in the change-characterisation when seagrass density differences are subtle. Designating subtle change as non-informative noise raised the accuracy of change-detection. Therefore, application of the method for seagrass change monitoring may consider discarding minor change by exclusion filter, focusing on change in high confidence classes, and factoring this into monitoring design at large scale.

Classification outcome for density by measured leaf area is strongly correlated with seagrass density, but inexact in specific class attribution (when 10-tiers of density scale granularity are used). Seagrass presence/absence estimates, calculated by way of density class intermediate processing, are highly reliable (Table 6.3 and Table 6.4). Type I and II error for presence/absence estimate were small for both class systems, indicating that both the false prediction of seagrass presence and the failure to detect seagrass presence are low. This further indicates that application of the method for binary seagrass extent mapping is reliable, noting that presence/absence mapping was modelled here by way of the end-member density classes.

The ten-tier class-set allows finer detail in change to be observed than the 3-tier class set. However, measuring coarse tendency in change (growth, static, decline) is still achievable using the lower scale granularity. Classifying images using digitised seagrass leaf area yields better classification performance than when using visual interpretation of classes. However digitising seagrass is significantly time-consuming. Visual interpretation of density scale is ~ 100-fold faster than tracing seagrass. The gain in classification performance by tracing seagrass may not be worth the time investment unless: i) time is not a limiting factor; ii) high scale granularity is required for the particular monitoring precision; or iii) a higher monitoring sensitivity is required than that of the visual interpretation method. Development of a reliable automated close-range seagrass feature extraction process from ground photography would neutralise this time-quality trade-off.

The classification accuracy metrics derived from the random forest algorithm indicate that better classification is possible by using the 3-tier density scale rather than 10-tiers. These accuracy measures are based on segmentation-polygons used for seagrass digitisation and training points. Applying independent test-squares of unknown mixed content for the purpose of outcome assessment, the 3-tier classification scale similarly yields higher class agreement per survey than the 10-tier scale (noting the different scale granularity) but performing worst in terms of agreement in change designation. Therefore, the three-tier scale is recommended for monitoring where coarse change in seagrass is required, and the ten-tier scale where fine detail of seagrass change is sought.

In this analysis, high density seagrass classified with higher accuracy and better outcome class agreement than sparse density seagrass. In a similar study that mapped the seagrass *Zostera marina*, Nahirnack et al. (2019b) demonstrated higher accuracy in dense seagrass, although their survey measured submerged seagrass using manually classified segmentation areas. Similarly, a study using high resolution Worldview 2 satellite imagery (Baumstark et al., 2016) demonstrated lower classification for the sparse seagrass classes as compared to their dense class. In contrast, seagrass research by Duffy et al. 2018 suggests that classification accuracy was greater in sparse rather than dense areas, noting their use of wide-band consumer imaging rather than multispectral narrow-band imaging without infra-red spectra.

Assessment of classification accuracy was based on 48-test-squares at six locations. Analysis could have benefitted from more test areas over more of the study area. This number was limited by the timeframe to accurately digitise seagrass and the requirement for high levels of spatial alignment. A recommendation for future research is

to develop automatic seagrass feature retrieval from the images taken at ground level, so that models are trained using large amounts of ground-observation data circumventing the manual overhead of accurately digitising seagrass density. This was attempted in the present study but was not easily applicable using the Parrot sequoia camera which has lens geometry arranged for flying heights above ~6 m (image misalignment was unusable).

It was difficult to avoid manual (human) judgement in forming the classification model and survey method. Classification of remote sensing images by human eye can be successful (e.g., Husson et al., 2014a), but also can be prone to subjective error (Congalton and Green 2009). Subjective bias potentially could arise through choice of the classification ontology, judgement of density class attribution in the training dataset, repositioning of segments to correct for misalignment in spatial overlay, ground-camera orientation control, and positioning of ground-control-point markers within the photogrammetry software. In terms of the seagrass survey, there could also be user bias in the choice of survey conditions and time of year, and in particular the timeframe since last major sediment/detritus/shell disturbance event.

Training of the classification model using accurately traced seagrass leaf area polygons as a measure of density indicates a likely ceiling for classification specificity using this camera and survey specification. Visual interpretation of training classes is less precise due to potential interpretation error, but the outcome is similar to that of the equivalent leaf area training class set (3-tiers) when modelled in this classification framework. Class agreement between predicted and actual maps is only slightly lower for the visual interpretation method than the measured leaf area in terms of the mapped outcome. The task of tracing leaf area polygons was time-consuming and effectively quadrupled the total data collection time compared to rapid visual interpretation of training density class. Visual interpretation was reliable at 3-tiers of class granularity, and results demonstrate that the method yields useful classification with 3-tiers. However visual interpretation may not be feasible at higher granularity, in which case investment in manual digitising may be warranted. Visual interpretation is still in common use in recent seagrass low altitude mapping research (Alexander et al., 2008; Barrell and Grant 2015; Chayhard et al., 2018b; Konar and Iken 2018; Nahirnick et al., 2019a; Nahirnick et al., 2019b). Visual interpretation also yields classification performance similar to that of an object-based image analysis workflow using high resolution satellite imagery (Baumstark et al., 2016). In the current study, visual interpretation yields similar classification outcomes (under 3-tier class set) as compared to the digitised and computed

leaf area, so these results illustrated the continued value of human visual interpretation for preparation of training data. In this study visually attributed per-segment seagrass classes agreed with measured leaf area in 88% of test-cases. This rate, and corresponding classification accuracy upon map-production, may improve under the guidance of a visual reference library for observer interpretation training and bias-elimination (an example is provided in Chapter 7 Appendix 7.8.1).

Classification of a secondary mid-altitude aircraft-sourced multispectral image using the primary RPA image results in good differentiation of seagrass from substrate, but poor density class attribution. Lack of seagrass density class agreement between the secondary classification and empirical ground observation may be related to difficulty in aligning imagery accurately to sub-pixel scale (on aircraft imagery), or due to sub-pixel content mixing as there was variation in seagrass density below the scale of individual mid-altitude pixels. Classification of seagrass presence/absence was accurate near to the ground observation points (e.g., up to ~30 m) but accuracy decayed with distance from the reference transects. This result indicates that additional ground reference transects would be required across the greater scene to fully model variability in substrate and wetness environment. In terms of applying the method at large scale, depending on estuary composition it may be more appropriate to use smaller RPA image patches allowing more sampling spread out over the range of estuary conditions than fewer large patches. Further development of this secondary classification was beyond the scope and design of the study which focussed on the RPA method at one site but warrants further investigation at estuary-scale of consideration where major estuary substrate environments can be modelled.

6.6 Conclusion

In this chapter, RPA-sourced multispectral survey images were classified using digitised horizontal leaf area to quantify seagrass density. Classification accuracy is good for dense seagrass classes, but less so for sparse seagrass. There is a high correlation and a significant linear relationship between predicted and actual seagrass density classes. Classification performance is maintained across a timeframe within which there is visible notable change in seagrass density across the study area. Consequently, image classification by horizontal leaf area is demonstrated as a viable seagrass mapping method. Class attribution for the training dataset yielded classified images with similar accuracy to that of the equivalent measured seagrass leaf area, so visual interpretation is a viable alternative if time is short for generating the training dataset. Ten classes detect

finer detail than three classes for depicting sparse seagrass condition and change but is also more susceptible to false inclusion of non-seagrass content as predicted sparse seagrass. Application of the method to condition monitoring at estuary scale could focus on the status and change in the extent of the medium and high-density seagrass.

CHAPTER 7

Chapter 7 Determining estuarine seagrass density measures from low altitude multispectral imagery flown by remotely piloted aircraft

7.1 Justification and purpose

Seagrass in New Zealand is considered to be under pressure with declines recorded in many places around the country. The overall status of seagrass nationally is not clear due to a deficiency of monitoring data for many sites. Considerable efforts are being made to expand the monitoring coverage in New Zealand and expand methodology beyond manual ground survey or map-digitising, to crowd-sourced data collection and/or automated remote sensing methods whereby monitoring return-on-investment can be elevated (Pohl 2015). There is as yet no standard agreed method for monitoring the condition of seagrass. Remote sensing methods are well established in terms of coarse satellite and aircraft image analysis, but there remains the challenge for these methods in differentiating sparsely growing seagrass from background and understanding the detection limits in terms of the seagrass density gradient. Sparse seagrass grows as a relatively dark silhouette against a bright sediment background. The training data required to classify satellite and aircraft imagery requires visitation to the estuarine site, with personnel traversing the flat terrain, wielding GPS-camera and quadrat, until a representative ground sample is attained. Travel across seagrass can damage the meadow and not all parts of the estuary are accessible on foot.

Remotely piloted aircraft are a relatively new technology that have potential to add capability and cost-efficiency to the task of large-scale estuarine seagrass monitoring, while reducing physical impacts to meadows via trampling. Remotely piloted aircraft provide the opportunity to improve on classification performance over satellite and aerial imagery due to their versatility for conducting spatially precise operations at low speed and low to the ground. (e.g., Feng et al., 2015; Tang and Shao 2015). In New Zealand piloted aircraft operating under visual flying rules (VFR) are limited to the minimum flying height of 500 feet above ground level (including most intertidal estuary areas) or 1000 feet over built-up areas or assembled persons (Civil Aviation Authority Rule Consolidation Part 91), imposing a physical limit on the achievable image detail. As flying height for aircraft survey is lowered, potential for motion-blur increases, so to

maintain image clarity the flight velocity needs to reduce proportionally to flying height. For fixed wing aircraft, a minimum air speed is required across the flight surfaces to maintain lift, stability and control, so there is a lower safety-limit on flying speed, that imposes a ground proximity-limit for camera survey. For example, a Cessna 172 requires air speed of approx. 70 kn (130 km/h or 36 m/s) for safe stable survey flight. At this speed, a camera with 1/2000th second shutter speed would experience motion blur of ~2cm across the ground, such that small objects (like seagrass) may blend problematically with adjacent materials thereby confusing an image classification. Aviation rules regulate normal RPA flight to the range 0-400 feet above ground level (Civil Aviation Authority 2018). Fixed-wing RPA with low wing loading can maintain flight at airspeed down to ~ 10 m/s, and multi-rotor RPA can sustain constant controlled speed to 1 m/s or lower depending on hardware setup and wind conditions. These precision flight characteristics allow very high-resolution imagery to be captured low to the ground with high feature definition, which may be important for differentiating the small structural dimensions of seagrass foliage from the small objects (shells, detritus, wrack, mangrove seeds, brown and green macroalgae) that are common on many estuaries.

7.2 Main findings by chapter

Chapter 3.

In this remote sensing method assessment, field research was conducted at Wharekawa Harbour on the eastern coast of Coromandel, North Island, New Zealand. This site exhibits a multi-decadal pattern of seagrass loss then regrowth (as far as can be discerned from historical aerial photography by visual interpretation), then reverting to loss again in recent years. Precision ground survey demonstrates marked seagrass loss over the year of the study following two major rainfall events and at a time of high vulnerability to plantation-forestry sediment-inflow. Seagrass survey using consumer hand-held GPS units (on a 2 m survey pole) yielded positional data with absolute accuracy of <3 m and typically less than 2 m, and <0.5 m for precision corrected GNSS under rapid survey.

Chapter 4.

Drainage of residual ebb waters from an estuary, after the bulk water column has drained, creates a mosaic of rapidly or slowly drying estuarine surface or permanent shallow waterlogging/pooling that has potential to interfere with spectral observations

during the survey of an estuary. Although minor shifts in spectral coordinates of seagrass, and other surface material were recorded, there was no discernible impact on image classification performance or classification outcome. In general, it is possible to generate valid seagrass density mapping across the whole window of time that the tide is out, with one notable exception: during the early stage of residual water drainage (i.e., immediately after the water column has ebbed), areas at the periphery of the photogrammetric image grid are susceptible to glint or glare interference that creates false surface feature-identification. This can be mitigated with RPA survey conducted with low sun angle (e.g., $<45^\circ$) and structured with high levels of photo-overlap such that the rendered image mosaic is comprised of image-parts at near-nadir camera orientation, which reduces this glare effect. Conversely though, nadir imagery taken with high sun angles contains significant direct sun reflection off wet parts of the surface that confound the spectral information. If fieldwork timing is flexible then setting the time of survey to later during the low-tide window (e.g., > 1 hour after bulk-water has cleared from the surface) will minimise this observed glint/glare effect so long as the sun angle is ~ 45 degrees or lower.

The use of a multispectral camera yields more accurate seagrass feature extraction compared to a conventional scouting camera in visual red-green-blue bands. This is largely due to the availability of red-edge and infra-red bands that allow highly contrasting vegetation indices and texture layers to be derived from camera bands and factored into classification and seagrass feature extraction. The benefits of the multispectral camera may also relate to the fast-global shutter (compared to the rolling shutter of the conventional camera) which provides better spatial consistency during RPA survey motion. Despite this, the scouting camera will generate basic seagrass mapping, indicating that a conventional camera may be suitable for feature extraction at some locations where there is good seagrass contrast against the scene background. Note that this is a comparison between 16 megapixel (consumer grade) and 1.2 mega pixel (multispectral) cameras contained in the same device housing: at time of capture the consumer camera has greater resolution to capture detail in the seagrass meadow structure but lower spectral detail than the multispectral sensor.

Chapters 5.

Object-based image analysis (OBIA) methods have provided improved classification performance in some applications where image-object geometry provides added feature-separability to a classification model, although OBIA benefits may be dependent upon the size of ground objects or the scale of land-cover features with respect

to image pixel size. For the case of seagrass feature extraction using RPA-mounted multispectral imagery flown at 30 m altitude (~2.7 cm pixel ground sampling distance) OBIA does not appear to convey classification benefits, and pixel-based image analysis (PBIA) yields the best feature-separability for demarcating seagrass presence/absence and estimating seagrass density. At this image scale, visually contaminating objects (such as shells, leaves, pinecones, and sticks) are approximately 1-2 pixel in size and become aggregated within segmentation polygon objects when OBIA is applied. RPA operation at a different altitude (i.e., pixel size) may well benefit from the OBIA approach, and each flying height should have an assessment of optimal segmentation scale (including pixel scale) for optimal classification performance.

Seagrass and sediment have separable spectra, but shell and detritus are major contaminants of the seagrass scene and confound the classification of seagrass density class. High density seagrass is distinct from other seagrass density classes and from sediment, but there is higher classification error for the sparse density seagrass classes. Modelling the density classes within the classifier yields accurate estimates of seagrass presence/absence. Survey for long term extent monitoring would benefit from i) avoiding post-storm conditions when transported shell and detritus cover a seagrass scene; and ii) selecting the time of year when seagrass density is near the annual maxima with minimum sediment burial. For Wharekawa Harbour and similar sites, the optimal survey window is estimated to be in the months of February and March, extending to April but prior to high rainfall events (i.e., after several weeks of settled weather conditions).

Three classifiers (linear discriminant analysis, support vector machine and random forest) and three feature selection options (no selection, collinearity reduction and recursive feature elimination) were assessed for classification performance. The assessment demonstrated that the classifiers support vector machine and random forest performed with greater accuracy than linear discriminant analysis. Furthermore, random forest performed with marginally greater accuracy than support vector machine for small segment and pixel-based image analysis. No benefit was identified for random forest in reducing the number of features (i.e., predictor variables) in the statistical classification model. The highest accuracy was achieved in models with all features fitted. Calculation of vegetation indices and texture layers each increased classification performance compared to only fitting the camera bands into the classification model, with the camera spectral bands and vegetation indices strongly influencing classification accuracy. Object geometry made only negligible contribution to classification accuracy under the mean-shift segmentation method used here. Available camera bands included red-edge (RE)

and near infra-red (NIR) bands. Secondary versions of vegetation indices were assessed by substituting RE in place of NIR in the vegetation index formulae, and results indicate classification improvement by using red-edge rather than NIR in the index equations, but noting that as individual predictors, NIR was more influential than red-edge. It appears that red-edge forms a good contrast reference against the red band where there is photosynthetic material. However maximum classification accuracy was greatest by including both NIR and equivalent red-edge-based indices together in the random forest model (i.e., fitting all available predictors).

Three repeated surveys classified seagrass with high overall accuracy, and the highest accuracy was achieved during the later surveys that were unaffected by the 2017 rainfall events. Microphytobenthos (MPB) and other chlorophyll sources appeared as sparse seagrass in the classification maps. Therefore, application of the method should factor in classes for this and other potential chlorophyll sources (e.g., the green algae *Ulva* spp.) and/or consider avoiding the conditions when MPB is prevalent. For Wharekawa Harbour, February was a time of high MPB (January was not sampled), March less so, and in April MPB largely absent. Therefore, as indicated above, RPA survey operations would benefit from a target time for survey in February but postponing if high MPB/algae levels are prevalent, and before more unsettled weather patterns set in during March or April. The 2017 rain events resulted in substantial detritus, shell and sediment deposition upon and around the seagrass, compromising seagrass density class estimation.

Chapter 6

This chapter demonstrates that an RPA fitted with a multispectral camera flying at 30m above ground level can detect change in seagrass coverage and presence with moderate agreement to actual change in leaf area.

The visual interpretation method used to attribute seagrass density to ground observation, agreed with precisely measured horizontally projected leaf area 88% of the time with some minor misattribution at mid-density (see Chapter 6). Classification accuracy was higher when seagrass was accurately traced from ground-level photography rather than estimated by eye. Classification was higher when modelled on the 3-tier class scale (low, medium, high density seagrass) compared to the 10-tier scale.

The timeframe required to trace the seagrass was substantial, being > 100-fold more time consuming than the visual interpretation method. The time-cost required to trace the seagrass may outweigh the return in additional classification accuracy, as visual

interpretation alone achieved good overall accuracy in the range 85-88%. Classification on a 10-tier decile scale would likely be too granular for accurate class-attribution by eye. Accordingly, if sensitive change detection was required on a decile scale, then leaf area tracing would be warranted.

7.3 Operationalising the method

An overarching purpose of this research was to test an RPA survey method to enable the collection of discrete precise seagrass coverage data, and to allow scalability to larger survey scales, including application to the task of training image classification for high-altitude long-range aircraft capture. There were three components considered as part of a coordinated (possibly adaptive) approach to estuarine survey for seagrass: i) image capture near to ground-level; ii) low altitude multispectral photography (30 m above ground); and iii) multispectral aircraft photography at ~300 m. The research demonstrates that ground and low altitude image collection may be collected on the same estuary excursion, and the aircraft photography imagery on the same or adjacent day if coordinated carefully with a pilot. Potentially all three could be captured using the same camera and therefore sample the same spectral information. This image consistency and potential for rapid deployability may be important for estuaries where conditions change rapidly with tidal water movement. In more detail:

Near to ground point capture:

The research collected ground-level high resolution photography on 5 m increments along a straight transect. Image frames were independent of other frames, and spatial positioning was a result of: i) consistent orientation normal to ground; ii) lens correction to bring about rectilinear pixel dimensions across the image; iii) GPS positional accuracy; and iv) orientation control with respect to the transect direction. This design was adopted to resemble an approach that could be implemented using an RPA with a flight programme on straight line of travel. To achieve the required positional accuracy, flights would need to be navigated by a decimetre-accurate positional control technology (e.g., the Emlid 'Reach' or Proficnc 'Here+' real-time-kinetic (RTK) differential GNSS modules), along with a gimbal to ensure the required normal-to-ground and heading orientation. In this way, the RPA acts as a mobile quadrat (Figure 7.1). This level of data provides the observer with the ability to determine unambiguously what material is on the ground, providing an empirical spatial and compositional reference for designing and training the classification of higher altitude imagery. A conventional

camera was used in this case, although there is potential to gain rich information and processing automations by using a multispectral camera at ground level if a lens correction and band alignment solution can be programmed. This was attempted in this study with unsatisfactory band alignment and hence was not adopted.

Low altitude multispectral photography:

The primary contribution of this thesis relates to image classification and seagrass feature extraction using low altitude (30 m) multispectral photography georeferenced to relate spatially to the ground-level reference photography. This tier of imagery provides a predicted seagrass density, as well as high-confidence presence/absence, and moderate capability to detect change at sub-meadow scale. There is sufficient detail in this imagery to identify the meadow structure, surface material and substrate topography, and assess the impact of classification contaminants such as detritus, shell, and MPB/algae. With sufficiently representative training data, predicted classes are sufficiently accurate to apply to the task of training higher-altitude imagery at greater coverage extent. However, capture of imagery at this detail level is slow to acquire (5 m/s) with high battery power demand per unit of coverage area, so may not be cost-effective for whole-estuary application (Figure 7.2). Radiometric normalisation between patches was not examined in this study and requires examining before widespread application can be recommended. However, this method is highly suitable with good repeatability for establishing permanent monitoring ‘plots’ for seagrass population condition monitoring and change detection as part of an estuary-wide long-term sampling network (Figure 7.3).

Aircraft multispectral photography at 300m:

Seagrass mapping by RPA is currently not suitable or cost-effective for large estuaries due to current battery, height and operational range limits, as well as complexities with regard to normalising imagery across long timeframes. Accordingly, RPA are not yet a viable technology for exhaustive regional scale estuary monitoring directed at obtaining consistent imagery for all estuaries around a regional coastline. RPA mounted multispectral camera imagery are demonstrated here to yield significant benefits in terms of image quality and classification outcome. The same type of camera can be mounted on a piloted fixed wing aircraft and generate useful imagery at whole estuary scale provided sufficient ground observation data is available to train a model. It is noted that large volumes of training data and scene-subsetting may be required to account for substrate and wetness variability across an estuary.

As such, application of this method could involve the rapid sequential launch of two-RPA flights per survey patch (ground reference + low altitude) with a concurrent flight (if a second multispectral camera is available) by a fixed wing aircraft sortie over the same site using the low-altitude tier for comprehensive training of the large-scale classification model.



Figure 7.1. An RPA flying under GPS guidance can target specific sampling points along programmed routes as a ‘mobile quadrat’. In the case below the RPA is flying along a reference transect for calibration purpose. Fitted with RTK-GNSS guidance and gimbal control of camera orientation, decimetre positional accuracy of image contents is feasible.

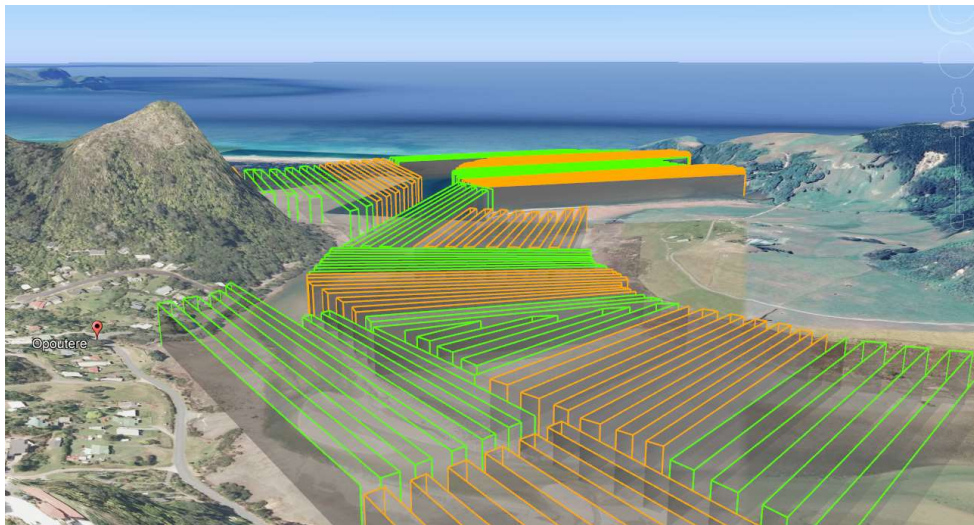


Figure 7.2. Hypothetical example of an operational work-breakdown for an exhaustive estuary-wide survey of Wharekawa Harbour using an RPA flying at 30 m altitude. Each nominally coloured segment represents the approximate safe flight-range achievable per RPA battery. Under operational deployment, within each segment would also be RPA-capture of ground reference photography under gimbal stabilisation and precise autopilot control (background imagery and terrain are Google Earth 3-D view with example flight-tracks overlain).

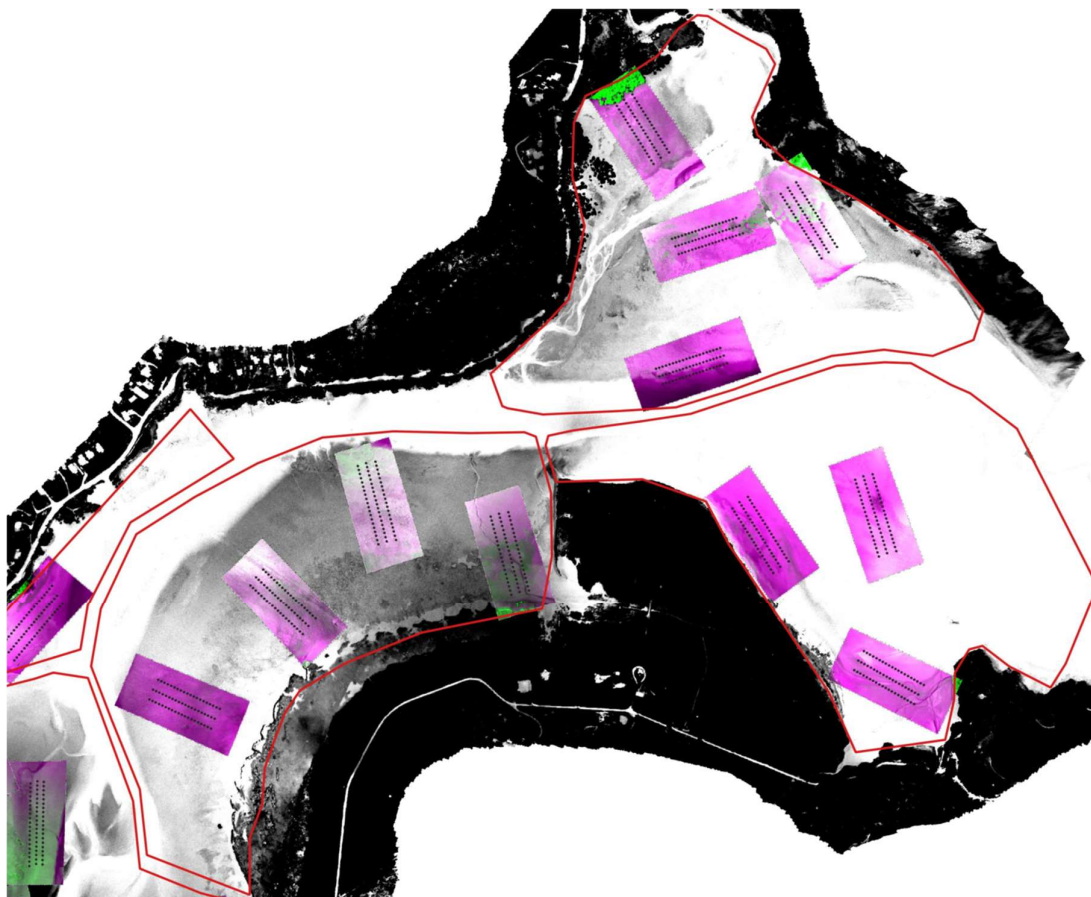


Figure 7.3. Hypothetical example of how the method described here might be escalated to estuary scale by sampling, to provide measures of seagrass condition for long term monitoring. Lines of dots are triggered positions for the RPA to capture near-ground-level reference photography; then at mid-level the purple→green rectangles indicate 30 m altitude high-precision multispectral feature extraction, trained using ground reference data, and with sufficient detail to detect change in seagrass density with accuracy; then at the highest level, the white→black background image (NDVI visualisation in this case), is derived by transferring the multispectral camera from RPA to fixed wing aircraft for estuary-wide capture, providing coarse presence/absence data and seagrass extent, trained using then mid-level imagery feature feature-extraction.

7.4 Linkage to management

The mandate to survey seagrass arises from a number of drivers ranging from local up to national in scale. At the national level, the Environmental Reporting Act 2015 and the Resource Management Act 1991 (RMA) are the key drivers for production of surveys in the coastal marine area. The NZ Coastal Policy Statement 2010 (NZCPS), prepared under the RMA, provides direction for the management of the coastal environment and includes policies directed at monitoring. Additionally, Regional Councils have the function to manage the coastal marine area, in conjunction with the Department of Conservation, under s 30(1)(d) of the RMA and for monitoring the state of the environment under s 35(2) of the RMA to the extent compatible with these functions.

Seagrass extents are currently collated at national scale by Department of Conservation around the New Zealand coastline under the SeaSketch programme (Pohl 2015) to enable quantitative marine spatial planning and habitat prioritisation. Largely this consumes regional and local data in varied format

Regional seagrass mapping provides information to quantify coastal habitat condition with respect to Council statutory responsibility under the NZCPS to maintain coastal habitat and ecological processes and protect from adverse effects (Department of Conservation 2010), and to monitor seagrass as a part of this scope under environmental reporting requirements (Waikato Regional Council 2012b; Ministry for the Environment & Stats 2016). Inter-regional co-management of a coastal zone can generate seagrass extents that augment regional habitat mapping and provide a local and community spatial information resource (Waikato Regional Council 2013; Sea Change 2017).

Local survey-need arises from Regional level plans including ‘Zone management’, ‘Catchment management’ and ‘Land Management’ plans (e.g., O’Donnell 2009) where estuaries are identified as natural resources or sites of cultural value, including seagrass as coastal or biogenic habitat (Needham et al., 2013; Morrison et al., 2014; Anderson 2016). Seagrass survey is also relevant to local community-oriented harbour care management plans and agreements, although seagrass mapping largely defers to agency-led status and trend mapping. Seagrass presence can be considered one indicator component of successful integrated catchment management in terms of appropriate land and natural resource use (e.g., Sea Change 2017).

Local targeted survey also has relevance for the production and audit of Assessments of Environmental Effects in the resource consent process under the RMA. (e.g., *Royal Forest & Bird Protection Society of New Zealand Inc v Bay of Plenty Regional Council* [27/9/2018]). In the coastal marine area, activities are controlled by

Regional Coastal Plans produced by Regional Council and activities are tested against the requirements of the plans. Upon grant of a consent, conditions may be imposed which require monitoring under s 108(4) of the RMA. Surveys may also be made for compliance assessment where targeted seagrass survey may establish a baseline against which impact can be measured. However, a database search of New Zealand resource management case decisions was unable to locate a decision of a New Zealand court where a specific area of seagrass had been monitored with respect to quantifying resource use activity.

The seagrass method tested in this research is applicable at local, regional and can provide value for national-scale data collation. The exact configuration the RPA survey (size of plot, length of transects and lighting parameters etc) would depend of the objective of the survey. Multispectral RPA survey at 30 m altitude provides detail about the structure of the scene with pixels of a size equating to the size of objects on the ground or smaller. Results show that coarse change can be detected reliably. The method is scalable. Small areas of seagrass under pressure, or areas that are the attention of potential adverse effect under a resource activity, can rapidly have a baseline documented by RPA survey, and change determined at a later survey so long as there is sufficient survey positional accuracy with respect to a fixed datum. Data can be collected on short notice and analysed later. Scaled up, the method can provide baseline, status and change for small estuaries or priority sections of larger estuaries for larger scale land use or water quality impact assessment (e.g., the effects of forestry sediment and/or stream bank erosion). Such RPA survey can also collect detailed data with which to potentially train larger-scale image classification for large estuaries or regional mapping. Success of this approach may be dependent on collating a sufficiently large and widespread ground reference sampling deployment such that models account for variability in estuary substrate and wetness environment (requires further research).

7.5 Method limitations

This research assessed the ability of remote sensing by RPA to distinguish seagrass from its background and assess condition, with focus upon one flying regime, and acknowledging that there are many other aerial survey configurations that could be applied (e.g., different flying heights and photogrammetric overlap). The 30 m flying height was chosen as a practical balance in the trade-off between pixel size, flying range per battery and a stable and blur-free minimum flying speed. Lower flying height may yield finer image resolution with potential improvement to classification accuracy with

reducing pixel size (e.g., Kovacs et al., 2018) but with reduction in useful survey area. The key limitations relevant to application of this 30 m RPA survey for seagrass feature extraction and condition measurement include the following.

- Results are most relevant to survey of an area similar to the study site, using RPA derived multi-spectral imagery flown slowly at 30 m altitude under 75-80% overlap in the photogrammetric survey plan. Other areas on this estuary may present a different optimal classification, and other estuaries may have varying substrate types. Each site may require a ground observation set under a design specific to the variability in seagrass presentation, substrate types and organic content of each estuary. Initial assessment (or higher-altitude widespread imagery capture) may be required prior to configuring a more detailed survey design conducted at 30 m.
- The research focused upon one survey site, and the method is relevant to any number of discrete survey sites with adequate ground reference data. However, integration of multiple patches of low-altitude multispectral imagery would require careful attention to radiometric equalisation between images. Anisotropic variation in glint/glare, reflection and/or polarisation were observed in the imagery of this study creating a shift in sensor value, appearing as a colour gradient in otherwise uniform scene content. Principally, this occurred at the edge of the orthomosaic, and the orthomosaic process normalised the images evenly where there is dense overlap in images (i.e., such that near-nadir image sections comprise the mosaic with similar reflectance estimation). However, some images contained these colour gradients that could not be explained or resolved using the observations taken, thereby highlighting the importance of ensuring dense flight lines (i.e., $\geq 80\%$ forwards- and side-lap).
- A significant challenge for RPA survey is radiometric standardisation between sorties. The maximum safe flight time for this RPA using the available battery type is 15 minutes (i.e., allowing ample reserve power for contingencies), resulting in image retrieval equivalent to a 200 m x 50 m quality orthomosaic at 30 m flying height and 5 m/s scan time. Due to subtle inconsistency in the lighting across the captured scenes, and limitations for radiometric normalisation in overcast conditions, the data in this study do not indicate an empirical optical relationship between seagrass and image digital number that could be applied independent of ground referencing at the time of survey. This study was conducted on one location within the estuary and there are variations on sediment

type and hydrological environment not sampled by the survey plot. Until classification performance is understood across the variability of estuary ground-cover types, it is recommended that there is ground sample and classifier refinement per section of estuary based on sediment type and drainage environment. As demonstrated here, this can be automated in a script to reduce data-handling time.

- At present, the limited flying range per battery, and the requirement for line-of-sight operation at all times for airspace safety assurance, limits the applicability of RPA as a primary data collection tool for estuarine monitoring. An estuary the size of Wharekawa may represent an approximate upper limit to what is feasible for comprehensive RPA survey: – for example two RPA pilot teams operating in parallel might achieve aerial survey capture across the entire surface area of Wharekawa Harbour (below the level of mean high water springs) in approx. 2-3 sessions across low tide (Figure 7.3), based on the low altitude format tested in this study. In the near future, when RPA radio control is sufficiently reliable for operation beyond visual range, use of RPA as a primary large-scale survey tool may become feasible. In the interim RPA can contribute to automated seagrass remote sensing for survey of small estuaries, or discrete focused precision survey of parts of larger estuaries, including provision of ground-level reference data to support remote sensing at higher altitude aircraft or satellite-based survey, and repeated survey at fixed monitoring plots as part of a long-term environmental monitoring network.
- As discussed above, the time of year for survey, recommended from data obtained under this research project, is approximately February to April for Wharekawa Harbour. This avoids times of high MPB early in this period, but also avoids site disturbance from high rainfall later in the period (Figure 7.4). This is consistent with the time of year of high seagrass productivity at other sites in New Zealand (Ismail 2001).
- Interference in classification from epibiotic fouling upon seagrass foliage was not assessed in this study. Epibiotic fouling has been found to have only minor impact on reflectance values in other seagrass targets (Bargain et al., 2013; Fyfe 2003). The highest levels of diatom and algal fouling observed during the survey year of the current study occurred in spring with little or no trace remaining by late summer, which further reinforced February-April as an optimum target of operational planning. Seagrass reduced in density considerably across the winter

as expected by the seasonal habit of *Zostera muelleri* (Turner and Schwartz 2006b), but with only minor change in meadow extent at the patch edges where there was sediment burial and damage from water flow (Figure 8.4).

- Sites comprising different sediment or hydrological estuarine characteristics may be less susceptible to MPB/algae accumulation or storm damage. Indeed, within Wharekawa Harbour there was spatial variability in these interferents. During the April 2018 seagrass census, summer MPB/algae was largely associated with river inflow points, algae-stained cockle shell accretions, a number of finite locations where large populations of swan or Canada goose aggregated and amassed droppings, or areas near to the low-tide water interface where foam, slime and mobile plant material accumulate (Figure 7.5).
- The study area for this research was positioned to sample an area of seagrass under pressure from sediment, detritus and shell deposition, but was insufficient in extent to sample the range of non-seagrass green content on the estuary. Given the variation of content on the estuary, it may not be possible to use a limited subset of the area for collecting the ground-level training data, and instead it may be necessary to divide the estuary in to sections and collect reference data from each section separately. Escalation of the method to estuary scale is discussed below.

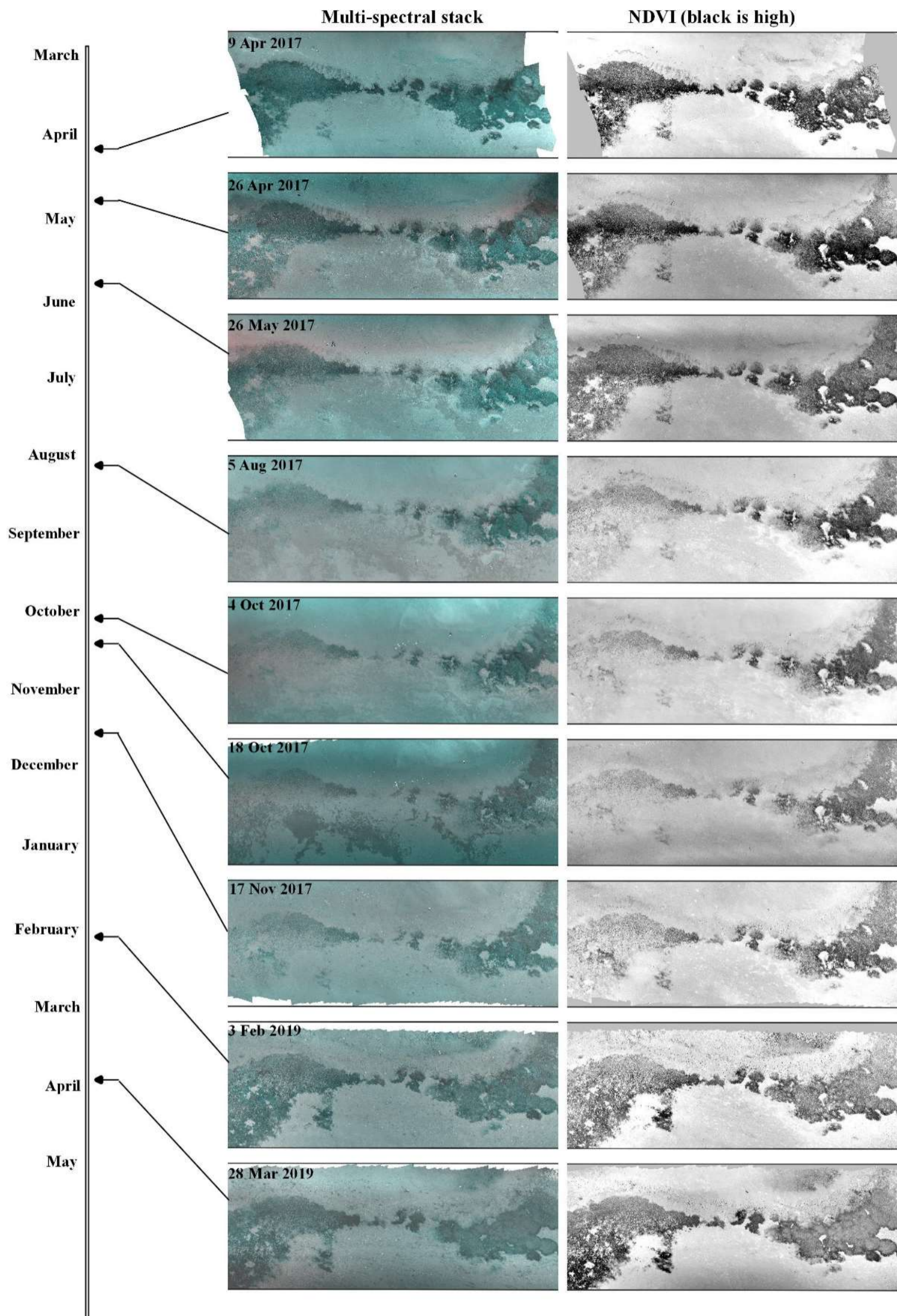


Figure 7.4. Change in seagrass across the year of the research study as estimated by NDVI levels (frames on the right), with equivalent multispectral false colour imagers for reference.

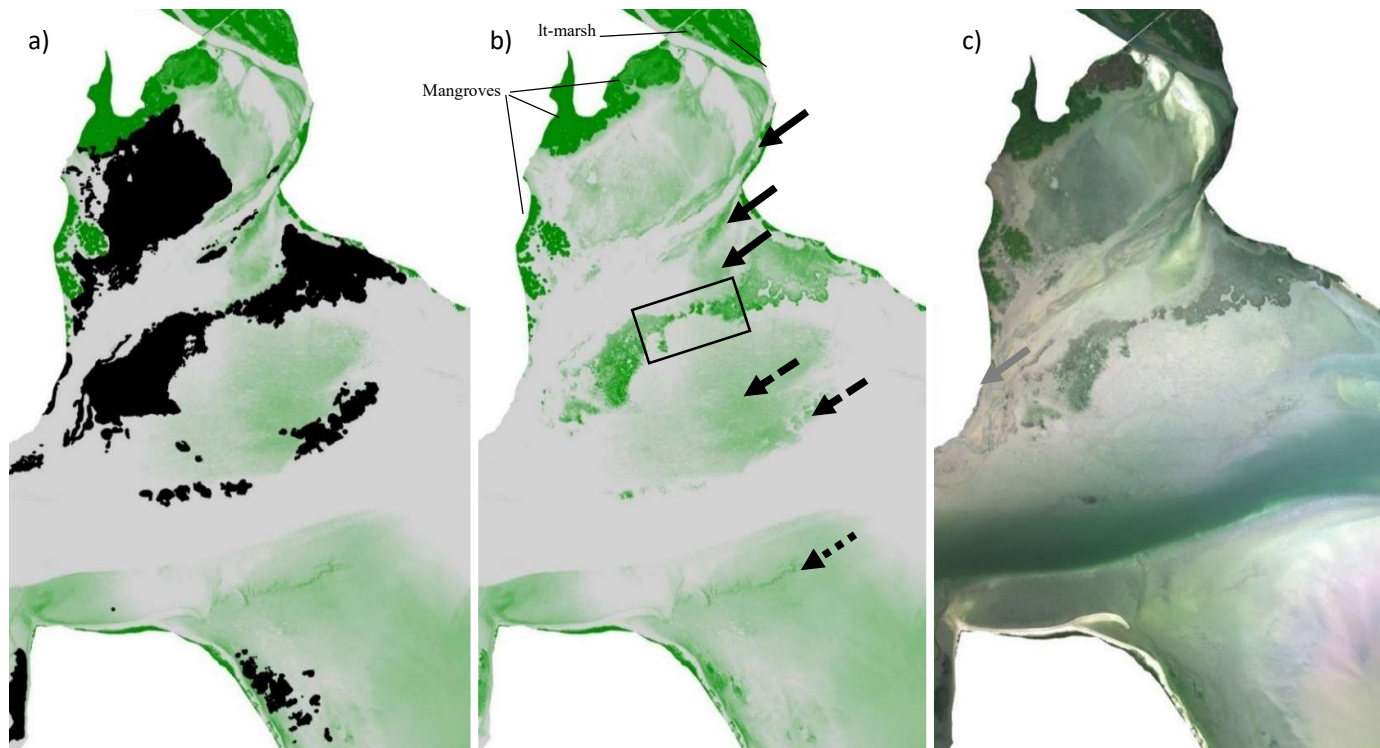


Figure 7.5. Illustration of the amount of non-seagrass photosynthetic material upon the northern half of Wharekawa Harbour as indicated by the NDVI channel (a and b). Key: green hues are NDVI intensity (low to high is white transition to rich-green); the black rectangle shows study area; black polygons (a) show verified seagrass (no black indicates verified seagrass absence); solid black arrows (b) show surface MPB/algae associated with river in-flow; dashed arrow shows algal staining in waterlogged sediment and cockle staining; dotted arrow shows algal presence at waterfowl feed/roosting areas (faeces + algae). Imagery is derived from a MicaSense Red-Edge multispectral camera flown by fixed wing aircraft ~300 m above ground level rendered to georeferenced mosaic, with concurrent ground-referencing.

7.6 Research recommendations

Further research questions that arise from this research, in terms of advancing this method for wider application for environmental monitoring, include:

- Is there an optimal RPA flying altitude under the trade-off between density class determination and RPA flying range?
- Does the state of low-tide residual water drainage affect classification accuracy and seagrass characterisation at other sites with differing seagrass and sediment character to the current study site, e.g., permanently waterlogged seagrass, static pooling or clay-mud?
- Is there an optimal change-sensitivity and monitoring interval timeframe for applying the RPA survey method to seagrass environmental reporting?
- What is the monitoring revisit frequency and sampling density required to correctly describe the true spatio-temporal variability in the seagrass at a site, and is does this differ between sites.
- What quantity of ground sampling effort (quantity of ground reference imagery) is required to consistently extract the seagrass feature and characterise density under this RPA method across an estuary?
- Can non-seagrass green-sources e.g., microphytobenthos, algae, detritus, stained shell, be sufficiently identified so as to eliminate these from seagrass estimates e.g., by spectra, texture analysis or object geometry (with estuary-wide focus)?

7.7 Conclusion

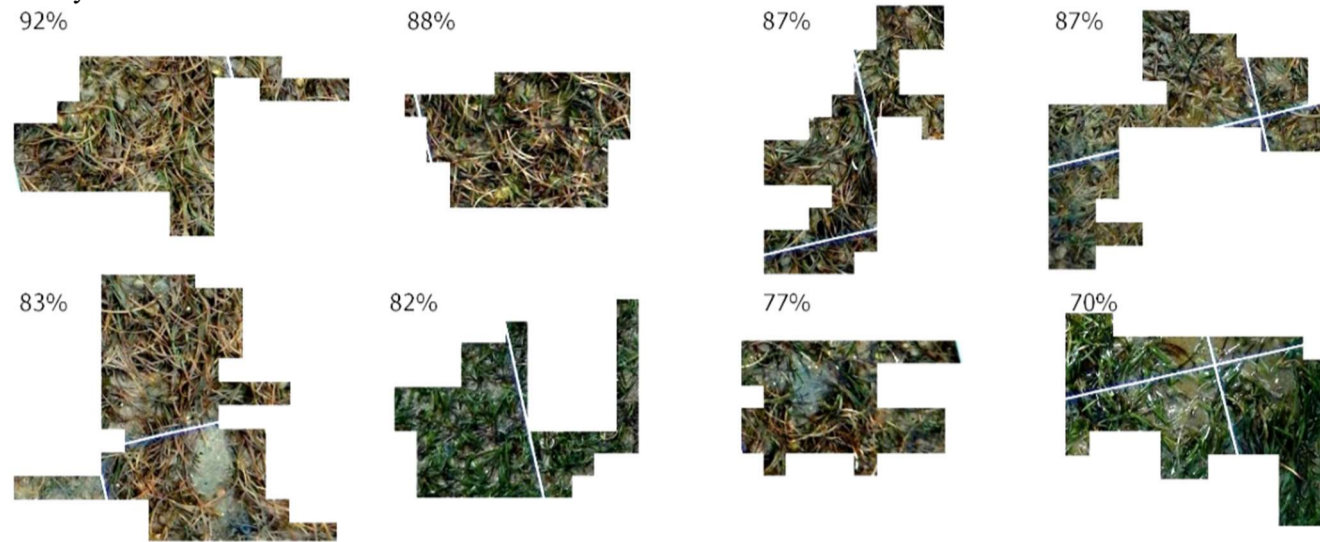
In conclusion, this research investigation led to the development and testing of a method for RPA survey of intertidal seagrass extent and condition with replication. Seagrass character was extracted from precisely geo-referenced multispectral imagery flown by low-altitude remotely piloted aircraft over an estuary with the tide drained. The spectral character of seagrass and non-seagrass materials was found to change with varying residual water drainage during the low-tide window when bulk-water was clear of the seagrass meadow, but not to the extent that image classification was compromised. Seagrass mapping is feasible across the duration that tidal water is clear of the ground. However, given flexibility in time of operation, later in the low-tide window is a preferential time to measure and map intertidal seagrasses to minimise glare and glint effects on wet surface.

An optimal classification procedure was identified from a small selection of candidate methods that achieved high classification accuracy with respect to seagrass detection and density measurement. The method also yielded good classification results at repeated survey times. In the case of RPA survey flown at 30 m using the Parrot Sequoia camera, pixel-based image analysis was of higher classification efficacy than the segmented image under object-based image analysis, and smaller segments yielded better seagrass characterisation than larger segments. The method tested here was able to detect change in seagrass density class between two survey times. This research demonstrates that seagrass feature extraction from low-altitude multispectral imagery flown by remotely piloted aircraft is a plausible option for seagrass population monitoring and environmental reporting but requires further calibration for whole- and multi-estuary application.

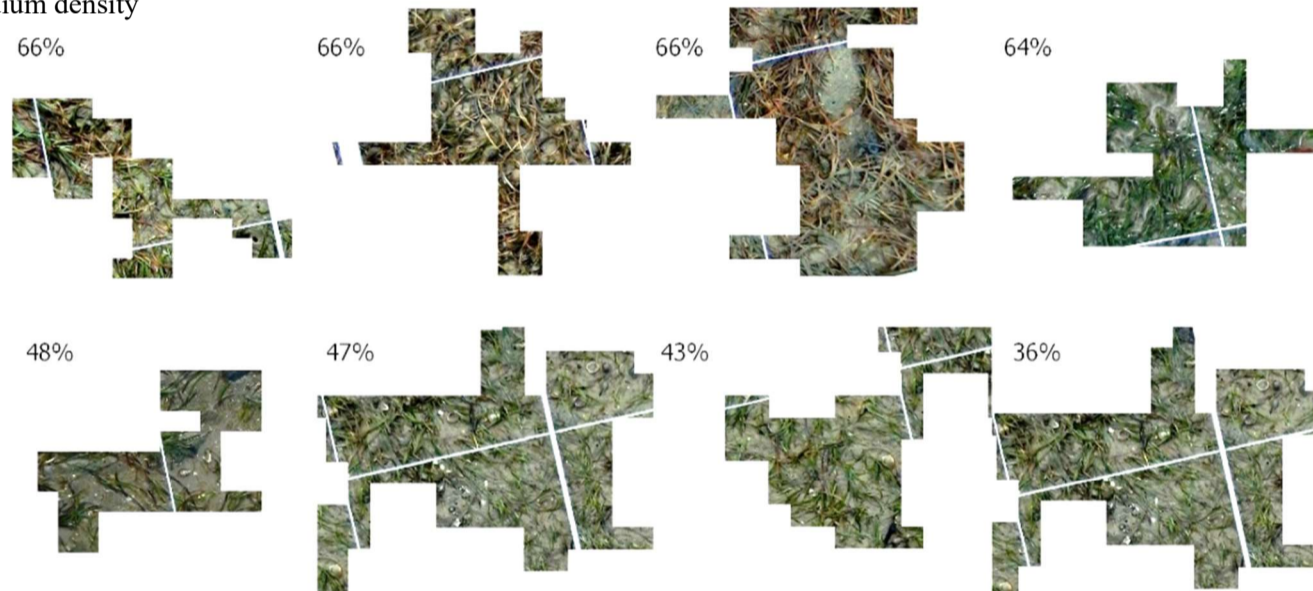
7.7.1 Chapter appendices

Appendix 7.8.1. Seagrass density visual guide for ground photography interpretation. Percentage values are calculated from digitised tracing of the horizontally projected leaf area with segmentation polygons.

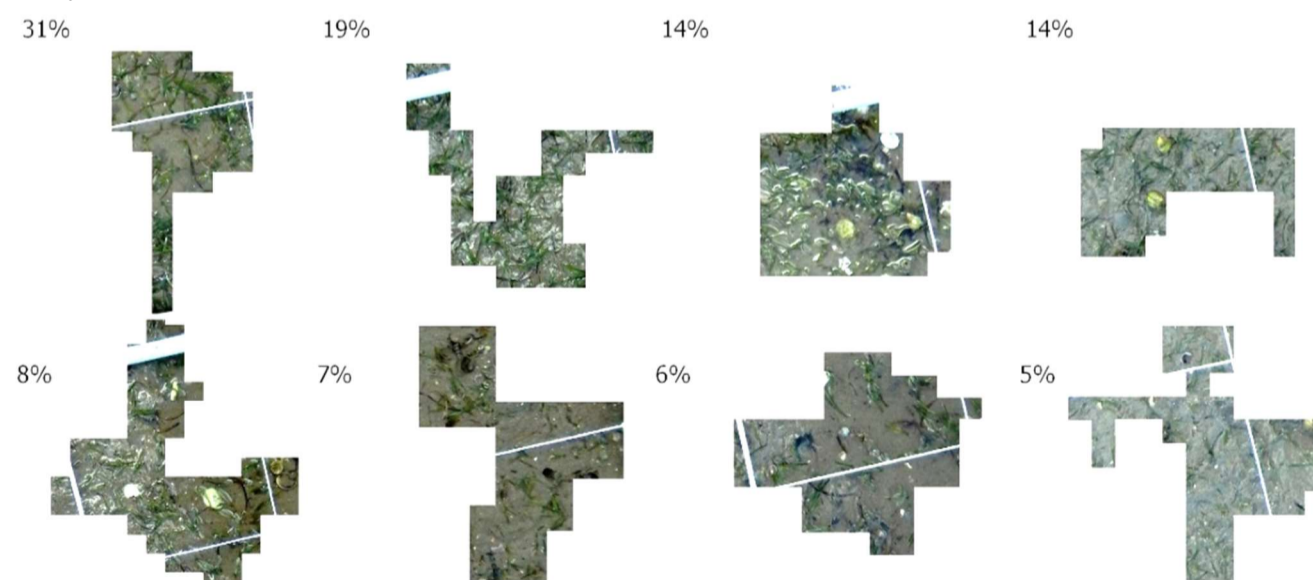
High density



Medium density



Low density



8 References

- Abe, B., Olugbara, O., & Marwala, T. (2014). Experimental comparison of support vector machines with random forests for hyperspectral image land cover classification. *Published by the Indian Academy of Sciences, 123*(4), 779-790. (DOI 10.1007/s12040-014-0436-x)
- Adam, E., Mutanga, O., & Rugege, D. (2010). Multispectral and hyperspectral remote sensing for identification and mapping of wetland vegetation: a review. *Wetlands Ecology and Management, 18*(3), 281-296. (DOI 10.1007/s11273-009-9169-z)
- Ahmed, A., Pradhan, B., Sameen, M., & Makky, A. (2018). An optimized object-based analysis for vegetation mapping using integration of Quickbird and Sentinel-1 data. *Arabian Journal of Geosciences, 11*(11), 1-10. (DOI 10.1007/s12517-018-3632-1)
- Ai, M., Hu, Q., Li, J., Wang, M., Yuan, H., & Wang, S. (2015). A robust photogrammetric processing method of low-altitude UAV images. *Remote Sensing, 7*(3), 2302-2333. (DOI 10.3390/rs70302302)
- Aitkenhead, M. J., & Aalders, I. H. (2011). Automating land cover mapping of Scotland using expert system and knowledge integration methods. *Remote Sensing of Environment, 115*(5), 1285-1295. (DOI 10.1016/j.rse.2011.01.012)
- Aldrich, S. M. (1995). *Volcanic Geology and Hydrothermal Alteration of the Onemana Area, Eastern Coromandel Peninsula*. MSc thesis, University of Waikato, Hamilton, New Zealand.
- Alexander, D. (2008). Remote sensing and the coast: Development of advanced techniques to map nuisance macro-algae in estuaries. *New Zealand Geographer, 64*, 157–161. (DOI 10.1111/j.1745-7939.2008.00140.x)
- Alexander, D. J., Hart, D. E., & Marsden, I. D. (2008). *Evaluation and Development of Techniques to Map Macroalgae in the Avon-Heathcote Estuary*. University of Canterbury. 84p.
- Alexander, K. B., & Harvey, M. (2014). *Cost-effective aerial imagery and soil CO₂ flux surveys for geothermal exploration*. Presented at the Proceedings 5th African Rift geothermal Conference, Arusha, Tanzania, 29-31 October 2014.
- Alfaro, A. C. (2010). Effects of mangrove removal on benthic communities and sediment characteristics at Mangawhai Harbour, northern New Zealand. *ICES Journal of Marine Science, 67*(6), 1087-1104. (DOI 10.1093/icesjms/fsq034)
- Allan, M. (2016). *Remote Sensing of Waikato Wetlands: a Literature Review* University of Waikato, Hamilton. 30p.
- Almela, E. D., Marbà, N., Álvarez, E., Santiago, R., Martínez, R., & Duarte, C. M. (2008). Patch dynamics of the Mediterranean seagrass *Posidonia oceanica*: Implications for recolonisation process. *Aquatic Botany, 89*(4), 397-403. (DOI 10.1016/j.aquabot.2008.04.012)
- Amo, A., Montero, J., Biging, G., & Cutello, V. (2004). Fuzzy classification systems. *European Journal of Operational Research, 156*(2), 495-507. (DOI 10.1016/S0377-2217(03)00002-X)
- Amran, M. A. (2010). Estimation of seagrass coverage by depth invariant indices on Quickbird imagery. *Biotropia, 17*(1), 42-50.
- Amran, M. A. (2017). Mapping seagrass condition using google earth imagery. *Journal of Engineering Science and Technology Review, 10*(1), 18-23. (DOI 10.25103/jestr.101.03)
- Anderson, K., & Gaston, K. J. (2013). Lightweight unmanned aerial vehicles will revolutionize spatial ecology. *Frontiers in Ecology and the Environment, 11*(3), 138-146. (DOI 10.1890/120150)

- Anderson, T. J., Morrison, M., MacDiarmid, A., Clark, M., D'Archino, R., Nelson, W., Tracey, D., Gordon, D., Read, G., Kettles, H., Morrisey, D., Wood, A., Anderson, O., Smith, A. M., Page, M., Paul-Burke, K., Schnabel, K., & S., W. (2019). *Review of New Zealand's Key Biogenic Habitats*. National Institute for Water and Atmospheric Research, Wellington. 190p.
- Andrade, F., & Ferreira, M. A. (2011). A method for monitoring shallow seagrass meadows (*Zostera* spp.) using terrestrial oblique large-scale photography. *Aquatic Botany*, 95(2), 103-109. (DOI 10.1016/j.aquabot.2011.04.002)
- Andrés, S., Arvor, D., Mougenot, I., Libourel, T., & Durieux, L. (2017). Ontology-based classification of remote sensing images using spectral rules. *Computers and Geosciences*, 102, 158-166. (DOI 10.1016/j.cageo.2017.02.018)
- Anker, Y., Hershkovitz, Y., Ben Dor, E., & Gasith, A. (2014). Application of aerial digital photography for macrophyte cover and composition survey in small rural streams. *River Research and Applications*, 30(7), 925-937. (DOI 10.1002/rra.2700)
- Apichanangkool, P., & Prathep, A. (2014). Changes in seagrass leaf reddening and morphology in response to emersion. *Botanica marina*, 57(6), 433-440. (DOI 10.1515/bot-2014-0004)
- Arifianto, O., & Farhood, M. (2015). Development and Modeling of a Low-Cost Unmanned Aerial Vehicle Research Platform. *Journal of Intelligent & Robotic Systems*, 80(1), 139-164.
- Armiger, L. C. (1964). An occurrence of *Labyrinthula* in New Zealand *Zostera*. *New Zealand Journal of Botany*, 2(1), 3-9. (DOI 10.1080/0028825X.1964.10428713)
- Arponen, H., & Boström, C. (2012). Responses of mobile epifauna to small-scale seagrass patchiness: is fragmentation important? *Hydrobiologia*, 680(1), 1-10. (DOI 10.1007/s10750-011-0895-x)
- Arumugam, R., Kannan, R. R. R., Saravanan, K. R., Thangaradjou, T., & Anantharaman, P. (2013). Hydrographic and sediment characteristics of seagrass meadows of the Gulf of Mannar Marine Biosphere Reserve, South India. *Environmental Monitoring and Assessment*, 185(10), 8411-8427. (DOI 10.1007/s10661-013-3183-6)
- Arvor, D., Durieux, L., Andrés, S., & Laporte, M.-A. (2013). Advances in Geographic Object-Based Image Analysis with ontologies: A review of main contributions and limitations from a remote sensing perspective. *ISPRS Journal of Photogrammetry and Remote Sensing*, 82, 125-137. (DOI 10.1016/j.isprsjprs.2013.05.003)
- Ashraf, S., Brabyn, L., Hicks, B. J., & Collier, K. (2010). Satellite remote sensing for mapping vegetation in New Zealand freshwater environments: A review. *New Zealand Geographer*, 66(1), 33-43. (DOI 10.1111/j.1745-7939.2010.01168.x)
- Asmat, A., Milton, E. J., & Atkinson, P. M. (2011). Empirical correction of multiple flightline hyperspectral aerial image mosaics. *Remote Sensing of Environment*, 115(10), 2664-2673. (DOI 10.1016/j.rse.2011.05.022)
- Asner, G. P., Martin, R. E., & Mascaro, J. (2017). Coral reef atoll assessment in the South China Sea using Planet Dove satellites. *Remote Sensing in Ecology and Conservation*, 3(2), 57-65. (DOI 10.1002/rse2.42)
- Asner, G. P., Scurlock, J. M. O., & A. Hicke, J. (2003). Global synthesis of leaf area index observations: implications for ecological and remote sensing studies. *Global Ecology and Biogeography*, 12(3), 191-205. (DOI 10.1046/j.1466-822X.2003.00026.x)
- Atzberger, C., Darvishzadeh, R., Immitzer, M., Schlerf, M., Skidmore, A., & Le Maire, G. (2015). Comparative analysis of different retrieval methods for mapping grassland leaf area index using airborne imaging spectroscopy. *International Journal of Applied Earth Observations and Geoinformation*, 43(C), 19-31. (DOI 10.1016/j.jag.2015.01.009)

- Austin, R. (2010). Part One - the design of UAV systems. In R. Austin (Ed.), *Unmanned Aircraft Systems : UAV Design, Development and Deployment*. Hoboken, NJ, USA: John Wiley & Sons.
- Ayhan, E., & Kansu, O. (2012). Analysis of image classification methods for remote sensing. *Experimental Techniques*, 36(1), 18-25. (DOI 10.1111/j.1747-1567.2011.00719.x)
- Bajjouk, T., Mouquet, P., Ropert, M., Quod, J. P., Hoarau, L., Bigot, L., Le Dantec, N., Delacourt, C., & Populus, J. (2019). Detection of changes in shallow coral reefs status: Towards a spatial approach using hyperspectral and multispectral data. *Ecological Indicators*, 96, 174-191. (DOI 10.1016/j.ecolind.2018.08.052)
- Bakr, N., Weindorf, D. C., Bahnassy, M. H., Marei, S. M., & El-Badawi, M. M. (2010). Monitoring land cover changes in a newly reclaimed area of Egypt using multi-temporal Landsat data. *Applied Geography*, 30(4), 592-605. (DOI 10.1016/j.apgeog.2009.10.008)
- Ball, D., Soto-Berelov, M., & Young, P. (2014). Historical seagrass mapping in Port Phillip Bay, Australia. *Journal of Coastal Conservation*, 18(3), 257-272. (DOI 10.1007/s11852-014-0314-3)
- Bandyopadhyay, D., Bhavsar, D., Pandey, K., Gupta, S., & Roy, A. (2017). Red edge index as an indicator of vegetation growth and vigor using hyperspectral remote sensing data. *Proceedings of the National Academy of Sciences, India Section A: Physical Sciences*, 87(4), 879-888. (DOI 10.1007/s40010-017-0456-4)
- Barbier, E. B., Hacker, S. D., Kennedy, C., Koch, E. W., Stier, A. C., & Silliman, B. R. (2011). The value of estuarine and coastal ecosystem services. *Ecological Monographs*, 81(2), 169-193. (DOI 10.1890/10-1510.1)
- Barclay, H. J. (1998). Conversion of total leaf area to projected leaf area in lodgepole pine and Douglas-fir. *Tree Physiology*, 18(3), 185-193. (DOI 10.1093/treephys/18.3.185)
- Bargain, A., Robin, M., Le Men, E., Huete, A., & Barillé, L. (2012). Spectral response of the seagrass *Zostera noltii* with different sediment backgrounds. *Aquatic Botany*, 98(1), 45-56. (DOI 10.1016/j.aquabot.2011.12.009)
- Bargain, A., Robin, M., Méléder, V., Rosa, P., Le Menn, E., Harin, N., & Barillé, L. (2013). Seasonal spectral variation of *Zostera noltii* and its influence on pigment-based vegetation indices. *Journal of Experimental Marine Biology and Ecology*, 446, 86-94. (DOI 10.1016/j.jembe.2013.04.012)
- Barillé, L., Robin, M., Harin, N., Bargain, A., & Launeau, P. (2010). Increase in seagrass distribution at Bourgneuf Bay (France) detected by spatial remote sensing. *Aquatic Botany*, 92(3), 185-194. (DOI 10.1016/j.aquabot.2009.11.006)
- Barnes, R. (2013). Distribution patterns of macrobenthic biodiversity in the intertidal seagrass beds of an estuarine system, and their conservation significance. *Biodiversity and Conservation*, 22(2), 357-372. (DOI 10.1007/s10531-012-0414-z)
- Barrell, J., Grant, J., Hanson, A., & Mahoney, M. (2015). Evaluating the complementarity of acoustic and satellite remote sensing for seagrass landscape mapping. *International Journal of Remote Sensing*, 36(16), 4069-4094. (DOI 10.1080/01431161.2015.1076208)
- Barton, I. (2017). Tairua Forest: a history. *The Treasury*, 10, 1-9.
- Basterretxea, G., Orfila, A., Jordi, A., Casas, B., Lynett, P., Liu, P. L. F., Duarte, C. M., & Tintoré, J. (2004). Seasonal dynamics of a microtidal pocket beach with *Posidonia oceanica* seabeds (Mallorca, Spain). *Journal of Coastal Research*, 20(4), 1155-1164. (DOI 10.2112/03-0027R.1)
- Baumstark, R., Dixon, B., Carlson, P., Palandro, D., & Kolasa, K. (2013). Alternative spatially enhanced integrative techniques for mapping seagrass in Florida's marine ecosystem. *International Journal of Remote Sensing*, 34(4), 1248-1264. (DOI 10.1080/01431161.2012.721941)

- Baumstark, R., Duffey, R., & Pu, R. (2016). Mapping seagrass and colonized hard bottom in Springs Coast, Florida using WorldView-2 satellite imagery. *Estuarine, Coastal and Shelf Science*, 181, 83-92. (DOI 10.1016/j.ecss.2016.08.019)
- Bell, J. (2014). *Machine Learning*. John Wiley & Sons.
- Bell, J., & Blayney, A. (2017). Use of mangrove habitat by banded rail (*Gallirallus philippensis assimilis*). Hamilton. 29p.
- Bell, S. S., Brooks, R. A., Robbins, B. D., Fonseca, M. S., & Hall, M. O. (2001). Faunal response to fragmentation in seagrass habitats: implications for seagrass conservation. *Biological Conservation*, 100(1), 115-123. (DOI 10.1016/S0006-3207(00)00212-3)
- Bell, S. S., Fonseca, M. S., & Kenworthy, W. J. (2008). Dynamics of a subtropical seagrass landscape: links between disturbance and mobile seed banks. *Landscape Ecology*, 23(S1), 67-74. (DOI 10.1007/s10980-007-9137-z)
- Belsley, D. A. (1980). *Regression diagnostics : identifying influential data and sources of collinearity*. New York: John Wiley & Sons.
- Benfield, S. L., Guzman, H. M., Mair, J. M., & Young, J. A. T. (2007). Mapping the distribution of coral reefs and associated sublittoral habitats in Pacific Panama: a comparison of optical satellite sensors and classification methodologies. *International Journal of Remote Sensing*, 28(22), 5047-5070. (DOI 10.1080/01431160701258062)
- Benham, C. F., Beavis, S. G., & Jackson, E. L. (2019). Tolerance of tropical seagrasses *Zostera muelleri* and *Halophila ovalis* to burial: Toward an understanding of threshold effects. *Estuarine, Coastal and Shelf Science*, 218, 131-138.
- Bertelli, C. M., & Unsworth, R. K. F. (2014). Protecting the hand that feeds us: Seagrass (*Zostera marina*) serves as commercial juvenile fish habitat. *Marine Pollution Bulletin*, 83(2), 425-429. (DOI 10.1016/j.marpolbul.2013.08.011)
- Biday, S. G., & Bhosle, U. (2010). Radiometric correction of multitemporal satellite imagery. *Journal of Computer Science*, 6(9), 1027-1036. (DOI 10.3844/jcssp.2010.1027.1036)
- Bishop, M. J., & Kelaher, B. P. (2013). Replacement of native seagrass with invasive algal detritus: impacts to estuarine sediment communities. *Biological Invasions*, 15(1), 45-59.
- Blakey, T., Melesse, A., & Hall, M. O. (2015). Supervised classification of benthic reflectance in shallow subtropical waters using a generalized pixel-based classifier across a time series. *Remote Sensing*, 7(5), 5098-5116. (DOI 10.3390/rs70505098)
- Blaschke, T., Hay, G. J., Kelly, M., Lang, S., Hofmann, P., Addink, E., Queiroz Feitosa, R., van Der Meer, F., van Der Werff, H., van Coillie, F., & Tiede, D. (2014). Geographic object-based image analysis - Towards a new paradigm. *ISPRS Journal of Photogrammetry and Remote Sensing*, 87(100), 180-191. (DOI 10.1016/j.isprsjprs.2013.09.014)
- Blom, J. D. (2009). *Unmanned aerial systems: a historical perspective*. Occasional Paper 37. Kansas, USA: Combat Studies Institute Press.
- Bolón-Canedo, V., Sánchez-Marroño, N., & Alonso-Betanzos, A. (2015). Recent advances and emerging challenges of feature selection in the context of big data. *Knowledge-Based Systems*, 86(C), 33-45. (DOI 10.1016/j.knosys.2015.05.014)
- Borfecchia, F., de Cecco, L., Martini, S., Ceriola, G., Bollanos, S., Vlachopoulos, G., Valiante, L. M., Belmonte, A., & Micheli, C. (2013a). *Posidonia oceanica* genetic and biometry mapping through high-resolution satellite spectral vegetation indices and sea-truth calibration. *International Journal of Remote Sensing*, 34(13), 4680-4701. (DOI 10.1080/01431161.2013.781701)
- Borfecchia, F., Micheli, C., Carli, F., De Martis, S. C., Gnisci, V., Piermattei, V., Belmonte, A., De Cecco, L., Martini, S., & Marcelli, M. (2013b). Mapping spatial patterns of *Posidonia oceanica* meadows by means of Daedalus ATM

- airborne sensor in the coastal area of Civitavecchia (Central Tyrrhenian Sea, Italy). *Remote Sensing*, 5(10), 4877-4899. (DOI 10.3390/rs5104877)
- Borra-Serrano, I., Peña, J. M., Torres-Sánchez, J., Mesas-Carrascosa, F. J., & López-Granados, F. (2015). Spatial quality evaluation of resampled unmanned aerial vehicle-imagery for weed mapping. *Sensors (Switzerland)*, 15(8), 19688-19708. (DOI 10.3390/s150819688)
- Bos, A. R., Bouma, T. J., de Kort, G. L. J., & van Katwijk, M. M. (2007). Ecosystem engineering by annual intertidal seagrass beds: Sediment accretion and modification. *Estuarine, Coastal and Shelf Science*, 74(1), 344-348. (DOI 10.1016/j.ecss.2007.04.006)
- Boström, C., Jackson, E. L., & Simenstad, C. A. (2006). Seagrass landscapes and their effects on associated fauna: A review. *Estuarine, Coastal and Shelf Science*, 68(3), 383-403. (DOI 10.1016/j.ecss.2006.01.026)
- Bouma, S. (2016). *Marine biodiversity stocktake of the Waikato region 2015*. Waikato Regional Council, Hamilton. 133p.
- Bouvet, M. (2014). Radiometric comparison of multispectral imagers over a pseudo-invariant calibration site using a reference radiometric model. *Remote Sensing of Environment*, 140, 141-154. (DOI 10.1016/j.rse.2013.08.039)
- Brakel, J., Werner, F. J., Tams, V., Reusch, T. B. H., & Bockelmann, A.-C. (2014). Current European *Labyrinthula zosterae* are not virulent and modulate seagrass (*Zostera marina*) defense gene expression. *PLoS one*, 9(4), e92448. (DOI 10.1371/journal.pone.0092448)
- Braun-Blanquet, J. (1965). *Plant Sociology: the study of plant communities*. (English translation). New York, USA: Hafner.
- Breckenridge, R., & Dakins, M. (2011). Evaluation of bare ground on rangelands using unmanned aerial vehicles: A case study. *GIScience and Remote Sensing*, 48(1), 74-85.
- Bréon, F. M., & Henriot, N. (2006). Spaceborne observations of ocean glint reflectance and modeling of wave slope distributions. *Journal of Geophysical Research: Oceans*, 111(6). (DOI 10.1029/2005JC003343)
- Brouwer, R. L., Matthieu, A. D. S., Rynne, P. F., Graham, F. J., Ad, J. H. M. R., & Macmahon, J. H. (2015). Surfzone monitoring using rotary wing unmanned aerial vehicles. *Journal of Atmospheric and Oceanic Technology*, 32(4), 855. (DOI 10.1175/JTECH-D-14-00122.1)
- Bryan, K. R., Tay, H. W., Pilditch, C. A., Lundquist, C. J., & Hunt, H. L. (2007). The effects of seagrass (*Zostera muelleri*) on boundary-layer hydrodynamics in Whangapoua Estuary, New Zealand. *Journal of Coastal Research*, SI 50, 688-672.
- Bryson, M., Johnson-Roberson, M., Murphy, R. J., & Bongiorno, D. (2013). Kite Aerial Photography for Low-Cost, Ultra-high Spatial Resolution Multi-Spectral Mapping of Intertidal Landscapes. *PLoS One*, 8(9), Article No. e73550.
- Burdick, D. M., & Kendrick, G. A. (2001). Standards for seagrass collection, identification and sample design. In F. T. Short & R. G. Coles (Eds.), *Global Seagrass Research Methods*. Amsterdam; New York: Elsevier.
- Burkholder, J. M., Tomasko, D. A., & Touchette, B. W. (2007). Seagrasses and eutrophication. *Journal of Experimental Marine Biology and Ecology*, 350(1), 46-72. (DOI 10.1016/j.jembe.2007.06.024)
- Burnett, C., & Blaschke, T. (2003). A multi-scale segmentation/object relationship modelling methodology for landscape analysis. *Ecological Modelling*, 168(3), 233-249. (DOI 10.1016/S0304-3800(03)00139-X)
- Civil Aviation Authority (2018). Part 101 CAA Consolidation - Gyrogliders, Parasails, Unmanned Aircraft (including Balloons), Kites, and Rockets - Operating Rules, Civil Aviation Authority of New Zealand.

- Cabaço, S., Santos, R., & Duarte, C. M. (2008). The impact of sediment burial and erosion on seagrasses: A review. *Estuarine, Coastal and Shelf Science*, 79(3), 354-366. (DOI 10.1016/j.ecss.2008.04.021)
- Cai, S., & Liu, D. (2013). A comparison of object-based and contextual pixel-based classifications using high and medium spatial resolution images. *Remote Sensing Letters*, 4(10), 998-1007. (DOI 10.1080/2150704X.2013.828180)
- Calleja, F., Galván, C., Silió-Calzada, A., Juanes, J. A., & Ondiviela, B. (2017). Long-term analysis of *Zostera noltei*: A retrospective approach for understanding seagrasses' dynamics. *Marine Environmental Research*, 130, 93-105. (DOI 10.1016/j.marenvres.2017.07.017)
- Campagne, C. S., Salles, J. M., Boissery, P., & Deter, J. (2015). The seagrass *Posidonia oceanica*: Ecosystem services identification and economic evaluation of goods and benefits. *Marine Pollution Bulletin*, 97(1-2), 391-400. (DOI 10.1016/j.marpolbul.2015.05.061)
- Campbell, M. L., Heppenstall, L. D., Hendry, R., Martin, R., Sørensen, S., Rubenstein, A. N., & Hewitt, C. L. (2018). Niche partitioning of intertidal seagrasses: evidence of the influence of substrate temperature. *New Phytologist*, 217(4), 1449-1462. (DOI 10.1111/nph.14944)
- Campbell, S. J., McKenzie, L. J., & Kerville, S. P. (2006). Photosynthetic responses of seven tropical seagrasses to elevated seawater temperature. *Journal of Experimental Marine Biology and Ecology*, 330(2), 455-468.
- Candiago, S., Remondino, F., De Giglio, M., Dubbini, M., & Gattelli, M. (2015). Evaluating multispectral images and vegetation indices for precision farming applications from UAV images. *Remote Sensing*, 7(4), 4026-4047. (DOI 10.3390/rs70404026)
- Canty, M. J. (2014). *Image analysis, classification and change detection in remote sensing: with algorithms for ENVI/IDL and Python*. (3rd ed.). Boca Raton, Florida, USA: CRC Press.
- Capello, E., Guglieri, G., Marguerettaz, P., & Quagliotti, F. (2012). Preliminary assessment of flying and handling qualities for mini-UAVs. *Journal of Intelligent & Robotic Systems*, 65(1), 43-61. (DOI 10.1007/s10846-011-9565-5)
- Carbonneau, P. E., Hervé, P., & Dunford, R. (2012). Hyperspatial imagery in riverine environments. In P. Carbonneau & H. Piégay (Eds.), *Fluvial remote sensing for science and management* (pp. 163-192). Hoboken, NJ, USA: John Wiley & Sons.
- Carlson, T. N., & Ripley, D. A. (1997). On the relation between NDVI, fractional vegetation cover, and leaf area index. *Remote Sensing of Environment*, 62(3), 241-252. (DOI 10.1016/S0034-4257(97)00104-1)
- Carr, J. A., D'Odorico, P., McGlathery, K. J., & Wiberg, P. L. (2012). Stability and resilience of seagrass meadows to seasonal and interannual dynamics and environmental stress. *Journal of Geophysical Research: Biogeosciences*, 117(1). (DOI 10.1029/2011JG001744)
- Carr, J. A., D'Odorico, P., McGlathery, K. J., & Wiberg, P. L. (2016). Spatially explicit feedbacks between seagrass meadow structure, sediment and light: Habitat suitability for seagrass growth. *Advances in Water Resources*, 93(PB), 315-325. (DOI 10.1016/j.advwatres.2015.09.001)
- Carter A.B., Mellors J.E., & Rasheed M.A. (2018). *Torres Strait Seagrass 2018 Report Card*. Report No. 18/25. James Cook University, Cairns, Australia.
- Casal, G., Sánchez-Carnero, N., Domínguez-Gómez, J. A., Kutser, T., & Freire, J. (2012). Assessment of AHS (Airborne Hyperspectral Scanner) sensor to map macroalgal communities on the Ría de vigo and Ría de Aldán coast (NW Spain). *Marine Biology*, 159(9), 1997-2013. (DOI 10.1007/s00227-012-1987-5)
- Chabot, D., & Bird, D. M. (2015). Wildlife research and management methods in the 21st century: Where do unmanned aircraft fit in? *Journal of Unmanned Vehicle Systems*, 3, 137-155. (DOI 10.1139/juvs-2015-0021)

- Chabot, D., Carignan, V., & Bird, D. M. (2014). Measuring habitat quality for least bitterns in a created wetland with use of a small unmanned aircraft. *Wetlands*, 34(3), 527-533. (DOI 10.1007/s13157-014-0518-1)
- Chabot, D., Craik, S. R., & Bird, D. M. (2015). Population census of a large common tern colony with a small unmanned aircraft. *PLoS One*, 10(4), e0122588. (DOI 10.1371/journal.pone.0122588)
- Chandrashekar, G., & Sahin, F. (2014). A survey on feature selection methods. *Computers and Electrical Engineering*, 40(1), 16-28. (DOI 10.1016/j.compeleceng.2013.11.024)
- Chayhard, S., Manthachitra, V., Nualchawee, K., & Buranapratheprat, A. (2018a). Multi-temporal mapping of seagrass distribution by using integrated remote sensing data in Kung Kraben Bay (KKB), Chanthaburi Province, Thailand. *International Journal of Agricultural Technology*, 14(2), 161-170.
- Chayhard, S., Manthachitra, V., Nualchawee, K., & Buranapratheprat, A. (2018b). Application of aerial photography with visible atmospherically resistant index by using unmanned aerial vehicles for seagrass bed classification in Kung Krabaen Bay, Thailand. *PeerJ PrePrints*. (DOI 10.7287/peerj.preprints.27407v1)
- Chefaoui, R. M., Duarte, C. M., & Serrão, E. A. (2018). Dramatic loss of seagrass habitat under projected climate change in the Mediterranean Sea. *Global Change Biology* 24(10), 4919-4928. (DOI 10.1111/gcb.14401)
- Chen, C., Chen, Z., Li, M., Liu, Y., Cheng, L., & Ren, Y. (2014). Parallel relative radiometric normalisation for remote sensing image mosaics. *Computers & Geosciences*, 73, 28-36. (DOI 10.1016/j.cageo.2014.08.007)
- Chen, D.-H., & Sun, Y.-N. (2000). A self-learning segmentation framework-the Taguchi approach. *Computerized Medical Imaging and Graphics*, 24(5), 283-296. (DOI 10.1016/S0895-6111(00)00023-9)
- Chen, J. M., & Black, T. A. (1991). Measuring leaf area index of plant canopies with branch architecture. *Agricultural and Forest Meteorology*, 57(1-3), 1-12. (DOI 10.1016/0168-1923(91)90074-Z)
- Chen, Y., Ming, D., & Lv, X. (2019). Superpixel based land cover classification of VHR satellite image combining multi-scale CNN and scale parameter estimation. *Earth Science Informatics*, 1-23. (DOI 10.1007/s12145-019-00383-2)
- Cheng, K. S., Su, Y. F., Yeh, H. C., Chang, J. H., & Hung, W. C. (2012). A path radiance estimation algorithm using reflectance measurements in radiometric control areas. *International Journal of Remote Sensing*, 33(5), 1543. (DOI 10.1080/01431161.2011.583290)
- Cho, D. (2004). Radio flyer: Reginald Denny's passion for model-aircraft building helped pave the way for robot planes. *Technology Review*, 107, 84.
- Cho, H. J., Ogashawara, I., Mishra, D., White, J., Kameronosky, A., Morris, L., Clarke, C., Simpson, A., & Banisakher, D. (2014). Evaluating Hyperspectral Imager for the Coastal Ocean (HICO) data for seagrass mapping in Indian River Lagoon, FL. *GIScience and Remote Sensing*, 51(2), 120-138. (DOI 10.1080/15481603.2014.895577)
- Christensen, B. R. (2015). Use of UAV or remotely piloted aircraft and forward-looking infrared in forest, rural and wildland fire management: evaluation using simple economic analysis. *New Zealand Journal of Forestry Science*, 45(1), 1-9. (DOI 10.1186/s40490-015-0044-9)
- Christianen, M. J. A., Govers, L. L., Bouma, T. J., Kiswara, W., Roelofs, J. G. M., Lamers, L. P. M., & Van Katwijk, M. (2012). Marine megaherbivore grazing may increase seagrass tolerance to high nutrient loads. *Journal of Ecology*, 100(2), 546-560. (DOI 10.1111/j.1365-2745.2011.01900.x)
- Chu, C., Hsu, A.-L., Chou, K.-H., Bandettini, P., & Lin, C. (2012). Does feature selection improve classification accuracy? Impact of sample size and feature selection on classification using anatomical magnetic resonance images. *NeuroImage*, 60(1), 59-70. (DOI 10.1016/j.neuroimage.2011.11.066)

- Chust, G., Galparsoro, I., Borja, A., Franco, J., & Uriarte, A. (2008). Coastal and estuarine habitat mapping, using LIDAR height and intensity and multi-spectral imagery. *Estuarine Coastal and Shelf Science*, 78(4), 633-643. (DOI 10.1016/j.ecss.2008.02.003)
- Ciollaro, M., & Wang, D. (2016). *Package 'MeanShift', The Comprehensive R Archive Network (CRAN) package repository*. <https://cran.rstudio.com/web/packages/MeanShift/>.
- Clemens, S. R. (2012). *Procedures for Correcting Digital Camera Imagery Acquired by the AggieAir Remote Sensing*. Thesis, Utah State University.
- Coles, R., & Fortes, M. (2001). Protecting Seagrass - Approaches and Methods. In F. T. Short & R. G. Coles (Eds.), *Global Seagrass Research Methods* (pp. 445-463). Amsterdam, Netherlands: Elsevier.
- Collier, C., & Waycott, M. (2009). *Drivers of change to seagrass distributions and communities on the Great Barrier Reef: Literature review and gaps analysis*. Report to the Marine and Tropical Sciences Research Facility. Reef and Rainforest Research Centre Limited, Cairns, Australia. 55p.
- Collings, S., & Caccetta, P. (2013). Radiometric calibration of very large digital aerial frame mosaics. *International Journal of Image and Data Fusion*, 4(3), 214. (DOI 10.1080/19479832.2012.760656)
- Colomina, I., & Molina, P. (2014). Unmanned aerial systems for photogrammetry and remote sensing: A review. *ISPRS Journal of Photogrammetry and Remote Sensing*, 92, 79-97. (DOI 10.1016/j.isprsjprs.2014.02.013)
- Comaniciu, D., & Meer, P. (2002). Mean shift: a robust approach toward feature space analysis. *IEEE Transactions on Pattern Analysis and Machine Intelligence*, 24(5), 603-619. (DOI 10.1109/34.1000236)
- Congalton, R. G. (1991). A review of assessing the accuracy of classifications of remotely sensed data. *Remote Sensing of Environment*, 37(1), 35-46. (DOI 10.1016/0034-4257(91)90048-b)
- Congalton, R. G., & Green, K. (2009). *Assessing the accuracy of remotely sensed data principles and practices*. New York, USA: CRC Press.
- Congalton, R. G., & Mead, R. A. (1983). A quantitative method to test for consistency and correctness in photointerpretation. *Photogrammetric Engineering and Remote Sensing*, 49(1), 69-74. (DOI 0099-11 12/83/4901-69\$02.25/)
- Cook, D. E., Strong, P. A., Garrett, S. A., & Marshall, R. E. (2013). A small unmanned aerial system (UAS) for coastal atmospheric research: preliminary results from New Zealand. *Journal of the Royal Society of New Zealand*, 43(2), 108-115. (DOI 10.1080/03036758.2012.695280)
- Cooper, J. (2015). *Does seagrass influence the behavioural and physiological response to flow in juvenile snapper (Pagrus auratus)?* MSc thesis, University of Waikato, Hamilton.
- Cortez, P., & Embrechts, M. J. (2013). Using sensitivity analysis and visualization techniques to open black box data mining models. *Information Sciences*, 225(C), 1-17. (DOI 10.1016/j.ins.2012.10.039)
- Cox, C., & Munk, W. (1954). Measurements of the roughness of the sea surface from photographs of the sun's glitter. *Journal of the Optical Society of America*, 44(1), 838-850. (DOI 10.1364/JOSA.44.000838)
- Cullen-Unsworth, L., & Unsworth, R. (Compiler) (2013). *Seagrass meadows, ecosystem services, and sustainability*. London, UK: Routledge.
- Cullen-Unsworth, L. C., Nordlund, L. M., Paddock, J., Baker, S., McKenzie, L. J., & Unsworth, R. K. F. (2014). Seagrass meadows globally as a coupled social-ecological system: Implications for human wellbeing. *Marine Pollution Bulletin*, 83(2), 387-397. (DOI 10.1016/j.marpolbul.2013.06.001)
- Cullen-Unsworth, L. C., & Unsworth, R. K. F. (2016). Strategies to enhance the resilience of the world's seagrass meadows. *Journal of Applied Ecology*. (DOI 10.1111/1365-2664.12637)

- Dalponte, M. (2018). *Package 'itcSegment', The Comprehensive R Archive Network (CRAN) package repository.*
- de Boer, W. F. (2007). Seagrass-sediment interactions, positive feedbacks and critical thresholds for occurrence: a review. *Hydrobiologia*, 591(1), 5-24. (DOI 10.1007/s10750-007-0780-9)
- de Klerk, H. M., Gilbertson, J., Lück-Vogel, M., Kemp, J., & Munch, Z. (2016). Using remote sensing in support of environmental management: A framework for selecting products, algorithms and methods. *Journal of Environmental Management*, 182, 564-573. (DOI 10.1016/j.jenvman.2016.07.073)
- Dekker, A. G., Brando, V. E., & Anstee, J. M. (2005). Retrospective seagrass change detection in a shallow coastal tidal Australian lake. *Remote Sensing of Environment*, 97(4), 415-433. (DOI 10.1016/j.rse.2005.02.017)
- Dekker, A. G., Phinn, S. R., Anstee, J., Bissett, P., Brando, V. E., Casey, B., Fearn, P., Hedley, J., Klonowski, W., Lee, Z. P., Lynch, M., Lyons, M., Mobley, C., & Roelfsema, C. (2011). Intercomparison of shallow water bathymetry, hydro-optics, and benthos mapping techniques in Australian and Caribbean coastal environments. *Limnology and Oceanography: Methods*, 9(9), 396-425. (DOI 10.4319/lom.2011.9.396)
- Del Pozo, S., Rodríguez-Gonzálvez, P., Hernández-López, D., & Felipe-García, B. (2014). Vicarious radiometric calibration of a multispectral camera on board an unmanned aerial system. *Remote Sensing*, 6(3), 1918-1937. (DOI 10.3390/rs6031918)
- den Hartog, C., & Kuo, J. (2006). Taxonomy and biogeography of seagrasses. In A. W. D. Larkum, R. J. Orth & C. M. Duarte (Eds.), *Seagrasses: Biology, Ecology, and Conservation*. Dordrecht, Netherlands: Springer.
- Dencer-Brown, A. M., Alfaro, A. C., Milne, S., & Perrott, J. (2018). A Review on Biodiversity, Ecosystem Services, and Perceptions of New Zealand's Mangroves: Can We Make Informed Decisions about Their Removal? *Resources*, 7(23), 1-21.
- Department of Conservation. (2010). *New Zealand Coastal Policy Statement*. Department of Conservation, Wellington.
- Dessau, O., & Sutton, T. (2011). The Quantum GIS project. *GeoInformatics*, 14(6), 26-28.
- Dhanachandra, N., Manglem, K., & Chanu, Y. J. (2015). Image segmentation using k-means clustering algorithm and subtractive clustering algorithm. *Procedia Computer Science*, 54(C), 764-771. (DOI 10.1016/j.procs.2015.06.090)
- Di Carlo, G., & Kenworthy, W. (2008). Evaluation of aboveground and belowground biomass recovery in physically disturbed seagrass beds. *Oecologia*, 158(2), 285-298. (DOI 10.1007/s00442-008-1120-0)
- Dierssen, H. M., Chlus, A., & Russell, B. (2015). Hyperspectral discrimination of floating mats of seagrass wrack and the macroalgae *Sargassum* in coastal waters of Greater Florida Bay using airborne remote sensing. *Remote Sensing of Environment*, 167, 247-258. (DOI 10.1016/j.rse.2015.01.027)
- Dierssen, H. M., Zimmerman, R. C., Drake, L. A., & Burdige, D. (2010). Benthic ecology from space: Optics and net primary production in seagrass and benthic algae across the Great Bahama Bank. *Marine Ecology Progress Series*, 411, 1-15. (DOI 10.3354/meps08665)
- Diesing, M., Mitchell, P., & Stephens, D. (2016). Image-based seabed classification: what can we learn from terrestrial remote sensing? *ICES Journal of Marine Science*, 73(10), 2425-2441. (DOI 10.1093/icesjms/fsw118)
- Dingle Robertson, L., & King, D. J. (2011). Comparison of pixel- and object-based classification in land cover change mapping. *International Journal of Remote Sensing*, 32(6), 1505-1529.
- Dogan, O. K., Akyurek, Z., & Beklioglu, M. (2009). Identification and mapping of submerged plants in a shallow lake using quickbird satellite data. *Journal of*

- Environmental Management*, 90(7), 2138-2143. (DOI 10.1016/j.jenvman.2007.06.022)
- Dormann, C. F., Elith, J., Bacher, S., Buchmann, C., Carl, G., Carré, G., Marquéz, J. R. G., Gruber, B., Lafourcade, B., Leitão, P. J., Münkemüller, T., McClean, C., Osborne, P. E., Reineking, B., Schröder, B., Skidmore, A. K., Zurell, D., & Lautenbach, S. (2013). Collinearity: a review of methods to deal with it and a simulation study evaluating their performance. *Ecography*, 36(1), 27-46. (DOI 10.1111/j.1600-0587.2012.07348.x)
- Dos Santos, V. (2011). *Impact of black swan grazing and anthropogenic contaminants on New Zealand seagrass meadows*. thesis, University of Waikato.
- Dowding, J. E. (2012). *Significance of the Ohui-Opoutere-Wharekawa Harbour area with respect to native birds*. DM Consultants contract report number 148 prepared for Opoutere Ratepayers and Residents Association, Inc., Christchurch, NZ. 14p.
- Dowding, J. E. (2013). *Sites of importance to coastal and estuarine birds on the east coast of the Waikato region*. Waikato Regional Council Technical Report 2013/53. Hamilton, New Zealand. 66p.
- Doxaran, D., Cherukuru, R. C. N., & Lavender, S. J. (2004). Estimation of surface reflection effects on upwelling radiance field measurements in turbid waters. *Journal of Optics A: Pure and Applied Optics*, 6(7), 690-697. (DOI 10.1088/1464-4258/6/7/006)
- Dronova, I. (2015). Object-based image analysis in wetland research: A review. *Remote Sensing*, 7(5), 6380-6413. (DOI 10.3390/rs70506380)
- Dronova, I., Gong, P., Clinton, N. E., Wang, L., Fu, W., Qi, S., & Liu, Y. (2012). Landscape analysis of wetland plant functional types: The effects of image segmentation scale, vegetation classes and classification methods. *Remote Sensing of Environment*, 127, 357-369. (DOI 10.1016/j.rse.2012.09.018)
- Dronova, I., Gong, P., & Wang, L. (2011). Object-based analysis and change detection of major wetland cover types and their classification uncertainty during the low water period at Poyang Lake, China. *Remote Sensing of Environment*, 115(12), 3220-3236. (DOI 10.1016/j.rse.2011.07.006)
- Dryanovski, I., Valenti, R. G., & Xiao, J. (2013). An open-source navigation system for micro aerial vehicles. *Autonomous Robots*, 34(3), 177-188. (DOI 10.1007/s10514-012-9318-8)
- Du, P., Xia, J., Zhang, W., Tan, K., Liu, Y., & Liu, S. (2012). Multiple classifier system for remote sensing image classification: A review. *Sensors*, 12(4), 4764-4792. (DOI 10.3390/s120404764)
- Du, Q., & Nekovei, R. (2005). Implementation of real-time constrained linear discriminant analysis to remote sensing image classification. *Pattern Recognition*, 38(4), 459-471. (DOI 10.1016/j.patcog.2004.09.008)
- Du, Y., Teillet, P. M., & Cihlar, J. (2002). Radiometric normalization of multitemporal high-resolution satellite images with quality control for land cover change detection. *Remote Sensing of Environment*, 82(1), 123-134. (DOI 10.1016/S0034-4257(02)00029-9)
- Duarte, C. M. (2002). The future of seagrass meadows. *Environmental Conservation*, 29(2), 192-206. (DOI 10.1017/S0376892902000127)
- Duarte, C. M., Fourqurean, J. W., Krause-Jensen, D., & Olesen, B. (2006). Dynamics of seagrass stability and change. In A. W. D. Larkum, R. J. Orth & C. M. Duarte (Eds.), *Seagrasses: Biology, Ecology, And Conservation*. Dordrecht, Netherlands: Springer.
- Duarte, C. M., Kennedy, H., Marbà, N., & Hendriks, I. (2013). Assessing the capacity of seagrass meadows for carbon burial: Current limitations and future strategies. *Ocean and Coastal Management*, 83, 32-38. (DOI 10.1016/j.ocecoaman.2011.09.001)

- Duarte, C. M., Marbà, N., & Santos, R. (2004). What may cause loss of seagrasses? . In J. Borum, C. M. Duarte, D. Krause-Jensen & T. M. Greve (Eds.), *European Seagrasses - An Introduction To Monitoring And Management* (pp. 24-32). The M&MS project.
- Duffy, J. P., Pratt, L., Anderson, K., Land, P. E., & Shutler, J. D. (2018). Spatial assessment of intertidal seagrass meadows using optical imaging systems and a lightweight drone. *Estuarine, Coastal and Shelf Science*, 200, 169-180. (DOI 10.1016/j.ecss.2017.11.001)
- Dulava, S., Bean, W. T., & Richmond, O. M. W. (2015). Environmental reviews and case studies: Applications of unmanned aircraft systems (UAS) for waterbird surveys. *Environmental Practice*, 17(3), 201-210. (DOI 10.1017/S1466046615000186)
- Dunford, R., Michel, K., Gagnage, M., Piégay, H., & Trémelo, M. L. (2009). Potential and constraints of unmanned aerial vehicle technology for the characterization of Mediterranean riparian forest. *International Journal of Remote Sensing*, 30(19), 4915-4935. (DOI 10.1080/01431160903023025)
- Durban, J. W., Fearnbach, H., Barrett-Lennard, L. G., Perryman, W. L., & Leroi, D. J. (2015). Photogrammetry of killer whales using a small hexacopter. *Journal of Unmanned Vehicle Systems*, 3, 131-135. (DOI 10.1139/juvs-2015-0020)
- Eckman, J. E. (1990). A model of passive settlement by planktonic larvae onto bottoms of differing roughness. *Limnology and Oceanography*, 35(4), 887-901. (DOI 10.4319/lo.1990.35.4.0887)
- Eckrich, C. E., & Holmquist, J. G. (2000). Trampling in a seagrass assemblage: direct effects, response of associated fauna, and the role of substrate characteristics. *Marine Ecology Progress Series*, 201, 199-209. (DOI 10.3354/meps201199)
- Edelsbrunner, H., Kirkpatrick, D. G., & Seidel, R. (1983). On the shape of a set of points in a plane. *Transactions on Information Theory*, 29(4), 551-559. (DOI 10.1109/TIT.1983.1056714)
- Einzmann, K., Immitzer, M., Böck, S., Bauer, O., Schmitt, A., & Atzberger, C. (2017). Windthrow detection in European forests with very high-resolution optical data. *Forests*, 8(1), 1:26. (DOI 10.3390/f8010021)
- Eitel, J. U. H., Vierling, L. A., Litvak, M. E., Long, D. S., Schulthess, U., Ager, A. A., Krofcheck, D. J., & Stoscheck, L. (2011). Broadband, red-edge information from satellites improves early stress detection in a New Mexico conifer woodland. *Remote Sensing of Environment*, 115(12), 3640-3646. (DOI 10.1016/j.rse.2011.09.002)
- Eldridge, P., Kaldy, J., & Burd, A. (2004). Stress response model for the tropical seagrass *Thalassia testudinum* : The interactions of light, temperature, sedimentation, and geochemistry. *Estuaries*, 27(6), 923-937. (DOI 10.1007/BF02803419)
- Erfteimeijer, P. L. A., & Robin Lewis, R. R. (2006). Environmental impacts of dredging on seagrasses: A review. *Marine Pollution Bulletin*, 52(12), 1553-1572. (DOI 10.1016/j.marpolbul.2006.09.006)
- Esmael, A., dos Santos, J., & Silva Torres, R. (2018). On the ensemble of multiscale object-based classifiers for aerial images: a comparative study. *Multimedia Tools and Applications*, 77(19), 24565-24592. (DOI 10.1007/s11042-018-6023-4)
- Espindola, G. M., Camara, G., Reis, I. A., Bins, L. S., & Monteiro, A. M. (2007). Parameter selection for region-growing image segmentation algorithms using spatial autocorrelation. *International Journal of Remote Sensing*, 27(14), 3035-3040. (DOI 10.1080/01431160600617194)
- Espino, F., Brito, A., Haroun, R., & Tuya, F. (2015a). Macroecological analysis of the fish fauna inhabiting *Cymodocea nodosa* seagrass meadows. *Journal of Fish Biology*, 87(4), 1000-1018. (DOI 10.1111/jfb.12771)
- Espino, F., González, J. A., Haroun, R., & Tuya, F. (2015b). Abundance and biomass of the parrotfish *Sparisoma cretense* in seagrass meadows: temporal and spatial differences between seagrass interiors and seagrass adjacent to reefs.

- Environmental Biology of Fishes*, 98(1), 121-133. (DOI 10.1007/s10641-014-0241-z)
- Eugenio, F., Martin, J., Marcello, J., & Fraile-Nuez, E. (2014). Environmental monitoring of El Hierro Island submarine volcano, by combining low and high resolution satellite imagery. *International Journal of Applied Earth Observations and Geoinformation*, 29, 53-66. (DOI 10.1016/j.jag.2013.12.009)
- Evans, L. J., Jones, T. H., Pang, K., Evans, M. N., Saimin, S., & Goossens, B. (2015). Use of drone technology as a tool for behavioral research: a case study of crocodylian nesting. *Herpetological Conservation and Biology*, 10(1), 90-98.
- Fauzan, M. A., Kumara, I. S. W., Yogyantoro, R., Suwardana, S., Fadhilah, N., Nurmalasari, I., Apriyani, S., & Wicaksono, P. (2017). Assessing the capability of Sentinel-2A data for mapping seagrass percent cover in Jerowaru, East Lombok. *Indonesian Journal of Geography*, 49(2), 195-203. (DOI 10.22146/ijg.28407)
- Fearn, P. R. C., Klonowski, W., Babcock, R. C., England, P., & Phillips, J. (2011). Shallow water substrate mapping using hyperspectral remote sensing. *Continental Shelf Research*, 31(12), 1249-1259. (DOI 10.1016/j.csr.2011.04.005)
- Felsing, M., & Giles, H. (2011). *Tairua Estuary Shellfish and Benthic Habitat Mapping and Assessment of Sediment Contamination (2009/10)*. Waikato Regional Council Technical Report 2011/31. Waikato Regional Council, Hamilton. 72p.
- Feng, Q. L., Liu, J. T., & Gong, J. H. (2015). UAV remote sensing for urban vegetation mapping using random forest and texture analysis. *Remote Sensing*, 7(1), 1074-1094. (DOI 10.3390/rs70101074)
- Fonseca, M., Whitfield, P. E., Kelly, N. M., & Bell, S. S. (2002). Modeling seagrass landscape pattern and associated ecological attributes. *Ecological Applications*, 12(1), 218-237. (DOI 10.1890/1051-0761(2002)012[0218:MSLPAA]2.0.CO;2)
- Fonseca, M. S., & Kenworthy, W. J. (1987). Effects of current on photosynthesis and distribution of seagrasses. *Aquatic Botany*, 27(1), 59-78. (DOI 10.1016/0304-3770(87)90086-6)
- Fonseca, M. S., Kenworthy, W. J., Griffith, E., Hall, M. O., Finkbeiner, M., & Bell, S. S. (2008). Factors influencing landscape pattern of the seagrass *Halophila decipiens* in an oceanic setting. *Estuarine, Coastal and Shelf Science*, 76(1), 163-174. (DOI 10.1016/j.ecss.2007.06.014)
- Fonseca, M. S., Zieman, J. C., Thayer, G. W., & Fisher, J. S. (1983). The role of current velocity in structuring eelgrass (*Zostera marina* L.) meadows. *Estuarine, Coastal and Shelf Science*, 17(4), 367-380. (DOI 10.1016/0272-7714(83)90123-3)
- Foody, G. M. (2002). Status of land cover classification accuracy assessment. *Remote Sensing of Environment*, 80(1), 185-201. (DOI 10.1016/S0034-4257(01)00295-4)
- Foody, G. M. (2004). Thematic map comparison: Evaluating the statistical significance of differences in classification accuracy. *Photogrammetric Engineering and Remote Sensing*, 70(5), 627-633. (DOI 10.14358/PERS.70.5.627)
- Forestier, G., Puissant, A., Wemmert, C., & Gańczarski, P. (2012). Knowledge-based region labeling for remote sensing image interpretation. *Computers, Environment and Urban Systems*, 36(5), 470-480. (DOI 10.1016/j.compenvurbsys.2012.01.003)
- Fourqurean, J. W., Duarte, C. M., Kennedy, H., Marbà, N., Holmer, M., Mateo, M. A., Apostolaki, E. T., Kendrick, G. A., Krause-Jensen, D., McGlathery, K. J., & Serrano, O. (2012). Seagrass ecosystems as a globally significant carbon stock. *Nature Geoscience*, 5(7), 505-509. (DOI 10.1038/ngeo1477)
- Freckleton, R. (2011). Dealing with collinearity in behavioural and ecological data: model averaging and the problems of measurement error. *Behavioral Ecology and Sociobiology*, 65(1), 91-101. (DOI 10.1007/s00265-010-1045-6)
- Frohn, R. C., Autrey, B. C., Lane, C. R., & Reif, M. (2011). Segmentation and object-oriented classification of wetlands in a karst Florida landscape using multi-season

- Landsat-7 ETM+ imagery. *International Journal of Remote Sensing*, 32(5), 1471-1489. (DOI 10.1080/01431160903559762)
- Froidefond, J.-M., Lafon, V., & de Montaudouin, X. (2014). Variations saisonniere et annuelle de l'indice ndvi en relation avec les herbiers de zosteres (*Zostera noltii*) par images satellites SPOT : exemple du bassin d'Arcachon (France). *Revue Française de Photogrammétrie et de Télédétection*, 197, 52-62.
- Furby, S. L., & Campbell, N. A. (2001). Calibrating images from different dates to 'like-value' digital counts. *Remote Sensing of Environment*, 77(2), 186-196. (DOI 10.1016/S0034-4257(01)00205-X)
- Fyfe, S. K. (2003). Spatial and temporal variation in spectral reflectance: Are seagrass species spectrally distinct? *Limnology and Oceanography*, 48(1), 464-479. (DOI 10.4319/lo.2003.48.1_part_2.0464)
- Gade, M., Wang, W., & Kemme, L. (2018). On the imaging of exposed intertidal flats by single- and dual-co-polarization Synthetic Aperture Radar. *Remote Sensing of Environment*, 205, 315-328. (DOI 10.1016/j.rse.2017.12.004)
- Gagnon, P., Scheibling, R. E., Jones, W., & Tully, D. (2008). The role of digital bathymetry in mapping shallow marine vegetation from hyperspectral image data. *International Journal of Remote Sensing*, 29(3), 879-904. (DOI 10.1080/01431160701311283)
- Gao, H., Tang, Y., Jing, L., Li, H., & Ding, H. (2017). A novel unsupervised segmentation quality evaluation method for remote sensing images. *Sensors*, 17(10). (DOI 10.3390/s17102427)
- Gao, Y., Mas, J. F., Kerle, N., & Navarrete Pacheco, J. A. (2011). Optimal region growing segmentation and its effect on classification accuracy. *International Journal of Remote Sensing*, 32(13), 3747-3763. (DOI 10.1080/01431161003777189)
- García-Lamont, F., Cervantes, J., López, A., & Rodriguez, L. (2018). Segmentation of images by color features: A survey. *Neurocomputing*, 292, 1-27. (DOI 10.1016/j.neucom.2018.01.091)
- Gera, A., Pagès, J. F., Arthur, R., Farina, S., Roca, G., Romero, J., & Alcoverro, T. (2014). The effect of a centenary storm on the long-lived seagrass *Posidonia oceanica*. *Limnology and Oceanography*, 59(6), 1910-1918. (DOI 10.4319/lo.2014.59.6.1910)
- Ghosh, A., & Joshi, P. K. (2014). A comparison of selected classification algorithms for mapping bamboo patches in lower Gangetic plains using very high resolution WorldView 2 imagery. *International Journal of Applied Earth Observations and Geoinformation*, 26(1), 298-311. (DOI 10.1016/j.jag.2013.08.011)
- Gibbes, C., Adhikari, S., Rostant, L., Southworth, J., & Qiu, Y. (2010). Application of object based classification and high resolution satellite imagery for savanna ecosystem analysis. *Remote Sensing*, 2(12), 2748-2772. (DOI 10.3390/rs2122748)
- Gibbs, M., & Bremner, D. (2008). *Wharekawa estuary sediment sources*. Environment Waikato Technical Report 2008/07 National Institute of Water and Atmospheric Research, Hamilton, New Zealand. 45p.
- Goebel, M. E., Perryman, W. L., Hinke, J. T., Krause, D. J., Hann, N. A., Gardner, S., & LeRoi, D. J. (2015). A small unmanned aerial system for estimating abundance and size of Antarctic predators. *Polar Biology*, 38(5), 619-630. (DOI 10.1007/s00300-014-1625-4)
- Göktoğan, A. H., Sukkarieh, S., Bryson, M., Randle, J., Lupton, T., & Hung, C. (2010). A rotary-wing unmanned air vehicle for aquatic weed surveillance and management. *Journal of Intelligent and Robotic Systems*, 57(1), 467-484. (DOI 10.1007/s10846-009-9371-5)
- Gómez, C., White, J. C., & Wolter, M. A. (2016). Optical remotely sensed time series data for land cover classification: A review. *ISPRS Journal of Photogrammetry and Remote Sensing*, 116, 55-72. (DOI 10.1016/j.isprsjprs.2016.03.008)

- Gomez, D., & Montero, J. (2008). Fuzzy sets in remote sensing classification. *A Fusion of Foundations, Methodologies and Applications*, 12(3), 243-249. (DOI 10.1007/s00500-007-0201-z)
- Gonçalves, J. A., & Henriques, R. (2015). UAV photogrammetry for topographic monitoring of coastal areas. *Isprs Journal of Photogrammetry and Remote Sensing*, 104, 101-111. (DOI 10.1016/j.isprsjprs.2015.02.009)
- González-Correa, J. M., Fernández-Torquemada, Y., & Sánchez-Lizaso, J. L. (2009). Short-term effect of beach replenishment on a shallow *Posidonia oceanica* meadow. *Marine Environmental Research*, 68(3), 143-150. (DOI 10.1016/j.marenvres.2009.06.002)
- Gordon, A. D. (1981). *Classification : methods for the exploratory analysis of multivariate data*. London: Chapman and Hall.
- Goward, S. N., Markham, B., Dye, D. G., Dulaney, W., & Yang, J. (1991). Normalized difference vegetation index measurements from the advanced very high resolution radiometer. *Remote Sensing of Environment*, 35, 257-277. (DOI 10.1016/0034-4257(91)90017-Z)
- Graeme, M. (1997). *Estuary vegetation survey pilot study Whangamata, Otahu, Wharekawa*. Unpublished report for Environment Waikato. Waikato Regional Council, Hamilton, NZ. 66p.
- Graeme, M. (2008). *Estuarine Vegetation Survey Wharekawa Harbour*. Environment Waikato Technical Report 2008/40. Hamilton, NZ. 39p.
- Graeme, M. (2012). *Estuarine vegetation survey - Raglan (Whaingaroa) Harbour*. Waikato Regional Council Technical Report 2012/35. Hamilton, NZ. 81p.
- Graeme, M., & Giles, H. (2013). *Wharekawa Harbour shellfish and benthic habitat mapping (2010)*. Waikato Regional Council Technical Report 2011/33. Hamilton, NZ. 68p.
- Graeme, M., & Kendall, H. (2001). *Saltwater Paspalum (Paspalum vaginatum) – a Weed Review*. Environment Waikato Technical Report 2001/18 Hamilton, NZ. 52p.
- Graham, R., & Koh, A. (2012). *Digital Aerial Survey : Theory and Practice*. Dunbeath ,Scotland: Whittles.
- Grech, A., Hanert, E., McKenzie, L., Rasheed, M., Thomas, C., Tol, S., Wang, M., Waycott, M., Wolter, J., & Coles, R. (2018). Predicting the cumulative effect of multiple disturbances on seagrass connectivity. *Global Change Biology*, 24(7), 3093-3104. (DOI 10.1111/gcb.14127)
- Greenwood, F. (2015). How to make maps with drones. In K. Kakaes, F. Greenwood, M. Lippincott, S. Dosemagen, P. Meier & S. A. Wich (Eds.), *Drones and Aerial Observation: New Technologies for Property Rights, Human Rights, and Global Development* (Chapter 4). Washington, DC, USA: New America.
- Greiner, J. T., McGlathery, K. J., Gunnell, J., & McKee, B. A. (2013). Seagrass restoration enhances "blue carbon" sequestration in coastal waters. *PLoS ONE*, 8(8), e72469. (DOI 10.1371/journal.pone.0072469)
- Greve, T. M., Krause-Jensen, D., Rasmussen, M. B., & Christensen, P. B. (2005). Means of rapid eelgrass (*Zostera marina* L.) recolonisation in former dieback areas. *Aquatic Botany*, 82(2), 143-156. (DOI 10.1016/j.aquabot.2005.03.004)
- Grizonnet, M., Michel, J., Poughon, V., Inglada, J., Savinaud, M., & Cresson, R. (2017). Orfeo ToolBox: open source processing of remote sensing images. *Open Geospatial Data, Software and Standards*, 2(1), 1-8. (DOI 10.1186/s40965-017-0031-6)
- Grum, F., & Luckey, G. W. (1968). Optical sphere paint and a working standard of reflectance. *Applied Optics*, 7(11), 2289-2294. (DOI 10.1364/AO.7.002289)
- Gu, Z., Shi, X., Li, L., Yu, D., Liu, L., & Zhang, W. (2011). Using multiple radiometric correction images to estimate leaf area index. *International Journal of Remote Sensing*, 32(24), 9441. (DOI 10.1080/01431161.2011.562251)
- Guan, S., Fukami, K., Matsunaka, H., Okami, M., Tanaka, R., Nakano, H., Sakai, T., Nakano, K., Ohdan, H., & Takahashi, K. (2019). Assessing Correlation of High-

- Resolution NDVI with Fertilizer Application Level and Yield of Rice and Wheat Crops Using Small UAVs. *Remote Sensing*, 11(2). (DOI 10.3390/rs11020112)
- Guan, X., Qi, W., He, J., Wen, Q., Chen, T., & Wang, Z. (2018). Purification of training samples based on spectral feature and superpixel segmentation. *The International Archives of the Photogrammetry*, 42(3), 425-430. (DOI 10.5194/isprs-archives-XLII-3-425-2018)
- Guichard, F., Bourget, E., & Agnard, J. P. (2000). High-resolution remote sensing of intertidal ecosystems: A low-cost technique to link scale-dependent patterns and processes. *Limnology and Oceanography*, 45(2), 328-338. (DOI 10.4319/lo.2000.45.2.0328)
- Gullström, M., Baden, S., Lindegarth, M., Systemekologiska, I., Stockholms, U., & Naturvetenskapliga, F. (2012). Spatial patterns and environmental correlates in leaf-associated epifaunal assemblages of temperate seagrass (*Zostera marina*) meadows. *Marine Biology*, 159(2), 413-425. (DOI 10.1007/s00227-011-1819-z)
- Guo, M., Li, J., Sheng, C., Xu, J., & Wu, L. (2017). A review of wetland remote sensing. *Sensors*, 17(4), 777. (DOI 10.3390/s17040777)
- Guo, Y., Graber, A., McBurney, R., & Balasubramanian, R. (2010). Sample size and statistical power considerations in high-dimensionality data settings: a comparative study of classification algorithms. *BMC Bioinformatics*, 11(1), 447. (DOI 10.1186/1471-2105-11-447)
- Ha, S. Y., Min, W.-K., Kim, D.-S., & Shin, K.-H. (2014). Trophic importance of meiofauna to polychaetes in a seagrass (*Zostera marina*) bed as traced by stable isotopes. *Journal of the Marine Biological Association of the United Kingdom*, 94(1), 1-7. (DOI 10.1017/S0025315413001148)
- Hachani, M. A., Ziadi, B., Langar, H., Sami, D. A., Turki, S., & Aleya, L. (2016). The mapping of the *Posidonia oceanica* (L.) Delile barrier reef meadow in the southeastern Gulf of Tunis (Tunisia). *Journal of African Earth Sciences*, 121, 358-364. (DOI 10.1016/j.jafrearsci.2016.05.030)
- Hahsler, M. (2015). Package 'dbscan', *The Comprehensive R Archive Network (CRAN) package repository*. <https://cran.r-project.org/web/packages/dbscan/index.html>.
- Hakala, T., Honkavaara, E., Saari, H., Mäkynen, J., Kaivosoja, J., Pesonen, L., & Pölönen, I. (2013). Spectral imaging from UAVs under varying illumination conditions. *International Archives of the Photogrammetry, Remote Sensing and Spatial Information Sciences*, Volume XL-1/W2, 189-194. (DOI 10.5194/isprsarchives-XL-1-W2-189-2013)
- Hall, F. G., Strelbel, D. E., Nickeson, J. E., & Goetz, S. J. (1991). Radiometric rectification: Toward a common radiometric response among multirate, multisensor images. *Remote Sensing of Environment*, 35(1), 11-27. (DOI 10.1016/0034-4257(91)90062-B)
- Hamylton, S., Hagan, A., Bunbury, N., Fleischer-Dogley, F., & Spencer, T. (2018). Mapping the lagoon at Aldabra Atoll, western Indian Ocean. *Atoll Research Bulletin*, 2018(619), 45-59. (DOI 10.5479/si.0077-5630.619)
- Hamylton, S. M., Hagan, A. B., & Doak, N. (2012). Observations of dugongs at Aldabra Atoll, western Indian Ocean: Lagoon habitat mapping and spatial analysis of sighting records. *International Journal of Geographical Information Science*, 26(5), 839-853. (DOI 10.1080/13658816.2011.616510)
- Hannam, M., & Moskal, L. M. (2015). Terrestrial laser scanning reveals seagrass microhabitat structure on a tideflat. *Remote Sensing*, 7(3), 3037-3055. (DOI 10.3390/rs70303037)
- Hansen, J. C. R., & Reidenbach, M. A. (2013). Seasonal growth and senescence of a *Zostera marina* seagrass meadow alters wave-dominated flow and sediment suspension within a coastal bay. *Estuaries and Coasts*, 36(6), 1099-1114. (DOI 10.1007/s12237-013-9620-5)
- Hao, C., Wu, S., & Xu, C. (2008). Comparison of some vegetation indices in seasonal information. *Chinese Geographical Science*, 18(3), 242-248.

- Haralick, R. M., Shanmugam, K., & Dinstein, I. (1973). Textural features for image classification. *IEEE Transactions on Systems, Man and Cybernetics*, *SMC-3*(6), 610-621. (DOI 10.1109/TSMC.1973.4309314)
- Haralick, R. M., & Shapiro, L. M. (1985). Image segmentation techniques. *Computer Vision, Graphics and Image Processing*, *29*, 100-132. (DOI 10.1016/0031-3200(85)90076-4)
- Hastedt, H., Ekkel, T., & Luhmann, T. (2016). Evaluation of the quality of action cameras with wide angle lenses in UAV photogrammetry. *The International Archives of the Photogrammetry*, 851-859. (DOI 10.5194/isprs-archives-XLI-B1-851-2016)
- Hay, G. J., Blaschke, T., Marceau, D. J., & Bouchard, A. (2003). A comparison of three image-object methods for the multiscale analysis of landscape structure. *ISPRS Journal of Photogrammetry and Remote Sensing*, *57*(5), 327-345. (DOI 10.1016/S0924-2716(02)00162-4)
- Hayes, G., Alcoverro, T., Christianen, M., Duarte, C., Hamann, M., Macreadie, P., Marsh, H., Rasheed, M., Thums, M., Unsworth, R., York, P., & Esteban, N. (2018). New tools to identify the location of seagrass meadows: Marine grazers as habitat indicators. *Frontiers in Marine Science*, *5*. (DOI 10.3389/fmars.2018.00009)
- Hedley, J., Roelfsema, C., Phinn, S., & Mumby, P. (2012). Environmental and Sensor Limitations in Optical Remote Sensing of Coral Reefs: Implications for Monitoring and Sensor Design. *Remote Sensing*, *4*(1), 271-302. (DOI 10.3390/rs4010271)
- Hedley, J., Russell, B., Randolph, K., & Dierssen, H. (2016). A physics-based method for the remote sensing of seagrasses. *Remote Sensing of Environment*, *174*, 134-147. (DOI 10.1016/j.rse.2015.12.001)
- Hedley, J. D., Harborne, A. R., & Mumby, P. J. (2005). Technical note: Simple and robust removal of sun glint for mapping shallow-water benthos. *International Journal of Remote Sensing*, *26*(10), 2107-2112. (DOI 10.1080/01431160500034086)
- Heiss, W. M., Smith, A. M., & Probert, P. K. (2000). Influence of the smalt intertidal seagrass *Zostera novazelandica* on linear water flow and sediment texture. *New Zealand Journal of Marine and Freshwater Research*, *34*(4), 689-694. (DOI 10.1080/00288330.2000.9516970)
- Hendriks, I., Cabanellas-Reboredo, M., Bouma, T., Deudero, S., & Duarte, C. (2011). Seagrass Meadows Modify Drag Forces on the Shell of the Fan Mussel *Pinna nobilis*. *Estuaries and Coasts*, *34*(1), 60-67. (DOI 10.1007/s12237-010-9309-y)
- Herbert, D. A., & Fownes, J. H. (1997). Effects of leaf aggregation in a broad-leaf canopy on estimates of leaf area index by the gap-fraction method. *Forest Ecology and Management*, *97*(3), 277-282. (DOI 10.1016/S0378-1127(97)00068-6)
- Herodowics, K. (2017). Influence of the distance between a reflectance sensor and soil samples with different roughness on their spectra. *Polish Journal of Soil Science*, *49*(2), 133-147. (DOI 10.17951/pjss.2016.49.2.133)
- Hill, V. J., Zimmerman, R. C., Bissett, W. P., Dierssen, H., & Kohler, D. D. R. (2014). Evaluating light availability, seagrass biomass, and productivity using hyperspectral airborne remote sensing in Saint Joseph's Bay, Florida. *Estuaries and Coasts*, *37*(6), 1467-1489. (DOI 10.1007/s12237-013-9764-3)
- Hillock, K., & Rohan, M. (2011). *Intertidal benthic habitats of Kawhia and Aotea Harbours*. Research & Development Series no.327. Department of Conservation, Wellington. 48p.
- Hladik, C., Schalles, J., & Alber, M. (2013). Salt marsh elevation and habitat mapping using hyperspectral and LIDAR data. *Remote Sensing of Environment*, *139*, 318-330. (DOI 10.1016/j.rse.2013.08.003)
- Hodgson, A., Kelly, N., & Peel, D. (2013). Unmanned Aerial Vehicles (UAVs) for Surveying Marine Fauna: A Dugong Case Study. *Plos One*, *8*(11), e79556. (DOI 10.1371/journal.pone.0079556)

- Hoffer, N. V., Coopmans, C., Jensen, A. M., & Chen, Y. (2014). A Survey and Categorization of Small Low-Cost Unmanned Aerial Vehicle System Identification. *Journal of Intelligent & Robotic Systems*, 74(1), 129-145. (DOI 10.1007/s10846-013-9931-6)
- Hogrefe, K. R., Ward, D. H., Donnelly, T. F., & Dau, N. (2014). Establishing a baseline for regional scale monitoring of eelgrass (*Zostera marina*) habitat on the lower Alaska Peninsula. *Remote Sensing*, 6(12), 12447-12477. (DOI 10.3390/rs61212447)
- Höhle, J. (2015). Assessment of the thematic accuracy of land cover maps. *ISPRS Annals of the Photogrammetry, II-3/W5*, 187-194. (DOI 10.5194/isprsannals-II-3-W5-187-2015)
- Holmes, K. W., Van Niel, K. P., Kendrick, G. A., & Radford, B. (2007). Probabilistic large-area mapping of seagrass species distributions. *Aquatic Conservation-Marine and Freshwater Ecosystems*, 17(4), 385-407. (DOI 10.1002/aqc.772)
- Hong, G., & Zhang, Y. (2008). A comparative study on radiometric normalization using high resolution satellite images. *International Journal of Remote Sensing*, 29(2), 425-438. (DOI 10.1080/01431160601086019)
- Honkavaara, E., Arbiol, R., Markelin, L., Martinez, L., Cramer, M., Bovet, S., Chandelier, L., Ilves, R., Klonus, S., Marshal, P., Schläpfer, D., Tabor, M., Thom, C., & Veje, N. (2009). Digital airborne photogrammetry-a new tool for quantitative remote sensing? A state-of-the-art review on radiometric aspects of digital photogrammetric images. *Remote Sensing*, 1(3), 577-605. (DOI 10.3390/rs1030577)
- Honkavaara, E., Markelin, L., Rosnell, T., & Nurminen, K. (2012). Influence of solar elevation in radiometric and geometric performance of multispectral photogrammetry. *ISPRS Journal of Photogrammetry and Remote Sensing*, 67, 13-26. (DOI 10.1016/j.isprsjprs.2011.10.001)
- Horinouchi, M., Tongnunui, P., Furumitsu, K., Nakamura, Y., Kanou, K., Yamaguchi, A., Okamoto, K., & Sano, M. (2012). Food habits of small fishes in seagrass habitats in Trang, southern Thailand. *Fisheries Science*, 78(3), 577-587. (DOI 10.1007/s12562-012-0485-5)
- Hossain, M. S., Bujang, J. S., Zakaria, M. H., & Hashim, M. (2015a). The application of remote sensing to seagrass ecosystems: an overview and future research prospects. *International Journal of Remote Sensing*, 36(1), 61-114. (DOI 10.1080/01431161.2014.990649)
- Hossain, M. S., Bujang, J. S., Zakaria, M. H., & Hashim, M. (2015b). Application of Landsat images to seagrass areal cover change analysis for Lawas, Terengganu and Kelantan of Malaysia. *Continental Shelf Research*, 110, 124-148. (DOI 10.1016/j.csr.2015.10.009)
- Hruska, R., Mitchell, J., Anderson, M., & Glenn, N. F. (2012). Radiometric and geometric analysis of hyperspectral imagery acquired from an unmanned aerial vehicle. *Remote Sensing*, 4(12), 2736-2752. (DOI 10.3390/rs4092736)
- Hsiao, L. H., & Cheng, K. S. (2013). Assessing uncertainties in accuracy of landuse classification using remote sensing images. *The International Archives of the Photogrammetry*, XL-2/W1, 19-23. (DOI 10.5194/isprsarchives-XL-2-W1-19-2013)
- Hu, C., Feng, L., Hardy, R. F., & Hochberg, E. J. (2015). Spectral and spatial requirements of remote measurements of pelagic *Sargassum* macroalgae. *Remote Sensing of Environment*, 167, 229-246. (DOI 10.1016/j.rse.2015.05.022)
- Huang, G., Li, X., Huang, C., Liu, S., Ma, Y., & Chen, H. (2016). Representativeness errors of point-scale ground-based solar radiation measurements in the validation of remote sensing products. *Remote Sensing of Environment*, 181, 198-206. (DOI 10.1016/j.rse.2016.04.001)

- Hung, C., Xu, Z., & Sukkarieh, S. (2014). Feature Learning Based Approach for Weed Classification Using High Resolution Aerial Images from a Digital Camera Mounted on a UAV. *Remote Sensing*, 6(12), 12037-12054.
- Huete, A. R. (1988). A soil-adjusted vegetation index (SAVI). *Remote Sensing of Environment*, 25(3), 295-309.
- Hufkens, K., Friedl, M., Sonnentag, O., Braswell, B. H., Milliman, T., & Richardson, A. D. (2012). Linking near-surface and satellite remote sensing measurements of deciduous broadleaf forest phenology. *Remote Sensing of Environment*, 117(C), 307-321. (DOI 10.1016/j.rse.2011.10.006)
- Hulet, A., Roundy, B., Petersen, S., Jensen, R., & Bunting, S. (2014). An Object-Based Image Analysis of Pinyon and Juniper Woodlands Treated to Reduce Fuels. *Environmental Management*, 53(3), 660-671. (DOI 10.1007/s00267-013-0227-1)
- Hume, T., Gerbeaux, P., Hart, D., Kettles, H., & Neale, D. (2016). A classification of NZ coastal hydrosystems for management purpose. National Institute for Water and Atmospheric Research (NIWA) Unpublished Technical Report prepared for Ministry of the Environment. 120p.
- Husson, E., Hagner, O., Ecke, F., Schmidlein, S., Luleå University of, T., Applied, G., Department of Civil, E., Natural Resources, E., Geosciences, & Environmental, E. (2014a). Unmanned aircraft systems help to map aquatic vegetation. *Applied Vegetation Science*, 17(3), 567-577. (DOI 10.1111/avsc.12072)
- Husson, E., Lindgren, F., & Ecke, F. (2014b). Assessing Biomass and Metal Contents in Riparian Vegetation Along a Pollution Gradient Using an Unmanned Aircraft System. *Water, Air, & Soil Pollution*, 225(6), 1-14. (DOI 10.1007/s11270-014-1957-2)
- Ihaka, R. (2009). R : Past and Future History. Unpublished white-paper. The University of Auckland. <https://cran.r-project.org/doc/html/interface98-paper/paper.html>
- Innangi, S., Tonielli, R., Romagnoli, C., Budillon, F., Di Martino, G., Innangi, M., Laterza, R., Le Bas, T., & Lo Iacono, C. (2019). Seabed mapping in the Pelagic Islands marine protected area (Sicily Channel, southern Mediterranean) using Remote Sensing Object Based Image Analysis (RSOBIA). *Marine Geophysical Research*, 40(3), 333-355. (DOI 10.1007/s11001-018-9371-6)
- Irving, A. D., Tanner, J. E., & Gaylard, S. G. (2013). An integrative method for the evaluation, monitoring, and comparison of seagrass habitat structure. *Marine Pollution Bulletin*, 66(1-2), 176-184. (DOI 10.1016/j.marpolbul.2012.10.017)
- Ismail, N. B. (2001). *Ecology of eelgrass, Zostera novazelandica Setchell*, in Otago Harbour, Dunedin, New Zealand. PhD thesis, University of Otago.
- Jacobs, S. W. L., Les, D. H., & Moody, M. L. (2006). New combinations in Australasian *Zostera* (Zosteraceae). *Telopea*, 11(2), 127-128. (DOI 10.7751/telopea20065714)
- Jaud, M., Grasso, F., Le Dantec, N., Verney, R., Delacourt, C., Ammann, J., Deloffre, J., & Grandjean, P. (2016). Potential of UAVs for monitoring mudflat morphodynamics (Application to the Seine Estuary, France). *ISPRS International Journal of Geo-Information*, 5(4). (DOI 10.3390/ijgi5040050)
- Jiang, Z., Huete, A. R., Didan, K., & Miura, T. (2008). Development of a two-band enhanced vegetation index without a blue band. *Remote Sensing of Environment*, 112(10), 3833-3845. (DOI 10.1016/j.rse.2008.06.006)
- John, B. M., Shirlal, K. G., & Rao, S. (2015). Effect of Artificial Sea Grass on Wave Attenuation- An Experimental Investigation. *Aquatic Procedia*, 4(C), 221-226. (DOI 10.1016/j.aapro.2015.02.030)
- Johnson, B., & Xie, Z. (2011). Unsupervised image segmentation evaluation and refinement using a multi-scale approach. *ISPRS Journal of Photogrammetry and Remote Sensing*, 66(4), 473-483. (DOI 10.1016/j.isprsjprs.2011.02.006)
- Johnson, G. D., & Patil, G. P. (2006). *Landscape pattern analysis for assessing ecosystem condition*. New York, NY: New York, NY : Springer.
- Jonckheere, I., Fleck, S., Nackaerts, K., Muys, B., Coppin, P., Weiss, M., & Baret, F. (2004). Review of methods for in situ leaf area index determination: Part I.

- Theories, sensors and hemispherical photography. *Agricultural and Forest Meteorology*, 121(1-2), 19-35. (DOI 10.1016/j.agrformet.2003.08.027)
- Jones, G. P., Pearlstine, L. G., & Percival, H. F. (2006). An assessment of small unmanned aerial vehicles for wildlife research. *Wildlife Society Bulletin*, 34(3), 750-758.
- Jones, H. (2008). *Coastal Sedimentation - what we know and the information gaps*. Environment Waikato Technical Report 2008/12.
- Jones, T. C., Gemmill, C. E. C., & Pilditch, C. A. (2008). Genetic variability of New Zealand seagrass (*Zostera muelleri*) assessed at multiple spatial scales. *Aquatic Botany*, 88(1), 39-46. (DOI 10.1016/j.aquabot.2007.08.017)
- Jordà, G., Marbà, N., & Duarte, C. M. (2012). Mediterranean seagrass vulnerable to regional climate warming. *Nature Climate Change*, 2(11), 821. (DOI 10.1038/nclimate1533)
- Jordan, C. F. (1969). Derivation of leaf-area index from quality of light on the forest floor. *Ecology*, 50(4), 663-666. (DOI 10.2307/1936256)
- Kaneko, T., Koyama, T., Yasuda, A., Takeo, M., Yanagisawa, T., Kajiwar, K., & Honda, Y. (2011). Low-altitude remote sensing of volcanoes using an unmanned autonomous helicopter: an example of aeromagnetic observation at Izu-Oshima volcano, Japan. *International Journal of Remote Sensing*, 32(5), 1491-1504. (DOI 10.1080/01431160903559770)
- Katwijk, M. M., Thorhaug, A., Marbà, N., Orth, R. J., Duarte, C. M., Kendrick, G. A., Althuizen, I. H. J., Balestri, E., Bernard, G., Cambridge, M. L., Cunha, A., Durance, C., Giesen, W., Han, Q., Hosokawa, S., Kiswara, W., Komatsu, T., Lardicci, C., Lee, K. S., Meinesz, A., Nakaoka, M., O'Brien, K. R., Paling, E. I., Pickerell, C., Ransijn, A. M. A., Verduin, J. J., & Österblom, H. (2016). Global analysis of seagrass restoration: the importance of large-scale planting. *Journal of Applied Ecology*, 53(2), 567-578. (DOI 10.1111/1365-2664.12562)
- Kaur, S., & Chawla, S. (2015). Evaluation of performance of fuzzy c means and mean shift based segmentation for multi-spectral images *International Journal of Computer Applications*, 120(16), 26-28. (DOI 10.5120/21312-4287)
- Kay, S., Hedley, J. D., & Lavender, S. (2009). Sun glint correction of high and low spatial resolution images of aquatic scenes: A review of methods for visible and near-infrared wavelengths. *Remote Sensing*, 1(4), 697-730. (DOI 10.3390/rs1040697)
- Kaya, E., Agca, M., Adiguzel, F., & Cetin, M. (2018). Spatial data analysis with R programming for environment. *Human and Ecological Risk Assessment: An International Journal*, 1-10. (DOI 10.1080/10807039.2018.1470896)
- Kelcey, J., & Lucieer, A. (2012). Sensor correction of a 6-band multispectral imaging sensor for UAV remote sensing. *Remote Sensing*, 4(5), 1462-1493. (DOI 10.3390/rs4051462)
- Kennedy, R. E., Townsend, P. A., Gross, J. E., Cohen, W. B., Bolstad, P., Wang, Y. Q., & Adams, P. (2009). Remote sensing change detection tools for natural resource managers: Understanding concepts and tradeoffs in the design of landscape monitoring projects. *Remote Sensing of Environment*, 113(7), 1382-1396. (DOI 10.1016/j.rse.2008.07.018)
- Khatami, R., Mountrakis, G., & Stehman, S. V. (2016). A meta-analysis of remote sensing research on supervised pixel-based land-cover image classification processes: General guidelines for practitioners and future research. *Remote Sensing of Environment*, 177, 89-100. (DOI 10.1016/j.rse.2016.02.028)
- Khatami, R., Mountrakis, G., & Stehman, S. V. (2017). Predicting individual pixel error in remote sensing soft classification. *Remote Sensing of Environment*, 199, 401-414. (DOI 10.1016/j.rse.2017.07.028)
- Khun, M. (2013). Predictive Modeling with R and the caret Package. Unpublished technical reference. https://www.r-project.org/conferences/useR-2013/Tutorials/kuhn/user_caret_2up.pdf.

- Kilminster, K., McMahon, K., Waycott, M., Kendrick, G. A., Scanes, P., McKenzie, L., O'Brien, K. R., Lyons, M., Ferguson, A., Maxwell, P., Glasby, T., & Udy, J. (2015). Unravelling complexity in seagrass systems for management: Australia as a microcosm. *Science of the Total Environment*, *534*, 97-109. (DOI 10.1016/j.scitotenv.2015.04.061)
- Kim, J.-H., Kim, Y. K., Kim, S. H., Park, J.-I., & Lee, K.-S. (2016). Growth dynamics of the seagrass. *Estuarine, Coastal and Shelf Science*, *175*, 1-9. (DOI 10.1016/j.ecss.2016.03.023)
- Kim, J.-H., Park, S. H., Kim, Y. K., Kim, S. H., Park, J.-I., & Lee, K.-S. (2014). Seasonal growth dynamics of the seagrass *Zostera caulescens* on the eastern coast of Korea. *Ocean Science Journal*, *49*(4), 391-402. (DOI 10.1007/s12601-014-0036-3)
- Kim, K., Choi, J. K., Ryu, J. H., Jeong, H. J., Lee, K., Park, M. G., & Kim, K. Y. (2015). Observation of typhoon-induced seagrass die-off using remote sensing. *Estuarine, Coastal and Shelf Science*, *154*, 111-121. (DOI 10.1016/j.ecss.2014.12.036)
- Kim, S.R., Lee, W.K., Kwak, D.A., Biging, G. S., Gong, P., Lee, J.H., & Cho, H.K. (2011). Forest cover classification by optimal segmentation of high resolution satellite imagery. *Sensors*, *11*(2), 1943-1958. (DOI 10.3390/s110201943)
- King, M. (1993). *The Coromandel*. Tandem Press. Auckland
- Kipp, S., Mistele, B., & Schmidhalter, U. (2014). The performance of active spectral reflectance sensors as influenced by measuring distance, device temperature and light intensity. *Computers and Electronics in Agriculture*, *100*(C), 24-33. (DOI 10.1016/j.compag.2013.10.007)
- Kirk, J. T. O. (2010). Absorption of light with the aquatic medium. In J. T. O. Kirk (Ed.), *Light and photosynthesis in aquatic ecosystems* (3rd ed., pp. 50-97). New York: Cambridge University Press.
- Kirkman, H. (1985). Community structure in seagrasses in southern western Australia. *Aquatic Botany*, *21*(4), 363-375. (DOI 10.1016/0304-3770(85)90077-4)
- Kirkman, H. (1996). Baseline and monitoring methods for seagrass meadows. *Journal of Environmental Management*, *47*(2), 191-201. (DOI 10.1006/jema.1996.0045)
- Kirkman, H., Cook, I. H., & Reid, D. D. (1982). Biomass and growth of *Zostera capricorni* Aschers. in port hacking, N.S.W., Australia. *Aquatic Botany*, *12*(C), 57-67. (DOI 10.1016/0304-3770(82)90006-7)
- Klemas, V. (2011). Remote sensing of wetlands: case studies comparing practical techniques. *Journal of Coastal Research*, *27*(3), 418-427. (DOI 10.2112/jcoastres-d-10-00174.1)
- Klemas, V. (2013). Remote sensing of emergent and submerged wetlands: an overview. *International Journal of Remote Sensing*, *34*(18), 6286-6320. (DOI 10.1080/01431161.2013.800656)
- Klemas, V. V. (2001). Remote sensing of landscape-level coastal environmental indicators. *International Journal for Decision Makers, Scientists and Environmental Auditors*, *27*(1), 47-57. (DOI 10.1007/s002670010133)
- Klemas, V. V. (2015). Coastal and environmental remote sensing from unmanned aerial vehicles: An overview. *Journal of Coastal Research*, *31*(5), 1260-1267. (DOI 10.2112/JCOASTRES-D-15-00005.1)
- Knudby, A., & Nordlund, L. (2011). Remote sensing of seagrasses in a patchy multi-species environment. *International Journal of Remote Sensing*, *32*(8), 2227-2244. (DOI 10.1080/01431161003692057)
- Kobayashi, S., & Sanga-Ngoie, K. (2008). The integrated radiometric correction of optical remote sensing imageries. *International Journal of Remote Sensing*, *29*(20), 5957-5985. (DOI 10.1080/01431160701881889)
- Koch, E. W., & Gust, G. (1999). Water flow in tide- and wave-dominated beds of the seagrass *Thalassia testudinum*. *Marine Ecology Progress Series*, *184*, 63-72. (DOI 10.3354/meps184063)

- Koch, M., Bowes, G., Ross, C., & Zhang, X. H. (2013). Climate change and ocean acidification effects on seagrasses and marine macroalgae. *Global Change Biology*, 19(1), 103-132. (DOI 10.1111/j.1365-2486.2012.02791.x)
- Koh, L. P., & Wich, S. A. (2012). Dawn of drone ecology: Low-cost autonomous aerial vehicles for conservation. *Tropical Conservation Science*, 5(2), 121-132. (DOI 10.5167/uzh-72781)
- Kohavi, R., & John, G. H. (1997). Wrappers for feature subset selection. *Artificial Intelligence*, 97(1), 273-324. (DOI 10.1016/S0004-3702(97)00043-X)
- Kohlmeier, D., Pilditch, C. A., Bornman, J. F., & Bischof, K. (2014). Site specific differences in morphometry and photophysiology in intertidal *Zostera muelleri* meadows. *Aquatic Botany*, 116, 104-109. (DOI 10.1016/j.aquabot.2014.02.011)
- Kohlus, J., Stelzer, K., Müller, G., & Smollich, S. (2020). Mapping seagrass (*Zostera*) by remote sensing in the Schleswig-Holstein Wadden Sea. *Estuarine, Coastal and Shelf Science*, 238. (DOI 10.1016/j.ecss.2020.106699)
- Konar, B., & Iken, K. (2018). The use of unmanned aerial vehicle imagery in intertidal monitoring. *Deep-Sea Research Part II*, 147, 79-86. (DOI 10.1016/j.dsr2.2017.04.010)
- Korytkowski, M., Rutkowski, L., & Scherer, R. (2016). Fast image classification by boosting fuzzy classifiers. *Information Sciences*, 327(C), 175-182. (DOI 10.1016/j.ins.2015.08.030)
- Koukal, T., & Atzberger, C. (2012). Potential of multi-angular data derived from a digital aerial frame camera for forest classification. *IEEE Journal of Selected Topics in Applied Earth Observations and Remote Sensing*, 5(1), 30-43. (DOI 10.1109/JSTARS.2012.2184527)
- Kovacs, E., Roelfsema, C., Lyons, M., Zhao, S., & Phinn, S. (2018). Seagrass habitat mapping: how do Landsat 8 OLI, Sentinel-2, ZY-3A, and Worldview-3 perform? *Remote Sensing Letters*, 9(7), 686-695. (DOI 10.1080/2150704X.2018.1468101)
- Kuenzer, C., Bluemel, A., Gebhardt, S., Quoc, T. V., & Dech, S. (2011). Remote sensing of mangrove ecosystems: a review. *Remote Sensing*, 3(12), 878-928. (DOI 10.3390/rs3050878)
- Kulkarni, N. M. (2017). Crop identification using unsupervised ISODATA and k-means from multispectral remote sensing imagery. *International Journal of Engineering Research and Application*, 7(4), 45-49. (DOI 10.9790/9622-0704014549)
- Kumar, S., Khan, Z., & Jain, A. (2012). A review of content based image classification using machine learning approach. *International Journal of Advanced Computer Research*, 2(3), 55-60. (DOI 10.1155/2019/9658350)
- Kuo, J., & den Hartog, C. (2006). Seagrass morphology, anatomy and ultrastructure. In A. W. D. Larkum, R. J. Orth & C. M. Duarte (Eds.), *Seagrasses: biology, ecology, and conservation*. Dordrecht: Springer.
- Kutser, T., Vahtmäe, E., Paavel, B., & Kauer, T. (2013). Removing glint effects from field radiometry data measured in optically complex coastal and inland waters. *Remote Sensing of Environment*, 133, 85-89. (DOI 10.1016/j.rse.2013.02.011)
- Kuzucu, A. K., & Balcik, F. B. (2017). Testing the potential of vegetation indices for land use/cover classification using high resolution data. *ISPRS Annals of the Photogrammetry, iv-4/w4(4)*, 279-283. (DOI 10.5194/isprs-annals-IV-4-W4-279-2017)
- La Manna, G., Donno, Y., Sara, G., & Ceccherelli, G. (2015). The detrimental consequences for seagrass of ineffective marine park management related to boat anchoring. *Marine Pollution Bulletin*, 90(1-2), 160-166. (DOI 10.1016/j.marpolbul.2014.11.001)
- Laliberte, A., & Rango, A. (2011). Image processing and classification procedures for analysis of sub-decimeter imagery acquired with an unmanned aircraft over arid rangelands. *GIScience and Remote Sensing*, 48(1), 4-23. (DOI 10.2747/1548-1603.48.1.4)

- Laliberte, A. S., Browning, D. M., & Rango, A. (2012). A comparison of three feature selection methods for object-based classification of sub-decimeter resolution UltraCam-L imagery. *International Journal of Applied Earth Observation and Geoinformation*, 15(1), 70-78. (DOI 10.1016/j.jag.2011.05.011)
- Laliberte, A. S., Goforth, M. A., Steele, C. M., & Rango, A. (2011). Multispectral remote sensing from unmanned aircraft: Image processing workflows and applications for rangeland environments. *Remote Sensing*, 3(12), 2529-2551. (DOI 10.3390/rs3112529)
- Landcare Research (Compiler) (2010). *Fundamental Soils GIS layer*. <https://soils.landcareresearch.co.nz/soil-data/fundamental-soil-layers/>.
- Lang, A. R. G., & Yueqin, X. (1986). Estimation of leaf area index from transmission of direct sunlight in discontinuous canopies. *Agricultural and Forest Meteorology*, 37(3), 229-243. (DOI 10.1016/0168-1923(86)90033-X)
- Lang, M. W., Bourgeau-Chavez, L. L., Tiner, R. W., & Klemas, V. V. (2015). Advances in remotely sensed data and techniques for wetland mapping and monitoring. In R. W. Tiner, M. W. Lang & V. Klemas (Eds.), *Remote sensing of wetlands: applications and advances*. Boca Raton: CRC Press, Taylor & Francis Group.
- Lapray, P.-J., Wang, X., Thomas, J.-B., & Gouton, P. (2014). Multispectral filter arrays: Recent advances and practical implementation. *Sensors*, 14(11), 21626-21659. (DOI 10.3390/s141121626)
- Larose, D. T. (2015). Data mining and predictive analytics. In C. D. Larose (Ed.), (2nd ed., ed.). Hoboken, New Jersey : John Wiley & Sons.
- Lathrop, R. G., Montesano, P., & Haag, S. (2006). A multi-scale segmentation approach to mapping seagrass habitats using airborne digital camera imagery. *Photogrammetric Engineering and Remote Sensing*, 72(6), 665-675.
- Lavery, P. S., Mateo, M.-Á., Serrano, O., & Rozaimi, M. (2013). Variability in the carbon storage of seagrass habitats and its implications for global estimates of blue carbon ecosystem service. *PLoS ONE*, 8(9), e73748. (DOI 10.1371/journal.pone.0073748)
- Leduc, D., & Probert, P. K. (2011). Small-scale effect of intertidal seagrass (*Zostera muelleri*) on meiofaunal abundance, biomass, and nematode community structure. *Journal of the Marine Biological Association of the United Kingdom*, 91(3), 579-591. (DOI 10.1017/s0025315410001645)
- Lee, K.-S., Park, S. R., & Kim, Y. K. (2007). Effects of irradiance, temperature, and nutrients on growth dynamics of seagrasses: A review. *Journal of Experimental Marine Biology and Ecology*, 350(1), 144-175. (DOI 10.1016/j.jembe.2007.06.016)
- Lee, S. Y., Fong, C. W., & Wu, R. S. S. (2001). The effects of seagrass (*Zostera japonica*) canopy structure on associated fauna: a study using artificial seagrass units and sampling of natural beds. *Journal of Experimental Marine Biology and Ecology*, 259(1), 23-50. (DOI 10.1016/S0022-0981(01)00221-0)
- Lee, T. M., & Yeh, H. C. (2009). Applying remote sensing techniques to monitor shifting wetland vegetation: A case study of Danshui River estuary mangrove communities, Taiwan. *Ecological Engineering*, 35(4), 487-496. (DOI 10.1016/j.ecoleng.2008.01.007)
- Lehmann, J. R. K., Münchberger, W., Knoth, C., Blodau, C., Nieberding, F., Prinz, T., Pancotto, V. A., & Kleinebecker, T. (2016). High-resolution classification of south Patagonian peat bog microforms reveals potential gaps in up-scaled CH₄ fluxes by use of unmanned aerial system (UAS) and CIR imagery. *Remote Sensing*, 8(3), 173. (DOI 10.3390/rs8030173)
- Lelong, C. C. D., Burger, P., Jubelin, G., Roux, B., Labbe, S., & Baret, F. (2008). Assessment of unmanned aerial vehicles imagery for quantitative monitoring of wheat crop in small plots. *Sensors*, 8(5), 3557-3585. (DOI 10.3390/s8053557)
- Lemmens, A., & Croux, C. (2006). Bagging and boosting classification trees to predict churn. *Journal of Marketing Research*, 43(2), 1. (DOI 10.1509/jmkr.43.2.276)

- Les, D. H., Moody, M. L., Surrey, W. L. J., & Bayer, R. J. (2002). Systematics of seagrasses (Zosteraceae) in Australia and New Zealand. *Systematic Botany*, 27(3), 468-484. (DOI 10.1043/0363-6445-27.3.468)
- Lesser, M., & Mobley, C. (2007). Bathymetry, water optical properties, and benthic classification of coral reefs using hyperspectral remote sensing imagery. *Journal of the International Society for Reef Studies*, 26(4), 819-829. (DOI 10.1007/s00338-007-0271-5)
- Levin, N., Ben-Dor, E., & Singer, A. (2005). A digital camera as a tool to measure colour indices and related properties of sandy soils in semi-arid environments. *International Journal of Remote Sensing*, 26(24), 5475-5492. (DOI 10.1080/01431160500099444)
- Lewis, M., & Britton, R. (2015). Harbour and Catchment Management Plan - Whangapoua 2015. Unpublished Waikato Regional Council Technical Report 2015/03. Hamilton.
- Li, H., Calder, C. A., & Cressie, N. (2007). Beyond Moran's i: Testing for spatial dependence based on the spatial autoregressive model. *Geographical Analysis*, 39(4), 357-375. (DOI 10.1111/j.1538-4632.2007.00708.x)
- Li, M., Ma, L., Blaschke, T., Cheng, L., & Tiede, D. (2016). A systematic comparison of different object-based classification techniques using high spatial resolution imagery in agricultural environments. *International Journal of Applied Earth Observations and Geoinformation*, 49(C), 87-98. (DOI 10.1016/j.jag.2016.01.011)
- Li, R., Liu, J.-K., Sukcharoenpong, A., Yuan, J., Zhu, H., & Zhang, S. (2012). A systematic approach toward detection of seagrass patches from hyperspectral imagery. *Marine Geodesy*, 35(3), 271. (DOI 10.1080/01490419.2012.699019)
- Li, S. (2018). *Seagrass Mapping and Human Impact Evaluation Using Remote Sensing Imagery at Core Banks, North Carolina*. MSc thesis, Duke University, Durham, NC, USA.
- Lidz, B. H., & Zawada, D. G. (2013). Possible return of *Acropora cervicornis* at Pulaski Shoal, Dry Tortugas National Park, Florida. *Journal of Coastal Research*, 29(2), 256-271. (DOI 10.2112/JCOASTRES-D-12-00078.1)
- Limnaios, G., & Tsourveloudis, N. (2012). Introduction. In P. J. Delves & P. P. Angelov (Eds.), *Sense and avoid in UAS: research and applications* (First edition ed., pp. 3-34). Hoboken, NJ, USA: John Wiley and Sons.
- Lin, G.-C., Wang, W.-J., Wang, C.-M., & Sun, S.-Y. (2010). Automated classification of multi-spectral MR images using linear discriminant analysis. *Computerized Medical Imaging and Graphics*, 34(4), 251-268. (DOI 10.1016/j.compmedimag.2009.11.001)
- Linchant, J., Lisein, J., Semeki, J., Lejeune, P., & Vermeulen, C. (2015). Are unmanned aircraft systems (UASs) the future of wildlife monitoring? A review of accomplishments and challenges. *Mammal Review*, 45(4), 239-252. (DOI 10.1111/mam.12046)
- Lisein, J., Michez, A., Claessens, H., & Lejeune, P. (2015). Discrimination of deciduous tree species from time series of unmanned aerial system imagery. *PLoS One*, 10(11), e0141006. (DOI 10.1371/journal.pone.0141006)
- Liu, D., & Xia, F. (2010). Assessing object-based classification: Advantages and limitations. *Remote Sensing Letters*, 1(4), 187-194. (DOI 10.1080/01431161003743173)
- Liu, J., Li, P., & Wang, X. (2015). A new segmentation method for very high resolution imagery using spectral and morphological information. *ISPRS Journal of Photogrammetry and Remote Sensing*, 101(11), 145-162. (DOI 10.1016/j.isprsjprs.2014.11.009)
- Liu, J. G., & Mason, P. J. (2009). *Essential image processing and GIS for remote sensing*. John Wiley & Sons, Ltd.

- Liu, Y., Condessa, F., Bioucas-Dias, J. M., Li, J., Du, P., & Plaza, A. (2018). Convex formulation for multiband image classification with superpixel-based spatial regularization. *IEEE Transactions on Geoscience and Remote Sensing*, *56*(5), 2704-2721. (DOI 10.1109/TGRS.2017.2782005)
- Liu, Y. G., Li, S. Z., Wu, W., & Huang, R. G. (2013). Dynamics of a mean-shift-like algorithm and its applications on clustering. *Information Processing Letters*, *113*(1-2), 8-16. (DOI 10.1016/j.ipl.2012.10.002)
- Loupe, G. (2014). *Understanding Random Forests: from Theory to Practice*. PhD thesis, University of Liège, Belgium.
- Lu, B., & He, Y. (2017). Species classification using Unmanned Aerial Vehicle (UAV)-acquired high spatial resolution imagery in a heterogeneous grassland. *ISPRS Journal of Photogrammetry and Remote Sensing*, *128*, 73-85. (DOI 10.1016/j.isprsjprs.2017.03.011)
- Lu, D., & Weng, Q. (2007). A survey of image classification methods and techniques for improving classification performance. *International Journal of Remote Sensing*, *28*(5), 823-870. (DOI 10.1080/01431160600746456)
- Lu, D. J., & Cho, H. J. (2011). An improved water-depth correction algorithm for seagrass mapping using hyperspectral data. *Remote Sensing Letters*, *2*(2), 91-97. (DOI 10.1080/01431161.2010.502152)
- Lu, Y., Lai, Z., Fan, Z., Cui, J., & Zhu, Q. (2015). Manifold discriminant regression learning for image classification. *Neurocomputing*, *166*(C), 475-486. (DOI 10.1016/j.neucom.2015.03.031)
- Lucieer, A., de Jong, S. M., & Turner, D. (2014). Mapping landslide displacements using Structure from Motion (SfM) and image correlation of multi-temporal UAV photography. *Progress in Physical Geography*, *38*(issue 1), 97-116.
- Lundquist, C., Chiaroni, L., Halliday, J., & Williston, T. (2004). *Biological Data for Identified Areas of Significant Conservation Value in the Waikato Coastal and Marine Environment*. Report prepared for DOC, Waikato Conservancy. NIWA client report HAM2004-039. NIWA, Hamilton, New Zealand.
- Lundquist, C. J., Morrissey, D., Gladstone-Gallagher, R. V., & Swales, A. (2014). Managing Mangrove Habitat Expansion in New Zealand. In I. Faridah-Hanum, A. Latiff, K. R. Hakeem & M. Ozturk (Eds.), *Mangrove Ecosystems of Asia: Status, Challenges and Management Strategies* (2014 ed., pp. 415-438). New York, NY: New York, NY: Springer New York.
- Lyons, M., Phinn, S., & Roelfsema, C. (2011). Integrating Quickbird multi-spectral satellite and field data: Mapping bathymetry, seagrass cover, seagrass species and change in Moreton Bay, Australia in 2004 and 2007. *Remote Sensing*, *3*, 42-64. (DOI 10.3390/rs3010042)
- Lyons, M., Roelfsema, C., & Phinn, S. (2013). Towards understanding temporal and spatial dynamics of seagrass landscapes using time-series remote sensing. *Estuarine, Coastal and Shelf Science*, *120*, 42-53. (DOI 10.1016/j.ecss.2013.01.015)
- Lyons, M. B., Phinn, S. R., & Roelfsema, C. M. (2012). Long term land cover and seagrass mapping using Landsat and object-based image analysis from 1972 to 2010 in the coastal environment of South East Queensland, Australia. *ISPRS Journal of Photogrammetry and Remote Sensing*, *71*, 34-46. (DOI 10.1016/j.isprsjprs.2012.05.002)
- Ma, L., Fu, T., & Li, M. (2018). Active learning for object-based image classification using predefined training objects. *International Journal of Remote Sensing*, *39*(9), 2746-2765. (DOI 10.1080/01431161.2018.1430398)
- Ma, L., Li, M., Ma, X., Cheng, L., Du, P., & Liu, Y. (2017). A review of supervised object-based land-cover image classification. *ISPRS Journal of Photogrammetry and Remote Sensing*, *130*, 277-293. (DOI 10.1016/j.isprsjprs.2017.06.001)
- Macreadie, P. I., York, P. H., Sherman, C. D. H., Keough, M. J., Ross, D. J., Ricart, A. M., & Smith, T. M. (2014). No detectable impact of small-scale disturbances on

- 'blue carbon' within seagrass beds. *Marine Biology*, 161(12), 2939-2944. (DOI 10.1007/s00227-014-2558-8)
- Madden, M., Jordan, T., Bernardes, S., Cotten, D. L., O'Hare, N., & Pasqua, A. (2015). *Unmanned Aerial Systems and Structure from Motion Revolutionize Wetlands Mapping*. Remote sensing of wetlands: applications and advances. Boca Raton, FL, USA: CRC Press, Taylor & Francis Group.
- Malengreau, B., Skinner, D., Bromley, C., & Black, P. (2000). Geophysical characterisation of large silicic volcanic structures in the Coromandel Peninsula, New Zealand. *New Zealand Journal of Geology and Geophysics*, 43(2), 171-186. (DOI 10.1080/00288306.2000.9514879)
- Marbà, N., Arias-Ortiz, A., Masqué, P., Kendrick, G. A., Mazarrasa, I., Bastyan, G. R., Garcia-Orellana, J., Duarte, C. M., & Lee, J. (2015). Impact of seagrass loss and subsequent revegetation on carbon sequestration and stocks. *Journal of Ecology*, 103(2), 296-302. (DOI 10.1111/1365-2745.12370)
- Marbà, N., Krause-Jensen, D., Alcoverro, T., Birk, S., Pedersen, A., Neto, J. M., Orfanidis, S., Garmendia, J. M., Muxika, I., Borja, A., Dencheva, K., & Duarte, C. M. (2013). Diversity of European seagrass indicators: patterns within and across regions. *Hydrobiologia*, 704(1), 265-278. (DOI 10.1007/s10750-012-1403-7)
- Marcello, J., Eugenio, F., Martín, J., & Marqués, F. (2018). Seabed mapping in coastal shallow waters using high resolution multispectral and hyperspectral imagery. *Remote Sensing*, 10(8). (DOI 10.3390/rs10081208)
- Marden, M., & Rowan, D. (2015). The effect of land use on slope failure and sediment generation in the Coromandel region of New Zealand following a major storm in 1995. *New Zealand Journal of Forestry Science*, 45(1), 1-18. (DOI 10.1186/s40490-015-0036-9)
- Markelin, L., Honkavaara, E., Hakala, T., Suomalainen, J., & Peltoniemi, J. (2010). Radiometric stability assessment of an airborne photogrammetric sensor in a test field. *ISPRS Journal of Photogrammetry and Remote Sensing*, 65(4), 409-421. (DOI 10.1016/j.isprsjprs.2010.05.003)
- Marsman, M., Waldorp, L., & Maris, G. (2017). A note on large-scale logistic prediction: using an approximate graphical model to deal with collinearity and missing data. *Behaviormetrika*, 44(2), 513-534. (DOI 10.1007/s41237-017-0024-x)
- Martin, R., Brabyn, L., & Beard, C. (2014). Effects of class granularity and cofactors on the performance of unsupervised classification of wetlands using multi-spectral aerial photography. *Journal of Spatial Science*, 59(2), 269-282. (DOI 10.1080/14498596.2014.913272)
- Matese, A., Toscano, P., Di Gennaro, S. F., Genesio, L., Vaccari, F. P., Primicerio, J., Belli, C., Zaldei, A., Bianconi, R., & Gioli, B. (2015). Intercomparison of UAV, aircraft and satellite remote sensing platforms for precision viticulture. *Remote Sensing*, 7(3), 2971-2990. (DOI 10.3390/rs70302971)
- Matheson, F., Dos Santos, V., Inglis, G., Pilditch, C., Reed, J., Morrison, M., Lundquist, C., Van Houte-Howes, K., Hailes, S., & Hewitt, J. (2009). *New Zealand seagrass - General Information Guide*. NIWA Information Series No. 72. NIWA, Wellington, New Zealand.
- Matheson, F. E., Lundquist, C. J., Gemmill, C. E. C., & Pilditch, C. A. (2011). New Zealand seagrass – More threatened than IUCN review indicates. *Biological Conservation*, 144, 2749-2750. (DOI 10.1016/j.biocon.2011.08.020)
- Matheson, F. E., & Schwarz, A. M. (2007). Growth responses of *Zostera capricorni* to estuarine sediment conditions. *Aquatic Botany*, 87(4), 299-306. (DOI 10.1016/j.aquabot.2007.07.002)
- McArthur, L. C., & Boland, J. W. (2006). The economic contribution of seagrass to secondary production in South Australia. *Ecological Modelling*, 196(1-2), 163-172. (DOI 10.1016/j.ecolmodel.2006.02.030)

- McDowell, M. L., & Kruse, F. A. (2016). Enhanced compositional mapping through integrated full-range spectral analysis. *Remote Sensing*, 8(9). (DOI 10.3390/rs8090757)
- McKenna, S., Jarvis, J., Sankey, T., Reason, C., Coles, R., & Rasheed, M. (2015). Declines of seagrasses in a tropical harbour, North Queensland, Australia, are not the result of a single event. *Published by the Indian Academy of Sciences*, 40(2), 389-398. (DOI 10.1007/s12038-015-9516-6)
- Mead, S., & Moores, A. (2005). Estuary Sedimentation : a review of estuarine sedimentation in the Waikato Region. Environment Waikato Technical Report Series 2005/13. ASR Ltd.
- Meier, L., Tanskanen, P., Heng, L., Lee, G. H., Fraundorfer, F., & Pollefeys, M. (2012). PIXHAWK: A micro aerial vehicle design for autonomous flight using onboard computer vision. *Autonomous Robots*, 33(1-2), 21-39. (DOI 10.1007/s10514-012-9281-4)
- Mejia, A. Y., Rotini, A., Lacasella, F., Bookman, R., Thaller, M. C., Shem-Tov, R., Winters, G., & Migliore, L. (2016). Assessing the ecological status of seagrasses using morphology, biochemical descriptors and microbial community analyses. A study in *Halophila stipulacea* (Forsk.) Aschers meadows in the northern Red Sea. *Ecological Indicators*, 60, 1150-1153. (DOI 10.1016/j.ecolind.2015.09.014)
- Meneguzzo, D., Liknes, G., & Nelson, M. (2013). Mapping trees outside forests using high-resolution aerial imagery: a comparison of pixel- and object-based classification approaches. *Environmental Monitoring and Assessment*, 185(8), 6261-6275.
- Michez, A., Piégay, H., Lisein, J., Claessens, H., & Lejeune, P. (2016). Classification of riparian forest species and health condition using multi-temporal and hyperspatial imagery from unmanned aerial system. *Environmental Monitoring and Assessment*, 188(3), 1-19. (DOI 10.1007/s10661-015-4996-2)
- Ministry for the Environment and Stats. (2016). *Our marine environment*. Ministry for the Environment, Statistics New Zealand, Wellington. <http://www.mfe.govt.nz/publications/marine-environmental-reporting/our-marine-environment-2016>.
- Misbari, S., & Hashim, M. (2016). Change detection of submerged seagrass biomass in shallow coastal water. *Remote Sensing*, 8(3), 200. (DOI 10.3390/rs8030200)
- Moore, K. A., Shields, E. C., & Parrish, D. B. (2014). Impacts of varying estuarine temperature and light conditions on *Zostera marina* (eelgrass) and its interactions with *Ruppia maritima* (widgeongrass). *Estuaries and Coasts*, 37(S1), 20-30. (DOI 10.1007/s12237-013-9667-3)
- Moore, K. A., & Short, F. T. (2006). *Zostera: Biology, Ecology, and Management*. In A. W. D. Larkum, R. J. Orth & C. M. Duarte (Eds.), *Seagrasses: biology, ecology, and conservation*. Dordrecht: Springer.
- Moores, M. (2018). *Package 'bayesImageS', The Comprehensive R Archive Network (CRAN) package repository*. [Computer application]. <https://cran.r-project.org/web/packages/bayesImageS/index.html>.
- Moreno-Marín, F., Brun, F. G., & Pedersen, M. F. (2018). Additive response to multiple environmental stressors in the seagrass *Zostera marina* L. *Limnology and Oceanography*, 63(4), 1528-1544. (DOI 10.1002/lno.10789)
- Moreton, J. (2017, 14 April). Cyclone Cook: The Storm That Was, *New Zealand Herald*. Retrieved from https://www.nzherald.co.nz/nz/news/article.cfm?c_id=1&objectid=11838356.
- Morrisey, D., Beard, C., Morrison, M., Craggs, R., & Lowe, M. (2007). The New Zealand mangrove: review of the current state of knowledge. Auckland Regional Council Technical Publication No. P325. Auckland. 162p.
- Morrison, M. A., Lowe, M. L., Grant, C. M., Smith, P. J., Carbines, G., Reed, J., Bury, S. J., & Brown, J. (2014). Seagrass meadows as biodiversity and productivity

- hotspots. New Zealand Aquatic Environment and Biodiversity Report No 137. Wellington. 151p.
- Mount, R. E. (2006). *Small format digital aerial photography for mapping and monitoring seagrass habitats in shallow temperate marine waters*. PhD thesis, University of Tasmania, Tasmania, Australia.
- Mount, R. E. (2007). Rapid monitoring of extent and condition of Seagrass habitats with aerial photography "mega-Quadrats". *Journal of Spatial Science*, 52(1), 105-119. (DOI 10.1080/14498596.2007.9635106)
- Muehlstein, L. (1989). Perspectives on the wasting disease of eelgrass *Zostera marina*. *Diseases of aquatic organisms*, 7(3), 211-221. (DOI 10.3354/dao007211)
- Muehlstein, L., Porter, D., & Short, F. (1988). *Labyrinthula* sp., a marine slime mold producing the symptoms of wasting disease in eelgrass, *Zostera marina*. *International Journal on Life in Oceans and Coastal Waters*, 99(4), 465-472. (DOI 10.1007/BF00392553)
- Mulero-Pázmány, M., Stolper, R., Essen, L. D. v., Negro, J. J., & Sassen, T. (2014). Remotely Piloted Aircraft Systems as a Rhinoceros Anti-Poaching Tool in Africa. *PLoS One*, 9(1), e83873. (DOI 10.1371/journal.pone.0083873)
- Myint, S. W., Gober, P., Brazel, A., Grossman-Clarke, S., & Weng, Q. (2011). Per-pixel vs. object-based classification of urban land cover extraction using high spatial resolution imagery. *Remote Sensing of Environment*, 115(5), 1145-1161. (DOI 10.1016/j.rse.2010.12.017)
- Nahirnick, N., Hunter, P., Costa, M., Schroeder, S., & Sharma, T. (2019a). Benefits and challenges of UAS imagery for eelgrass (*Zostera marina*) mapping in small estuaries of the Canadian West Coast. *Journal of Coastal Research*, 35(3), 673-683. (DOI 10.2112/JCOASTRES-D-18-00079.1)
- Nahirnick, N. K., Reshitnyk, L., Campbell, M., Hessing-Lewis, M., Costa, M., Yakimishyn, J., & Lee, L. (2019b). Mapping with confidence; delineating seagrass habitats using Unoccupied Aerial Systems (UAS). *Remote Sensing in Ecology and Conservation*, 5(2), 121-135. (DOI 10.1002/rse2.98)
- Nebiker, S., Lack, N., Abächerli, M., & Läderach, S. (2016). Light-weight multispectral UAV sensors and their capabilities for predicting grain yield and detecting plant diseases. *ISPRS - International Archives of the Photogrammetry, Remote Sensing and Spatial Information Sciences, XLI-B1*, 963-970. (DOI 10.5194/isprsarchives-XLI-B1-963-2016)
- Neckles, H. A., Kopp, B. S., Peterson, B. J., & Pooler, P. S. (2012). Integrating scales of seagrass monitoring to meet conservation needs. *Estuaries and Coasts*, 35(1), 23-46. (DOI 10.1007/s12237-011-9410-x)
- Needham, H., Townsend, M., Hewitt, J., & Hailles, S. (2013). *Intertidal habitat mapping for ecosystem goods and services: Waikato estuaries*. Waikato Regional Council Technical Report 2014/39, National Institute of Water & Atmospheric Research Ltd, Hamilton.
- Nelson, W. G. (2017). Development of an epiphyte indicator of nutrient enrichment: Threshold values for seagrass epiphyte load. *Ecological Indicators*, 74, 343-356. (DOI 10.1016/j.ecolind.2016.11.035)
- Nicodemus, F. E., Richmond, J. C., Hsia, J. J., Ginsberg, I. W., & Limperis, T. (1977). Geometrical consideration and nomenclature for reflectance. Unpublished report for U.S. Department of Commerce. <https://graphics.stanford.edu/courses/cs448-05-winter/papers/nicodemus-brdf-nist.pdf>.
- Nishar, A., Richards, S., Breen, D., Robertson, J., & Breen, B. (2016). Thermal infrared imaging of geothermal environments and by an unmanned aerial vehicle (UAV): A case study of the Wairakei - Tauhara geothermal field, Taupo, New Zealand. *Renewable Energy*, 86, 1256-1264. (DOI 10.1016/j.renene.2015.09.042)
- Nobi, E. P., Dilipan, E., Sivakumar, K., & Thangaradjou, T. (2012). Estimation of the Aerial Cover of Seagrasses of Lakshadweep Islands (India) Using Indian Remote

- Sensing Satellite (IRS P6 LISS IV). *Journal of the Indian Society of Remote Sensing*, 40(3), 467-481. (DOI 10.1007/s12524-011-0179-y)
- Nobi, E. P., & Thangaradjou, T. (2012). Evaluation of the spatial changes in seagrass cover in the lagoons of Lakshadweep islands, India, using IRS LISS III satellite images. *Geocarto International*, 27(8), 647-660. (DOI 10.1080/10106049.2012.665501)
- O'Donnell, E. (2009). Wharekawa harbour and catchment management plan. Environment Waikato Technical Report 2009/12. Waikato Regional Council, Hamilton.
- Okudan, E. S., Demir, V., Kalkan, E., & Karhan, S. Ü. (2011). Anchoring damage on seagrass meadows (*Posidonia oceanica* (L.) Delile) in Fethiye-Göcek Specially Protected Area (Eastern Mediterranean Sea, Turkey). *Journal of Coastal Research*(61), 417-420. (DOI 10.2112/SI61-001.51)
- Oles, A., Pau, G., Smith, M., Sklyar, O., Huber, W., Barry, J., & Marais, P. A. (2016). Package 'EBImage', *The Comprehensive R Archive Network (CRAN) package repository*. <https://www.rdocumentation.org/packages/EBImage/versions/4.14.2>.
- Oliver, J. M. (2017). Current status of the use of small unmanned aerial systems for environmental monitoring. *Environmental Claims Journal*, 29(2), 159-170. (DOI 10.1080/10406026.2017.1307009)
- Olsen, Y. S., Potouroglou, M., Garcias-Bonet, N., & Duarte, C. M. (2015). Warming reduces pathogen pressure on a climate-vulnerable seagrass species. *Estuaries and Coasts*, 38(2), 659-667. (DOI 10.1007/s12237-014-9847-9)
- O'Neill, J. D., & Costa, M. (2013). Mapping eelgrass (*Zostera marina*) in the Gulf Islands National Park Reserve of Canada using high spatial resolution satellite and airborne imagery. *Remote Sensing of Environment*, 133, 152-167. (DOI 10.1016/j.rse.2013.02.010)
- Orth, R. J., Harwell, M. C., Bailey, E. M., Bartholomew, A., Jawad, J. T., Lombana, A. V., Moore, K. A., Rhode, J. M., & Woods, H. E. (2000). A review of issues in seagrass seed dormancy and germination: Implications for conservation and restoration. *Marine Ecology Progress Series*, 200, 277-288. (DOI 10.3354/meps200277)
- Orth, R. J., Harwell, M. C., & Inglis, G. J. (2006a). Ecology of Seagrass Seeds and Seagrass Dispersal Processes. In A. W. D. Larkum, R. J. Orth & C. M. Duarte (Eds.), *Seagrasses: Biology, Ecology, and Conservation*. Dordrecht: Springer.
- Orth, R. J., Tim J. B. C., Dennison, W. C., Duarte, C. M., Fourqurean, J. W., Kenneth L. Heck, J. R., Hughes, A. R., Kendrick, G. A., Kenworthy, W. J., Olyarnik, S., Short, F. T., Waycott, M., & Williams, S. L. (2006b). A global crisis for seagrass ecosystems. *BioScience*, 56(12), 987-996. (DOI 10.1641/0006-3568(2006)56[987:AGCFSE]2.0.CO;2)
- Overstreet, B. T., & Legleiter, C. J. (2017). Removing sun glint from optical remote sensing images of shallow rivers. *Earth Surface Processes and Landforms*, 42(2), 318-333. (DOI 10.1002/esp.4063)
- Ozesmi, S. L., & Bauer, M. E. (2002). Satellite remote sensing of wetlands. *Wetlands Ecology and Management*, 10(5), 381-402. (DOI 10.1023/a:1020908432489)
- Pal, M., & Mather, P. M. (2005). Support vector machines for classification in remote sensing. *International Journal of Remote Sensing*, 26(5), 1007-1011. (DOI 10.1080/01431160512331314083)
- Pal, N. R., & Pal, S. K. (1993). A review on image segmentation techniques. *Pattern Recognition*, 26(9), 1277-1294. (DOI 10.1016/0031-3203(93)90135-J)
- Pan, Z., Glennie, C., Fernandez-Diaz, J. C., & Starek, M. (2016). Comparison of bathymetry and seagrass mapping with hyperspectral imagery and airborne bathymetric lidar in a shallow estuarine environment. *International Journal of Remote Sensing*, 37(3), 516-536. (DOI 10.1080/01431161.2015.1131869)
- Park, S. (2016). *Extent of seagrass in the Bay of Plenty in 2011*. Bay of Plenty Regional Council, Whakatane.

- Parker, T. (2017). Tasman Tempest storm cost \$62m, *New Zealand Herald*. Retrieved from https://www.nzherald.co.nz/personal-finance/news/article.cfm?c_id=12&objectid=11891601.
- Pasqualini, V., Pergent-Martini, C., Pergent, G., Agreil, M., Skoufas, G., Sourbes, L., & Tsirika, A. (2005). Use SPOT 5 for mapping seagrasses: and application to *Posidonia oceanica*. *Remote Sensing of Environment*, *94*, 39-45. (DOI 10.1016/j.rse.2005.08.001)
- Paulose, N. E., Dilipan, E., & Thangaradjou, T. (2013). Integrating Indian remote sensing multi-spectral satellite and field data to estimate seagrass cover change in the Andaman and Nicobar Islands, India. *Ocean Science Journal*, *48*(2), 173-181. (DOI 10.1007/s12601-013-0014-1)
- Pegau, W. S., Gray, D., & Zaneveld, J. R. V. (1997). Absorption and attenuation of visible and near-infrared light in water: Dependence on temperature and salinity. *Applied Optics*, *36*(24), 6035-6046. (DOI 10.1364/AO.36.006035)
- Peña, J. M., Torres-Sánchez, J., de Castro, A. I., Kelly, M., & López-Granados, F. (2013). Weed mapping in early-season maize fields using object-based analysis of unmanned aerial vehicle (UAV) images. *PLoS ONE*, *8*(10). (DOI 10.1371/journal.pone.0077151)
- Peneva, E., Griffith, J. A., & Carter, G. A. (2008). Seagrass mapping in the northern Gulf of Mexico using airborne hyperspectral imagery: A comparison of classification methods. *Journal of Coastal Research*, *24*(4), 850-856. (DOI 10.2112/06-0764.1)
- Peng, Z., & Jun, C. (2011). Weed recognition using image blur information. *Biosystems Engineering*, *110*(2), 198-205. (DOI 10.1016/j.biosystemseng.2011.08.003)
- Petitjean, F., Kurtz, C., Passat, N., & Gançarski, P. (2012). Spatio-temporal reasoning for the classification of satellite image time series. *Pattern Recognition Letters*, *33*(13), 1805-1815. (DOI 10.1016/j.patrec.2012.06.009)
- Pham, L. T. H., Brabyn, L., & Ashraf, S. (2016). Combining QuickBird, LiDAR, and GIS topography indices to identify a single native tree species in a complex landscape using an object-based classification approach. *International Journal of Applied Earth Observation and Geoinformation*, *50*, 187-197. (DOI 10.1016/j.jag.2016.03.015)
- Phan, T., & Kappas, M. (2018). Comparison of Random Forest, k-Nearest Neighbor, and Support Vector Machine classifiers for land cover classification using Sentinel-2 imagery. *Sensors*, *18*(1), 18. (DOI 10.3390/s18010018)
- Phillips, C., Marden, M., & Basher, L. (2007). Review of sediment generation processes in exotic forestry and the applicability of using compound-specific isotopes to understand sediment movement. Landcare Research Contract Report: LC0607/151.
- Phinn, S., Roelfsema, C., Dekker, A., Brando, V., & Anstee, J. (2008). Mapping seagrass species, cover and biomass in shallow waters: An assessment of satellite multi-spectral and airborne hyper-spectral imaging systems in Moreton Bay (Australia). *Remote Sensing of Environment*, *112*(8), 3413-3425. (DOI 10.1016/j.rse.2007.09.017)
- Pinkerton, M., Gall, M., and Wood, S. (2014). Remote sensing of suspended solids in Lyttelton Harbour/Whakaraupō water using satellite images. Report No. R14/55 prepared for Environment Canterbury by National Institute of Water and Atmospheric Research Ltd. Wellington.
- Pipaud, I., & Lehmkuhl, F. (2017). Object-based delineation and classification of alluvial fans by application of mean-shift segmentation and support vector machines. *Geomorphology*, *293*, 178-200. (DOI 10.1016/j.geomorph.2017.05.013)
- Pohl, I. (2015). *SeaSketch: Putting science and technology into collaborative Marine Protected Areas planning*. [Poster]. Presented at the New Zealand Marine Sciences Society Conference, Auckland, New Zealand, retrieved from <https://www.doc.govt.nz/about-us/science-publications/conservation-publications/marine-and-coastal/marine-science-posters/>.

- Pollard, P. C., & Greenway, M. (2013). Seagrasses in tropical Australia, productive and abundant for decades decimated overnight. *Journal of Biosciences*, 38(1), 157-166. (DOI 10.1007/s12038-013-9299-6)
- Pontius, R. G., & Millones, M. (2011). Death to Kappa: birth of quantity disagreement and allocation disagreement for accuracy assessment. *International Journal of Remote Sensing*, 32(15), 4407-4429. (DOI 10.1080/01431161.2011.552923)
- Pont-Tuset, J., & Marques, F. (2016). Supervised evaluation of image segmentation and object proposal techniques. *Pattern Analysis and Machine Intelligence*, 38(7), 1465-1478. (DOI 10.1109/TPAMI.2015.2481406)
- Potgieter, A. B., George-Jaeggli, B., Chapman, S. C., Laws, K., Cadavid, L. A. S., Wixted, J., Watson, J., Eldridge, M., Jordan, D. R., & Hammer, G. L. (2017). Multi-Spectral Imaging from an unmanned aerial vehicle enables the assessment of seasonal leaf area dynamics of sorghum breeding lines. *Frontiers in Plant Science*, 8. (DOI 10.3389/fpls.2017.01532)
- Poursanidis, D., Topouzelis, K., & Chrysoulakis, N. (2018). Mapping coastal marine habitats and delineating the deep limits of the Neptune's seagrass meadows using very high resolution Earth observation data. *International Journal of Remote Sensing*, 39(23), 8670-8687.
- Pu, R., Bell, S., & Meyer, C. (2014). Mapping and assessing seagrass bed changes in Central Florida's west coast using multitemporal Landsat TM imagery. *Estuarine, Coastal and Shelf Science*, 149, 68-79. (DOI 10.1016/j.ecss.2014.07.014)
- Pu, R., Bell, S., Meyer, C., Baggett, L., & Zhao, Y. (2012). Mapping and assessing seagrass along the western coast of Florida using Landsat TM and EO-1 ALI/Hyperion imagery. *Estuarine, Coastal and Shelf Science*, 115, 234-245. (DOI 10.1016/j.ecss.2012.09.006)
- Puliti, S., Ørka, H. O., Gobakken, T., & Næsset, E. (2015). Inventory of small forest areas using an unmanned aerial system. *Remote Sensing*, 7(8), 9632-9654. (DOI 10.3390/rs70809632)
- Qiuying, H. A. N., & Dongyan, L. (2014). Macroalgae blooms and their effects on seagrass ecosystems. *Journal of Ocean University of China*, 13(5), 791-798. (DOI 10.1007/s11802-014-2471-2)
- Raeva, P. L., Šedina, J., & Dlesk, A. (2018). Monitoring of crop fields using multispectral and thermal imagery from UAV. *European Journal of Remote Sensing*, 52(1), 192-201. (DOI 10.1080/22797254.2018.1527661)
- Rahman, M., Ullah, R., Lan, M., Sri Sumantyo, J. T., Kuze, H., & Tateishi, R. (2013). Comparison of Landsat image classification methods for detecting mangrove forests in Sundarbans. *International Journal of Remote Sensing*, 34(4), 1041-1056. (DOI 10.1080/01431161.2012.717181)
- Ralph, P. J., Durako, M. J., Enriquez, S., Collier, C. J., & Doblin, M. A. (2007). Impact of light limitation on seagrasses. *Journal of Experimental Marine Biology and Ecology*, 350(1), 176-193. (DOI 10.1016/j.jembe.2007.06.017)
- Ralph, P. J., & Short, F. T. (2002). Impact of the wasting disease pathogen, *Labyrinthula zosterae*, on the photobiology of eelgrass *Zostera marina*. *Marine Ecology Progress Series*, 226, 265-271. (DOI 10.3354/meps226265)
- Ramsey, C. L., Griffiths, P. A., & Stokes, T. R. (2014). Multi-rotor unmanned aerial vehicles (UAVs) and high-resolution compact digital cameras: a promising new method for monitoring changes to surface karst resources. *Acta Carsologica*, 43(2/3), 269. (DOI 10.3986/ac.v43i2.625)
- Rango, A., Laliberte, A., Herrick, J., Winters, C., Havstad, K., Steele, C., & Browning, D. (2009). Unmanned aerial vehicle-based remote sensing for rangeland assessment, monitoring, and management. *Journal of Applied Remote Sensing*, 3. (DOI 10.1117/1.3216822)
- Rapinel, S., Hubert-Moy, L., & Clement, B. (2015). Combined use of LiDAR data and multispectral earth observation imagery for wetland habitat mapping.

- International Journal of Applied Earth Observation and Geoinformation*, 37, 56-64. (DOI 10.1016/j.jag.2014.09.002)
- Räsänen, A., & Virtanen, T. (2019). Data and resolution requirements in mapping vegetation in spatially heterogeneous landscapes. *Remote Sensing of Environment*, 230, 111207. (DOI 10.1016/j.rse.2019.05.026)
- Ratheesh, R., Chaudhury, N. R., Rajput, P., Arora, M., Gujrati, A., Arunkumar, S. V. V., Shetty, A., Baral, R., Patel, R., Joshi, D., Patel, H., Pathak, B., Jayappa, K. S., Samal, R. N., & Rajawat, A. S. (2019). Coastal sediment dynamics, ecology and detection of coral reef macroalgae from AVIRIS-NG. *Current Science*, 116(7), 1157-1165. (DOI 10.18520/cs/v116/i7/1157-1165)
- Rebello, L. M., Finlayson, C. M., & Nagabhatla, N. (2009). Remote sensing and GIS for wetland inventory, mapping and change analysis. *Journal of Environmental Management*, 90(7), 2144-2153. (DOI 10.1016/j.jenvman.2007.06.027)
- Reidenbach, M., & Timmerman, R. (2019). Interactive Effects of Seagrass and the Microphytobenthos on Sediment Suspension Within Shallow Coastal Bays. *Estuaries and Coasts*, 42(8), 2038-2053.
- Reshitnyk, L., Costa, M., Robinson, C., & Dearden, P. (2014). Evaluation of WorldView-2 and acoustic remote sensing for mapping benthic habitats in temperate coastal Pacific waters. *Remote Sensing of Environment*, 153, 7-23. (DOI 10.1016/j.rse.2014.07.016)
- Resource Management Act (1991). <http://www.legislation.govt.nz/act/public/1991/0069/latest/DLM230265.html>
- Ricart, A. M., Dalmau, A., Pérez, M., & Romero, J. (2015). Effects of landscape configuration on the exchange of materials in seagrass ecosystems. *Marine Ecology Progress Series*, 532, 89-100. (DOI 10.3354/meps11384)
- Richardson, A. J., & Wiegand, C. L. (1977). Distinguishing vegetation from soil background information. *Photogrammetric Engineering and Remote Sensing*, 43(12), 1541-1552.
- Robertson, B., Gillespie, P., Asher, R., Frisk, S., Keeley, N., Hopkins, G., Thompson, S., & Tuckey, B. (2002). *Estuarine environmental assessment and monitoring: - a national protocol*. Sustainable Management Contract No. 5096 Cawthron Institute Nelson, NZ. 47p.
- Robertson, H., & Funnell, E. (2012). Aquatic plant dynamics of Waituna Lagoon, New Zealand: trade-offs in managing opening events of a Ramsar site. *Wetlands Ecology and Management*, 20(5), 433-445. (DOI 10.1007/s11273-012-9267-1)
- Robledo, L., & Soler, A. (2000). Estimation of direct illuminance on a horizontal surface for clear and intermediate skies. *Renewable Energy*, 19(1), 55-60. (DOI 10.1016/S0960-1481(99)00015-4)
- Roca, G., Alcoverro, T., Krause-Jensen, D., Balsby, T. J. S., van Katwijk, M. M., Marbà, N., Santos, R., Arthur, R., Mascaró, O., Fernández-Torquemada, Y., Pérez, M., Duarte, C. M., & Romero, J. (2016). Response of seagrass indicators to shifts in environmental stressors: A global review and management synthesis. *Ecological Indicators*, 63, 310-323. (DOI 10.1016/j.ecolind.2015.12.007)
- Rocchini, D., Foody, G. M., Nagendra, H., Ricotta, C., Anand, M., He, K. S., Amici, V., Kleinschmit, B., Färster, M., Schmidtlein, S., Feilhauer, H., Ghisla, A., Metz, M., & Neteler, M. (2013). Uncertainty in ecosystem mapping by remote sensing. *Computers & Geosciences*, 50, 128-135. (DOI 10.1016/j.cageo.2012.05.022)
- Roderick, M., Smith, R., & Cridland, S. (1996). The precision of the NDVI derived from AVHRR observations. *Remote Sensing of Environment*, 56, 57-65. (DOI 10.1016/0034-4257(95)00213-8)
- Rodríguez, A., Negro, J. J., Mulero, M., Rodríguez, C., Hernández-Pliego, J., & Bustamante, J. (2012). The eye in the sky: Combined use of unmanned aerial systems and GPS data loggers for ecological research and conservation of small birds. *PLoS One*, 7(12), e50336. (DOI 10.1371/journal.pone.0050336)

- Roelfsema, C., Kovacs, E. M., Saunders, M. I., Phinn, S., Lyons, M., & Maxwell, P. (2013). Challenges of remote sensing for quantifying changes in large complex seagrass environments. *Estuarine Coastal and Shelf Science*, *133*, 161-171. (DOI 10.1016/j.ecss.2013.08.026)
- Roelfsema, C., Lyons, M., Dunbabin, M., Kovacs, E. M., & Phinn, S. (2015). Integrating field survey data with satellite image data to improve shallow water seagrass maps: the role of AUV and snorkeller surveys? *Remote Sensing Letters*, *6*(2), 135-144. (DOI 10.1080/2150704x.2015.1013643)
- Roelfsema, C. M., Lyons, M., Kovacs, E. M., Maxwell, P., Saunders, M. I., Samper-Villarreal, J., & Phinn, S. R. (2014). Multi-temporal mapping of seagrass cover, species and biomass: A semi-automated object based image analysis approach. *Remote Sensing of Environment*, *150*, 172-187. (DOI 10.1016/j.rse.2014.05.001)
- Román, M., Fernández, E., Zamborain-Mason, J., & Méndez, G. (2019). Anthropogenic Impact on *Zostera noltei* Seagrass Meadows (NW Iberian Peninsula) Assessed by Carbon and Nitrogen Stable Isotopic Signatures. *Journal of the Coastal and Estuarine Research Federation*, *42*(4), 987-1000. (DOI 10.1007/s12237-019-00549-7)
- Rosnell, T., & Honkavaara, E. (2012). Point cloud generation from aerial image data acquired by a quadcopter type micro unmanned aerial vehicle and a digital still camera. *Sensors*, *12*(1), 453-480. (DOI 10.3390/s120100453)
- Ross, J. (1981). *The radiation regime and architecture of plant stands*. (1st ed. 1981.. ed.). Dordrecht, Netherlands Springer.
- Röttgers, R., McKee, D., & Utschig, C. (2014). Temperature and salinity correction coefficients for light absorption by water in the visible to infrared spectral region. *Optics Express*, *22*(21), 25093-25108. (DOI 10.1364/OE.22.025093)
- Royal Forest & Bird Protection Society of New Zealand Inc v Bay of Plenty Regional Council. (2018). Court File Number: ENV-2015-AKL-129, ENV-2015-AKL-140, ENV-2015-AKL-141. Judgement date 27/9/2018. Environment Court, Auckland.
- Ruwaimana, M., Otero, V., Muslim, A., Muhammad, S., Raymaekers, D., & Koedam, N. (2018). The advantages of using drones over space-borne imagery in the mapping of mangrove forests. *PLoS One*, *13*(7), e0200288. (DOI 10.1371/journal.pone.0200288)
- Samiappan, S., Turnage, G., Hathcock, L., Casagrande, L., Stinson, P., & Moorhead, R. (2017). Using unmanned aerial vehicles for high-resolution remote sensing to map invasive *Phragmites australis* in coastal wetlands. *International Journal of Remote Sensing*, *38*(8-10), 2199-2217. (DOI 10.1080/01431161.2016.1239288)
- Sánchez-Carnero, N., Rodríguez-Pérez, D., Couñago, E., Aceña, S., & Freire, J. (2012). Using vertical Sidescan Sonar as a tool for seagrass cartography. *Estuarine, Coastal and Shelf Science*, *115*, 334-344. (DOI 10.1016/j.ecss.2012.09.015)
- Sankaran, S., Khot, L. R., Espinoza, C. Z., Jarolmasjed, S., Sathuvalli, V. R., Vandemark, G. J., Miklas, P. N., Carter, A. H., Pumphrey, M. O., Knowles, N. R., & Pavek, M. J. (2015). Low-altitude, high-resolution aerial imaging systems for row and field crop phenotyping: A review. *European Journal of Agronomy*, *70*, 112-123. (DOI 10.1016/j.eja.2015.07.004)
- Satapathy, S., Sri Madhava Raja, N., Rajinikanth, V., Ashour, A., & Dey, N. (2018). Multi-level image thresholding using Otsu and chaotic bat algorithm. *Neural Computing and Applications*, *29*(12), 1285-1307. (DOI 10.1007/s00521-016-2645-5)
- Saunders, M. I., Bayraktarov, E., Roelfsema, C. M., Leon, J. X., Samper-Villarreal, J., Phinn, S. R., Lovelock, C. E., & Mumby, P. J. (2015). Spatial and temporal variability of seagrass at Lizard Island, Great Barrier Reef. *Botanica Marina*, *58*(1), 35-49. (DOI 10.1515/bot-2014-0060)
- Sawayama, S., Nurdin, N., Akbar As, M., Sakamoto, S. X., & Komatsu, T. (2015). Introduction of geospatial perspective to the ecology of fish-habitat relationships

- in Indonesian coral reefs: A remote sensing approach. *Ocean Science Journal*, 50(2), 343-352. (DOI 10.1007/s12601-015-0032-2)
- Schaepman-Strub, G., Schaepman, M. E., Painter, T. H., Dangel, S., & Martonchik, J. V. (2006). Reflectance quantities in optical remote sensing—definitions and case studies. *Remote Sensing of Environment*, 103(1), 27-42. (DOI 10.1016/j.rse.2006.03.002)
- Scherer, S., Rehder, J., Achar, S., Cover, H., Chambers, A., Nuske, S., & Singh, S. (2012). River mapping from a flying robot: State estimation, river detection, and obstacle mapping. *Autonomous Robots*, 33(1-2), 189-214. (DOI 10.1007/s10514-012-9293-0)
- Schmidt, A. L., Wysmyk, J. K. C., Craig, S. E., & Lotze, H. K. (2012). Regional-scale effects of eutrophication on ecosystem structure and services of seagrass beds. *Limnology and Oceanography*, 57(5), 1389-1402. (DOI 10.4319/lo.2012.57.5.1389)
- Schowengerdt, R. A. (2007). *Remote sensing, models, and methods for image processing*. (3rd ed.). Burlington, MA: Burlington, MA : Academic Press.
- Schultz, S. T., Kruschel, C., Bakran-Petricioli, T., & Petricioli, D. (2015). Error, power, and blind sentinels: The statistics of seagrass monitoring. *PloS one*, 10(9), e0138378. (DOI 10.1371/journal.pone.0138378)
- Schwarz, A., Morrison, M., Hawes I., and Halliday, J. (2006). *Physical and biological characteristics of a threatened marine habitat: sub-tidal seagrass beds of offshore islands*. Science for Conservation no.269. Wellington: Department of Conservation.
- Schwert, B., Rogan, J., Giner, N. M., Ogneva-Himmelberger, Y., Blanchard, S. D., & Woodcock, C. (2013). A comparison of support vector machines and manual change detection for land-cover map updating in Massachusetts, USA. *Remote Sensing Letters*, 4(9), 882-890. (DOI 10.1080/2150704X.2013.809497)
- Sea change. (2017). Sea Change Tai Timu Tai Pari. <https://www.seachange.org.nz>.
- Serrano, O., Lavery, P., Masque, P., Inostroza, K., Bongiovanni, J., & Duarte, C. (2016). Seagrass sediments reveal the long-term deterioration of an estuarine ecosystem. *Global Change Biology*, 22(4), 1523-1531. (DOI 10.1111/gcb.13195)
- Sevara, C., Pregesbauer, M., Doneus, M., Verhoeven, G., & Trinks, I. (2016). Pixel versus object - a comparison of strategies for the semi-automated mapping of archaeological features using airborne laser scanning data. *Journal of Archaeological Science: Reports*, 5(C), 485-498. (DOI 10.1016/j.jasrep.2015.12.023)
- Shah, S., Marshall, S., & Murray, P. (2017). Removal of specular reflections from image sequences using feature correspondences. *Machine Vision and Applications*, 28(3), 409-420. (DOI 10.1007/s00138-017-0826-6)
- Shaw, W. B., & Allen, R. B. (2003). *Ecological impacts of sea couch and saltwater paspalum in Bay of Plenty estuaries*. Wellington, NZ. 18p.
- Shi, W., Liu, K., & Zhang, H. (2011). A study of supervised classification accuracy in fuzzy topological methods. *International Journal of Applied Earth Observations and Geoinformation*, 13(1), 89-99. (DOI 10.1016/j.jag.2010.07.001)
- Shi, W., & Wang, M. (2014). Ocean reflectance spectra at the red, near-infrared, and shortwave infrared from highly turbid waters: A study in the Bohai Sea, Yellow Sea, and East China Sea. *Limnology and Oceanography*, 59(2), 427-444. (DOI 10.4319/lo.2014.59.2.0427)
- Short, F., Carruthers, T., Dennison, W., & Waycott, M. (2007). Global seagrass distribution and diversity: A bioregional model. *Journal of Experimental Marine Biology and Ecology*, 350(1), 3-20. (DOI 10.1016/j.jembe.2007.06.012)
- Short, F. T., & Coles, R. G. (2001). *Global seagrass research methods*. Amsterdam;New York;: Elsevier.

- Short, F. T., Mathieson, A. T., & Nelson, J. I. (1986). Recurrence of the eelgrass wasting disease at the border of New Hampshire and Maine. *Marine Ecology Progress Series*, 29, 89-92. (DOI 10.3354/meps029089)
- Short, F. T., McKenzie, L. J., Coles, R. G., Vidler, K. P., & Gaeckle, J. L. (2006). *SeagrassNet Manual for Scientific Monitoring of Seagrass Habitat, Worldwide edition*. University of New Hampshire Publication, New Hampshire. 75p.
- Short, F. T., Polidoro, B., Livingstone, S. R., Carpenter, K. E., Bandeira, S., Bujang, J. S., Calumpang, H. P., Carruthers, T. J. B., Coles, R. G., Dennison, W. C., Erfteimeijer, P. L. A., Fortes, M. D., Freeman, A. S., Jagtap, T. G., Kamal, A. H. M., Kendrick, G. A., Judson Kenworthy, W., La Nafie, Y. A., Nasution, I. M., Orth, R. J., Prathep, A., Sanciangco, J. C., Tussenbroek, B. v., Vergara, S. G., Waycott, M., & Zieman, J. C. (2011). Extinction risk assessment of the world's seagrass species. *Biological Conservation*, 144(7), 1961-1971. (DOI 10.1016/j.biocon.2011.04.010)
- Sieberth, T., Wackrow, R., & Chandler, J. H. (2014). Motion blur disturbs – the influence of motion-blurred images in photogrammetry. *The Photogrammetric Record*, 29(148), 434-453. (DOI 10.1111/phor.12082)
- Singleton, P. (2017). *Wharekawa Catchment Condition - 2017*. Unpublished report by Natural Knowledge Ltd. Hamilton. 31p.
- Smith, R. C., & Baker, K. S. (1981). Optical properties of the clearest natural waters (200-800 nm). *Applied Optics*, 20(2), 177-184. (DOI 10.1364/AO.20.000177)
- Soissons, L. M., Li, B., Han, Q., van Katwijk, M. M., Ysebaert, T., Herman, P. M. J., & Bouma, T. J. (2016). Understanding seagrass resilience in temperate systems: the importance of timing of the disturbance. *Ecological Indicators*, 66, 190-198. (DOI 10.1016/j.ecolind.2016.01.030)
- Sousa, A. I., da Silva, J. F., Azevedo, A., & Lillebø, A. I. (2019). Blue Carbon stock in *Zostera noltei* meadows at Ria de Aveiro coastal lagoon (Portugal) over a decade. *Scientific Reports*, 9(1). (DOI 10.1038/s41598-019-50425-4)
- Springer, P. J. (2013). *Military robots and drones: a reference handbook*. Santa Barbara, CA, USA: ABC-CLIO.
- Sridhar, R., Thangaradjou, T., Kannan, L., & Astalakshmi, S. (2010). Assessment of coastal bio-resources of the Palk Bay, India, using IRS-LISS-III data. *Journal of the Indian Society of Remote Sensing*, 38(3), 565-575. (DOI 10.1007/s12524-010-0040-8)
- Stehman, S. V. (1997). Selecting and interpreting measures of thematic classification accuracy. *Remote Sensing of Environment Science and Forestry*, 62, 77-80. (DOI 10.1016/S0034-4257(97)00083-7)
- Stehman, S. V., & Czaplewski, R. L. (1998). Design and analysis for thematic map accuracy assessment: Fundamental principles. *Remote Sensing of Environment*, 64(3), 331-344. (DOI 10.1016/S0034-4257(98)00010-8)
- Stevens, L., & Asher, R. (2005). *Broad scale intertidal habitat mapping of Haldane Estuary*. 16p.
- Stokes, D. (2010). The physical and ecological impacts of mangrove expansion and mangrove removal Tauranga Harbour, New Zealand. PhD thesis, University of Waikato.
- Strong, C., Burnside, N., & Llewellyn, D. (2017). The potential of small-Unmanned Aircraft Systems for the rapid detection of threatened unimproved grassland communities using an Enhanced Normalized Difference Vegetation Index. *PLoS One*, 12(10), e0186193. (DOI 10.1371/journal.pone.0186193)
- Su, T. (2018). An improved unsupervised image segmentation evaluation approach based on under- and over-segmentation aware. *ISPRS Annals of the Photogrammetry*, 4(3), 197-204.
- Sullivan, B. K., Sherman, T. D., Damare, V. S., Lilje, O., & Gleason, F. H. (2013). Potential roles of *Labyrinthula spp.* in global seagrass population declines. *Fungal Ecology*, 6(5), 328-338. (DOI 10.1016/j.funeco.2013.06.004)

- Suomalainen, J., Anders, N., Iqbal, S., Roerink, G., Franke, J., Wenting, P., Hänniger, D., Bartholomeus, H., Becker, R., & Kooistra, L. (2014). A lightweight hyperspectral mapping system and photogrammetric processing chain for unmanned aerial vehicles. *Remote Sensing*, 6(11), 11013-11030. (DOI 10.3390/rs6111013)
- Suykerbuyk, W., Bouma, T. J., Govers, L. L., Giesen, K., de Jong, D. J., Herman, P., Hendriks, J., & van Katwijk, M. M. (2016). Surviving in changing seascapes: Sediment dynamics as bottleneck for long-term seagrass presence. *Ecosystems*, 19(2), 296-310. (DOI 10.1007/s10021-015-9932-3)
- Swales, A., & Hume, T. (1995). Sedimentation history and potential future impacts of production forestry on the Wharekawa Estuary, Coromandel Peninsula. Prepared for Carter Holt Harvey Forests Ltd. . Report no. CHH004 by National Institute of Water and Atmospheric Research Ltd. Wellington.
- Szantoi, Z., Escobedo, F., Abd-Elrahman, A., Smith, S., & Pearlstine, L. (2013). Analyzing fine-scale wetland composition using high resolution imagery and texture features. *International Journal of Applied Earth Observations and Geoinformation*, 23(1), 204-212. (DOI 10.1016/j.jag.2013.01.003)
- Tang, L., & Shao, G. (2015). Drone remote sensing for forestry research and practices. *Journal of Forestry Research*, 26(4), 791-797. (DOI 10.1007/s11676-015-0088-y)
- Thomas, B. T. (2014). Autonomous weapon systems: the anatomy of autonomy and the legality of lethality. *Houston Journal of International Law*, 37(1), 235-274.
- Thompson, S., & Saulnier, A. (2015). The "rise" of unmanned aerial vehicles (UAVs) in Canada: An analysis of special flight operation certificates (sfocs) from 2007 to 2012. *Canadian Public Policy-Analyse De Politiques*, 41(3), 207-222. (DOI 10.3138/cpp.2014-038)
- Thorhaug, A., Richardson, A. D., & Berlyn, G. P. (2007). Spectral reflectance of the seagrasses: *Thalassia testudinum*, *Halodule wrightii*, *Syringodium filiforme* and five marine algae. *International Journal of Remote Sensing*, 28(7-8), 1487-1501. (DOI 10.1080/01431160600954662)
- Thrush, S. F., Hewitt, J. E., Cummings, V. J., Ellis, J. I., Hatton, C., Lohrer, A., & Norkko, A. (2004). Muddy Waters: Elevating Sediment Input to Coastal and Estuarine Habitats. *Frontiers in Ecology and the Environment*, 2(6), 299-306.
- Tilton, J., Aksoy, S., & Tarabalka, Y. (2015). Image segmentation algorithms for land categorization. In *Remotely Sensed Data Characterization, Classification, and Accuracies* (pp. 317-338).
- Timm, B. C., & McGarigal, K. (2012). Fine-scale remotely-sensed cover mapping of coastal dune and salt marsh ecosystems at Cape Cod National Seashore using Random Forests. *Remote Sensing of Environment*, 127, 106-117. (DOI 10.1016/j.rse.2012.08.033)
- Tinel, C., Grizonnet, M., Fontannaz, D., de Boissezon, H., & Giros, A. (2012). Orfeo the Pleiades accompaniment program and its users thematic commissioning. *The International Archives of the Photogrammetry, XXXIX-B3*, 569-572. (DOI 10.5194/isprsarchives-XXXIX-B3-569-2012)
- Tiner, R. W. (2015). *Early Applications of Remote Sensing for Mapping Wetlands*. Remote sensing of wetlands: applications and advances. Boca Raton: CRC Press, Taylor & Francis Group.
- Tiner, R. W., Lang, M. W., & Klemas, V. (2015). *Remote sensing of wetlands: applications and advances*. Boca Raton: CRC Press, Taylor & Francis Group.
- Tiwari, S., Shukla, V. P., Biradar, S. R., & Singh, A. K. (2014). Blur parameters identification for simultaneous defocus and motion blur. *CSI Transactions on ICT*, 2(1), 11-22.
- Topouzelis, K., Makri, D., Stoupas, N., Papakonstantinou, A., & Katsanevakis, S. (2018). Seagrass mapping in Greek territorial waters using Landsat-8 satellite images. *International Journal of Applied Earth Observation and Geoinformation*, 67, 98-113. (DOI 10.1016/j.jag.2017.12.013)

- Torres-Pulliza, D., Wilson, J. R., Darmawan, A., Campbell, S. J., & Andrefouet, S. (2013). Ecoregional scale seagrass mapping: A tool to support resilient MPA network design in the Coral Triangle. *Ocean & Coastal Management*, *80*, 55-64. (DOI 10.1016/j.ocecoaman.2013.04.005)
- Touchette, B. W. (2007). Seagrass-salinity interactions: Physiological mechanisms used by submersed marine angiosperms for a life at sea. *Journal of Experimental Marine Biology and Ecology*, *350*(1), 194-215. (DOI 10.1016/j.jembe.2007.05.037)
- Townsend, A. J., Lange, P. J., Duffy, C. A. J., Miskelly, C. M., Molloy, J., & Norton, D. A. (2008). New Zealand threat classification system manual. Department of Conservation, Wellington, N.Z.
- Traganos, D., & Reinartz, P. (2018a). Machine learning-based retrieval of benthic reflectance and *Posidonia oceanica* seagrass extent using a semi-analytical inversion of Sentinel-2 satellite data. *International Journal of Remote Sensing*, *39*(24), 9428-9452. (DOI 10.1080/01431161.2018.1519289)
- Traganos, D., & Reinartz, P. (2018b). Mapping Mediterranean seagrasses with Sentinel-2 imagery. *Marine Pollution Bulletin*, *134*, 197-209. (DOI 10.1016/j.marpolbul.2017.06.075)
- Travaille, K. L., Salinas-de-León, P., & Bell, J. J. (2015). Indication of visitor trampling impacts on intertidal seagrass beds in a New Zealand marine reserve. *Ocean & Coastal Management*, *114*, 145-150. (DOI 10.1016/j.ocecoaman.2015.06.002)
- Trevathan-Tackett, S. M., Sullivan, B. K., Robinson, K., Lilje, O., Macreadie, P. I., & Gleason, F. H. (2018). Pathogenic *Labyrinthula* associated with Australian seagrasses: Considerations for seagrass wasting disease in the southern hemisphere. *Microbiological Research*, *206*, 74-81. (DOI 10.1016/j.micres.2017.10.003)
- Trias-Sanz, R., Stamon, G., & Louchet, J. (2008). Using colour, texture, and hierarchical segmentation for high-resolution remote sensing. *ISPRS Journal of Photogrammetry and Remote Sensing*, *63*, 156-168. (DOI 10.1016/j.isprsjprs.2007.08.005)
- Troya-Galvis, A., Gancarski, P., Passat, N., & Berti-Equille, L. (2015). Unsupervised Quantification of Under- and Over-Segmentation for Object-Based Remote Sensing Image Analysis. *IEEE Journal of Selected Topics in Applied Earth Observations and Remote Sensing*, *8*(5), 1936-1945. (DOI 10.1109/JSTARS.2015.2424457)
- Tsai, Y. H., Stow, D., & Weeks, J. (2011). Comparison of object-based image analysis approaches to mapping new buildings in Accra, Ghana using multi-temporal Quickbird satellite imagery. *Remote Sensing*, *3*(12), 2707-2726. (DOI 10.3390/rs3122707)
- Tucker, C. J. (1979). Red and photographic infrared linear combinations for monitoring vegetation. *Remote Sensing of Environment*, *8*, 127-150. (DOI 10.1016/0034-4257(79)90013-0)
- Tucker, C. J., Vanpraet, C. L., Sharman, M. J., & Vanittersum, G. (1985). Satellite remote sensing of total herbaceous biomass production in the Senegalese Sahel, 1980-1984 *Remote Sensing of Environment*, *17*, 233-249. (DOI 10.1016/0034-4257(85)90097-5)
- Tuominen, J., & Lipping, T. (2016). Spectral characteristics of common reed beds: Studies on spatial and temporal variability. *Remote Sensing*, *8*(3), 181. (DOI 10.3390/rs8030181)
- Turner, D., Lucieer, A., & de Jong, S. M. (2015). Time series analysis of landslide dynamics using an unmanned aerial vehicle (UAV). *Remote Sensing*, *7*(2), 1736-1757. (DOI 10.3390/rs70201736)
- Turner, S. J. (2007). Growth and productivity of intertidal *Zostera capricorni* in New Zealand estuaries. *New Zealand Journal of Marine and Freshwater Research*, *41*(1), 77. (DOI 10.1080/00288330709509897)

- Turner, S., & Schwarz, A.-M. (2006a). *Management and conservation of seagrass in New Zealand: an introduction*. Science for Conservation 264, Department of Conservation. Wellington. 90p.
- Turner, S. J., & Schwarz, A. M. (2006b). Biomass development and photosynthetic potential of intertidal *Zostera capricorni* in New Zealand estuaries. *Aquatic Botany*, 85(1), 53-64. (DOI 10.1016/j.aquabot.2005.12.006)
- Tuya, F., Haroun, R., & Espino, F. (2014). Economic assessment of ecosystem services: Monetary value of seagrass meadows for coastal fisheries. *Ocean and Coastal Management*, 96, 181-187. (DOI 10.1016/j.ocecoaman.2014.04.032)
- Udy, J. W., & Dennison, W. C. (1997). Physiological responses of seagrasses used to identify anthropogenic nutrient inputs. *Marine and Freshwater Research*, 48(7), 605-614. (DOI 10.1071/MF97001)
- United Nations. (2016). *Map Accuracy Assessment and Area Estimation: A Practical Guideline*. National Forest Monitoring Assessment Working Paper No.46/E. Food and Agriculture Organization of the United Nations, Rome, Italy. 69p.
- Unsworth, R. K. F., Cullen, L. C., Pretty, J. N., Smith, D. J., & Bell, J. J. (2010). Economic and subsistence values of the standing stocks of seagrass fisheries: Potential benefits of no-fishing marine protected area management. *Ocean and Coastal Management*, 53(5), 218-224. (DOI 10.1016/j.ocecoaman.2010.04.002)
- Unsworth, R. K. F., Nordlund, L. M., & Cullen-Unsworth, L. C. (2019). Seagrass meadows support global fisheries production. *Conservation Letters*, 12(1). (DOI 10.1111/conl.12566)
- Ursani, A. A., Kpalma, K., Lelong, C. C. D., & Ronsin, J. (2012). Fusion of textural and spectral information for tree crop and other agricultural cover mapping with very-high resolution satellite images. *IEEE Journal of Selected Topics in Applied Earth Observations and Remote Sensing*, 5(1), 225-235. (DOI 10.1109/JSTARS.2011.2170289)
- Valle, M., Palà, V., Lafon, V., Dehouck, A., Garmendia, J. M., Borja, A., & Chust, G. (2015). Mapping estuarine habitats using airborne hyperspectral imagery, with special focus on seagrass meadows. *Estuarine, Coastal and Shelf Science*, 164, 433-442. (DOI 10.1016/j.ecss.2015.07.034)
- van Eijk, A. M. J., Kusmierczyk-Michulec, J. T., Francius, M. J., Tedeschi, G., Piazzola, J., Merritt, D. L., & Fontana, J. D. (2011). Sea-spray aerosol particles generated in the surf zone. *Journal of Geophysical Research*, 116(D19). (DOI 10.1029/2011JD015602)
- Van Kreveld, M., Van Lankveld, T., & Veltkamp, R. C. (2011). On the shape of a set of points and lines in the plane. *Computer Graphics Forum*, 30(5), 1553-1562. (DOI 10.1111/j.1467-8659.2011.02029.x)
- Vandermeulen, H. (2014). Bay-scale assessment of eelgrass beds using sidescan and video. *Helgoland Marine Research*, 68(4), 559-569. (DOI 10.1007/s10152-014-0412-5)
- Vasuki, Y., Holden, E.-J., Kovesi, P., & Micklethwaite, S. (2014). Semi-automatic mapping of geological Structures using UAV-based photogrammetric data: An image analysis approach. *Computers & Geosciences*, 69, 22-32. (DOI 10.1016/j.cageo.2014.04.012)
- Ventura, D., Bonifazi, A., Gravina, M., Belluscio, A., & Ardizzone, G. (2018). Mapping and Classification of Ecologically Sensitive Marine Habitats Using Unmanned Aerial Vehicle (UAV) Imagery and Object-Based Image Analysis (OBIA). *Remote Sensing*, 10(9). (DOI 10.3390/rs10091331)
- Ventura, D., Bruno, M., Jona Lasinio, G., Belluscio, A., & Ardizzone, G. (2016). A low-cost drone based application for identifying and mapping of coastal fish nursery grounds. *Estuarine, Coastal and Shelf Science*, 171, 85-98. (DOI 10.1016/j.ecss.2016.01.030)
- Vergeer, L. H. T., & den Hartog, C. (1994). Omnipresence of Labyrinthulaceae in seagrasses. *Aquatic Botany*, 48(1), 1-20. (DOI 10.1016/0304-3770(94)90070-1)

- Vermeulen, C., Lejeune, P., Lisein, J., Sawadogo, P., & Bouché, P. (2013). Unmanned aerial survey of elephants. *PLoS One*, *8*(2), e54700. (DOI 10.1371/journal.pone.0054700)
- Wahidin, N., Siregar, V. P., Nababan, B., Jaya, I., & Wouthuyzen, S. (2015). Object-based image analysis for coral reef benthic habitat mapping with several classification algorithms. *Procedia Environmental Sciences*, *24*(C), 222-227. (DOI 10.1016/j.proenv.2015.03.029)
- Waikato Regional Council (Compiler) (2011). *Waikato Regional Coastal Plan*: Waikato Regional Council, Hamilton
- Waikato Regional Council. (2012a). *Aerial Photography - WRAPS 2012 - GIS Layer*. http://data.waikatoregion.govt.nz:8080/ords/f?p=140:12:0::NO::P12_METADATA_A_ID:3.
- Waikato Regional Council. (2012b). *Extent of coastal habitats - Results - data and trends*. from <http://www.waikatoregion.govt.nz/Environment/Environmental-information/Environmental-indicators/Coasts/coastal-habitats-report/co2-data/>.
- Waikato Regional Council (Compiler) (2013). *Hauraki Gulf Marine Spatial Plan - GIS Layer*http://data.waikatoregion.govt.nz:8080/ords/f?p=140:12:28861662811822::NO::P12_METADATA_ID:967.
- Waikato Regional Council (Compiler) (2014). *Estuarine Vegetation and Harbours - GIS Layer*. http://data.waikatoregion.govt.nz:8080/ords/f?p=140:12:829106124005::NO::P12_METADATA_ID:942
- Wang, B., Li, W., Liu, L., & Huang, G. H. (2016). Influence of sludge reflux ratios on biodegradation performance in a coupled landfill leachate treatment process based on UASB and submerged MBR. *Journal of Environmental Science and Health - Part A Toxic/Hazardous Substances and Environmental Engineering*, *51*(9), 701-706. (DOI 10.1080/10934529.2016.1170428)
- Wang, C., Yu, J.-Y., Wang, P.-F., & Guo, P.-C. (2009). Flow structure of partly vegetated open-channel flows with eelgrass. *Journal of Hydrodynamics, Ser.B*, *21*(3), 301-307. (DOI 10.1016/S1001-6058(08)60150-X)
- Warner, T. (2011). Kernel-based texture in remote sensing image classification. *Geography Compass*, *5*(10), 781-798. (DOI 10.1111/j.1749-8198.2011.00451.x)
- Watts, A. C., Ambrosia, V. G., & Hinkley, E. A. (2012). Unmanned aircraft systems in remote sensing and scientific research: Classification and considerations of use. *Remote Sensing*, *4*(6), 1671-1692. (DOI 10.3390/rs4061671)
- Watts, A. C., Perry, J. H., Smith, S. E., Burgess, M. A., Wilkinson, B. E., Szantoi, Z., Ifju, P. G., & Percival, H. F. (2010). Small unmanned aircraft systems for low-altitude aerial surveys. *Journal of Wildlife Management*, *74*(7), 1614-1619. (DOI 10.2193/2009-425)
- Waycott, M., Duarte, C. M., Carruthers, T. J. B., Orth, R. J., Dennison, W. C., Olyarnik, S., Calladine, A., Fourqurean, J. W., Heck, K. L., Hughes, A. R., Kendrick, G. A., Kenworthy, W. J., Short, F. T., Williams, S. L., & Paine, R. T. (2009). Accelerating loss of seagrasses across the globe threatens coastal ecosystems. *Proceedings of the National Academy of Sciences of the United States of America*, *106*(30), 12377-12381. (DOI 10.1073/pnas.0905620106)
- Webb, A. R. (2003). *Statistical Pattern Recognition*. (2nd ed.). West Sussex, England: Wiley.
- Weissensteiner, M. H., Poelstra, J. W., & Wolf, J. B. W. (2015). Low-budget ready-to-fly unmanned aerial vehicles: an effective tool for evaluating the nesting status of canopy-breeding bird species. *Journal of Avian Biology*, *46*(4), 425-430. (DOI 10.1111/jav.00619)
- Whitehead, K., Hugenholtz, C. H., Myshak, S., Brown, O., LeClair, A., Tamminga, A., Barchyn, T. E., Moorman, B., & Eaton, B. (2014). Remote sensing of the environment with small unmanned aircraft systems (UASs), part 2: scientific and

- commercial applications. *Journal of Unmanned Vehicle Systems*, 02(03), 86-102. (DOI 10.1139/juvs-2014-0007)
- Whiteside, T. G., Boggs, G. S., & Maier, S. W. (2011). Comparing object-based and pixel-based classifications for mapping savannas. *International Journal of Applied Earth Observations and Geoinformation*, 13(6), 884-893. (DOI 10.1016/j.jag.2011.06.008)
- Whiteside, T. G., Maier, S. W., & Boggs, G. S. (2014). Area-based and location-based validation of classified image objects. *International Journal of Applied Earth Observations and Geoinformation*, 28(1), 117-130. (DOI 10.1016/j.jag.2013.11.009)
- Widdows, J., Pope, N. D., Brinsley, M. D., Asmus, H., & Asmus, R. M. (2008). Effects of seagrass beds (*Zostera noltii* and *Z. marina*) on near-bed hydrodynamics and sediment resuspension. *Marine Ecology Progress Series*, 358, 125-136. (DOI 10.3354/meps07338)
- Wildi, O. (2013). *Static Predictive Modelling*. Chichester, UK: John Wiley & Sons.
- Wilkes, R., Bennion, M., McQuaid, N., Beer, C., McCullough-Annett, G., Colhoun, K., Inger, R., & Morrison, L. (2017). Intertidal seagrass in Ireland: Pressures, WFD status and an assessment of trace element contamination in intertidal habitats using *Zostera noltei*. *Ecological Indicators*, 82, 117-130. (DOI 10.1016/j.ecolind.2017.06.036)
- Wilson, K. L., Skinner, M. A., & Lotze, H. K. (2019). Eelgrass (*Zostera marina*) and benthic habitat mapping in Atlantic Canada using high-resolution SPOT 6/7 satellite imagery. *Estuarine, Coastal and Shelf Science*, 226. (DOI 10.1016/j.ecss.2019.106292)
- Wing, M. G., Eklund, A., & Kellog, L. D. (2005). Consumer-grade global positioning system (GPS) accuracy and reliability. *Journal of Forestry*, 103(4), 169-173. (DOI 10.1093/jof/103.4.169)
- Wood, N., & Lavery, P. (2000). Monitoring seagrass ecosystem health—the role of perception in defining health and indicators. *Ecosystem Health*, 6(2), 134-148. (DOI 10.1046/j.1526-0992.2000.00015.x)
- Xiang, S., Nie, F., Meng, G., Pan, C., & Zhang, C. (2012). Discriminative least squares regression for multiclass classification and feature selection. *IEEE Transactions on Neural Networks and Learning Systems*, 23(11), 1738-1754. (DOI 10.1109/TNNLS.2012.2212721)
- Xu, C., & Anwar, A. (2013). Based on the decision tree classification of remote sensing image classification method application. *Applied Mechanics and Materials*, 316-317, 193. (DOI 10.4028/www.scientific.net/AMM.316-317.193)
- Xu, C., Li, Y., Hu, J., Yang, X., Sheng, S., & Liu, M. (2012). Evaluating the difference between the normalized difference vegetation index and net primary productivity as the indicators of vegetation vigor assessment at landscape scale. *Environmental Monitoring and Assessment*, 184, 1275-1286. (DOI 10.1007/s10661-011-2039-1)
- Xu, S., Xu, S., Zhou, Y., Zhao, P., Yue, S., Song, X., Zhang, X., Gu, R., Wang, P., & Zhang, Y. (2019). Single beam sonar reveals the distribution of the eelgrass *Zostera marina* L. and threats from the green tide algae *Chaetomorpha linum* K. in Swan-Lake lagoon (China). *Marine Pollution Bulletin*, 145, 611-623. (DOI 10.1016/j.marpolbul.2019.06.022)
- Xue, J., & Su, B. (2017). Significant remote sensing vegetation indices: A review of developments and applications. *Journal of Sensors*, 2017. (DOI 10.1155/2017/1353691)
- Yang, C.-C., Prasher, S. O., Enright, P., Madramootoo, C., Burgess, M., Goel, P. K., & Callum, I. (2003). Application of decision tree technology for image classification using remote sensing data. *Agricultural Systems*, 76(3), 1101-1117. (DOI 10.1016/S0308-521X(02)00051-3)

- Yang, D., & Qin, S. (2016). Restoration of partial blurred image based on blur detection and classification. *Journal of Electrical and Computer Engineering, ID 2374926*, 1-12. (DOI 10.1155/2016/2374926)
- Yang, D., & Yang, C. (2009). Detection of seagrass distribution changes from 1991 to 2006 in Xincun Bay, Hainan, with satellite remote sensing. *Sensors, 9*(2), 830-844. (DOI 10.3390/s90200830)
- Yang, L., Mansaray, L., Huang, J., & Wang, L. (2019). Optimal segmentation scale parameter, feature subset and classification algorithm for geographic object-based crop recognition using multisource satellite imagery. *Remote Sensing, 11*(5). (DOI 10.3390/rs11050514)
- Ye, S., Pontius, R. G., & Rakshit, R. (2018). A review of accuracy assessment for object-based image analysis: From per-pixel to per-polygon approaches. *ISPRS Journal of Photogrammetry and Remote Sensing, 141*, 137-147. (DOI 10.1016/j.isprsjprs.2018.04.002)
- Yengoh, G. T., Dent, D., Olsson, L., Tengberg, A. E., & Tucker Iii, C. J. (2015). *Use of the Normalized Difference Vegetation Index (NDVI) to Assess Land Degradation at Multiple Scales: Current Status, Future Trends, and Practical Considerations*. (1st ed. 2015 ed.). Cham: Springer International Publishing.
- York, P., Gruber, R., Hill, R., Ralph, P., Booth, D., & Macreadie, P. (2013). Physiological and morphological responses of the temperate seagrass *Zostera muelleri* to multiple stressors: Investigating the interactive effects of light and temperature. *PLoS One, 8*(10), e76377. (DOI 10.1371/journal.pone.0076377)
- Young, D., Clinton, P., & Specht, D. (2010). Mapping intertidal eelgrass (*Zostera marina* L.) in three coastal estuaries of the Pacific Northwest USA using false colour near-infrared aerial photography. *International Journal of Remote Sensing, 31*(7), 1699-1715. (DOI 10.1080/01431160902926590)
- Zahawi, R. A., Dandois, J. P., Holl, K. D., Nadwodny, D., Reid, J. L., & Ellis, E. C. (2015). Using lightweight unmanned aerial vehicles to monitor tropical forest recovery. *Biological Conservation, 186*, 287-295.
- Zaman, M., & Hirose, H. (2011). Classification performance of bagging and boosting type ensemble methods with small training sets. *New Generation Computing, 29*(3), 277-292. (DOI 10.1007/s00354-011-0303-0)
- Zanotta, D. C., Zortea, M., & Ferreira, M. P. (2018). A supervised approach for simultaneous segmentation and classification of remote sensing images. *ISPRS Journal of Photogrammetry and Remote Sensing, 142*, 162-173. (DOI 10.1016/j.isprsjprs.2018.05.021)
- Zhang, D. (2019). *Fundamentals of Image Data Mining Analysis, Features, Classification and Retrieval*. (1st ed. 2019. ed.). Cham: Springer International Publishing : Imprint: Springer.
- Zhang, J. (2013). The Study of Remote Sensing Image Classification Based on Support Vector Machine. *Sensors & Transducers, 159*(11), 46-53.
- Zhang, H., Fritts, J. E., & Goldman, S. A. (2008). Image segmentation evaluation: A survey of unsupervised methods. *Computer Vision and Image Understanding, 110*(2), 260-280. (DOI 10.1016/j.cviu.2007.08.003)
- Zhang, H., Zheng, J., Dorr, G., Zhou, H., & Ge, Y. (2014). Testing of GPS accuracy for precision forestry applications. *Arabian Journal for Science and Engineering, 39*(1), 237-245. (DOI 10.1007/s13369-013-0861-1)
- Zhang, L., & Baas, A. C. W. (2012). Mapping functional vegetation abundance in a coastal dune environment using a combination of LSMA and MLC: a case study at Kenfig NNR, Wales. *International Journal of Remote Sensing, 33*(16), 5043. (DOI 10.1080/01431161.2012.657369)
- Zheng, H., Cheng, T., Li, D., Zhou, X., Yao, X., Tian, Y., Cao, W., & Zhu, Y. (2018). Evaluation of RGB, color-infrared and multispectral images acquired from unmanned aerial systems for the estimation of nitrogen accumulation in rice. *Remote Sensing, 10*(6), 1-17. (DOI 10.3390/rs10060824)

- Zhu, H., Meng, F., Cai, J., & Lu, S. (2016). Beyond pixels: A comprehensive survey from bottom-up to semantic image segmentation and cosegmentation. *Journal of Visual Communication and Image Representation*, 34(C), 12-27. (DOI 10.1016/j.jvcir.2015.10.012)
- Zieliński, T., Petelski, T., Makuch, P., Strzałkowska, A., Ponczkowska, A., Markowicz, K. M., Chourdakis, G., Georgoussis, G., Kratzer, S., Systemekologiska, i., Stockholms, u., & Naturvetenskapliga, f. (2012). Studies of aerosols advected to coastal areas with the use of remote techniques. *Acta Geophysica*, 60(5), 1359-1385. (DOI 10.2478/s11600-011-0075-4)
- Zolderdo, A. J., Struthers, D. P., Cooke, S. J., Stemberger, H. L. J., & Lawrence, M. J. (2015). The effects of modern war and military activities on biodiversity and the environment. *Environmental Reviews*, 23(4), 443-460. (DOI 10.1139/er-2015-0039)
- Zomer, R. J., Trabucco, A., & Ustin, S. L. (2009). Building spectral libraries for wetlands land cover classification and hyperspectral remote sensing. *Journal of Environmental Management*, 90(7), 2170-2177. (DOI 10.1016/j.jenvman.2007.06.028)
- Zweig, C. L., Burgess, M. A., Percival, H. F., & Kitchens, W. M. (2015). Use of unmanned aircraft systems to delineate fine-scale wetland vegetation communities. *Wetlands*, 35(2), 303-309. (DOI 10.1007/s13157-014-0612-4)